



**Titre:** Dually-Polarized Microwave Components Based on Polarization-  
Title: Selective Coupling for Green Wireless Systems

**Auteur:** Ahmed Sakr  
Author:

**Date:** 2018

**Type:** Mémoire ou thèse / Dissertation or Thesis

**Référence:** Sakr, A. (2018). Dually-Polarized Microwave Components Based on Polarization-  
Citation: Selective Coupling for Green Wireless Systems [Thèse de doctorat, École  
Polytechnique de Montréal]. PolyPublie. <https://publications.polymtl.ca/3136/>

 **Document en libre accès dans PolyPublie**  
Open Access document in PolyPublie

**URL de PolyPublie:** <https://publications.polymtl.ca/3136/>  
PolyPublie URL:

**Directeurs de  
recherche:** Ke Wu  
Advisors:

**Programme:** génie électrique  
Program:

UNIVERSITÉ DE MONTRÉAL

DUALLY-POLARIZED MICROWAVE COMPONENTS BASED ON POLARIZATION-  
SELECTIVE COUPLING FOR GREEN WIRELESS SYSTEMS

AHMED SAKR

DÉPARTEMENT DE GÉNIE ÉLECTRIQUE  
ÉCOLE POLYTECHNIQUE DE MONTRÉAL

THÈSE PRÉSENTÉE EN VUE DE L'OBTENTION  
DU DIPLÔME DE PHILOSOPHIAE DOCTOR  
(GÉNIE ÉLECTRIQUE)

JUIN 2018

© Ahmed Sakr, 2018.

UNIVERSITÉ DE MONTRÉAL

ÉCOLE POLYTECHNIQUE DE MONTRÉAL

Cette thèse intitulée :

DUALLY-POLARIZED MICROWAVE COMPONENTS BASED ON POLARIZATION-  
SELECTIVE COUPLING FOR GREEN WIRELESS SYSTEMS

présentée par : SAKR Ahmed

en vue de l'obtention du diplôme de : Philosophiae Doctor

a été dûment acceptée par le jury d'examen constitué de :

M. LAURIN Jean-Jacques, Ph. D., président

M. WU Ke, Ph. D., membre et directeur de recherche

M. DJERAFI Tarek, Ph. D., membre

M. KISHK Ahmed, Ph. D., membre externe

## **DEDICATION**

*To my parents*

## ACKNOWLEDGMENTS

I would never have been possible to finish my dissertation without the help of ALLAH. May ALLAH shower us always with his mercy and blessings. Amen! Above all, I would like to thank my mother for her personal support and great patience at all times. My father, brother, sisters and brother-in-law have given me their unequivocal support throughout, as always, for which my mere expression of thanks likewise does not suffice. I cannot find words that express my deepest gratitude to Dr. Walid Dyab, a postdoctoral fellow in our group. Honestly speaking and without any hesitation, I would say that the work of this dissertation could not be accomplished without his contribution. Dr. Dyab has a main contribution in every single point presented in this dissertation. My greatest thanks goes to him. After two years of working together, I believe Dr. Dyab is an outstanding researcher and rising research star. He has manifested a very high level of creativity in scientific research. Foremost among, I extend my sincere and deepest gratitude to my research advisor, Prof. Ke Wu, for his excellent guidance, caring, patience, and providing me with an excellent atmosphere for doing research. It is a great experience to work under the supervision of Prof. Wu with his well-known outstanding academic records. This increased my responsibilities and accordingly my motivation to meet his expectations from my side. I wish I did so! Our published journals would not have been possible without his experience and instructions. I have also taken a graduate course with Prof. Wu that greatly enhanced my knowledge in electromagnetics. The good advice, support, and friendship of Prof. Wu, has been invaluable on both an academic and a personal level, for which I am extremely grateful. His enthusiasm and passion to our work have always motivated me to work harder. I am very thankful to my advisor. I would like to acknowledge the financial, academic and technical support of PERSWADE in the award of a postgraduate scholarship. I would like to thank all the technical staffs of Poly-Grames Research Center and the administration staff as well. I also take this opportunity to express a deep sense of gratitude to Mr. Ossama Elmogy, Dr. Ahmed Sadek, Dr. Ahmed Korashy, Ahmed Medhat, Adham Ismail and Zaki Ajabi on the personal level, the discussions with them were really invaluable and shared in supporting me during my PhD studies and for the enjoyable times that we spent together throughout my PhD. Last, but no means least, I thank my master advisor Prof. Alaa Abdelmageed, my friends Islam Hashem, Tarek Ameen, Mohamed Zaghloul, Amr Mahmoud, and Ahmed Elshaikh for their support and encouragement. For any errors or inadequacies that may remain in this work, of course, the responsibility is entirely my own.

## RÉSUMÉ

Avec le développement rapide et continu de technologies et de réseaux sans fil de nouvelle génération tels que la 5G et avec les ressources limitées d'énergie et de spectre disponibles pour soutenir ces développements sans fil rapides, l'exploration des bandes millimétriques sous-utilisées devient incontournable. Il devient de plus en plus crucial de se concentrer sur la réduction de la consommation d'énergie dans les futurs systèmes sans fil. Le moyen le plus efficace de réception d'énergie d'onde électromagnétique est de capturer complètement les deux composantes orthogonales de son vecteur de champ de propagation en relation avec la diversité de polarisation. De plus, l'utilisation d'ondes bi-polarisées permet l'amélioration d'une capacité de transmission via la réception simultanée de deux canaux orthogonaux. Cette thèse montre comment proposer et exploiter le concept très original de la diversité de polarisation sur la bande de fréquences mmW qui a été assignée aux applications sans fil. Auparavant, la diversité de polarisation était mise en œuvre dans des profils non planaires, ce qui compliquait son intégration avec l'application de carte de circuit imprimé (PCB). Par conséquent, la motivation principale de cette thèse est de mettre en œuvre la diversité de polarisation dans les profils planaires aux bandes de fréquence récemment assignées autour de 28 GHz et 38 GHz pour être intégrée dans la cinquième génération (5G) de communication sans fil.

Ceci est fait en développant la théorie du fonctionnement et de la procédure de conception des composants MMW à double polarisation. La nouveauté présentée dans ce travail de thèse réside dans le développement d'un principe de fonctionnement permettant de concevoir et de mettre en évidence une classe de composants mmW bi-polarisés, à savoir les coupleurs 3dB, les coupleurs 0dB et les déphaseurs. Cela permet le développement de réseaux de formation de faisceau bi-polarisés tels que la matrice de Butler et les systèmes de télédétection à polarisation, basés sur une jonction à six ports à double polarisation. Une procédure de conception analytique complète est présentée avec des vérifications à travers des simulations pleine onde et des mesures de prototypes.

La diversité de polarisation a été un facteur essentiel dans la performance et l'amélioration de la capacité de divers systèmes sans fil, y compris les réseaux cellulaires. Par conséquent, la conception et le développement de structures d'alimentation d'antenne bi-polarisées dans la bande mmW sont indispensables. Tout d'abord, en tant que dispositif bipolaire de base, une conception de transducteur orthomode compact (OMT) dans la bande Ka est proposée. La nouveauté de l'OMT

proposée découle d'un concept distinct de traitement des signaux bi-polarisés basés sur un coupleur sélectif de polarisation (PSC). La théorie du PSC est développée et comprise à travers l'analyse de ses guides d'ondes constitutifs. De tels guides d'ondes sont des formes hybrides de guide d'ondes diélectrique non radiatif intégré au substrat (SINRD) et de guide d'ondes intégré au substrat (SIW). Une procédure analytique basée sur le terrain est ensuite présentée et développée pour une modélisation précise des paramètres effectifs du guide d'onde SINRD. Ce modèle est basé sur l'analyse de mode propre d'un matériau de substrat diélectrique perforé avec des trous d'air et enfermé entre deux plaques métalliques horizontales. A partir de ce modèle, on trouve que la constante diélectrique effective résultante d'une géométrie périodique du guide d'onde SINRD dépend de la direction d'un vecteur de champ électrique par rapport à la périodicité du matériau. En d'autres termes, les parties guidantes des guides d'onde SINRD agissent comme des matériaux anisotropes. Le modèle proposé fournit un schéma pour l'isotropisation des substrats anisotropes. Ceci est en plus de clarifier les régimes exacts de fonctionnement à l'intérieur du guide d'onde SINRD basé sur le mécanisme de guidage.

PSC pourrait alors être réalisé dans les structures intégrées en raison de différents mécanismes par lesquels les modes orientés orthogonalement sont guidés. Des niveaux de couplage théoriques de 0 dB sont possibles dans la structure conçue. L'analyse analytique et les étapes de conception sont détaillées. Cette analyse facilite un contrôle complet de l'opération monomode pour chaque polarisation. Ce contrôle, outre que la structure est plane, représente les principaux avantages de la structure proposée. Ensuite, un prototype est mis en œuvre et mesuré où un excellent accord est obtenu avec les résultats de la simulation. Un modèle de circuit équivalent est déduit pour la modélisation des caractéristiques de dispersion du PSC. Par conséquent, des méthodologies de conception soutenues par une étude théorique complète et une analyse de simulation pour un OMT basé sur la PSC sont élaborées et examinées.

La conception générale d'un OMT à base de PSC dépend essentiellement d'un guide d'ondes de coupleur de plaque diélectrique avec une paroi de polariseur PEC périodique en son milieu. En d'autres termes, la structure PSC peut être considérée comme deux guides d'ondes fusionnés en parallèle. Lorsque l'un des guides d'ondes est excité par une onde bi-polarisée, la polarisation verticale reste dans le guide d'onde excité tandis que la polarisation horizontale est entièrement couplée à l'autre. Des limitations pratiques pour cette conception sont discutées et supportées avec

des solutions utilisant un coupleur de fente supérieur proposé au lieu du coupleur de dalle diélectrique. Des équations de forme fermée sont obtenues en tant que recettes de conception pour calculer les dimensions de la structure et la largeur de bande en fonction de la fréquence de fonctionnement et des paramètres du matériau. La structure proposée est prototypée et mesurée.

En tant qu'application, une jonction à six ports est développée sur la base de la PSC. Le six ports est le module le plus fondamental pour développer des émetteurs-récepteurs interférométriques. Cette jonction est présentée dans cette thèse sous une nouvelle forme. Dans la nouvelle forme, la jonction à six ports applique sa fonctionnalité sur deux polarisations orthogonales simultanément. La jonction à six ports bi-polarisés est inventée en ajoutant la caractéristique bi-polarisée à chacun de ses composants constitutifs, à savoir les diviseurs de puissance, les coupleurs hybrides 3dB et les déphaseurs à courbure circulaire. Ces composants sont étudiés analytiquement et ré-inventés pour être bi-polarisés en utilisant le concept de PSC susmentionné. La jonction à six ports doublement polarisée est prototypée et mesurée. De même, un dispositif de matrice de Butler à double polarisation est mis en œuvre sur la base du PSC approprié pour des applications de formation de faisceau.

## ABSTRACT

With the rapid and continuous development of new generation wireless technologies and networks such as 5G and with the limited enabling energy and spectrum resources available in support of such fast-moving wireless developments, exploring the underutilized millimeter-wave (mmW) bands becomes inescapable. It becomes more and more crucial to focus on the reduction of energy use in future wireless systems. The most efficient way of electromagnetic wave energy reception is to fully capture the two orthogonal components of its propagating field vector in connection with polarization diversity. In addition, the use of dually-polarized waves allows the enhancement of a transmission capability via the simultaneous reception of two orthogonal channels. This thesis shows how to propose and exploit the highly original concept of polarization diversity over the mmW frequency band which has been assigned for wireless applications. Previously, the polarization diversity was implemented within non-planar profiles which complicates its integration with the printed circuit board (PCB) application. Therefore, the main motivation of this thesis is to implement the polarization diversity within planar profiles at the recently assigned frequency bands around 28 GHz and 38 GHz to be suitable for integration in the fifth generation (5G) of wireless communication.

This is done by developing the theory of operation and design procedure of dually-polarized mmW components. The novelty presented in this thesis work lies in developing a principle of operation to come up with the design and demonstration of a class of dually-polarized mmW components, namely 3dB couplers, 0dB couplers and phase shifters. This allows the development of dually-polarized beamforming networks such as Butler matrix and polarization-inclusive remote sensing systems based on a dually-polarized six-port junction. A full analytical design procedure is presented with verifications through full-wave simulations and prototype measurements.

Polarization diversity has been an essential factor in the performance and capacity enhancement of various wireless systems including cellular networks. Accordingly, the design and development of dually-polarized antenna feeding structures in the mmW band is a must. Firstly, as the basic dual-polarized device, a compact orthomode transducer (OMT) design in the Ka-band is proposed. The novelty of the proposed OMT stems from a distinct concept of handling dually-polarized signals based on a polarization selective coupler (PSC). The theory of PSC is developed and understood

through the analysis of its constituent waveguides. Such waveguides are hybrid forms of substrate integrated nonradiative dielectric (SINRD) waveguide and substrate integrated waveguide (SIW).

A field-based analytical procedure is then presented and developed for accurate modelling of the effective parameters of SINRD waveguide. This model is based on the eigenmode analysis of a dielectric substrate material perforated with air-holes and enclosed between two horizontal metallic plates. From this model, it is found that the resulting effective dielectric constant of a periodic geometry of the SINRD waveguide is dependent on the direction of an electric field vector with respect to the material periodicity. In other words, the guiding parts of the SINRD waveguides act as anisotropic materials. The proposed model provides a scheme for the isotropization of anisotropic substrates. This is in addition to clarifying the exact regimes of operation inside the SINRD waveguide based on the guiding mechanism.

PSC could then be realized in the integrated structures due to different mechanisms by which orthogonally oriented modes are guided. Theoretical coupling levels of 0dB are possible in the designed structure. Theoretical analysis and design steps are given in details. This analysis facilitates a complete control on the single mode operation for each polarization. Besides the structure being planar, this control represents the main advantages of the proposed structure. Then, a prototype is implemented and measured where an excellent agreement is achieved with the simulation results. An equivalent circuit model is deduced for modeling dispersion characteristics of the PSC. Consequently, design methodologies supported through comprehensive theoretical study and simulation analysis for a PSC-based OMT are developed and examined.

The general design of a PSC-based OMT basically depends on a dielectric slab coupler waveguide with a longitudinal periodic PEC polarizer wall in its middle. In other words, The PSC structure can be considered as two waveguides which are fused together in parallel. When one of the waveguides is excited by a dually-polarized wave, the vertical polarization remains in the excited waveguide while the horizontal polarization is fully coupled to the other one. Practical limitations of this design are discussed and supported by solutions using a proposed top slot coupler instead of the dielectric slab coupler. Closed-form equations are obtained as design recipes for computing structure dimensions and bandwidth based on operating frequency and the material parameters. The proposed structure is prototyped and measured.

As an application, a six-port junction is developed based on the PSC. The six-port is the most fundamental module for developing interferometric transceivers. This junction is presented in this thesis in a new form. In the new form, the six-port junction applies its functionality on two orthogonal polarizations simultaneously. The dually-polarized six-port junction is invented by adding the dually-polarized feature to each of its constituent components, namely the power dividers, the hybrid 3dB couplers and the circularly-bent phase shifters. These components are analytically studied and re-invented to be dually-polarized using the aforementioned PSC concept. The dually-polarized six-port junction is prototyped and measured. Similarly, a dually-polarized Butler matrix device is implemented based on the PSC suitable for beamforming applications.

## TABLE OF CONTENTS

DEDICATION .....	III
ACKNOWLEDGMENTS.....	IV
RÉSUMÉ.....	V
ABSTRACT .....	VIII
LIST OF FIGURES.....	XIV
LIST OF SYMBOLS AND ABBREVIATIONS.....	XXI
LIST OF APPENDICES .....	XXIII
CHAPTER 1 INTRODUCTION.....	1
1.1 General Discussion.....	1
1.2 State-of-the-art of Polarization Diversity .....	4
1.3 Thesis organization .....	8
CHAPTER 2 SPECIAL DUALY-POLARIZED INTEGRATED WAVEGUIDES.....	9
2.1 SIW guiding structures for polarization diversity .....	10
2.2 NRD guiding structures and its image form.....	12
2.2.1 Modelling Effective Anisotropy of SINRD Waveguide.....	14
2.2.2 Integrated NRD Waveguide .....	32
2.2.3 Image-NRD waveguide.....	36
2.3 Hybrid NRD-SIW guiding structure and its image form .....	37
2.3.1 Hybrid NRD-SIW waveguide .....	38
2.3.2 Image-NRD-SIW waveguide .....	39
2.4 Conclusion and design rules discussion .....	41
CHAPTER 3 POLARIZATION SEPARATION AND COMBINATION.....	44

3.1	Polarization selective coupling (PSC).....	44
3.1.1	Image-NRD coupler .....	44
3.1.2	The Concept of Polarization Selectivity for Polarization Discrimination.....	50
3.1.3	Validation of the Isotropization Concept using PSC .....	55
3.1.4	Orthomode Transducer design based on Polarization Selective Coupler .....	58
3.2	Effective polarization independent coupling (EPIC) .....	76
3.2.1	EPIC Operation .....	76
3.2.2	Controllability of the Dielectric Constant .....	78
3.2.3	Results and Discussions .....	80
3.3	Conclusion.....	81
CHAPTER 4 APPLICATIONS – PLANAR DUAL-POLARIZED PSC-BASED MICROWAVE COMPONENTS.....		83
4.1	Polarization Selective Coupling .....	86
4.2	Dual-polarized power divider.....	88
4.3	Dual-polarized hybrid coupler .....	90
4.4	Waveguide bend for dual-polarization phase equalization .....	92
4.5	Dually-polarized six-port junction .....	96
4.6	Operation principle of dually-polarized Butler matrix.....	102
4.6.1	Dually-polarized couplers with dual-phase-shifts.....	104
4.6.2	Dually-Polarized Phase Shifter .....	110
4.6.3	The Complete Dually Polarized Butler Matrix .....	113
4.7	Conclusion.....	122
CHAPTER 5 INTEGRATED POLARIZATION CONVERTER FOR PLANAR CROSS- POLARIZED MILLIMETER WAVE COMPONENTS.....		123
5.1	Motivation: Feasibility of Planar Integrated Cross-Polarized mmW Components.....	123

5.2	Field Rotation in Uniaxial Media: Wave-Plates .....	125
5.3	Design Methodology and Performance Analysis of Uniaxial Polarization Converter	126
5.4	Prototype of an Integrated Planar Mode Converter .....	128
CHAPTER 6	CONCLUSION AND RECOMMENDATIONS.....	132
BIBLIOGRAPHY	.....	136

## LIST OF FIGURES

Figure 1.1: Signal transmission-reception procedure in the downlink (base station to handset) of current wireless communication systems, and the proposed greening technology. ....	2
Figure 1.2: Conceptual block diagram for Ka-band dually polarized base-station antenna feeding system.....	6
Figure 2.1. Cross-comparison of SIW cross-sectional dimensions in the mmW range.....	11
Figure 2.2. Physical structure of a two-dimensional periodic medium and its unit cell. ....	14
Figure 2.3. Theoretical and simulation dispersion curves for the first two modes of the periodic medium in Figure 2.2 at $i=0$ . ....	18
Figure 2.4. Theoretical and simulation field distributions for the first two modes of the periodic medium in Figure 2.2 at $i=0$ . ....	19
Figure 2.5. Physical structure a two-dimensional double periodic medium with its unit cell. ....	21
Figure 2.6. The calculated cross-sectional spatial relative permittivity based on (13). ....	21
Figure 2.7. Theoretical and simulation dispersion curves for the first two modes of the periodic medium in Figure 2.5 at $i=0$ . ....	22
Figure 2.8. Theoretical and simulation field distributions for the first two modes of the periodic medium in Figure 2.5 at $i=0$ . ....	23
Figure 2.9. Validation example for the eigenmode analysis of a two-dimensional periodic medium: (a) waveguide structure, (b) field distribution, (c) magnitude of scattering parameters and (d) propagation constant. ....	24
Figure 2.10. Validation example for the isotropization using periodic medium: (a) magnitude of the scattering parameters and (b) propagation constant. ....	27
Figure 2.11. Nonradiative dielectric waveguide: (a) equivalent structure, (b) equivalent circuit model, (c) dispersion curves for horizontally oriented modes and (d) field vector distribution for $LSM_{01}$ mode. ....	28

Figure 2.12. SINRD waveguide: (a) equivalent structure, (b) effective dielectric constant for the periodic medium, field distribution for LSM <sub>01</sub> mode at (c) 20 GHz, (d) 26 GHz and (e) 35 GHz. ....	30
Figure 2.13. NRD waveguide: (a) equivalent structure and (b) equivalent circuit model. ....	33
Figure 2.14. NRD waveguide characteristics: (a) dispersion curves, (b) cross-sectional field distribution of LSE <sub>00</sub> mode and (c) LSM <sub>01</sub> mode. ....	35
Figure 2.15. Image-NRD waveguide: (a) equivalent structure, (b) cross-sectional field distribution of LSM <sub>01</sub> mode and (c) dispersion curves. ....	37
Figure 2.16. Hybrid-NRD-SIW waveguide: (a) equivalent structure and (b) dispersion curves. ....	39
Figure 2.17. Image-NRD-SIW waveguide: (a) equivalent structure, (b) dispersion curves, (c) field distribution of TE <sub>10</sub> mode and (d) field distribution of LSM <sub>01</sub> mode. ....	40
Figure 3.1. Image-NRD coupler: (a) equivalent structure, (b) equivalent circuit model and (c) dispersion curves. ....	45
Figure 3.2. Field characteristics of image-NRD coupler at 38 GHz: (a) field distribution of LSE <sub>10</sub> mode, (b) power alternation for LSE <sub>10</sub> mode, (c) field distribution of LSM <sub>01</sub> mode and (d) power alternation for LSM <sub>01</sub> mode. ....	47
Figure 3.3. Polarization selective coupler (PSC): (a) equivalent structure supported with theoretical field vectors for the excited and coupled modes, (b) dispersion curves of horizontally polarized modes and (c) field distribution when adding input and output waveguides. ....	49
Figure 3.4. The parametric analysis for both of (a) the spacing $d$ and (b) the coupling length $L_c$ of the PSC-based OMT design. ....	52
Figure 3.5. The scattering parameters with field distributions at the input and output ports for the PSC-based OMT for the vertically polarized TE <sub>10</sub> mode (Mode1) and the horizontally polarized TE <sub>01</sub> mode (Mode2). ....	54
Figure 3.6. (a) Polarization selective coupler (PSC), (b) dispersion curves for the common waveguide, (c) full coupling length versus frequency and (d) field distribution in the PSC at 38 GHz. ....	56
Figure 3.7. Magnitude of scattering parameters for (a) TE <sub>10</sub> mode and (b) TE <sub>01</sub> mode. ....	58

Figure 3.8. Different views for the general form of a dielectric-filled PSC-based OMT shown in elevation, side view, plan, and isometric cuts. ....	59
Figure 3.9. PSC-based OMT filled with an anisotropic dielectric material (Roger RT/Duroid 6010): (a) dispersion curves, (b) full coupling length versus frequency, (c) field distribution and (d) simulated S parameters. ....	62
Figure 3.10. PSC-based OMT filled with isotropic dielectric material (Roger 6002) (a) prototype and (b) measured versus simulated S parameters of the coupled mode $TE_{01}$ . Coupling length $L_c = 21$ mm, optimized matching length $L_m = 9.2$ mm and the waveguide cross-section. ....	65
Figure 3.11. PSC-based OMT prototype: (a) the dielectric substrate, (b) the metallic enclosure and (c) the overall structure. ....	68
Figure 3.12. Scattering parameters for the PSC-based OMT integrated with a square horn antenna (a) simulation and (b) measurements. ....	69
Figure 3.13. Simulated and measured antenna gain at 37 GHz for different excitations: (a) port 1: azimuth cut, (b) port 2: azimuth cut, (c) port 1: elevation cut and (d) port 2: elevation cut. .	70
Figure 3.14. Air-filled PSC-based OMT integrated with horn antenna: (a) isotropic view of the design (b) implemented prototype and (c) measurement setup in antenna anechoic chamber. ....	71
Figure 3.15. Performance analysis of the structure shown in Figure 3.14: (a) simulated field distribution in the receiving case. The polarization state of the incoming wave is arbitrarily chosen to be circular and (b) measured and simulated S parameters in the transmission case. ....	74
Figure 3.16. Simulated and measured results at (a) port 1: azimuth cut, (b) port 2: azimuth cut, (c) port 1: elevation cut and (d) port 2: elevation cut. ....	75
Figure 3.17. Effective polarization-independent coupler (EPIC): (a) general isometric view with its symbol, (b) effective permittivity tensor of a Rogers/duroid 6002 substrate perforated with air holes having the unit cell distribution in Figure 2.2 where $r = 0.2$ mm and $p = 0.8$ mm, (c) dispersion curves of the common waveguide when an effective material with the permittivity tensor in Figure 3.17 (b) fills the waveguide structure in Figure 3.17 (a), and (d) coupling lengths for the vertical and horizontal polarizations with the ratio between them. ....	77

- Figure 3.18. Effective polarization independent coupler (EPIC): (a) Physical prototype, (b) effective homogeneous permittivity tensor, (c) scattering parameters of the  $TE_{10}$  mode, (d) scattering parameters of the  $TE_{01}$  mode and (e) field distribution of the two modes. .... 79
- Figure 4.1. Conceptual block diagram for dually-polarized microwave components based on PSC versus typical microwave components..... 84
- Figure 4.2. Polarization selective coupler (PSC): (a) isometric structural view and (b) dispersion curves for horizontally polarized modes. .... 85
- Figure 4.3. Dually-polarized power divider based on PSC: (a) equivalent structure, (b) field distribution, (c) magnitude of scattering parameters for  $TE_{10}$  mode, (d) phase of scattering parameters for  $TE_{10}$  mode, (e) magnitude of scattering parameters for  $TE_{01}$  mode and (f) phase of scattering parameters for  $TE_{01}$  mode. .... 88
- Figure 4.4. Dually-polarized hybrid coupler based on PSC: (a) equivalent structure, (b) field distribution, (c) prototype, (d) magnitude of scattering parameters for  $TE_{10}$  mode, (e) magnitude of scattering parameters for  $TE_{01}$  mode and (f) phase of scattering parameters for both of the  $TE_{10}$  and  $TE_{01}$  modes. .... 90
- Figure 4.5. Phase shift bend equalizer: (a) equivalent structure and (b) phase difference between port 1 and port 2 for both of the  $TE_{10}$  and  $TE_{01}$  resulted from theory and HFSS simulation. 93
- Figure 4.6. Polarization-inclusive remote sensing (PIRS) as a possible application for the dually-polarized six-port junction. .... 95
- Figure 4.7. Dually-polarized six-port junction based on PSC: (a) block diagram with the ideal theoretical scattering parameters and (b) the overall equivalent structure. .... 97
- Figure 4.8. (a) Phase shift variation for the  $TE_{10}$  and  $TE_{01}$  modes due to a circular bend versus its inner radius and (b) phase difference variation between two circular bends versus frequency. .... 99
- Figure 4.9. Prototype of a dual-polarized six-port junction based on PSC: (a) overall structure and (b) transition to WR28 waveguide. .... 100
- Figure 4.10. Scattering parameters of dually-polarized six-port junction, simulation is solid line while measurement is dotted line: (a) magnitude when exciting  $TE_{10}$  from port 1, (b)

- magnitude when exciting  $TE_{01}$  from port 1 (c) magnitude when exciting  $TE_{10}$  from port 2 (d) magnitude when exciting  $TE_{01}$  from port 2 (e) phase when exciting  $TE_{10}$  from port 1 and port 2, (f) phase when exciting  $TE_{01}$  from port 1 and port 2. .... 101
- Figure 4.11. Dually-polarized Butler matrix, (a) Architecture of a base-station (BS) incorporating a dually-polarized 4-by-4 Butler matrix and (b) the structure of its internal components... 102
- Figure 4.12. Geometry of the proposed dually-polarized waveguide coupler made of metal and filled with arbitrary dielectric. The circular pins with diameter,  $g$ , are made of metal. .... 105
- Figure 4.13. Design of dually-polarized couplers, (a) dispersion curves of the common waveguide section, (b) S-parameters and field distribution of the vertically-polarized mode in a 3dB-coupler, (c) S-parameters and field distribution of the horizontally-polarized mode in a 3dB-coupler, (d) phase response of the 0dB coupler for the two polarizations, (e) S-parameters and field distribution of the vertically-polarized mode in a 0dB-coupler and (f) S-parameters and field distribution of the horizontally-polarized mode in a 0dB-coupler..... 108
- Figure 4.14. Dually-polarized phase shifter, (a) block diagram and principle of operation, (b) detailed geometry of phase shifter and full-wave simulation results for the whole unit. .... 111
- Figure 4.15. The complete assembly of the dually-polarized Butler matrix with detailed tabulated dimensions of each component. Ports 5 to 8 can be connected directly to the radiating cross-polarized antennas. In the prototype shown in the next section, those ports are connected to a mirrored image of the four curved paths connected at the input ports 1 to 4. All ports are connected to WR-15 transitions via the matching section shown in the top left corner. The width,  $a=3.21\text{mm}$ , is made slightly larger than  $b=3.2\text{mm}$  to be able to differentiate between the modes numerically. .... 113
- Figure 4.16. The complete prototype of the proposed dually-polarized Butler matrix, (a) Aluminum block with the waveguide cavities engraved into it, (b) A transition from square waveguide to the standard WR15 transition, (c) Field distribution for the vertical polarization calculated on HFSS at 60 GHz and (d) horizontal polarization. .... 116
- Figure 4.17. Measurement results of the prototype using Agilent vector network analyzer PNA-X from 58 to 62 GHz. The network is excited sequentially by vertical polarization at (a) port 1,

(b) port 2, (c) port 3, and (d) port 4 and by horizontal polarization at (e) port 1, (f) port 2, (g) port 3 and (h) port 4. The dashed lines represent the theoretical result to be achieved. .... 118

Figure 4.18. Progressive phase shift between the output ports of the dually polarized Butler matrix when excited sequentially by vertical polarization at (a) port 1, (b) port 2, (c) port 3, (d) port 4, and by horizontal polarization at (e) port 1, (f) port 2, (g) port 3 and (h) port 4. The dashed lines represent the theoretical result to be achieved. .... 119

Figure 4.19. The array radiation pattern calculated based on the measured S-parameters (solid lines) as compared to the theoretical pattern (dashed lines): (a) vertical polarization, and (b) horizontal polarization..... 121

Figure 4.20. Performance of back-to-back square-to-WR15 transitions ( $S_{11}$  and  $S_{21}$ ) and the cross-talk between the two orthogonal polarizations within the fabricated network ( $S_{vh}$ ). .... 121

Figure 5.1. Block diagram of cross-polarized mmW printed circuits including the polarization converter which is proposed in this dissertation. .... 124

Figure 5.2. Concept of field rotation in uniaxially anisotropic media, (a) Unbounded slab of uniaxial medium, (b) Bounded slab of uniaxial medium enclosed by the metallic walls of a square waveguide. In the coordinate system of the waveguide, the material is called skew uniaxial dielectric [2] and (c) Artificially induced anisotropy and skewness in isotropic materials by tilted air-hole perforations. .... 125

Figure 5.3. Design procedure, simulation and fabrication of the polarization converter, (a) Geometry of the air-hole perforations and the possible range of air-hole diameters limited by the technology used for drilling, (b) Maximum frequency below which the perforated medium can be modelled as an effective homogenous medium with a constant permittivity tensor, (c) Effective uniaxial permittivity versus perforation diameters, (d) Dispersion of a 2mm square waveguide filled with perforated RT/duroid6006 with period,  $p=0.9\text{mm}$ ,  $d/p$  ratio of 0.5 and tilting angle of 45 degrees, (e) Setup for fabrication and (f) Electric field distribution and s-parameters of the prototype..... 127

Figure 5.4. Structure of an approximate mode converter made of Rogers RT/duroid 6002..... 129

Figure 5.5. Dispersion curves and field distribution for the ordinary and extraordinary modes for the approximate mode converter with one tilted slot over the cross-section diagonal. .... 129

Figure 5.6. The mode converter prototype and the setup for measurement.....	131
Figure 5.7. The resultant scattering parameters. ....	131

**LIST OF SYMBOLS AND ABBREVIATIONS**

mmW	Millimeter-Wave
RF	Radio Frequency
PCB	Printed Circuit Board
5G	Fifth Generation
LTE	Long-Term Evolution
OMT	Orthomode Transducer
SIW	Substrate Integrated Waveguide
NRD	Nonradiative Dielectric Waveguide
SINRD	Substrate Integrated Nonradiative Dielectric Waveguide
PSC	Polarization-Selective Coupler
EPIC	Effective Polarization-Independent Coupler
FDTD	Finite Difference Time Domain
VIE	Volume Integral Equation
PEC	Perfect Electric Conductor
HFSS	High-Frequency Structure Simulator
TE	Transverse Electric
TM	Transverse Magnetic
V-Pol	Vertical Polarization
H-Pol	Horizontal Polarization
LSE	Longitudinal Section Electric
LSM	Longitudinal Section Magnetic
ESIW	Extended Substrate Integrated Waveguide
VNA	Vector Network Analyzer

WR	Waveguide Rectangular
CNC	Computer Numerical Control
BW	Bandwidth
PIRS	Polarization-Inclusive Remote Sensing
CPW	Coplanar Waveguide
AF	Array Factor
CMOS	Complementary Metal-Oxide-Semiconductor
IC	Integrated Circuit

**LIST OF APPENDICES**

Appendix A – LIST OF PUBLICATIONS.....144

## CHAPTER 1 INTRODUCTION

### 1.1 General Discussion

Data communication is expanding dramatically due to the growing demand for ever-increasing voice, video and data transmissions and mobile interactions. This increase inherently means higher energy consumption. This should be tackled by enhancing the transmission efficiency and power consumption of future wireless communication systems such as 5G and beyond. The proposed idea for the efficiency enhancement is the development of *compact systems empowered by polarization diversity*, which provides a unique and alternative solution compared to all the existing techniques.

By definition, wireless systems communicate through electromagnetic wave propagation in air, free from any cables or physical or wired connections. The time varying behaviour of the tip of the electric field vector of the wave is called the wave polarization. Most of the terrestrial wireless systems utilize linearly polarized waves. In other words, they handle only one directional component of the received signal. The highest efficiency of wave reception occurs when the receiver is aligned with the incoming wave polarization. In mobile communications, we can never fully align the receiver with the incoming wave. This is because, in the terrestrial mobile channel, the wave suffers from different reflections, refractions, and diffractions. Therefore, current handsets of communication system depend on reception just on a single spatial component of the received electromagnetic field vector which is aligned with their integrated antenna. Statistically, this causes a waste of about fifty percent of the received signal energy. Previously, a typical solution to such situation is pumping more power from the transmitting base station in order to compensate for this possible loss at the handset receiver. This increase of power consumption could not be tolerated in the future green wireless systems, see Figure 1.1.

In the last few decades, wireless system designers have been more interested in solving the aforementioned problem by what is called *Polarization Diversity* receivers. These receivers consist of different antennas which are aligned with two orthogonal directions. Thus, whatever the orientation of the incoming wave, both of its components are received effectively. This has always been implemented on the uplink at the base stations only, and never on the downlink in the receiver handsets. This is due to the space requirements needed to mount two orthogonally polarized antennas and their supporting waveguides. Our idea is to develop and implement a new

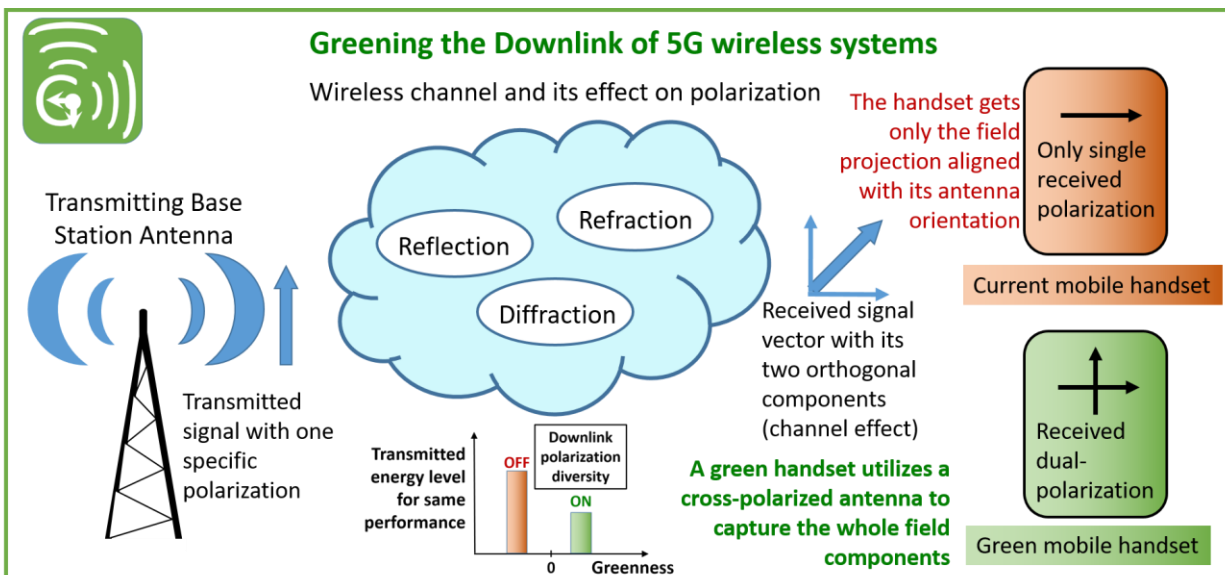


Figure 1.1: Signal transmission-reception procedure in the downlink (base station to handset) of current wireless communication systems, and the proposed greening technology.

and compact polarization diversity technology suitable for integration in the receiver handsets as well, thus stopping the waste of energy that has been going on for decades.

The integration of polarization diversity, *dual-polarization*, in the mobile handsets is not an easy task. This is because all the circuits constituting any mobile system must be planar in order to undergo the printed circuit board (PCB) fabrication restrictions. On the other hand, the previous and current devices that allow handling dual-polarized signals are not planar in nature, and physically complicated which make their integration with the running mobile systems impossible. Therefore, implementing a planar dual-polarized circuit which can be integrated with the mobile systems will result directly in saving the wasted percent of the received energy. This is done by treating both of the orthogonal components of the received signal, and not only one component as before.

Briefly, the proposed idea presented in this dissertation mainly depends on using two different types of integrated waveguides combined together to form this newly invented technology for guiding millimeter-waves (mmW), which is supposed to deal with the frequency band of interest in the future wireless systems. In this technology, each type of waveguide is responsible for guiding and treating one component of the two orthogonal polarizations through two different field-polarized modes in those waveguides. Designed in a scientific and deliberate procedure, the

invented waveguides handle those orthogonal polarizations independently by means of the natural behavior of orthogonal signals, i.e. how each of the two components acts toward each used technology? For this newly invented technology, prototypes-based lab tests are held in the mmW band and show great potential in realizing the dually-polarized capability in many integrated microwave components. Empowered by those promising prototype tests, we seek renovation of all the current single polarized handheld devices and components. This renovation means to be dually-polarized instead of dealing with just one vector component, as shown in Figure 1.1. This is a real improvement of the energy efficiency as well as channel efficiency in the future wireless systems from our perspective.

Currently, most of the designers and researchers are looking forward to implementing various circuits in the mmW band which suits the next generation of mobile communication. In accordance with that, and with the potential of integrating the dual-polarization feature in the mmW circuits, it is highly required to add this feature in the transmitting and receiving circuitries of the communication systems and remote sensing applications. This will directly enhance the overall system efficiency and accordingly its capacity. Our responsibility is to raise and spread this issue globally and to share this technology with other researchers and developers. We should motivate and encourage all the interested specialists to consider the dual-polarization feature in their designs. In this case, the wasted percent of power in the un-received polarization of the signal will be used to enhance the system performance without the need of pumping more power or adding any complication to the existing systems.

The call for the fifth generation (5G) of mobile communications has already started, and many researchers worldwide are working hard toward the implementation of this new generation in order to create a wide range of wireless applications in the future. Keeping up with that and with our environmental constraints in mind, we call for this new communication systems to be the fifth in a generation, but the first in greenness. Greening the future communication systems, in our vision, is highly related to the optimum use of information in any signal. Integrated circuits empowered by the dually-polarized features will make it easy for the designers to increase the level of greenness in future wireless systems. Based on the previous general discussion, let's move to a more technically specialized explanation for the proposed idea.

## 1.2 State-of-the-art of Polarization Diversity

A signal quality degradation caused by fluctuations in fading channels has been one of the greatest challenges facing the designers of mobile and cellular communication networks [1]. Since the late decades of the last century, receiving diversity techniques have presented reliable solutions for this challenge. Starting with the first generation of cellular communication and until the latest 4G LTE digital networks, base-stations have always involved one sort of signal diversity implemented [2]. Receiving diversity could be designed and made possible in the form of spatially separated antennas with inter-distance in the order of ten wavelengths. This is called spatial diversity. Another form of interest is polarization diversity achieved by having two orthogonally oriented receiving antennas. The previously mentioned types have widely been used since the development of the second generation of cellular networks, such as in the popular GSM networks. Multipath temporal diversity was also achieved and made possible using RAKE receivers in earlier code division multiple access networks [1].

The current generation of cellular networks including the state of the art 4G LTE networks still works in the frequency range 0.8-2.1 GHz [3]. This frequency range has proved suitable for terrestrial indoor/outdoor wave propagation with tolerable path loss and fading level. However, the existing and emerging demand for higher capacity techniques and more connected devices has urged the need to explore the underutilized 5-6 GHz band and beyond, for example, higher 28-38 GHz band. Since the latest band lies in the starting edge of the mmW band, new components, circuits and techniques have to be developed to cope with the development. Therefore, one of the most important functions of base-station antenna feeding structures remains to provide a polarization diversity capability in the mmW band. This function necessitates the existence of fully integrated dually-polarized microwave components.

Furthermore, with the current evolutionary growth of the mobile system and wireless communication demand, augmenting the capacity and the efficiency of such systems has become a stipulated research concern [1]. This required capacity enhancement should not be at the expense of a system bandwidth which is the main resource in a wireless communication system. Fortunately, mmW band with its broad bandwidth from 30 GHz to 300 GHz and beyond could be proposed as a candidate for the 5G network to fulfill the required wideband communication services [4, 5]. The importance of the mmW band comes in the company of drawbacks such as

propagation loss [6, 7] and multipath reflections from ground, buildings and other physical objects [8]. In order to achieve the highest possible exploitation of the mmW band, its efficiency must be boosted to overcome its drawbacks. One potential solution for that is the deployment of polarization diversity [2]. The polarization diversity has gained much interest in many applications; thanks to its capability in enhancing the efficiency of transmitting and/or receiving circuitries [9-11]. In particular, a backhaul/fronthaul point-to-point wireless links showed a great potential toward the 5G wireless communication [12].

The basic microwave component that can handle dually-polarized signal is called Orthomode Transducer (OMT). An OMT is a waveguide polarizer device with three physical ports. Its function is to separate or combine two spatially orthogonal signals within the same frequency band simultaneously. OMTs can hold many names as appear in the literature like Orthomode junctions, polarization diplexers, and dual-mode transducers.

Recently, OMTs have attracted growing interest, especially for integrated circuits, in dually-polarized systems. OMTs are commonly implemented to duplicate the capacity in modern communication systems within the same band of frequencies [13, 14]. They are essential components in remote sensing applications [15], satellite communications [16], multiple antenna systems [17, 18], and dually-polarized substrate integrated waveguide (SIW) systems [19].

There are many techniques to construct an OMT, but most of them are complicated and non-planar. This is because in those designs, the concept of separating and combining orthogonal signals is basically depends on structure geometry and internal transitions which are not the case in the proposed idea which depends on selective coupling as presented later. For a wideband operation, the Bøifot [20] and the turnstile junctions [21, 22] are the most common approaches. At high frequencies, a potter horn [23] has yielded good scattering parameters when used with an OMT device. In addition, a compact OMT for the band of 180-270 GHz [24] is implemented in split-block based on Bøifot as well. Some designs were based on symmetric reverse coupling as in [25, 26]. Many waveguide configurations have been used in the OMT design like tilted waveguide T-junction [27], septum polarizer [28], micro-machined transducer [29], platelet manufacturing strategy [30], single-ridged triangular waveguides [31], based on substrate integrated waveguide (SIW) technologies [32, 33] and based on turnstile junction using superimposition of three aluminum blocks [14].

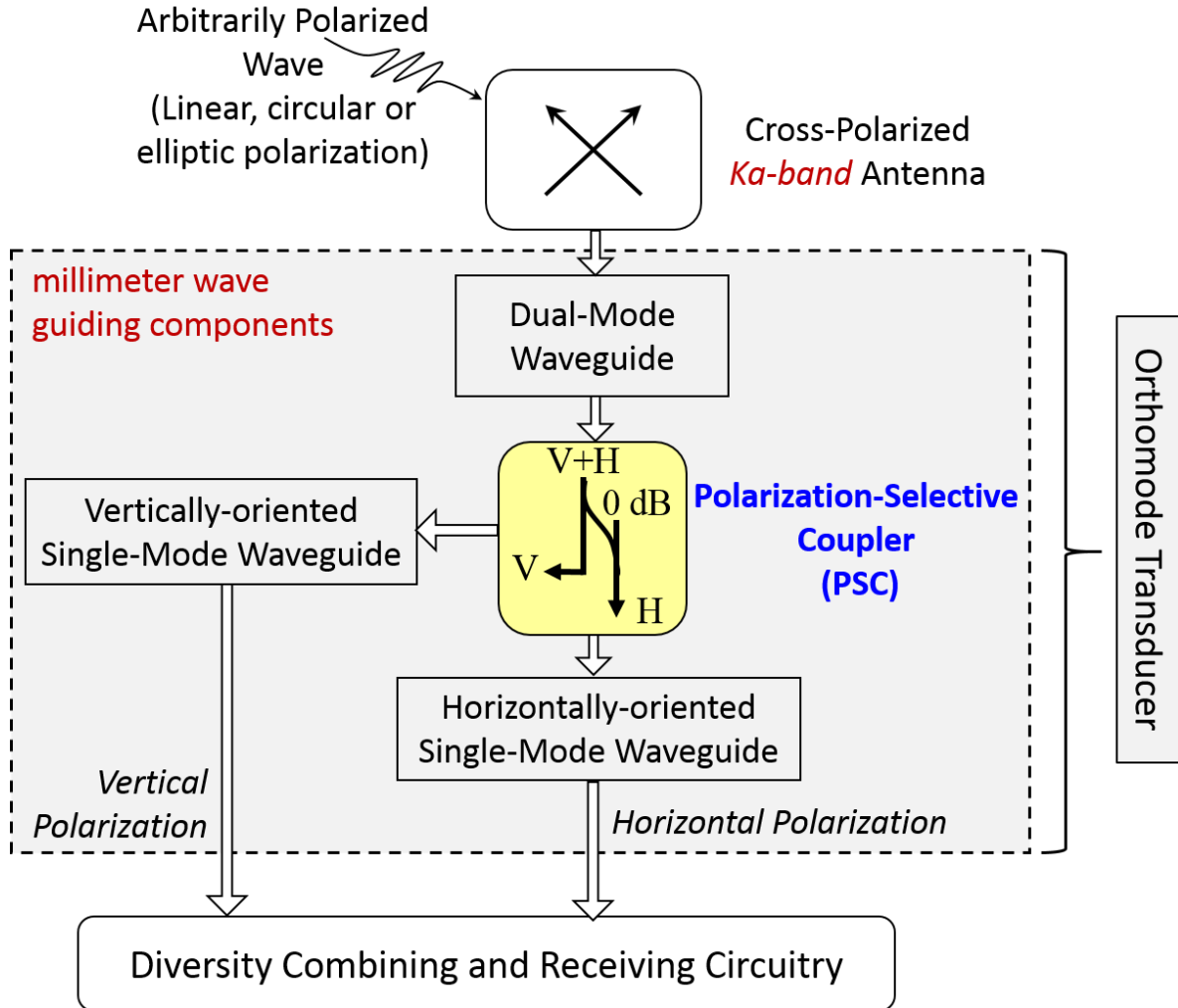


Figure 1.2: Conceptual block diagram for Ka-band dually polarized base-station antenna feeding system

It is well known that planar microwave components are easier to fabricate and integrate with other components at low cost. Due to a large number of connected devices and hot spots targeted in the future 5G networks, the scope of this thesis focuses only on the planar designs such as the one reported in [19].

The substrate integrated waveguide design reported in [19] achieved some great advantages such as being planar and easy to fabricate. That design depends on exciting one waveguide with the two orthogonal modes to be separated. The mode separation is achieved by using two metallic vias which allow the propagation of the horizontally oriented mode and prevent the vertically oriented one. This vertical mode can then be extracted through a planar bend. In this thesis, we show a new

concept for mode separation suitable for OMT design in substrate integration technology. Thus, the idea presented in this thesis differs from that of [19] in terms of the mode separation mechanism. In the design introduced here, the mode separation is achieved by an evanescent coupling designed specifically for only one of the two modes to be separated. This is done by a deliberate combination between two different guiding mechanisms, the substrate integrated waveguide (SIW) and substrate integrated nonradiative dielectric waveguide (SINRD), together within one substrate. Each mechanism is responsible for guiding specific orientation of the electric field vector. The full demonstration and analysis of the modes propagation through such hybrid waveguide is presented in the following chapter.

The block diagram of the proposed OMT structure and its function in the base station of a cellular network is shown in Figure 1.2. This block diagram depicts a base-station antenna receiving an arbitrarily polarized wave. The function of the OMT is to collect the power received by the antenna and separate its two orthogonal field components. These two components are then delivered to the diversity combiner and the receiving circuitry independently.

The significant part of this thesis is about the design and analysis of the OMT block shown in Figure 1.2. The signal received by the antenna is fed into the OMT through a dual-mode guiding structure, which will involve the hybrid integration of two different modes guided by two different waveguides. This signal is then passed to a polarization-selective coupler (PSC). To the best of our knowledge, this PSC is based on a novel idea that has not been presented to date, hence the main contribution of this thesis. The PSC function is to fully couple or navigates one of the two orthogonal polarizations to a separate waveguide. After the two modes are separated, they are fed independently to vertically and horizontally oriented waveguides, and each is designed for single mode operation. Then each polarization is fed to the diversity combiner and the receiving circuitry as shown in Figure 1.2.

The main objective of this thesis is to develop the theory of PSC, and then apply it to the design of an mmW OMT integrated with a square horn antenna. This concept can then be applied to empower any microwave component with the dual-polarization feature as presented throughout the thesis chapters.

### 1.3 Thesis organization

This thesis focuses on the implementation of full-scale polarization diversity in integrated planar microwave components. This is presented firstly by introducing the main conceptual idea that is based on a unique polarization selective coupling (PSC). Based on this idea, dually-polarized microwave components are introduced accordingly and subsequently. The thesis is organized as follows:

Special forms of integrated waveguides that can handle dual-polarizations are studied in chapter 2. These forms are mainly based on the (SIW) and (SINRD) with their image forms. Then, the analysis and design of the separation and combination of orthogonal polarizations as an application to the design of planar orthomode transducer based on PSC which is the main idea of this thesis is presented in chapter 3. This is in addition to another proposed idea for the planar polarization separation and combination which we call effective polarization-independent coupling (EPIC).

After that, some microwave component designs based on the technique of PSC are implemented in chapter 4. These implementations are supported by theoretical, simulation and measurement results through a series of experimental prototypes. Those components are dually-polarized power divider, dually-polarized 0dB and 3dB hybrid couplers, dually-polarized phase shifter, dually-polarized six-port junction and dually-polarized Butler matrix.

In chapter 5, a polarization rotation mode conversion is proposed seeking for the fully integrated planar dual-polarized structures. The mode rotation is achieved by drilling tilted air holes in the dielectric substrate. This is introduced with a full theoretical analysis and simulation.

Finally, a summary of the work presented in this thesis is elucidated. This is supported by some concluding remarks and some interesting research tracks to be followed in the future based on the introduced ideas through this dissertation.

## CHAPTER 2 SPECIAL DUALY-POLARIZED INTEGRATED WAVEGUIDES

This chapter is concerned with a complete analysis of special types of integrated waveguides. Those waveguides are the building blocks of the main ideas of this thesis which are the polarization selective coupling (PSC) and the effective polarization independent coupling (EPIC). This is for the purpose of the dual-polarization handling within planar integrated circuits.

The proposed idea about separating or combining the two orthogonal signals using the selective coupling mechanism simplifies the analysis and design as introduced through the thesis. This is achieved by designing only one coupler which acts differently for different polarization. This simplifies the geometry when compared to other OMT structures which depends on two separate couplers oriented on different planes such as that discussed in [34]. This also relatively reduces the structure size compared to other OMT designs. For example, the dielectric-based design in [35] has a physical size of  $30 \times 20.9 \times 20.7 \text{ mm}^3$  when operating around 30 GHz with a bandwidth of 150 MHz, but the proposed dielectric-filled PSC-based OMT has a physical size of  $45 \times 18 \times 3 \text{ mm}^3$  when working around 38 GHz with a bandwidth of 5 GHz. For the air-filled designs, the structure in [14] has a physical size of  $34 \times 52 \times 68 \text{ mm}^3$ , without the antenna, when operating around 32 GHz with a bandwidth of 42% while the proposed air-filled PSC-based OMT including the horn antenna has a physical size of  $23 \times 42 \times 69 \text{ mm}^3$  when operating around 32 GHz with a bandwidth of 23%. From these straightforward comparisons, the proposed OMT structure shows an interesting reduction in profile. Moreover, the design in [36] showed an interesting compact OMT, but it cannot be integrated within dielectric substrates in the printed circuit board (PCB) designs while the proposed OMT with its reduced planar profile (without the metal enclosure designed only for measurement) in this work shows a great possibility for integration with PCB and other processes-based planar structure enabled applications. However, the proposed OMT has a relatively limited bandwidth governed by the appearance of modes necessary for coupling as explained later in the next chapter.

Complete analysis and design of the previously mentioned couplers, and accordingly OMTs, are considered in this thesis based on nonradiative dielectric (NRD) guide [37] and SIW [38]

technologies. By means of those technologies, a compact OMT with planar profile is designed based on theoretical analysis and experimental observation.

## 2.1 SIW guiding structures for polarization diversity

The building blocks of microwave circuits and components are transmission lines and waveguides. Historically, with every new type of RF transmission line, there is an associated spin-off in the wireless industry. Depending on the physical structure and energy guiding mechanism, each type of RF transmission line becomes more suitable in one frequency range than the other. For example, microstrip lines are efficient only up to few GHz while rectangular waveguides, RWG, are more effective and practical in size in the range of few tens of GHz.

Another very effective transmission line, is the Substrate Integrated Waveguide, SIW, which bridged this gap between microstrip lines and RWG, enabling the integration of the two technologies [39].

Conventionally, in SIW the dominant mode of operation is the regular RWG  $TE_{10}$  mode. The bandwidth of single-mode operation is always determined by the cutoff frequency of the second higher order mode. It is conventionally guaranteed that the second higher order mode is the  $TE_{20}$  given that the cross-section dimensions satisfy the inequality  $a > 2b$ , where  $a$  and  $b$  are the cross sectional dimensions of the SIW as shown in the inset of Figure 2.1. One can observe that in the mm-wave band, and given the typical thickness of widely used microwave substrates, the design inequality mentioned above can hardly be satisfied.

To validate this idea, consider the design process of the SIW shown in Figure 2.1. A designer would first decide on the dielectric substrate to use. The commercially available materials would have the relative permittivity  $\epsilon_r$ , ranging from about 2.2 to 10.2 with typical thickness,  $b$ , ranging from about 10 to 75 mils. If the SIW is to operate in the mm-wave band, the designer will calculate  $a$  according to the typical equation derived from the cutoff frequency of the  $TE_{10}$  mode shown in the top of Figure 2.1.

The designer would then face the problem that the calculated value,  $a$ , will be in the range of  $b$  and the second higher order mode will no longer be the  $TE_{20}$  mode, but would rather be the orthogonally polarized  $TE_{01}$  mode. The condition is even worse taking into consideration the anisotropy of the typical dielectric substrate, where the effective permittivity seen by the horizontally polarized  $TE_{01}$

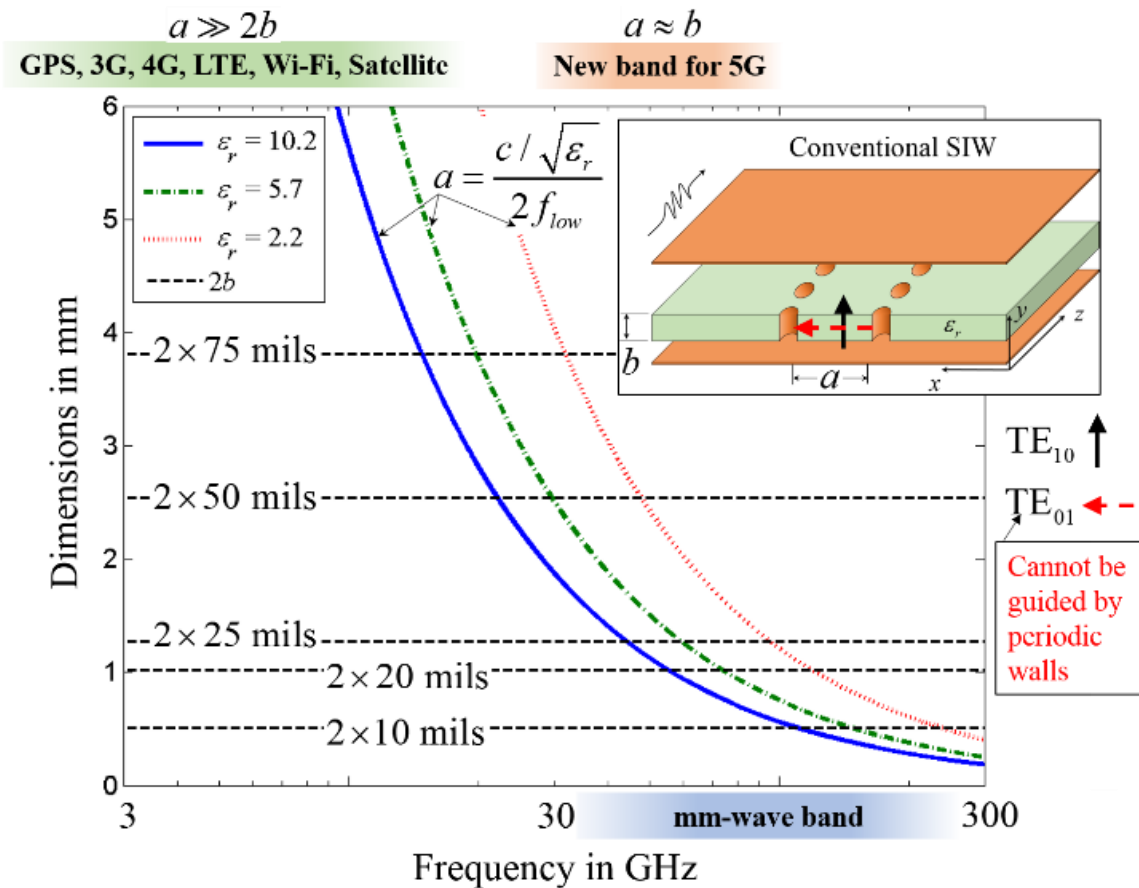


Figure 2.1. Cross-comparison of SIW cross-sectional dimensions in the mmW range.

mode is higher than that seen by the vertical field of the  $TE_{10}$  mode. Electrically, this makes  $b$  even larger than the values shown in Figure 2.1.

Thinking of the horizontally polarized  $TE_{01}$  mode in an SIW structure raises interesting research questions. The periodic wall is suitable only for guiding the vertical  $TE_{10}$  mode, so how to guide the horizontal mode to utilize it efficiently rather than trying to suppress it? Is it going to radiate and leak into the substrate? Dielectric slab waveguides are well known in optics and well utilized to build useful components and enabling technologies, is it useful to utilize them in the mmW band? The main idea in this chapter is to study the combination of the dielectric slab guiding mechanism and the conventional SIW in one physical structure.

The following sections study this combination deeply starting from a comprehensive analysis of the SINRD waveguides.

## 2.2 NRD guiding structures and its image form

The SIW structure presented in the previous section is one of the most efficient guiding structures due to its simple implementation and integration in RF and mmW circuits [40]. Another sort of integrated waveguides is the substrate integrated nonradiative dielectric (SINRD) waveguide [41-43]. The SINRD waveguide does not compete with the SIW structures due to its long-perceived-complicated analysis, bulkiness and the difficulty to achieve single mode operation. This chapter attempts to clarify the analysis of the NRD guides in a way that facilitates the most effective use of such guides.

SINRD waveguide is an integrated form of the well-known dielectric slab waveguide [44]. In such waveguides, the wave guidance occurs due to a step in the value of permittivity of the dielectric material constituting the waveguide; with lower permittivity on the bilateral sides than that of the main central guide. In the SINRD waveguide, the permittivity of the sides can be decreased by perforating air-holes in the same material composing the substrate or other means as long as there is a contrast of dielectric constant along the transverse direction according to SINRD design rules. In accordance with that, SINRD technology does not require metal plating inside the air-holes as the substrate integrated waveguides (SIW) [38, 40]. This fact proposes a promising low-loss, low-cost and high-performance guiding technology for mmW applications [37, 42, 45].

This interesting technology with the previously mentioned advantages has been used in constructing various designs for integrated circuits applications and antennas. For example, the NRD technology showed a great performance and mechanical improvements for designing abridged coupler for mmW applications [46]. The same concept was used for implementing a cruciform coupler as well [47]. This is in addition to the capability of implementing leaky wave antennas based on NRD technology [48, 49].

Integrating such SINRD waveguides with planar circuits is highly sensitive to the required maximum operating frequency [50]. This frequency is related to the effective permittivity of the periodic part of the SINRD waveguide. This is in addition to the need for the exact effective parameter values of the NRD periodic part in order to get the dispersion characteristics for such waveguides. This is required to get more precise designing procedures based on the selected mode of operation. Therefore, the analysis of the NRD periodic part is essential for any application based

on this technology. This analysis is required to extract the effective parameters for all electric field orientations.

In previous work, this effective permittivity is mainly calculated based on huge computationally intensive numerical methods such as the finite difference time domain (FDTD) technique [42, 51] or the volume integral equation (VIE) analysis [52, 53]. Those methods showed proper results, but with a complicated procedure and expensive computation. On the other hand, approximate empirical formulations for the effective permittivity of the periodic part were given in [54], but those empirical formulations might lead to inaccurate estimations for the design parameters and accordingly imprecise results.

Moreover, the need for polarization diversity in enhancing the microwave component efficiency [2, 55, 56] makes it essential to yield an accurate analysis for different polarizations of the electric field components. Unfortunately, most of the existing analysis methodologies for the SINRD concerns only single polarization [51, 57]. Based on this, an extensive analytical study for the SINRD waveguide towards various polarizations is needed for accurate calculation of its effective parameters which might lead to more precise designs of dually-polarized microwave components [19, 58, 59].

In this chapter, an exact analytical procedure is introduced for modelling the periodic part of the SINRD waveguide based on eigenmode analysis [60]. This procedure determines the dispersion characteristics of the periodic medium in different directions when it is enclosed between two horizontal metallic plates. The interesting result is that the periodic medium acts as an anisotropic material with different effective permittivity depending on the electric field direction with respect to the periodic air-holes, which has never been reported before in connection with the NRD technology.

The proposed method is validated through many examples and compared with the simulation results where excellent agreement is achieved, and valuable observations are recorded for the interested designers. For example, a specific perforation for the air-holes might lead to converting the anisotropic substrate to isotropic one. Furthermore, the guidance by the periodic part shows three regimes of operation for each specific mode depending on the variation of its effective permittivity with frequency.

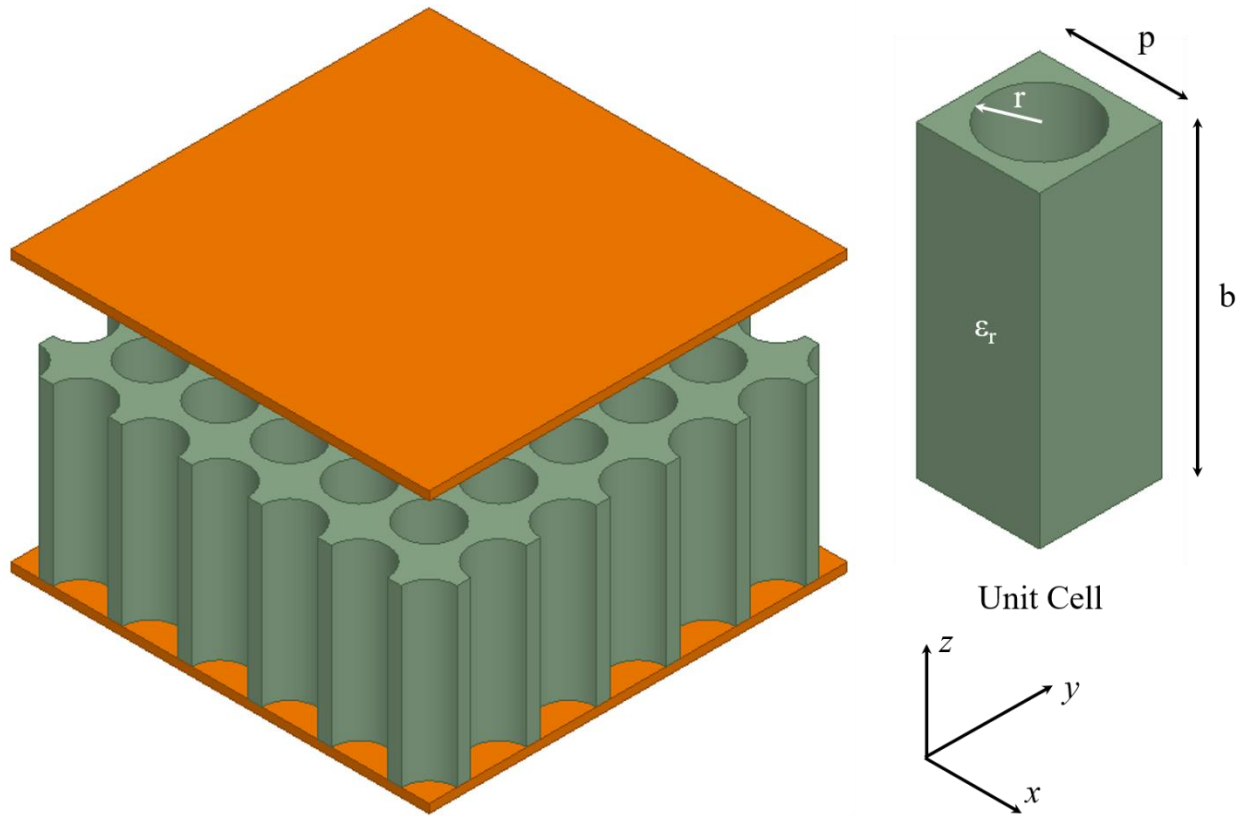


Figure 2.2. Physical structure of a two-dimensional periodic medium and its unit cell.

### 2.2.1 Modelling Effective Anisotropy of SINRD Waveguide

In this section, the extraction of effective parameters of the periodic medium is developed based on an eigenmode analysis. Then, this method is validated through the eigenmode solver of the HFSS simulation tools. After that, a setup for a possible validation is introduced using a rectangular waveguide filled with the perforated medium and its effectively equivalent medium together in a cascade that is constructed specifically for the presented problem. It is also shown that anisotropic material can be converted to isotropic one using this geometrical alteration of the material structure via air-holes. This process, we call isotropization. Later, the application of the presented technique is utilized in designing an SINRD waveguide supported with detailed explanations for the regimes of operation.

### 2.2.1.1 Extraction of effective permittivity tensor

Any SINRD waveguide consists of three regions, the main guide in the center and two periodic parts surrounding it. Considering the periodic part structure which is shown in Figure 2.2. It consists of a periodic dielectric medium enclosed between two horizontal metallic plates. The unit cell with specified dimensions and parameters is presented in the same figure.

The Helmholtz wave equation for electric field  $\mathbf{E}$  in such a structure can be easily written as,

$$\frac{1}{\epsilon(x, y)} \nabla \times \nabla \times \mathbf{E}(x, y, z; \omega) = \frac{\omega^2}{c^2} \mathbf{E}(x, y, z; \omega) \quad (2.1)$$

$$\text{where, } \mathbf{E}(x, y, z; \omega) = \hat{a}_x \hat{E}_x + \hat{a}_y \hat{E}_y + \hat{a}_z \hat{E}_z \quad (2.2)$$

Due to the medium periodicity, the reciprocity of the physical relative permittivity can be expanded as a double Fourier series as,

$$\frac{1}{\epsilon(x, y)} = \sum_u \sum_v \epsilon_{uv} e^{j \left[ \left( \frac{2\pi u}{p} \right) x + \left( \frac{2\pi v}{p} \right) y \right]} \quad (2.3)$$

where the Fourier coefficient  $\epsilon_{uv}$  is given by,

$$\epsilon_{uv} = \frac{1}{A} \iint_A \frac{1}{\epsilon(x, y)} e^{-j \left[ \left( \frac{2\pi u}{p} \right) x + \left( \frac{2\pi v}{p} \right) y \right]} dA \quad (2.4)$$

where  $A = p^2$  is the cross-sectional area of the unit cell. For the specific case in Figure 2.2, the function  $\epsilon_{uv}$  which is related to the geometrical distribution of the periodic medium can be written explicitly by the help of [61] in the form,

$$\epsilon_{uv} = \begin{cases} 2 \left( 1 - \frac{1}{\epsilon_r} \right) \pi \left( \frac{r}{p} \right)^2 \frac{J_1(Gr)}{Gr} & G \neq 0 \\ \pi \left( \frac{r}{p} \right)^2 + \frac{1}{\epsilon_r} \left( 1 - \pi \left( \frac{r}{p} \right)^2 \right) & G = 0 \end{cases} \quad (2.5)$$

where  $r$  is the air-hole radius and  $G$  is defined by,

$$G = 2\pi \sqrt{u^2 + v^2} \quad (2.6)$$

According to Floquet theorem, the electric field can also be expanded as a periodic function in the  $xy$ -plane with period  $p$  where the propagation constants in  $x$ - and  $y$ -directions are  $k_x$  and  $k_y$ , respectively.

$$\hat{E}_x(x, y, z; \omega) = \sum_m \sum_n e^{j\left[\left(k_x + \frac{2\pi m}{p}\right)x + \left(k_y + \frac{2\pi n}{p}\right)y\right]} \begin{bmatrix} E_x|_{mn} \sin\left(\frac{i\pi}{b} z\right) \\ + D_x|_{mn} \cos\left(\frac{i\pi}{b} z\right) \end{bmatrix} \quad (2.7)$$

where the  $\sin$  and  $\cos$  functions are used to consider the effect of the two PEC plates enclosing the whole structure. Taking  $i = 0$  corresponds to uniform field distribution in the  $z$ -direction between the two plates. The  $y$ - and  $z$ -components  $\hat{E}_y$  and  $\hat{E}_z$  of the electric field are expanded in a form identical to (2.7).

Taking a Fourier series expansion of (2.1) is achieved simply by substituting (2.7) and (2.3) in (2.1), where multiplication on the left-hand side is converted to a spatial convolutional sum expressed by three coupled equations for the field components in the different directions shown below,

$$\sum_{-N}^N \sum_{-N}^N \epsilon_{u-m, v-n} \left\{ \begin{array}{l} \left[ \left(k_y + \frac{2\pi n}{p}\right)^2 + \left(\frac{i\pi}{b}\right)^2 \right] E_x|_{mn} - \\ \left(k_x + \frac{2\pi m}{p}\right) \left(k_y + \frac{2\pi n}{p}\right) E_y|_{mn} + \\ \left(k_x + \frac{2\pi m}{p}\right) \left(\frac{i\pi}{b}\right) E_z|_{mn} \end{array} \right\} = \frac{\omega^2}{c^2} E_x|_{uv} \quad (2.8)$$

$$\sum_{-N}^N \sum_{-N}^N \epsilon_{u-m, v-n} \left\{ \begin{array}{l} -\left(k_x + \frac{2\pi m}{p}\right) \left(k_y + \frac{2\pi n}{p}\right) E_x|_{mn} + \\ \left[ \left(k_x + \frac{2\pi m}{p}\right)^2 + \left(\frac{i\pi}{b}\right)^2 \right] E_y|_{mn} + \\ \left(k_y + \frac{2\pi n}{p}\right) \left(\frac{i\pi}{b}\right) E_z|_{mn} \end{array} \right\} = \frac{\omega^2}{c^2} E_y|_{uv} \quad (2.9)$$

$$\sum_{-N}^N \sum_{-N}^N \epsilon_{u-m,v-n} \left\{ \begin{array}{l} \left( k_x + \frac{2\pi m}{p} \right) \left( \frac{i\pi}{b} \right) E_x|_{mn} + \\ \left( k_y + \frac{2\pi n}{p} \right) \left( \frac{i\pi}{b} \right) E_y|_{mn} + \\ \left[ \left( k_x + \frac{2\pi m}{p} \right)^2 + \left( k_y + \frac{2\pi n}{p} \right)^2 \right] E_z|_{mn} \end{array} \right\} = \frac{\omega^2}{c^2} E_z|_{uv} \quad (2.10)$$

where the double summations are on  $m$  and  $n$ , respectively. Equations (2.8), (2.9) and (2.10) can be combined and recast in a matrix form such as,

$$\begin{pmatrix} [S_{xx}] & [S_{xy}] & [S_{xz}] \\ [S_{yx}] & [S_{yy}] & [S_{yz}] \\ [S_{zx}] & [S_{zy}] & [S_{zz}] \end{pmatrix} \begin{pmatrix} [E_x] \\ [E_y] \\ [E_z] \end{pmatrix} = \frac{\omega^2}{c^2} \begin{pmatrix} [E_x] \\ [E_y] \\ [E_z] \end{pmatrix} \quad (2.11)$$

where matrix  $S_{hh}$  has a dimension of  $(2N+1)^2 \times (2N+1)^2$  and vector entry  $E_h$  has a dimension of  $(2N+1)^2 \times 1$ . The eigenvalues of the  $S$ -matrix provide the frequency corresponding to each specific wavenumber used to build the  $S$ -matrix. In other words, one should specify the wavenumber and then look for the corresponding frequency (eigenvalue). The corresponding eigenvectors give the three-dimensional field distribution through the medium for that specific frequency and wavenumber. The components of the effective permittivity tensor of the periodic medium can be calculated as the rate of change of the eigenvalues of (2.11) with respect to the wavenumber as:

$$\epsilon_{eff} = \left( \frac{c}{\partial k / \partial \omega} \right)^2 \quad (2.12)$$

In the following section, this procedure is validated using the theoretical technique presented above and the finite element method through HFSS eigenmode simulations.

Furthermore, the calculated field components cannot be considered as a pure TE or a pure TM polarization due to the existence of the horizontal metallic plates that causes essential coupling between the field equations in different directions. This coupling is released when the dependency on the substrate thickness disappears which happens for the modes where  $i = 0$ .

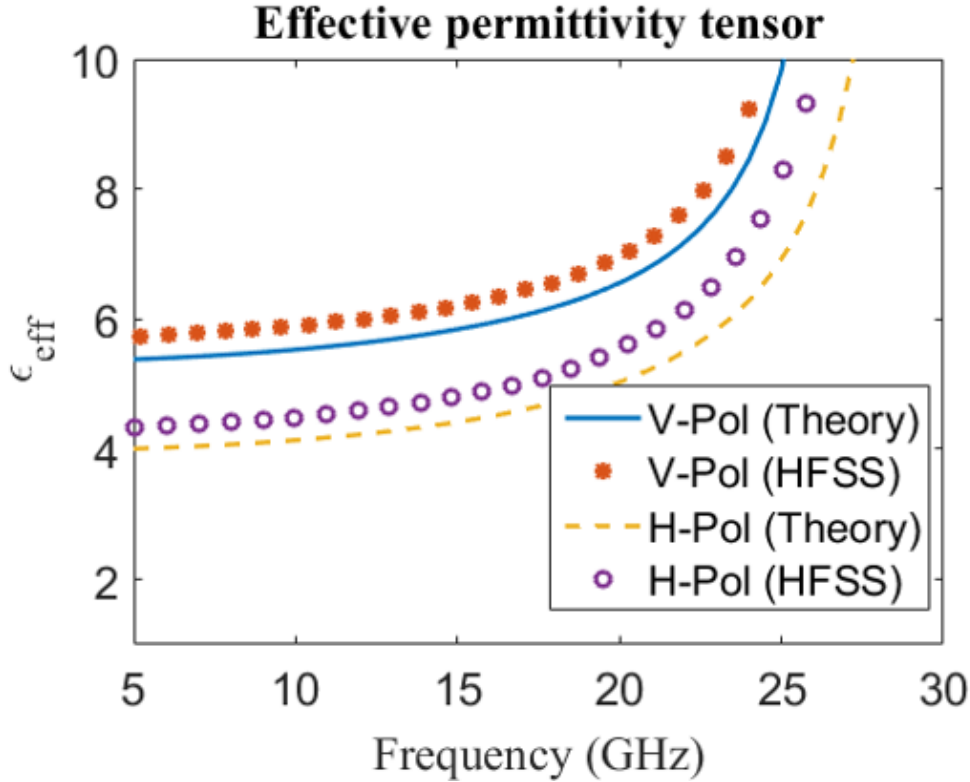


Figure 2.3. Theoretical and simulation dispersion curves for the first two modes of the periodic medium in Figure 2.2 at  $i=0$ .

### 2.2.1.2 Validation using eigenmode solver

In order to validate the proposed procedure for accurately evaluating the effective parameters of the periodic medium in Figure 2.2, a comparison is presented versus the numerical simulator HFSS [62]. Consider the following numerical example, the substrate used in this comparison is the Rogers RT/Duroid 6010 which has a dielectric constant of 10.2. The substrate is assumed to be isotropic in this example. The thickness of the substrate is chosen to be 2 mm, the period is 2 mm as well and the air-hole diameter is 0.8 mm. For the numerical implementation of the theoretical expressions explained above, let us take  $N=5$ ,  $k_x = [0 \ \pi]$  and  $k_y = 0$ . This corresponds to a dimension of the  $S$ -matrix of  $3(2N+1)^2 \times 3(2N+1)^2 = 363 \times 363$ . The first two eigenvalues when  $i=0$  correspond to the first two propagating modes. The electric field of the first mode is vertically polarized (V-Pol), while the second mode is horizontally polarized (H-Pol).

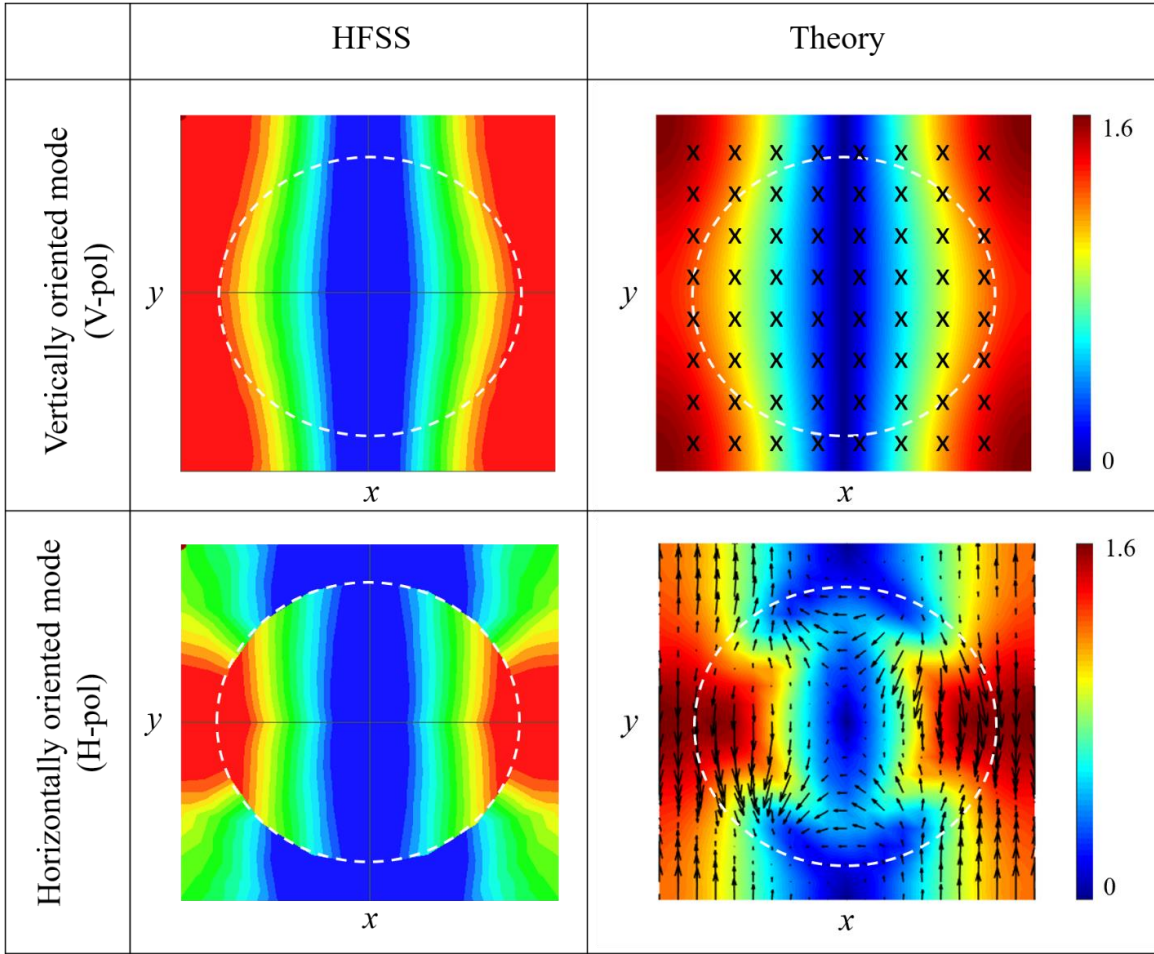


Figure 2.4. Theoretical and simulation field distributions for the first two modes of the periodic medium in Figure 2.2 at  $i=0$ .

The same unit cell is implemented through the HFSS eigenmode solver where the dispersion diagram can be obtained and from which the effective permittivity can be extracted. The effective permittivity of the first two modes propagating through the specified medium is shown in Figure 2.3 using the presented theoretical formulation in (2.12) and the numerical HFSS simulation. From the comparison presented in this figure, it can be clearly observed that the proposed method-generated results coincide with those of the HFSS with a very good agreement.

Consequently, an important conclusion can be inferred from Figure 2.3 which is for the different orientations of electric fields, this periodic medium produces different characteristics. This means that the effective permittivity of this periodic medium depends on the direction of the electric field.

Therefore, when this periodic part is used for guiding the electromagnetic wave, it acts as an anisotropic medium depending on the propagating mode through the waveguide.

For further illustration, the field distribution of this periodic medium is presented in Figure 2.4. This field distribution is obtained theoretically from the eigenvectors of (2.11),  $[E_x]$ ,  $[E_y]$  and  $[E_z]$  corresponding to the first two eigenvalues. It is found that the first eigenmode is that whose coefficients  $[E_x] = [E_y] = [0]$ , whereas for the second mode  $[E_z] = [0]$ . We call the first mode the vertically polarized  $z$ -oriented mode, while the latter is called the horizontally polarized mode. The space domain plot is calculated using the inverse Fourier series expansion in (2.7) (and its similar equations) to get the values of  $\hat{E}_x$ ,  $\hat{E}_y$  and  $\hat{E}_z$ .

For comparison, the field distribution for these two first eigenmodes is simulated using HFSS eigenmode solver. The achieved plots are shown in Figure 2.4 from which another confirmation for the validity of the presented technique is obvious. The color-map in the figure represents the magnitude where the black arrows represent the direction of the field.

### 2.2.1.3 Analysis of more complicated unit cells

The presented technique can be applied to different periodic unit cells with more complicated structure. Let us consider the shape of the unit cell shown in Figure 2.5. The key to a successful analysis is to write a precise expression for the coefficients of the Fourier series expansion of the relative permittivity. To get this expression for the unit cell shown in Figure 2.5, one should realize that such a unit cell consists of two non-identical unit cells overlapped together with a shift in the  $x$ - and  $y$ -directions. This allows the application of the properties of a Fourier series expansion, where the shift in the space domain can be expressed as an exponential multiplicative constant in the spatial frequency domain ( $k_x$ - $k_y$  domain).

Thus, the relative permittivity of the unit cell shown in Figure 2.5 can be written as:

$$\epsilon_{uv} = \epsilon_{uv}(r_1) + \epsilon_{uv}(r_2)e^{-j[(u\pi)+(v\pi)]} \quad (2.13)$$

where  $\epsilon_{uv}(r_1)$  and  $\epsilon_{uv}(r_2)$  can be calculated using (2.5). The exponential term in the above equation is calculated according to the fact that the shift is exactly half a period in both the  $x$ - and  $y$ -directions. This is not straightforward to get to any unit cell structure.

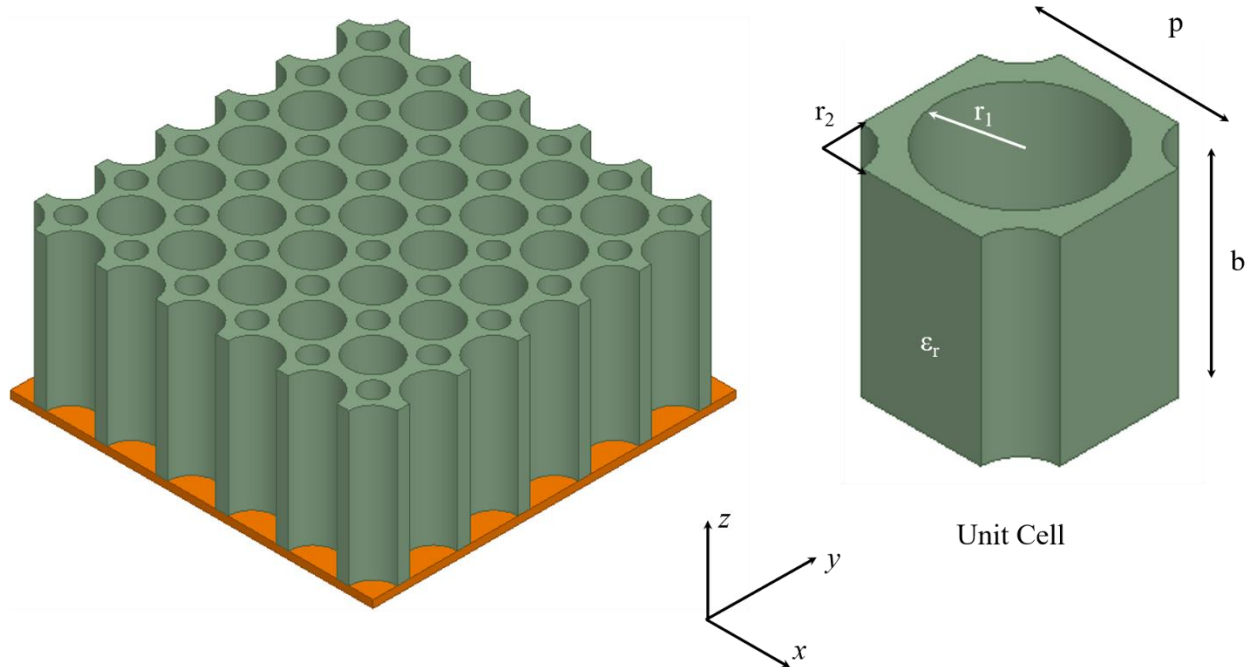


Figure 2.5. Physical structure a two-dimensional double periodic medium with its unit cell.

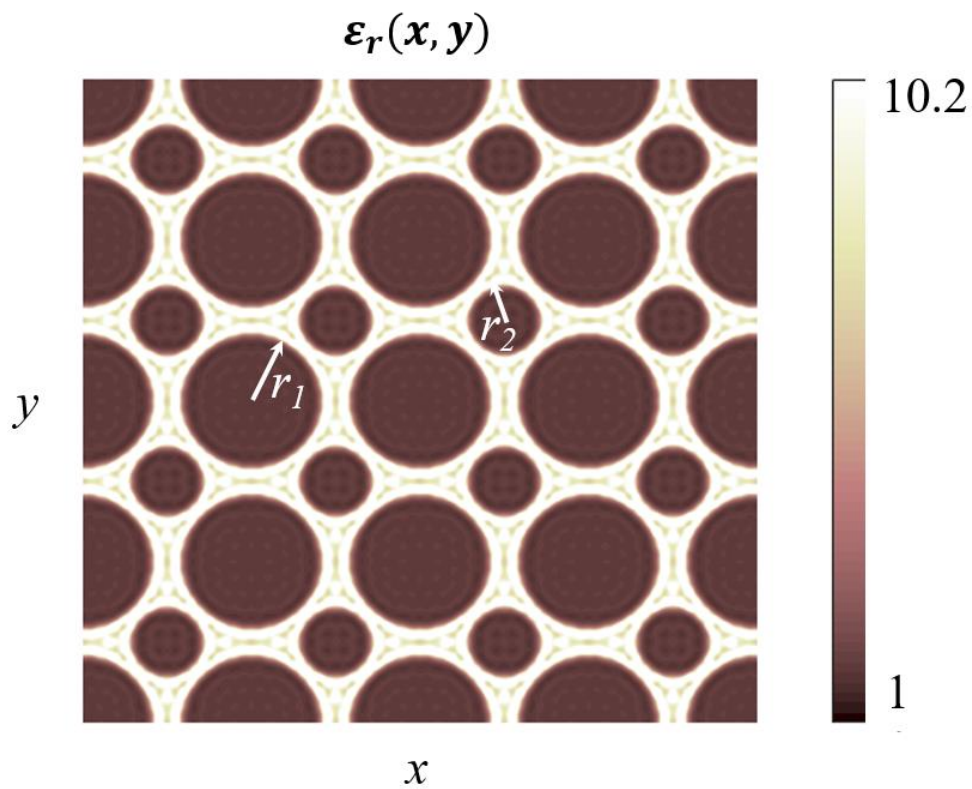


Figure 2.6. The calculated cross-sectional spatial relative permittivity based on (13).

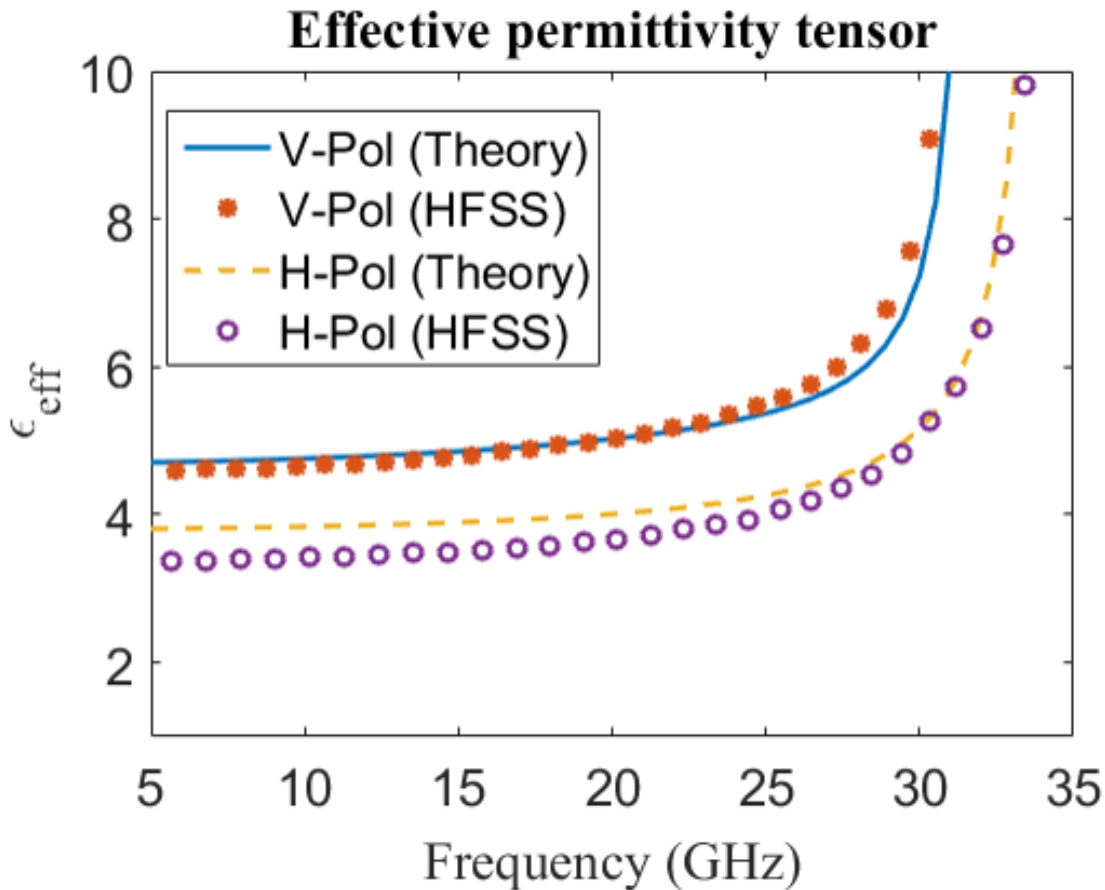


Figure 2.7. Theoretical and simulation dispersion curves for the first two modes of the periodic medium in Figure 2.5 at  $i=0$ .

Therefore, it is always recommended to check the expression written for the permittivity by plotting it in the space domain according to (2.3). We have done this validation for the expression shown in (2.13), and the plot is shown in Figure 2.6, where it agrees exactly with the expected shape illustrated in Figure 2.5 except for the Gibbs phenomenon [63] known due to the truncation of the summations in (2.3).

The same procedure used for obtaining the effective permittivity and field distributions of the unit cell in Figure 2.2 is followed here for the unit cell in Figure 2.5. The effective permittivity is shown in Figure 2.7 for the first two modes. A great agreement is achieved with the eigenmode simulation results of the HFSS. The structure shows the same anisotropy achieved before, but with a lower

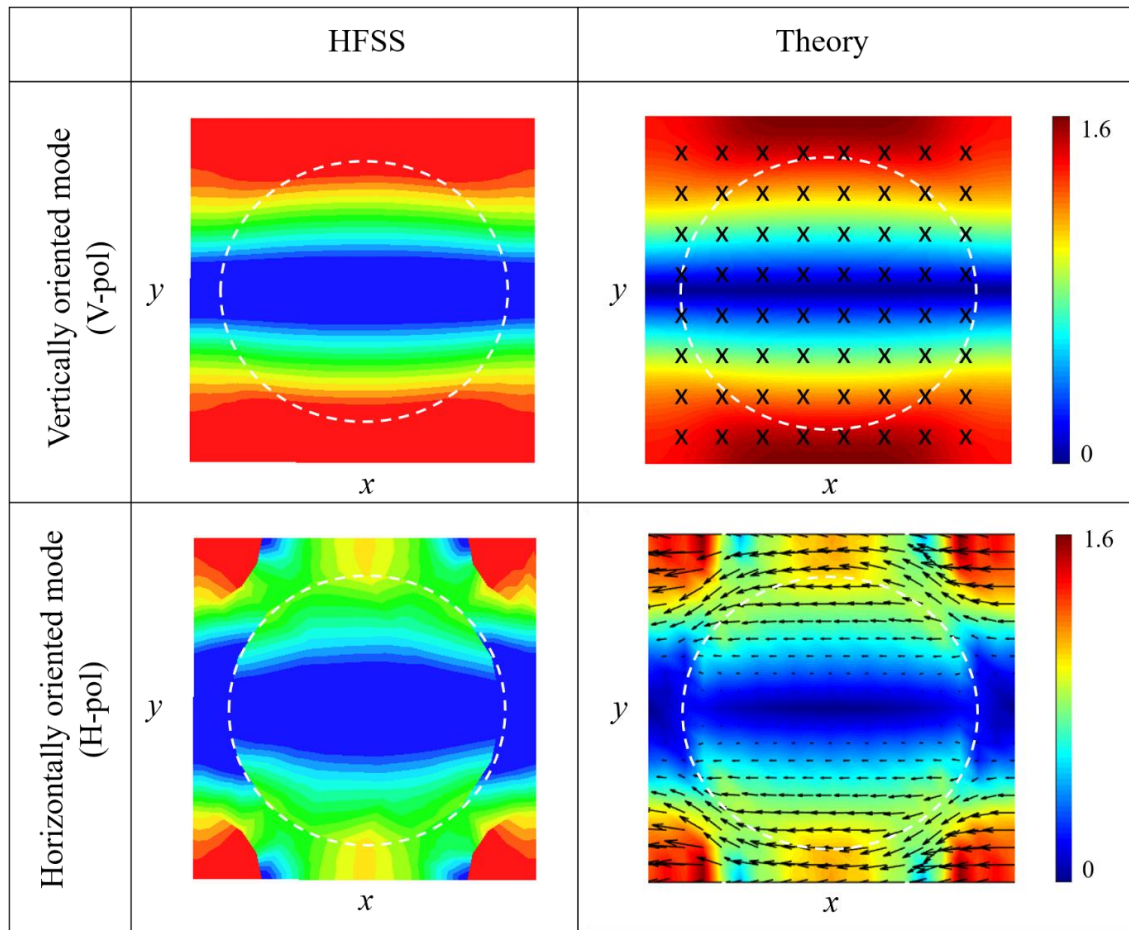


Figure 2.8. Theoretical and simulation field distributions for the first two modes of the periodic medium in Figure 2.5 at  $i=0$ .

dielectric constant because of an increase of the volume of the air medium inside the dielectric substrate. In this fashion, one can take into consideration the mechanical constraints required to keep the rigidity of the perforated dielectric substrate. The corresponding field distribution is presented in Figure 2.8 which infers that the first mode is vertically polarized while the second mode is horizontally polarized.

Based on the previous discussions, any periodic medium can be simply replaced with an effective anisotropic medium which has the calculated effective permittivity using the specified method. The logical validation of this is to implement it inside a rectangular waveguide and confirm that this periodic medium acts exactly as the equivalent effective medium, as discussed in the following section.

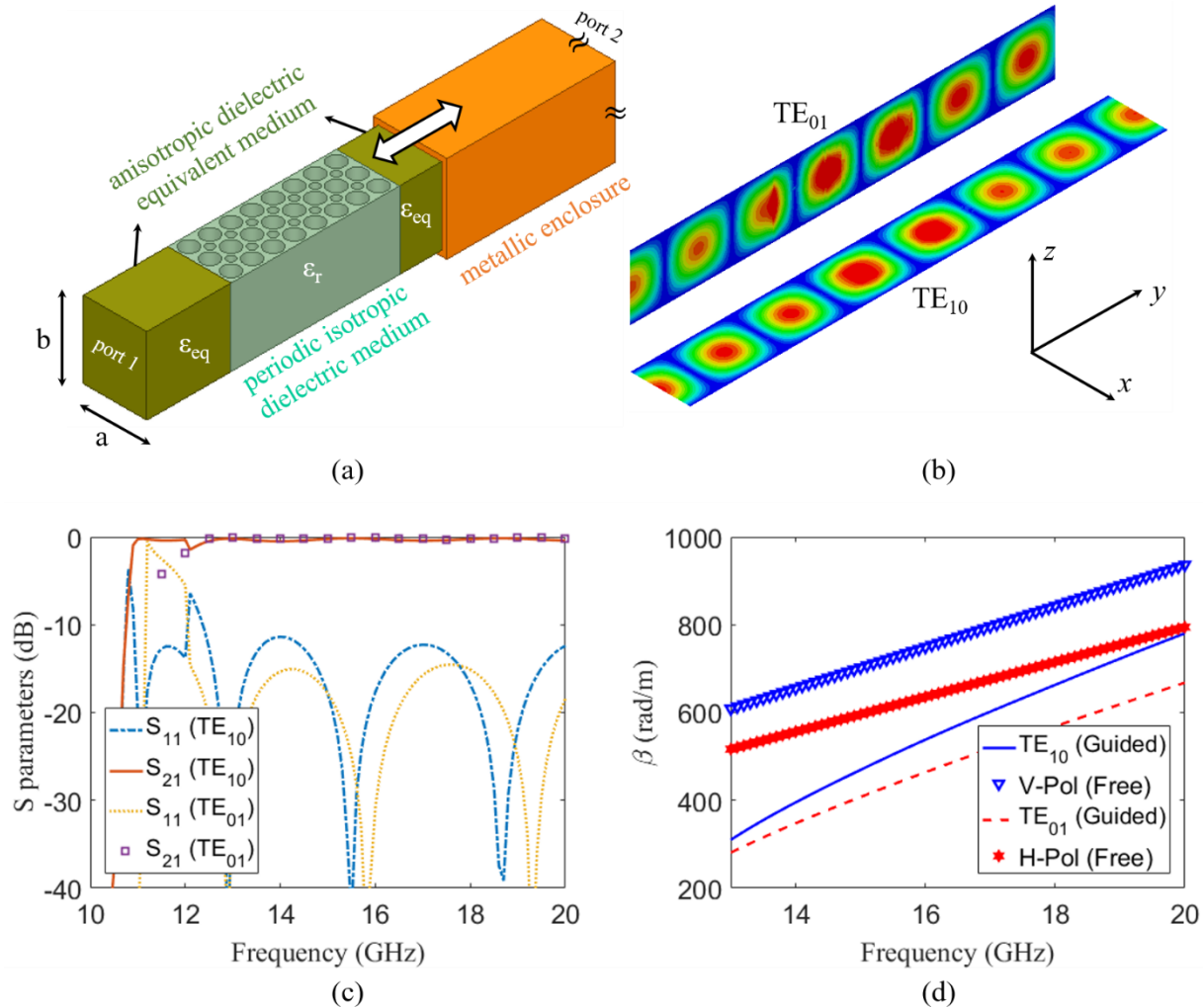


Figure 2.9. Validation example for the eigenmode analysis of a two-dimensional periodic medium: (a) waveguide structure, (b) field distribution, (c) magnitude of scattering parameters and (d) propagation constant.

#### 2.2.1.4 Validation using rectangular waveguide example

In this section, the validity of the introduced method is examined through a rectangular waveguide problem. It can be concluded from the previous discussions that the periodic dielectric medium can be replaced with an equivalent medium whose effective parameters can be calculated precisely. Moreover, this effective medium should be considered as an anisotropic medium due to its different behaviors towards propagating wave depending on its polarization.

The structure of the example presented in this section consists of three cascaded square waveguides as shown in Figure 2.9 (a). The waveguide in the middle is the periodic dielectric medium while the other two waveguides are normal waveguides with permittivity that is equal to the effective permittivity of the periodic medium calculated in the first section. The unit cell used of the periodic medium is the same as of Figure 2.5 with the same dimensions and parameters used in the previous subsection. The material of the equivalent waveguides are chosen to have an anisotropic permittivity tensor that is identical to that of Figure 2.7, that is for this specific numerical example up to 25 GHz,

$$\epsilon_{eff} = \begin{bmatrix} 3.6 & 0 & 0 \\ 0 & 3.6 & 0 \\ 0 & 0 & 5 \end{bmatrix} \quad (2.14)$$

The described structure is simulated through the HFSS where the field distribution and the scattering parameters are shown in Figure 2.9 (b) and (c), respectively. The field distribution in the  $xy$ -plane represents the  $TE_{10}$  mode while the field distribution in the  $yz$ -plane represents the  $TE_{01}$  mode. From those distributions, it can be clearly observed that the disturbance of the field due to the medium change is negligible which confirms that the periodic medium acts exactly like the two enclosing anisotropic medium. Furthermore, the magnitude of scattering parameters confirms this fact as well. In Figure 2.9 (d), the anisotropy of the periodic medium appears in the difference occurred between the propagation phase delay of both of the  $TE_{10}$  and the  $TE_{01}$  modes. Recall that in a square waveguide both of those modes have exactly the same dispersion given the dielectric filling is isotropic.

After the previous discussions and validations, it can be straightly inferred that perforating air-holes in any isotropic dielectric substrate would result in converting this substrate into an anisotropic substrate with a lower permittivity.

### 2.2.1.5 Isotropization of naturally anisotropic materials

This important phenomenon described above has a great power if utilized in a carefully and adequately engineered way. Naturally, there exist materials with inheriting anisotropy due to its molecular composition. This anisotropy also arises in high frequency laminates manufactured to achieve high relative permittivity. For example, the ceramic based substrates of Rogers which have a relatively high permittivity automatically develop a certain level of anisotropy in the

manufacturing process. This is always reported in the data sheets of Rogers as different  $\epsilon_z$  and  $\epsilon_{xy}$  values [64]. That is the field oriented normally to the plane of a thin substrate experiences a certain value of relative permittivity different than that experienced by an electric field oriented in parallel to the plane. For many applications where the electric field is not totally perpendicular to the substrate, this causes some design problems if the anisotropy is not taken into consideration. Moreover, for dually-polarized microwave components, this also causes a problem if not taken in the design consideration.

A solution for this problem can be developed based on the technique presented in this chapter. As noted above, the periodic perforation of dielectric substrates introduces a certain type of anisotropy. If one can neutralize the molecular anisotropy with a geometrically induced one that would be a great achievement. That is one can introduce a certain periodic profile of perforation in the anisotropic substrate to convert it into isotropic one. This process, we call, isotropization.

To validate this idea, we build the same simulation model shown in Figure 2.9 (a) but with the true realistic anisotropic parameters of the Rogers 6010 substrate reported in the Rogers datasheets [64], where the permittivity tensor is approximately given by

$$\epsilon_r = \begin{bmatrix} 13.4 & 0 & 0 \\ 0 & 13.4 & 0 \\ 0 & 0 & 10.2 \end{bmatrix} \quad (2.15)$$

Fortunately, the horizontal permittivity is higher than the vertical one and the periodic perforation studied in this chapter introduces a more reduction in the horizontal permittivity than that of the vertical direction. This means an isotropization could be achieved if the dimension of the unit cell is designed properly.

The numerical procedure to achieve this isotropization is summarized here. First of all, we take the vertical permittivity of the 6010 substrate which is 10.2 and substitute in the eigenequation (2.11), then we take the effective permittivity solution for only the vertical mode. Then, we take the horizontal permittivity which is 13.2 and solve to get the effective permittivity for the horizontally polarized mode. We try different unit cell dimensions until the two effective permittivities for both polarizations coincide. We found out that the unit cell shown in Figure 2.2 can achieve this

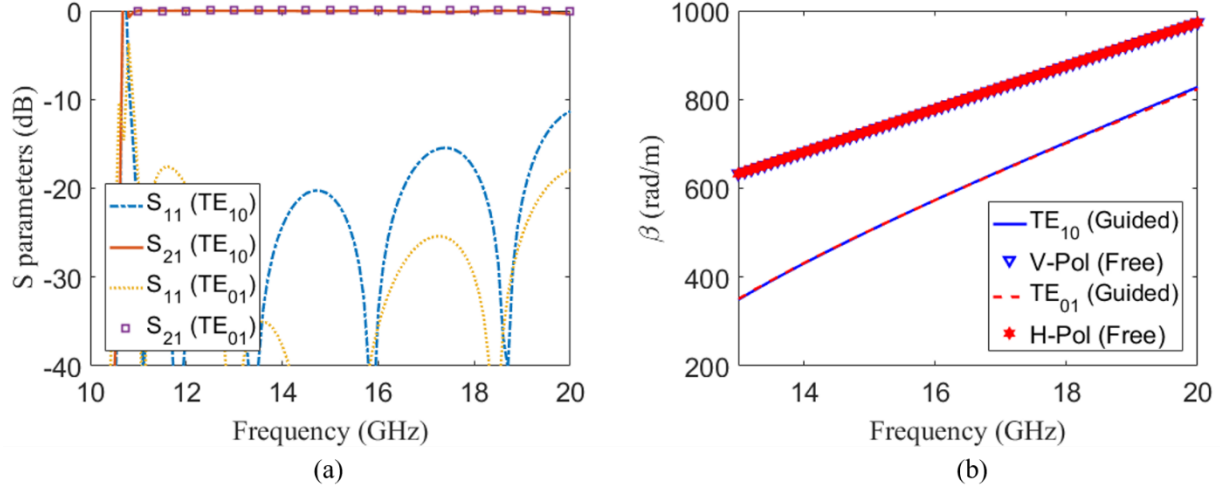


Figure 2.10. Validation example for the isotropization using periodic medium: (a) magnitude of the scattering parameters and (b) propagation constant.

isotropization. This unit cell has  $r = 0.8$  mm,  $b = 6$  mm and  $p = 2$  mm. The resultant effective permittivity tensor using this perforation for the specified anisotropic substrate is,

$$\epsilon_r = \begin{bmatrix} 13.4 & 0 & 0 \\ 0 & 13.4 & 0 \\ 0 & 0 & 10.2 \end{bmatrix} \xrightarrow{\text{perforation}} \epsilon_{eff} = \begin{bmatrix} 5.4 & 0 & 0 \\ 0 & 5.4 & 0 \\ 0 & 0 & 5.4 \end{bmatrix} \quad (2.16)$$

Based on this, the two enclosing equivalent waveguides in Figure 2.9(a) are chosen to have isotropic permittivity  $\epsilon_{eq} = 5.4 = \epsilon_{eff}$ . The magnitude of the scattering parameters shown in Figure 2.10 (a) confirms the coincidence of the three cascaded waveguides where the reflections are below 15 dB from 10 GHz up to 20 GHz. On the other hand, the isotropization can be clearly confirmed in Figure 2.10 (b) where the phase delay achieved for both of the  $TE_{10}$  and the  $TE_{01}$  mode is the same. This simply means that the anisotropic substrate can be converted to an isotropic counterpart using the air-hole perforation.

### 2.2.1.6 Application to SINRD design

In this section, another important application of the modeling technique presented in this work is discussed. This application is to design a substrate integrated version of the well-known dielectric slab waveguide. A typical form of the dielectric slab waveguide is shown in Figure 2.11 (a).

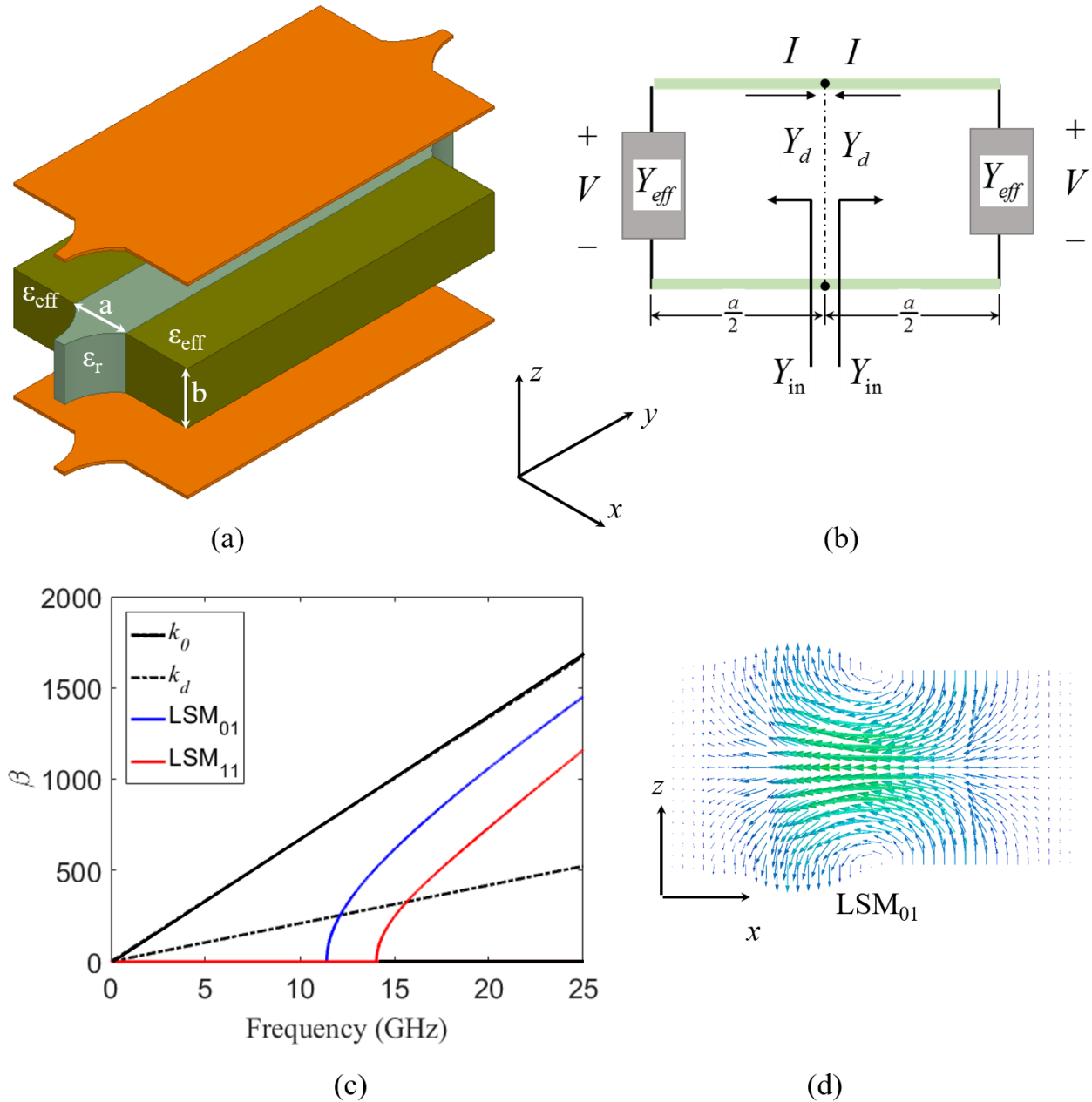


Figure 2.11. Nonradiative dielectric waveguide: (a) equivalent structure, (b) equivalent circuit model, (c) dispersion curves for horizontally oriented modes and (d) field vector distribution for  $LSM_{01}$  mode.

This kind of waveguides consists of three dielectric regions. The center region has a high permittivity compared to the left and right guiding regions. The guided modes along such a structure can be easily studied using the equivalent circuit model shown in Figure 2.11 (b).

The solution of the transverse resonance condition of an equivalent circuit depicted in this figure gives all possible guided modes in the dielectric slab waveguide. Those modes have some which are vertically polarized called the longitudinal sectional electric (LSE) modes and other which are horizontally polarized called longitudinal sectional magnetic (LSM) modes.

In order to obtain the equivalent circuit, a vertical line of symmetry should divide the structure into two identical parts. Each part can be considered as a transmission line with an equivalent characteristic admittance  $Y_d$  and terminated with a load  $Y_{eff}$  as shown in Figure 2.11 (b). The condition that ensures the operation of this equivalent circuit is to have  $Y_{in} = 0$  or  $Y_{in} \rightarrow \infty$  where  $Y_{in}$  can be obtained from the law of the transmission line input admittance, then a transcendental equation can be written as,

$$\left(Y_d + Y_{eff} \coth(ua / 2)\right)\left(Y_{eff} + Y_d \coth(ua / 2)\right) = 0 \quad (2.17)$$

The first bracket gives the solution for the even modes while the second bracket gives the solution for the odd modes.

The method where this equation is obtained is known as the transverse resonance technique. The dispersion relation in (2.17) is valid for both types of modes, where for the LSE modes,

$$Y_d = u / j\omega\mu_o \quad \& \quad Y_{eff} = v / j\omega\mu_o \quad (2.18)$$

while for the LSM modes,

$$Y_d = j\omega\epsilon_o\epsilon_d / u \quad \& \quad Y_{eff} = j\omega\epsilon_o\epsilon_{eff} / v \quad (2.19)$$

The conditions of ensuring the phase matching for both of LSE and LSM even and odd symmetric solutions are,

$$u_m^2 + \beta_{mn}^2 + \left(\frac{n\pi}{b}\right)^2 = k_d^2 = \omega^2 \mu_o \epsilon_d \quad (2.20)$$

$$-v_m^2 + \beta_{mn}^2 + \left(\frac{n\pi}{b}\right)^2 = k_0^2 = \omega^2 \mu_o \epsilon_o \quad (2.21)$$

Solving the dispersion relation in (2.17) along with (2.20) and (2.21) yields all the possible modes.

The LSE modes are usually converted to rectangular waveguide modes using the well-known substrate integrated waveguide technology SIW. This is done easily by having periodic plated vias along the edges of the central region as discussed later in this thesis.

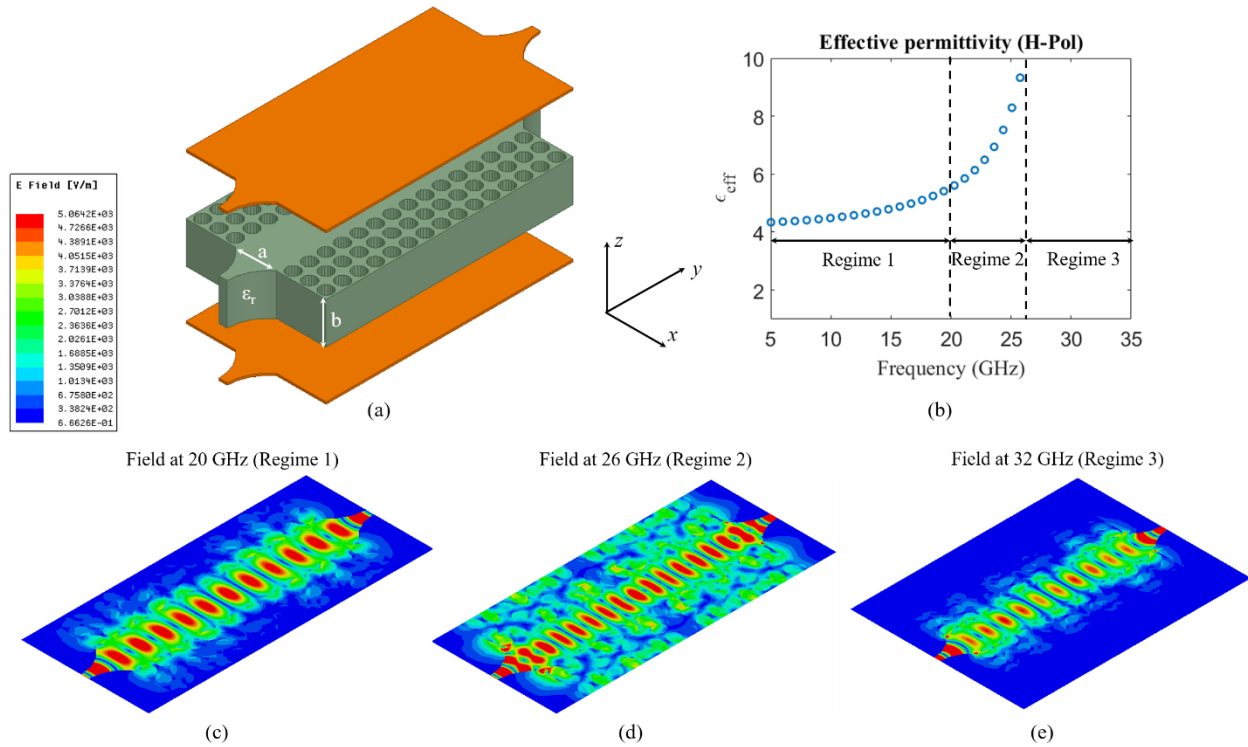


Figure 2.12. SINRD waveguide: (a) equivalent structure, (b) effective dielectric constant for the periodic medium, field distribution for  $LSM_{01}$  mode at (c) 20 GHz, (d) 26 GHz and (e) 35 GHz.

However, for SIW, the horizontally polarized modes cannot be guided by the periodic vias. Therefore, SINRD is the only solution for guiding horizontally oriented modes. In this work, we present the design methodology of an SINRD waveguide useful for studying the horizontally polarized modes.

The resulting dispersion curves for the horizontally oriented modes are shown in Figure 2.11 (c), with the dominant mode being the  $LSM_{01}$  mode. The cross-sectional field distribution for the  $LSM_{01}$  mode is shown in Figure 2.11 (d). This field distribution shows that the  $LSM_{01}$  mode has most of its electrical field vector oriented in the horizontal  $x$ -direction.

The idea of the SINRD depends on realizing the left and right guiding regions by perforating the same material with a certain profile. This perforation should reduce the effective permittivity of the material giving enough step in value to ensure non-radiative guidance of the wave in the central region. From the study presented above in the previous subsection, we learn that the perforation induces a certain level of anisotropy in the material. This means that a certain diameter of the air-

holes will cause the effective permittivity in the vertical direction to be reduced by a certain factor, while that in the horizontal direction is reduced by a different factor. The numerical values for this reduction factor are shown in Figure 2.3 and Figure 2.7 for different perforation profiles.

If the LSM<sub>01</sub> mode is the mode of interest to be guided in the SINRD waveguide, then it is important to calculate the effective permittivity of the perforated regions in the horizontal direction rather than the vertical one. Applying this concept, we designed a simulation model shown in Figure 2.12 (a). For simplicity, the substrate is assumed to be isotropic with permittivity  $\epsilon_r = 10.2$ . The unit cell used in the periodic medium is identical to that of Figure 2.2 with  $r = 0.8$  mm,  $b = 5$  mm and  $p = 2$  mm where the guided region has a width of  $a = 5$  mm.

The effective permittivity of the periodic medium is shown in Figure 2.12 (b). Based on our understanding and observation of this problem, we divide the spectrum into three different regimes of operation depending on the guiding capability of the periodic medium. For the first regime which starts from the low frequencies up to 20 GHz, the guidance caused by the periodic medium is achieved due to the step in the dielectric constant. This is because the effective medium acts equivalently as a dielectric material with permittivity that is approximately around 5 while the main guide in the center has a permittivity of 10.2. This drop in the dielectric constant is sufficient to guarantee the required guidance. This appears clearly in the field distribution of Figure 2.12 (c). For the second regime which starts after 20 GHz up to 26 GHz, an exponential increase occurs for the effective permittivity. This increase makes the periodic medium has an effective permittivity that is close to the main guide substrate. The difference between these permittivities is not sufficient for ensuring the best required guidance. This appears clearly in the field distribution of Figure 2.12 (d) where a considerable part of the field penetrates inside the periodic medium. For the third regime of operation, the periodic medium cannot be considered as an effective medium because of the appearance of a band gap due to the periodicity. In this case, full guidance is achieved, but with a different concept as shown in the field distribution of Figure 2.12 (e).

In the previous sections, the problem of the SINRD waveguide is studied from a different perspective. The two-dimensional periodic part used for guiding the wave propagation is tackled using eigenmode analysis. From this analysis, it is confirmed that this periodic medium acts as an anisotropic material which means each mode experiences different dielectric constant depending on its orientation. This concept is validated by the eigenmode solver of the HFSS. More

interestingly, a specific perforation for the substrate can be utilized in order to convert the anisotropic substrate into isotropic one using the same introduced analysis. A complete design procedure is presented for the SINRD waveguide using the specified concept. The model presented for the periodic medium clarifies a new observation which is any SINRD waveguide works in three different regimes where guidance occurs in two of them, but with different mechanisms, while leakage occurs in the third one.

### 2.2.2 Integrated NRD Waveguide

The NRD waveguide consists of a dielectric substrate enclosed between two metallic plates as shown in Figure 2.13 (a). The wave is supposed to be guided in the dielectric region,  $\epsilon_d$ . The regions to the left and right sides represent the guiding walls and should have a dielectric constant,  $\epsilon_{eff}$ , less than that of the middle dielectric region. This low dielectric constant could be physically achieved in many ways. The difference or contrast between this effective dielectric constant and that of the substrate creates the mechanism of “nonradiative wave guidance” by which the wave is guided. Thus, the SINRD guide is equivalent to a conventional dielectric slab waveguide as shown in Figure 2.13 (a). The key element in designing useful devices using any guiding structure is understanding its dispersion relation and possible modes of operation, not only in the band of interest but also in the whole spectrum. A simple way to derive the dispersion relation of NRD waveguides and to solve for the possible modes of operation is summarized below.

Consider plane wave solutions for Maxwell’s equations in the frequency domain with harmonic time variation in the form  $\exp(j\omega t)$ . Since the inhomogeneity of dielectric permittivity is in the  $x$ -direction, full-wave solutions can be found as either  $TM_x$  (also called longitudinal sectional magnetic LSM) or  $TE_x$  solutions (also called longitudinal sectional electric LSE) [44].

The solution is summarized here for both of the LSE and the LSM modes. Let us assume a scalar wave function  $\psi$ , satisfying  $\mathbf{H} = \nabla \times \hat{a}_x \psi$  and  $\mathbf{E} = -j\omega\mu_0(\hat{a}_x \psi) + \nabla(\nabla \cdot \hat{a}_x \psi) / j\omega\epsilon_0\epsilon_i$ , where  $\mathbf{E}$  and  $\mathbf{H}$  are the electric and magnetic field vectors,  $\mu_0$  and  $\epsilon_0$  are the permeability and permittivity of free space and  $\epsilon_i$  is the relative permittivity being  $\epsilon_d$  in the middle region and  $\epsilon_{eff}$  in the outer regions. For the LSM modes, the solutions for  $\psi$  will take either an even or odd form in  $x$ ,

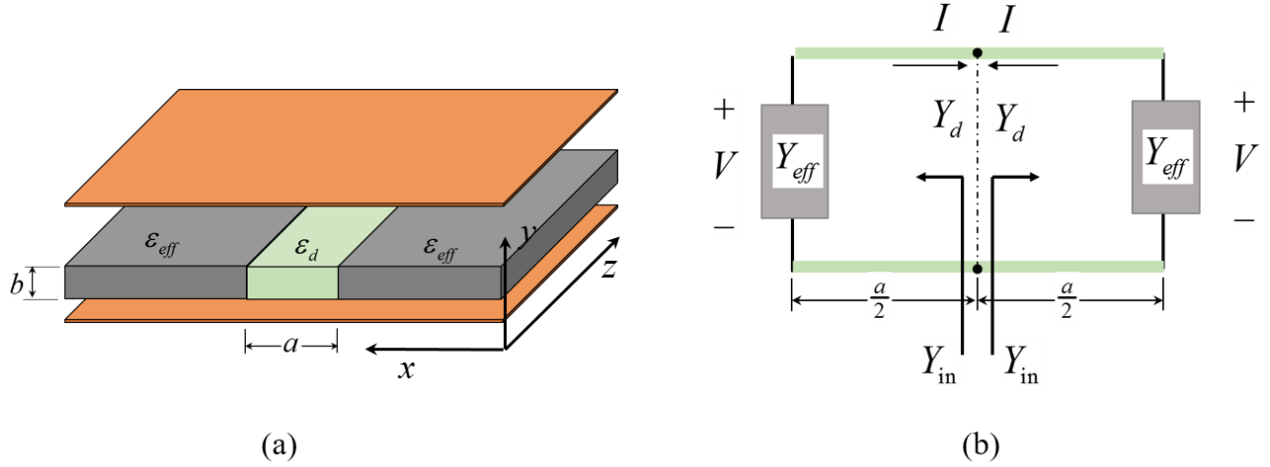


Figure 2.13. NRD waveguide: (a) equivalent structure and (b) equivalent circuit model.

$$\psi^{even} = \begin{cases} A \cos(u_m^e x) \sin(\frac{n\pi}{b} y) e^{-j\beta_{mn}^e z} & , |x| < a/2 \\ B e^{-v_m^e |x|} \sin(\frac{n\pi}{b} y) e^{-j\beta_{mn}^e z} & , |x| > a/2 \end{cases} \quad (2.22)$$

$$\psi^{odd} = \begin{cases} A \sin(u_m^o x) \sin(\frac{n\pi}{b} y) e^{-j\beta_{mn}^o z} & , |x| < a/2 \\ \text{sgn}(x) B e^{-v_m^o |x|} \sin(\frac{n\pi}{b} y) e^{-j\beta_{mn}^o z} & , |x| > a/2 \end{cases} \quad (2.23)$$

where  $u_m^e$  and  $v_m^e$  are the solutions of  $\epsilon_0 u \tan(\frac{ua}{2}) = \epsilon_d v$ , with  $m = 0, 2, \dots$  while  $u_m^o$  and  $v_m^o$  are the solutions of  $\epsilon_0 u \cot(\frac{ua}{2}) = -\epsilon_d v$ , with  $m = 1, 3, \dots$ . In this case of LSM,  $n$  cannot be zero because of the orientation of the x-component of the electric field is parallel to the metallic plates, so  $n = 1, 2, \dots$ .

The choice of the value of  $m$  should receive proper attention; otherwise confusion would likely arise when some researchers call the first LSM mode as LSM<sub>01</sub> [65] while others call it as LSM<sub>11</sub> [42, 66]. We see the proper choice for the first value of  $m$  to be zero, and accordingly, the first LSM mode is the LSM<sub>01</sub> mode. This choice really reflects the symmetry of the mode as explained later in this chapter.

For the LSE modes, equations (2.22) and (2.23) would take the same form except for a cosine variation in the y-direction instead of the sine variation shown above. In this case,  $u_m^e$  and  $v_m^e$  are the solutions of  $u \tan(\frac{ua}{2}) = v$ , with  $m = 0, 2, \dots$  while  $u_m^o$  and  $v_m^o$  are the solutions of  $u \cot(\frac{ua}{2}) = -v$

, with  $m = 1, 3, \dots$ . In this case of the LSE modes,  $n$  can start from zero and thus the first LSE mode of this structure is the LSE<sub>00</sub> mode.

For both LSE and LSM even and odd symmetric solutions,

$$\begin{aligned} u_m^2 + \beta_{mn}^2 + \left(\frac{n\pi}{b}\right)^2 &= k_d^2 = \omega^2 \mu_o \epsilon_d \\ -v_m^2 + \beta_{mn}^2 + \left(\frac{n\pi}{b}\right)^2 &= k_0^2 = \omega^2 \mu_o \epsilon_0 \end{aligned} \quad (2.24)$$

The same dispersion relation could be derived from an equivalent circuit approach or transverse resonance method which is usually preferred from a designer's perspective. Again we summarize the equivalent circuit model, a vertical line of symmetry divides the structure into two equal parts. Each part is considered as a transmission line with an equivalent characteristic admittance  $Y_d$  and terminated with a load  $Y_{eff}$  as shown in Figure 2.13 (b).

The condition that ensures the operation of this equivalent circuit is to have  $Y_{in} = 0$  or  $Y_{in} \rightarrow \infty$  where  $Y_{in}$  can be obtained from the law of the transmission line input admittance, then again a transcendental equation can be written as,

$$\left(Y_d + Y_{eff} \coth(ua / 2)\right) \left(Y_{eff} + Y_d \coth(ua / 2)\right) = 0 \quad (2.25)$$

The dispersion relation in (2.25) is valid for both types of modes, where for the LSE modes

$$\begin{aligned} Y_d &= u / j\omega\mu_o \\ Y_{eff} &= v / j\omega\mu_o \end{aligned} \quad (2.26)$$

while for the LSM modes

$$\begin{aligned} Y_d &= j\omega\epsilon_o\epsilon_d / u \\ Y_{eff} &= j\omega\epsilon_o\epsilon_{eff} / v \end{aligned} \quad (2.27)$$

The first bracket gives the solution for the even modes while the second bracket gives the solution for the odd modes. Solving the dispersion relation in (2.25) yields all the possible modes.

For the sake of simplicity and without loss of generality, the effective medium is assumed to be free space,  $\epsilon_{eff} = 1$ . From DC to 40 GHz frequency range, the dispersion curves for the LSE<sub>mn</sub> and LSM<sub>mn</sub> are shown in Figure 2.14 (a) for a permittivity  $\epsilon_d = 10.2$  and width  $a = 4\text{mm}$  and thickness

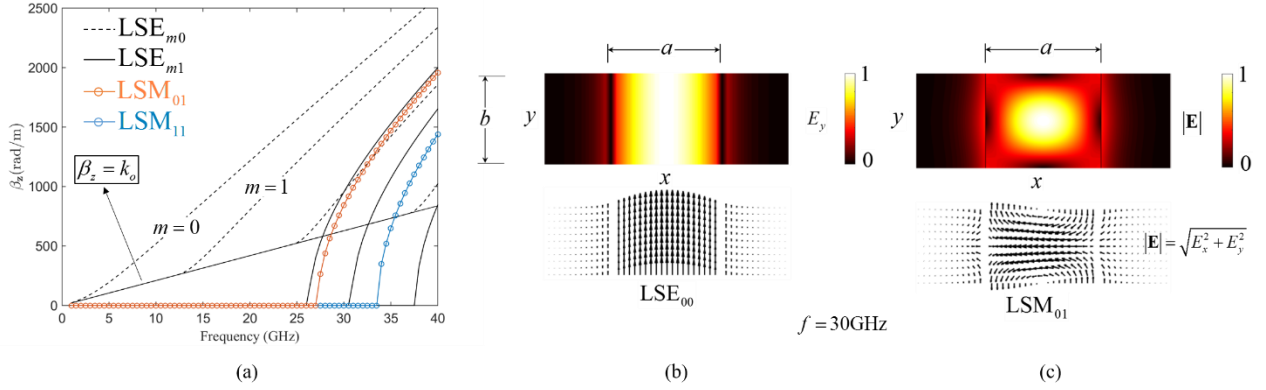


Figure 2.14. NRD waveguide characteristics: (a) dispersion curves, (b) cross-sectional field distribution of LSE<sub>00</sub> mode and (c) LSM<sub>01</sub> mode.

$b = 1.9\text{mm}$ . It is clear that the dominant mode is the LSE<sub>00</sub>, not the LSM<sub>01</sub> as it might be inferred from [42]. The LSE modes that appear at lower frequencies before the LSM<sub>01</sub> could cause a cross coupling and intermodal distortion. This may be one of the reasons why the NRD guide is not widely utilized.

However, in this chapter, this problem is handled by using special kinds of hybrid waveguides that supports a full control on those modes as explained later in section 2.3.

According to the solution procedure mentioned above, one can write the  $y$ -component of the electric field of the LSE<sub>00</sub> as,

$$E_y^{\text{LSE}_{00}} = \begin{cases} \frac{(k_d^2 - u_0^2)}{j\omega\epsilon_d} A \cos(u_0 x) e^{-j\beta z}, & |x| < a/2 \\ \frac{(k_0^2 + v_0^2)}{j\omega\epsilon_0} B e^{-v_0|x|} e^{-j\beta z}, & |x| > a/2 \end{cases} \quad (2.28)$$

the  $x$ -component of electric field of the LSM<sub>01</sub> as:

$$E_x^{\text{LSM}_{01}} = \begin{cases} \frac{(k_d^2 - u_0^2)}{j\omega\epsilon_d} A \cos(u_0 x) \sin(\frac{\pi}{b} y) e^{-j\beta z}, & |x| < a/2 \\ \frac{(k_0^2 + v_0^2)}{j\omega\epsilon_0} B e^{-v_0|x|} \sin(\frac{\pi}{b} y) e^{-j\beta z}, & |x| > a/2 \end{cases} \quad (2.29)$$

and the  $y$ -component,  $E_y$ , of the LSM<sub>01</sub> modes:

$$E_y^{\text{LSM}_{01}} = \begin{cases} -\frac{u(\frac{x}{b})}{j\omega\epsilon_0\epsilon_d} \sin(ux) \cos(\frac{x}{b}y) e^{-j\beta z}, & |x| < \frac{a}{2} \\ -\text{sgn}(x) \frac{v(\frac{x}{b})}{j\omega\epsilon_0} \cos(ua/2) e^{-v|x-\frac{a}{2}|} \\ \cos(\frac{x}{b}y) e^{-j\beta z}, & |x| > \frac{a}{2} \end{cases} \quad (2.30)$$

where all other components, namely  $E_z$ ,  $H_y$  and  $H_z$  are calculated from the wave function  $\psi$ , as mentioned above.

The field distribution of the dominant  $\text{LSE}_{00}$  and  $\text{LSM}_{01}$  modes is shown in Figure 2.14 (b) and Figure 2.14 (c), respectively for  $\epsilon_d = 10.2$ ,  $a = 4\text{mm}$ ,  $b = 1.9\text{mm}$  and  $f = 30\text{GHz}$ . This distribution shows that the wave is guided in the middle region while outside this region it has an evanescent nature. Those evanescent fields will be the basis of the PSC explained later in Chapter 3. The problem, however, is that all the modes regardless their spatial orientation possess this evanescent nature. It is our task now to propose a new kind of guiding structure in which this evanescent nature is a characteristic of only those modes that have a specific spatial orientation, namely the  $\text{LSM}_{01}$  and the like. This structure is explained in Sec. 2.3. However, before we move to Sec. 2.3, it is interesting to present another form of the NRD waveguide which has interesting features shown in the following subsection.

### 2.2.3 Image-NRD waveguide

It can be noticed from Figure 2.14 (a) that the dominant modes for the conventional NRD waveguides are the  $\text{LSE}_{m0}$  modes. Those modes have no cut off frequency, so they cannot be fully controlled or guided which might cause radiation [44]. This drawback along with the bulkiness of those waveguides made this type of NRD guides of low interest in practical applications. The solution to those drawbacks, as shown later, is to add a vertical PEC wall at  $x = 0$  as shown in Figure 2.15 (a). This image-NRD guide was used before as a linear array that composes a leaky wave antenna as in [67], but here we have a different usage as explained below. To explain this, let us recall from the previous subsection that the  $\text{LSM}_{01}$  mode has an odd symmetry in its  $y$ -component around the  $y$ -axis, which is a distinct feature that differentiates it from its lower order vertically oriented modes.

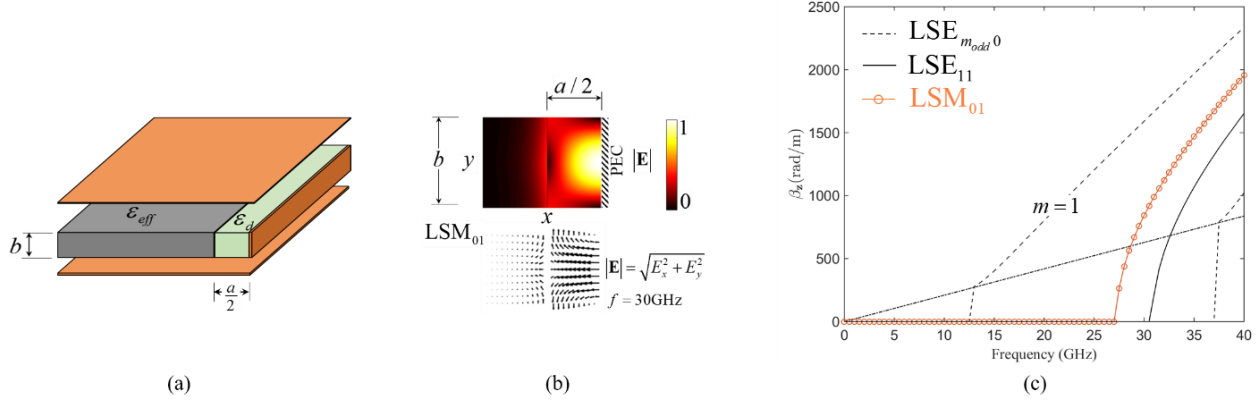


Figure 2.15. Image-NRD waveguide: (a) equivalent structure, (b) cross-sectional field distribution of  $LSM_{01}$  mode and (c) dispersion curves.

This odd symmetry can be deduced from equation (2.30) where the field distribution and dispersion diagram of the  $LSM_{01}$  mode is not affected as in Figure 2.15 (b) and from Figure 2.15 (c), respectively. Thus, adding a PEC wall at  $x = 0$  does not have any effect on the  $LSM_{01}$  mode. The effect of this wall, however, is to suppress any other mode that has a non-zero vertical electric field component.

The dispersion curves in Figure 2.15 (c) show that the resulting image NRD waveguide suppresses all the even LSE modes ( $LSE_{00}$ ,  $LSE_{20}$ ,  $LSE_{01}$ , and  $LSE_{21}$ ) and the odd LSM modes ( $LSM_{11}$  and beyond) that appear in the dispersion relation of Figure 2.14 (a). The dominant modes of the image-NRD waveguide is the  $LSE_{10}$  mode for a vertically oriented field and the  $LSM_{01}$  for a horizontally oriented field with a broader bandwidth compared to the same modes of the NRD waveguide of Sec. 2.2.2. This is due to the mode suppression explained earlier.

Due to this reduction of size and number of possible modes, we choose this type of image-NRD waveguide to construct half of the PSC proposed in this thesis. To achieve the polarization selective coupling, the other half will be an image-NRD-SIW waveguide which is presented below in Sec. 2.3.

### 2.3 Hybrid NRD-SIW guiding structure and its image form

The conventional SIW structure supports the regular rectangular waveguide vertically oriented modes ( $TE_{m0}$ ). The horizontally oriented modes ( $TE_{0n}$ ) are not guided in the middle region; this is

because the vertical periodic wall which is built by vias is transparent to any electric field orthogonal to them [40]. This did not cause any problem in conventional SIW-based devices because the dominant mode is the  $TE_{10}$  mode which is tangential to the metallic vias.

In the waveguide presented in this section, which is a modified version of SIW, the dielectric substrate is bounded by an effective medium with a lower dielectric constant  $\epsilon_{eff}$  filling the region behind the periodic wall. In this case, the  $TE_{0n}$  modes are still guided in the middle region due to the change in the dielectric constant as explained in Sec. 2.2.2. Those modes correspond to the LSM modes of the NRD waveguide. So this waveguide can support the  $TE_{m0}$  modes of the SIW in addition to the LSM modes of the NRD waveguide. Unlike the work in [68] that called the structure which combines the SINRD along with the SIW as an extended substrate integrated waveguide (ESIW), in this work, we called this modified version of the SIW as Hybrid NRD-SIW waveguide and it is shown in Figure 2.16 (a). We choose this name because we have no need for a huge periodic medium outside the metallic vias which guides the horizontally oriented modes. Getting rid of the periodic medium is because our PSC device, presented in chapter 3, mainly depends on the presence of a very thin effective medium which cannot be supported by the ESIW in [68]. This is explained in details in the following sections.

### 2.3.1 Hybrid NRD-SIW waveguide

To simplify the analysis of this structure, it is important to note that the effect of the periodic wall is seen only by the  $y$ - component of the electric field. The  $x$ -component only experiences the sudden change in the dielectric permittivity. In other words, any mode whose main field component is horizontal sees the structure as a dielectric slab waveguide enclosed by the metallic ground planes at  $y = 0$  and  $y = b$ , exactly as the one described in Sec. 2.2.2, while the orthogonally oriented mode sees the structure as a regular SIW as shown in Figure 2.16 (a) for the same parameters used in Sec. 2.2.

The dispersion curves for a Hybrid NRD-SIW waveguide could be constructed from the dispersion curve shown in Figure 2.14 (a) by omitting all the LSE modes and replacing them by the regular  $TE_{m0}$  modes of a rectangular waveguide of width  $a$ . At the same time, all the LSM modes should be kept the same. In this structure, the first modes in order are the  $TE_{10}^{SIW}$ ,  $TE_{20}^{SIW}$ , and the  $LSM_{01}$  modes as shown in the dispersion curves of Figure 2.16 (b).

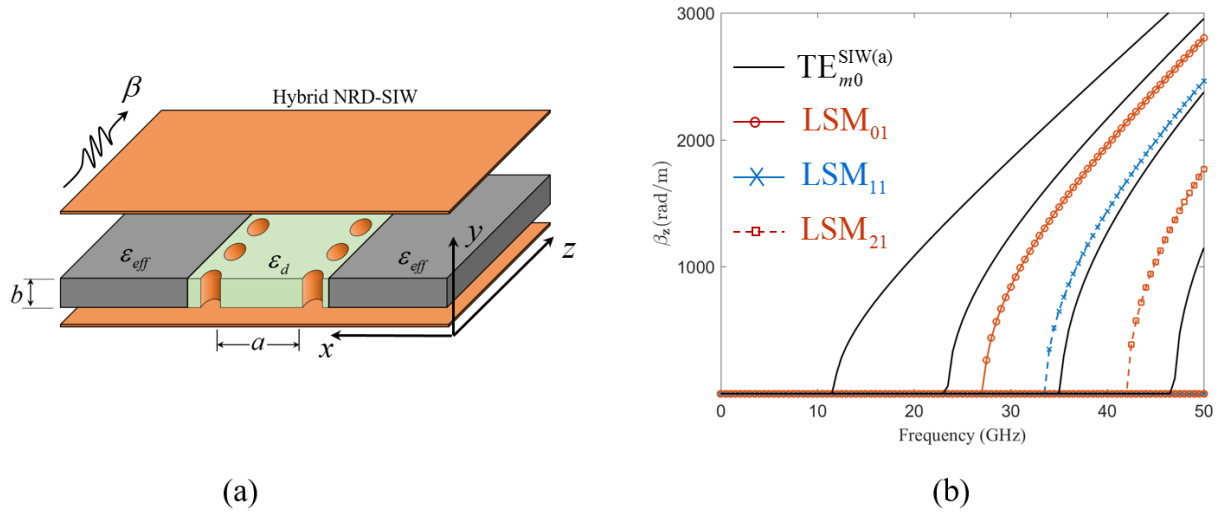


Figure 2.16. Hybrid-NRD-SIW waveguide: (a) equivalent structure and (b) dispersion curves.

In those curves, the  $LSM_{01}$  appears as the third higher order mode. In other words, one cannot achieve a single mode operation where the  $LSM_{01}$  mode is the only propagating mode. This always causes a problem when it comes to designing a microwave component relying on the  $LSM_{01}$  mode propagation.

The interesting feature of this Hybrid NRD-SIW waveguide is that the two sorts of the propagating modes,  $TE_{m0}$  and  $LSM_{mn}$ , are guided by two independent mechanisms, metallic vias and effective medium, respectively. The fact that the  $LSM_{mn}$  modes penetrate through the metallic vias, while the  $TE_{m0}$  modes are totally confined between them is the main concept of the polarization selectivity on which we build our proposed PSC structure explained in chapter 3.

Before we leave this section, it is interesting to see the effect of adding a PEC wall at  $x = 0$ , exactly as done for the image-NRD waveguide in Sec. 2.2.3. This effect is explained in details in section 2.3.2 below.

### 2.3.2 Image-NRD-SIW waveguide

The effect of adding a PEC wall at  $x = 0$  to the Hybrid NRD-SIW waveguide is studied in this subsection and shown in Figure 2.17 (a). This wall has the same effect on the LSM modes as explained in Sec. 2.2.3 which is the suppression of the LSM modes with odd symmetries while keeping those with even symmetries the same. Regarding the  $TE_{m0}$  modes of the SIW, the PEC

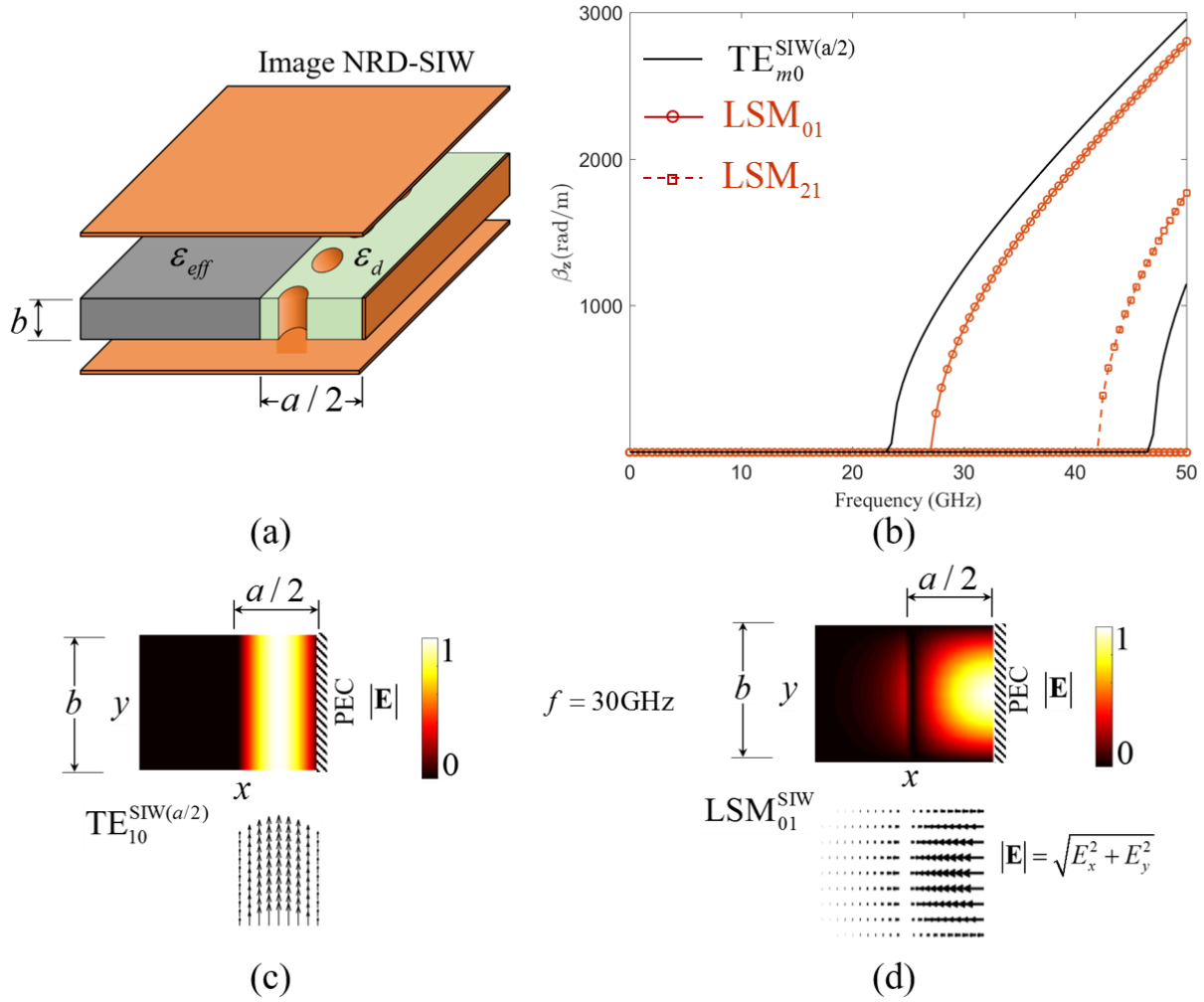


Figure 2.17. Image-NRD-SIW waveguide: (a) equivalent structure, (b) dispersion curves, (c) field distribution of  $TE_{10}$  mode and (d) field distribution of  $LSM_{01}$  mode.

wall decreases the substrate width to be  $a/2$  which doubles the cut off frequencies of the  $TE_{m0}$  modes compared to the Hybrid NRD-SIW waveguide. We call this type as image NRD-SIW and the dispersion relation of this structure is shown in Figure 2.17 (b). The field distribution of the first two modes; namely  $TE_{10}$  and  $LSM_{01}$  modes are shown in Figure 2.17 (c) and Figure 2.17 (d), respectively and given by:

$$E_y^{TE_{10}^{SIW}} = E_o \sin(2\pi x / a) e^{-j\beta_{10}^{TE} z}, \quad -\frac{a}{2} \leq x \leq 0 \quad (2.31)$$

and

$$E_x^{\text{LSM}_{01}^{\text{SIW}}} = \begin{cases} \frac{(k_d^2 - u_0^2)}{j\omega\epsilon_d} A \cos(u_0 x) \sin(\frac{\pi}{b} y) e^{-j\beta_{01}^{\text{LSM}} z}, & -\frac{a}{2} \leq x \leq 0 \\ \frac{(k_0^2 + v_0^2)}{j\omega\epsilon_0} B e^{v_0 x} \sin(\frac{\pi}{b} y) e^{-j\beta_{01}^{\text{LSM}} z}, & x \leq -\frac{a}{2} \end{cases} \quad (2.32)$$

where  $E_x$  and  $E_z$  are zeros for the  $\text{TE}_{10}^{\text{SIW}}$  mode. For the  $\text{LSM}_{01}^{\text{SIW}}$  mode, there is no  $y$ -component for the electric field which is its main difference from the regular  $\text{LSM}_{01}$  mode of the image-NRD waveguide. The  $\text{TE}_{10}^{\text{SIW}}$  takes the same distribution as that of the rectangular waveguide [69].

It is clear that the field of the  $\text{TE}_{10}^{\text{SIW}}$  is strictly confined to the region between the vias and the PEC wall, while the field lines of the  $\text{LSM}_{01}$  mode initiate at the PEC wall and decay exponentially into the effective dielectric region in the left-hand side of the vias as shown in the vector field representation in Figure 2.17 (d).

Furthermore, one can see that the number of possible modes in the image NRD-SIW structure is well controlled over a wideband of operation from DC up to 50 GHz. For example, for the parameters specified in Sec. 2.2.3, this waveguide has only two possible modes of operation from about 20 GHz up to 40 GHz as appears in Figure 2.17 (b). Based on this study, it is concluded that the image NRD-SIW presented in this section possess the following features:

- Supports only one vertical mode for a BW of 20 GHz.
- Supports only one horizontal mode for a BW of 15 GHz.
- Only the horizontally-polarized mode penetrates outside the periodic metallic wall with an evanescent nature.

Therefore, we choose this type of waveguides to construct the other half of the PSC proposed in this chapter, besides the image-NRD guide explained earlier in Sec. 2.2.3.

## 2.4 Conclusion and design rules discussion

Typically, a high dielectric constant ceramic-based material is not purely isotropic [70]. This, in short means, that the horizontal field of the  $\text{LSM}_{01}$  mode sees a dielectric constant that is higher than that seen by the field of the  $\text{TE}_{10}$  mode of the SIW. This has the effect of making the dimension

$b$  electrically larger than  $a$ , thus the  $\text{LSM}_{01}$  becomes the dominant mode of the structure with about 1 GHz of the bandwidth of this single mode operation. In Figure 2.17(b), one can also observe that for about 15 GHz of bandwidth, the only modes of operation are the  $\text{LSM}_{01}$  and the  $\text{TE}_{10}$ . Being orthogonally polarized, and guided by two different mechanisms, those two modes pave the way for the design of cross-polarized mm-wave components such as orthomode transducers, dually polarized couplers, and diplexing systems for 5G basestations.

An important feature of the presented Image-NRD-SIW waveguide, is the different mechanisms by which the *two dominant* modes of operation are guided. This distinction is clear in the field plots shown for the two modes in Figure 2.17 at 30 GHz. The vertically oriented  $\text{TE}_{10}$  mode is almost fully confined in the region  $0 < x < a/2$  whereas the  $\text{LSM}_{01}$  penetrates behind the periodic wall and then decays exponentially with the constant  $\nu_0$ . This feature allows one to estimate the cutoff frequency of the  $\text{LSM}_{01}$  without really solving the nonlinear dispersion relation for the value of  $u$  in (2.24). This could be achieved by comparing field distribution of the  $\text{LSM}_{01}$  mode in a hybrid NRD-SIW to the  $\text{TE}_{11}$  mode of RWG with cross section  $a \times b$ , noticing that  $u_0$  satisfies the inequality  $0 < u_0 < \pi/a$ . This is not to be confused, however, with the fact that in the Image-NRD, the  $\text{LSM}_{01}$  mode resembles the  $\text{TE}_{01}$  mode of an RWG with cross-section  $(a/2) \times b$ . Accordingly, one can get a good approximation of the cutoff frequency of the LSM modes by the following equation,

$$f_{c_{\text{LSM}_{m1}}} \leq \frac{c}{2\sqrt{\epsilon_{r_{xz}}}} \sqrt{\left(\frac{m+1}{a}\right)^2 + \left(\frac{1}{b}\right)^2} \quad (2.33)$$

and then design mmW components based specifically on this penetration such as full-wave couplers widely used in the optics applications. Experimental prototypes of a few of those applications show great potential and will be presented later.

The PSC can be constructed by placing the image-NRD and the image-NRD-SIW guides in parallel with an air gap (as an effective medium) in-between which is the general form of the PSC. This PSC is supposed to be the basic unit in the proposed planar OMT structure. One can imagine the wave propagation mechanism through this PSC when exciting the structure with two orthogonally

polarized modes simultaneously, namely  $TE_{10}^{SIW}$  and  $LSM_{01}$  modes. If the image-NRD-SIW guide, is excited with a dually-polarized signal, the vertically polarized signal ( $TE_{10}^{SIW}$ ) propagates only through this guide because it is completely confined by the metallic vias without coupling to the adjacent guide. On the contrary, for the horizontally polarized signal ( $LSM_{01}$ ), the periodic conducting wall is transparent for such a horizontal mode, so this mode penetrates exponentially through the air gap (which represents the effective medium in this case) then couples to the adjacent image-NRD guide, and gets fully received there if it has an appropriate coupling length. So the vertically polarized mode  $TE_{10}^{SIW}$  is received at the end of the image-NRD-SIW guide while the horizontally polarized mode  $LSM_{01}$  is received at the end of the image-NRD guide. Therefore, the vertically polarized  $TE_{10}$  mode is incapable to get coupled from the image-NRD-SIW guide to the image-NRD guide, while the horizontally polarized  $LSM_{01}$  mode has the ability to couple from the image-NRD-SIW guide to the image-NRD guide which is the main function of an OMT. This mechanism is provided in details in the following chapter.

## CHAPTER 3 POLARIZATION SEPARATION AND COMBINATION

In this chapter, the concept of separating and/or combining orthogonal signals is introduced. The device that can separate or combine orthogonal signals is called orthomode transducer (OMT). Unlike the previously-introduced OMTs, we aim at the design of a planar OMT based on the motivations stated in the first chapter. In this thesis, we provide two techniques for implementing a planar OMT that can be integrated with printed circuit board (PCB) applications.

### 3.1 Polarization selective coupling (PSC)

#### 3.1.1 Image-NRD coupler

The main objective is to build a device that supports two orthogonal polarizations, but at the same time performs different functions on those supported polarizations. In the previous chapter, two special types of waveguides are discussed, namely the Image-NRD and the Image NRD-SIW. To achieve this objective, it is important to study how those special types of waveguides can construct directional couplers.

Thus, this section shows the analytical development of a forward wave coupler based on the Image-NRD waveguide [71]. The forward directional coupler is a well-known device that finds its way in many applications in integrated microwave and photonic communication circuits. The underlying theory behind such couplers can be found in [72]. This kind of coupler usually consists of two closely separated waveguides where one of them is considered to be the main transmission line that carries the signal, and the other one is to carry the coupled signal. Those conventional couplers couple any modes on the main transmission line regardless their orientations. For each mode, those couplers also have a different behavior. First, the coupling of all modes on an image-NRD coupler without any polarization selectivity is shown in this section; then one can study how to prevent the coupling of unwanted polarizations.

The geometry of the image-NRD waveguide coupler studied in this section is illustrated in Figure 3.1 (a). This image-NRD waveguide coupler consists of two identical dielectric slab waveguides, guides A and B, with relative permittivity  $\epsilon_d$  and width  $a/2$ . The two guides are separated with distance  $d$ , and surrounded by an effective medium with relative permittivity  $\epsilon_{eff}$ .

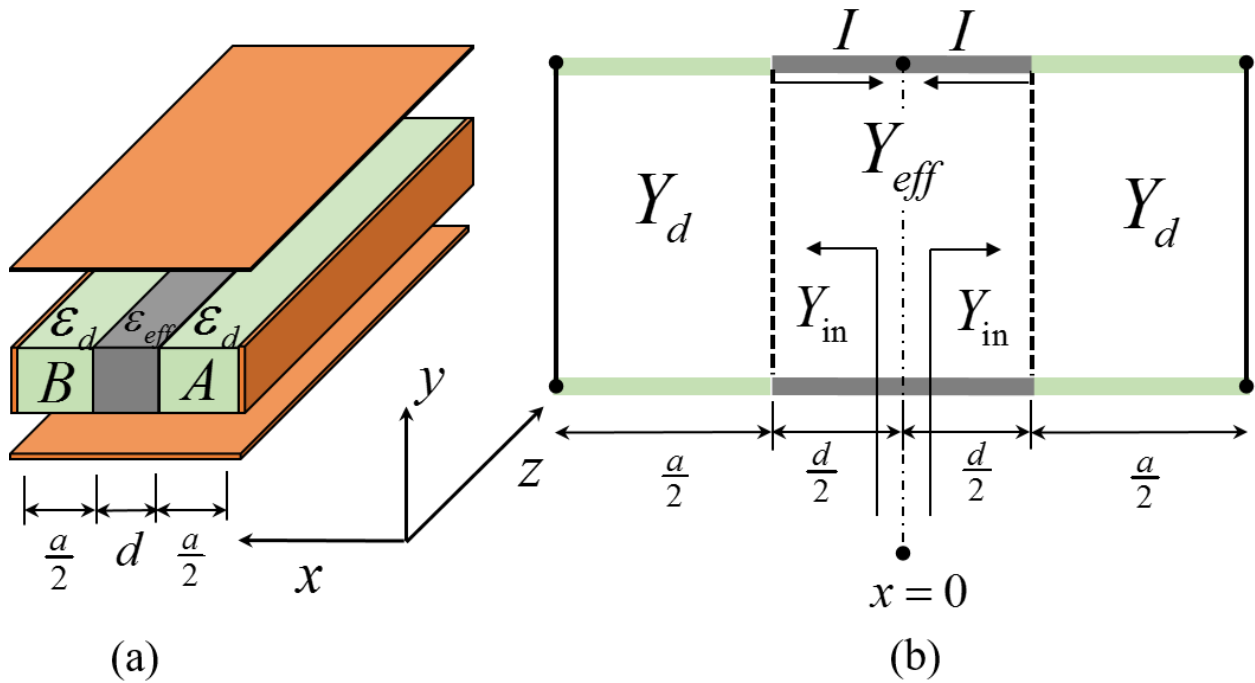


Figure 3.1. Image-NRD coupler: (a) equivalent structure, (b) equivalent circuit model and (c) dispersion curves.

A complete analysis of the NRD coupler (not the image version of it) is derived in [73], whereas in this section, the image-NRD waveguide coupler is studied.

Assume the  $y$ -component of the magnetic field,  $H_y$ , of the LSM mode to be in this form [44],

$$H_y = H_y(x) \sin\left(\frac{n\pi}{b} y\right) e^{-j\beta z}, \quad \text{where} \quad (3.1)$$

$$H_y(x) = \begin{cases} B_m \sin u\left(x + \frac{d}{2}\right) + C_m \cos u\left(x + \frac{d}{2}\right), & -a - \frac{d}{2} \leq x \leq -\frac{d}{2} \\ D_m \sinh vx + E_m \cosh vx, & -\frac{d}{2} \leq x \leq \frac{d}{2} \\ F_m \sin u\left(x - \frac{d}{2}\right) + G_m \cos u\left(x - \frac{d}{2}\right), & \frac{d}{2} \leq x \leq a + \frac{d}{2} \end{cases} \quad (3.2)$$

where  $u$  and  $v$  are the unknowns to be solved for, and one should note that they are different from those for an isolated waveguide explained in the previous chapter.

To solve for those unknowns, the dispersion equation can be obtained by applying the boundary conditions at the interfaces for both the  $H_y$  and  $E_z$  components. The same dispersion equation can also be obtained through the equivalent circuit shown in Figure 3.1 (b) based on the transverse resonance method, which has been discussed in the previous chapter. In this equivalent circuit, the dielectric regions (guides A and B) and the effective region in the gap are modeled as transmission lines with characteristic admittances  $Y_d$  and  $Y_{eff}$ , respectively. The image PEC walls on the left and right sides are modeled as short circuit loads. Due to the symmetry of the structure, the condition which guarantees the operation of this equivalent circuit is to have  $Y_{in} = 0$  or  $Y_{in} \rightarrow \infty$  which gives the solution for the even and odd modes, respectively, where

$$Y_{in} = Y_{eff} \frac{Y_{eff} + Y_d \cot(ua) \coth(vd/2)}{Y_{eff} \coth(vd/2) + Y_d \cot(ua)} \quad (3.3)$$

and  $Y_d$  and  $Y_{eff}$  are given in (2.27) for the LSM modes. Substituting (2.27) in (3.3), the final dispersion relation for the LSM modes has the following form,

$$u\epsilon_{eff} \sin(ua) + v\epsilon_d \cos(ua) \pm \left(u\epsilon_{eff} \sin(ua) - v\epsilon_d \cos(ua)\right) e^{-vd} = 0 \quad (3.4)$$

where the negative and positive signs give the solution for even and odd modes, respectively. The interested reader could derive the same form in (3.4) by applying the proper boundary conditions using fields in (3.2). The field coefficients written in (3.2) can be easily calculated by using the

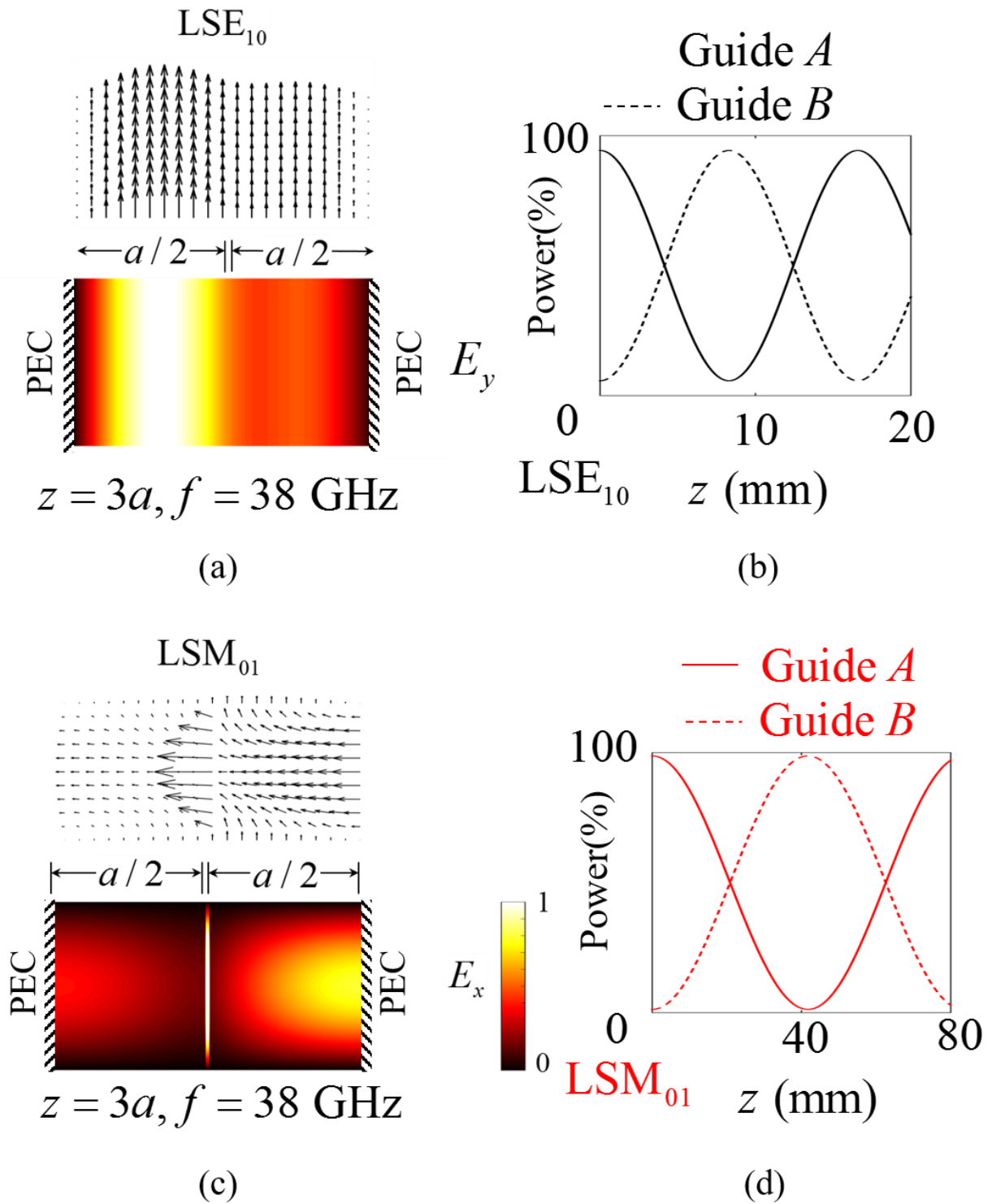


Figure 3.2. Field characteristics of image-NRD coupler at 38 GHz: (a) field distribution of  $LSE_{10}$  mode, (b) power alternation for  $LSE_{10}$  mode, (c) field distribution of  $LSM_{01}$  mode and (d) power alternation for  $LSM_{01}$  mode.

following matrix form obtained from the boundary conditions of the electric and magnetic fields. The coefficients can be easily evaluated as the eigenvectors which correspond to the zero eigenvalue of the following  $6 \times 6$  dispersion matrix:

$$\begin{bmatrix} \Lambda_{11} & \Lambda_{12} & 0 & 0 & 0 & 0 \\ 0 & 1 & \Lambda_{23} & \Lambda_{24} & 0 & 0 \\ \Lambda_{31} & 0 & \Lambda_{33} & \Lambda_{34} & 0 & 0 \\ 0 & 0 & \Lambda_{43} & \Lambda_{44} & 0 & -1 \\ 0 & 0 & \Lambda_{53} & \Lambda_{54} & \Lambda_{55} & 0 \\ 0 & 0 & 0 & 0 & \Lambda_{65} & \Lambda_{66} \end{bmatrix} \begin{bmatrix} B_n \\ C_n \\ D_n \\ E_n \\ F_n \\ G_n \end{bmatrix} = 0 \quad (3.5)$$

where the coefficients  $\Lambda_{ij}$  are given by:

$$\begin{aligned} \Lambda_{11} &= \Lambda_{65} = \cos(ua) \\ \Lambda_{12} &= -\Lambda_{66} = \sin(ua) \\ \Lambda_{31} &= -\Lambda_{55} = u\varepsilon_o / \varepsilon_d \\ \Lambda_{23} &= \Lambda_{35} / v = \Lambda_{43} = \Lambda_{54} / v = \sinh(vd / 2) \\ \Lambda_{24} &= \Lambda_{34} / v = -\Lambda_{44} = -\Lambda_{53} / v = -\cosh(vd / 2) \end{aligned} \quad (3.6)$$

This matrix represents a simpler form of the solution as compared to the one that used the mode orthogonality [73]. The same analysis can be done for the LSE modes. According to the analysis in the previous section, each mode is represented using its even and odd components of symmetry about  $x = 0$ . That is

$$E^{\text{LSM}_{01}}(z) = \left\{ E^{\text{LSM}_{01}} \right\}_{\text{even}} e^{-j\beta_{\text{even}}z} + \left\{ E^{\text{LSM}_{01}} \right\}_{\text{odd}} e^{-j\beta_{\text{odd}}z} \quad (3.7)$$

where  $\beta_{\text{even}}$  and  $\beta_{\text{odd}}$  are calculated by substituting the first two solutions of (3.4) in (2.24). This even and odd symmetry is not to be confused with the even and odd orders for the LSE and LSM modes.

To know the first two modes of this image-NRD waveguide coupler, one can revisit Figure 2.15 (c). It is clear that the first two modes on each waveguide which constitutes the coupler are the  $\text{LSE}_{10}$  and the  $\text{LSM}_{01}$  modes. The decomposition of those modes into their even and odd symmetry distributions is shown in Figure 3.1 (c). In Figure 3.2, the behavior of the structure is illustrated at  $f = 38 \text{ GHz}$  and using the same parameters specified in the previous examples of the chapter, the field distribution conveys that coupling is achieved between the image guides A and B. At  $z = 3a$ , it can be observed that the field strength at the coupled guide (B) is higher than that of the excited

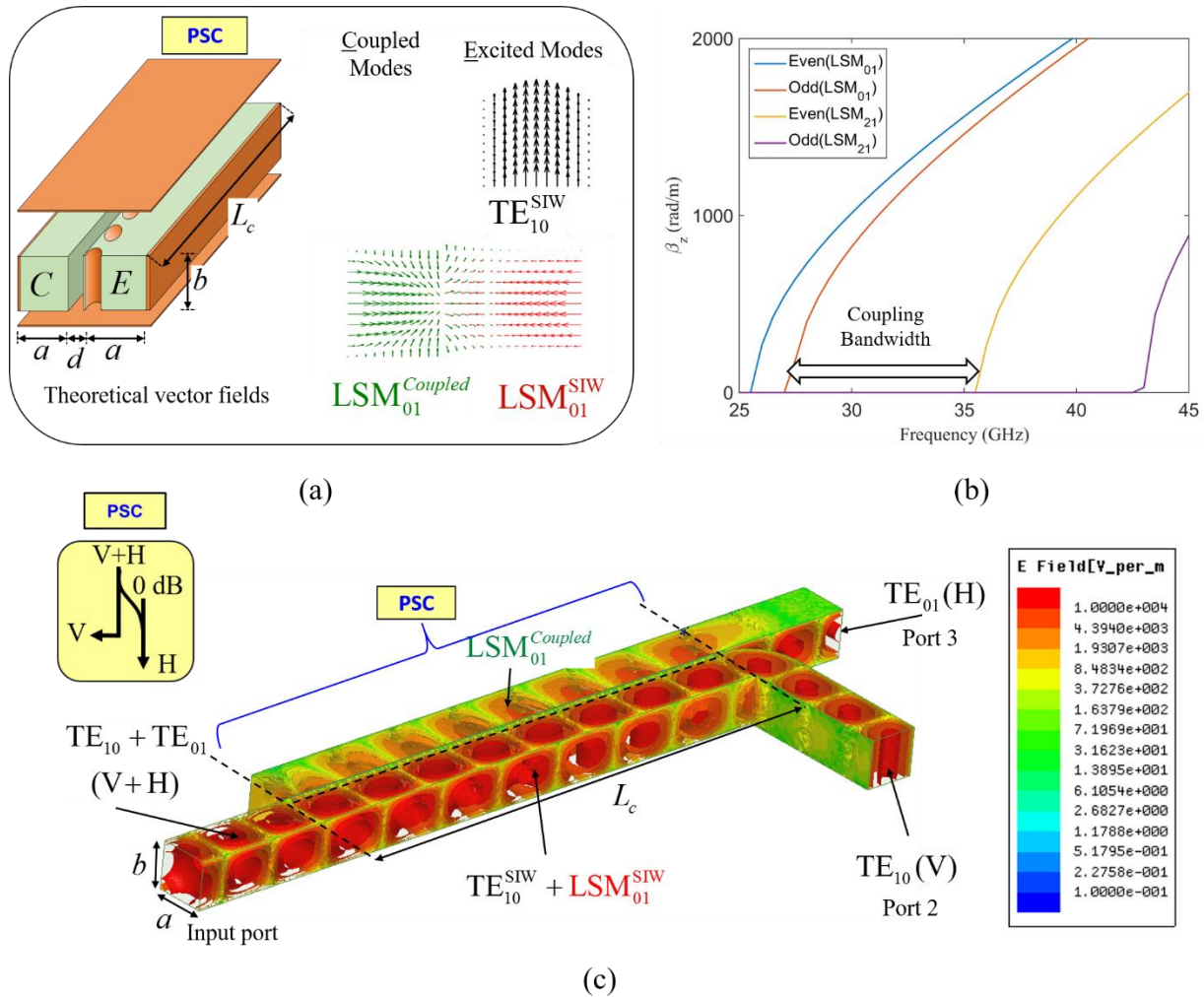


Figure 3.3. Polarization selective coupler (PSC): (a) equivalent structure supported with theoretical field vectors for the excited and coupled modes, (b) dispersion curves of horizontally polarized modes and (c) field distribution when adding input and output waveguides.

guide (A) in the case of the  $LSE_{10}$  mode as in Figure 3.2 (a). On the contrary, at the same value of  $z$ , the field strength at guide B is smaller than that of guide A for the  $LSM_{01}$  mode as in Figure 3.2 (c). This can be illustrated by the power percentage of both guides shown in Figure 3.2 (b) and Figure 3.2 (d). From those plots, one can infer that for the  $LSE_{10}$  mode, the full coupling is achieved at a smaller length than in the  $LSM_{01}$  mode.

Thus, the Image-NRD waveguide coupler is able to couple both types of vertically and horizontally oriented modes, namely the  $LSE_{10}$  and  $LSM_{01}$  modes. Each mode of them totally couples at a

different length which can be extracted from the power percentage plots. The main objective is how to allow a specific mode to couple to the other guide while keeping the other mode in the main guide. This is the idea of the proposed PSC which is introduced in the next section.

### 3.1.2 The Concept of Polarization Selectivity for Polarization Discrimination

In this work, it is proposed for the first time to build a coupler that works specifically for the second higher order mode while the fundamental mode remains uncoupled on the main transmission line. This kind of coupler, we call it, *Polarization-Selective Coupler (PSC)*. The polarization selectivity is added to the image-NRD waveguide coupler explained in Sec. 3.1.1 by replacing the main waveguide with an image-NRD-SIW waveguide explained in Sec. 2.3.2. As shown in Figure 3.3 (a), the image-NRD-SIW is the main transmission line (guide  $E$ ) while the image-NRD waveguide is the coupled transmission line (guide  $C$ ). The guide  $C$  is brought beside the guide  $E$  with a small distance  $d$ . It has been explained in Sec. 2.3.2 that the field distribution of the  $LSM_{01}$  mode penetrates outside the metallic vias while the  $TE_{10}^{SIW}$  mode is confined between them. Therefore, if guide  $E$  is excited by two orthogonal polarizations; the  $LSM_{01}$  mode propagates through the guide  $E$ , and not confined by the metallic vias, so it has the ability to couple to the guide  $C$ , while the  $TE_{10}^{SIW}$  mode stays confined by the vias and cannot couple to guide  $C$ . This can be easily demonstrated by the field distribution for both modes as shown in Figure 3.3 (c). The electric field magnitude of the  $LSM_{01}$  mode which has a horizontal polarization can be obtained from (2.32) .

In the vector field distribution shown in Figure 3.3 (a), the excited  $LSM_{01}^{SIW}$  mode is shown in red, while the coupled mode  $LSM_{01}$  is shown in green. We can distinguish between those modes by keeping in mind that the  $LSM$  mode in the SIW guide, the red one, has no  $y$ -component which vanishes due to the vias as explained earlier.

The coupling appears due to a close separation between the two waveguides. This coupling distance depends on the exponential term that dictates the behavior of the electric field in the region outside the periodic wall, as written in (2.30). The distance  $d$  should be selected as small as possible in order to guarantee that the electric field has not decayed completely. To ensure that the  $LSM_{01}$  mode completely couples from guide  $E$  to guide  $C$ , the coupling length can be extracted from the power alternation plot in Figure 3.2 (d).

For the horizontally polarized modes, the PSC structure acts exactly as the image-NRD coupler. Therefore, the same way of obtaining the dispersion curves of the image-NRD coupler based on (3.4) can be followed for finding the dispersion curves for the horizontally polarized modes of the PSC as shown in Figure 3.3 (b). These dispersion curves contain the even and odd components of the  $LSM_{01}$  and  $LSM_{21}$  modes for a PSC filled with dielectric substrate Rogers RT/Duroid 6010 that has a dielectric constant of 10.2, dielectric loss of 0.0023, width  $a/2 = 2$  mm, thickness  $b = 1.9$  mm and air gap width  $d = 0.05$  mm. The even and odd components of the  $LSM_{01}$  mode are the necessary components for achieving a forward coupling. The appearance of the even component of the  $LSM_{21}$  mode prevents the coupling occurrence and limits the bandwidth to about 9 GHz around the operating frequency at 32 GHz.

At the end of the structure longitudinal length, which is designed for full coupling as mentioned above, guide  $E$  has just the vertically oriented mode  $TE_{10}^{SIW}$ , while guide  $C$  has just the horizontally oriented mode  $LSM_{01}$ . If we can extract each mode separately, an OMT device can be designed based on the PSC as explained in the next subsection.

As explained previously, the PSC shows that it can support the propagation of dual modes with orthogonal polarizations ( $TE_{10}^{SIW}$  and  $LSM_{01}$ ) independently. If the coupling level of the horizontal LSM polarization is adjusted to reach 0dB, which is theoretically possible [43], then the two polarizations could be completely separated. This is the same function as an OMT device. As shown in Figure 1.2, the OMT is based on the proposed PSC supported with the receiving dual-mode input waveguide and then, the vertically, and horizontally oriented output waveguides.

It is shown in Figure 1.2 that the OMT block is connected from one side to a cross-polarized antenna. The antenna is supposed to receive an arbitrarily polarized wave. It will be the function of our OMT to decompose the received wave into vertical and horizontal polarizations. Regarding the input section, it is required to support both  $TE_{10}^{SIW}$  and  $LSM_{01}$  modes in the same frequency range. This restricts the cross-section of the input guide to be almost a square. For the output sections, it is required to support single mode operation for each polarization on its corresponding output port. Since the new band for the 5G network includes the starting edge of the mmW band is 28-38 GHz, we choose as a proof of concept to design an OMT at the center frequency of 32 GHz.

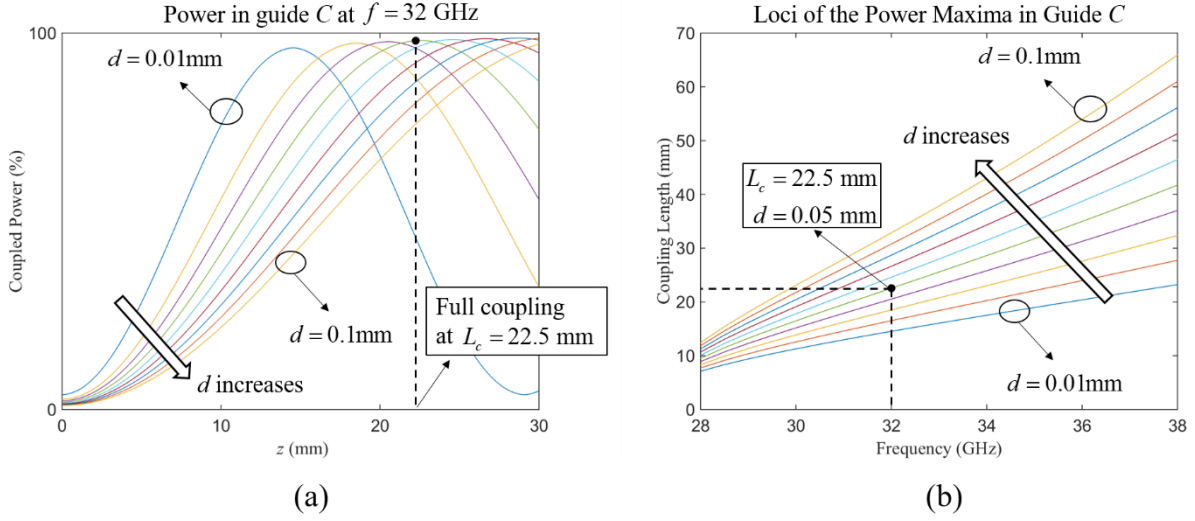


Figure 3.4. The parametric analysis for both of (a) the spacing  $d$  and (b) the coupling length  $L_c$  of the PSC-based OMT design.

For the vertically and horizontally oriented waveguides. The complete design steps of the OMT at 32 GHz can be started by designing the core block which is the PSC. The PSC guides have almost a rectangular cross section of dimension  $a \times b$ , which will be determined according to the required band of operation. The cut-off frequencies of the propagating  $TE_{10}^{SIW}$  and  $LSM_{01}$  are,

$$f_{c_{TE_{10}^{SIW}}} = \frac{c}{2\sqrt{\epsilon_r}} \frac{m}{a} \quad (3.8)$$

$$f_{c_{LSM_{m1}}} \leq \frac{c}{2\sqrt{\epsilon_r}} \sqrt{\left(\frac{m+1}{2a}\right)^2 + \left(\frac{1}{b}\right)^2} \quad (3.9)$$

Equation (3.9) follows from the main concept of the Hybrid image-NRD-SIW structure. The factor of 2 under the square root in (3.9) is multiplied by the dimension  $a$  because of the symmetry of the  $LSM_{01}$  mode around the  $y$ -axis as explained earlier.

From the previous cut off frequencies, the range of the dimensions  $a$  and  $b$  can be designed such that the operating frequency satisfies the following inequality,

$$f_{c_{LSM_{01}}} < f_{op} < f_{c_{LSM_{21}}} \quad (3.10)$$

For an operating frequency 32 GHz and a medium dielectric constant of 10.2, a possible choice of the dimensions  $a$  and  $b$  that guarantees the satisfaction of (3.10) is 2 mm and 1.9 mm, respectively.

Based on (3.7), it is straightforward to derive the length required for full coupling to be [72]:

$$L_c = \frac{\pi}{\beta_{even} - \beta_{odd}} \quad (3.11)$$

where  $\beta_{even}$  and  $\beta_{odd}$  values are calculated from the solution of (3.4) and appear in Figure 3.1 (c).

Equation (3.4) is solved using different values of  $d$ , and the dependence of  $L_c$  on  $d$  is shown in Figure 3.4 (a).

From this figure, it is concluded, as should be expected, that as  $d$  decreases the full coupling length also decreases. However, for practical implementation,  $d$  is limited by the technology used to realize the gap between the two guides. For a laser micro-machining, this limit is the beam width of the laser used to cut the substrate. A practical value for this beam width is about 50 microns, as suggested by the technical guides of our Poly-Grames Research Center. Thus, the separation between guide  $E$  and guide  $C$  in this example is chosen to be of that value. Using the parameters obtained above, the optimum coupling length for full coupling is 22.5 mm with a spacing between the waveguides of 0.05 mm, as shown in Figure 3.4 (b).

For the metallic vias, their diameters should be carefully selected in a way which guarantees the propagation of the TE<sub>10</sub> mode [74]. A small distance between the periodic vias is also preferred for minimizing the leakage of the TE<sub>10</sub> mode [74]. For the structure simulated through the HFSS package, there are 51 metallic vias over the coupling length with a diameter of 0.2 mm for each via, and a period of 0.4 mm.

In Figure 3.5, the results of our proposed PSC-based OMT is presented using the parameters specified above. A linearly polarized wave with 45° to the  $x$ -axis is illuminated to the PSC-based OMT. At port 2, the vertically oriented mode is received with complete isolation from the horizontally oriented mode as appears in the scattering parameters and in the field distribution at port 2. On the other hand, the horizontally oriented mode is received with complete isolation from the vertically oriented mode as appears in the scattering parameters and in the field distribution at port 3.

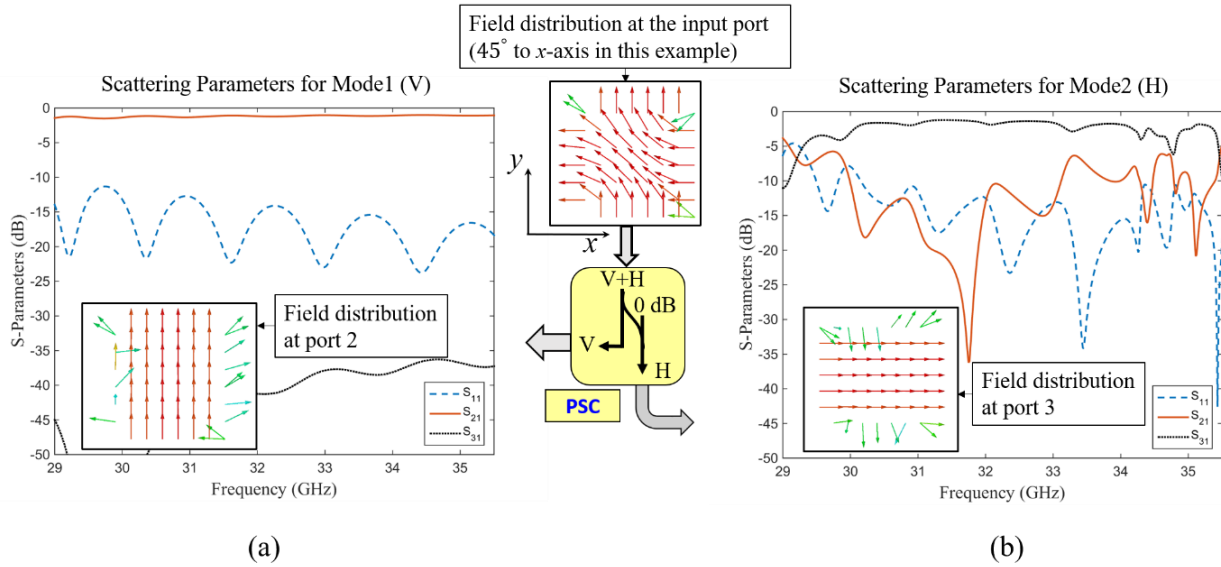


Figure 3.5. The scattering parameters with field distributions at the input and output ports for the PSC-based OMT for the vertically polarized TE<sub>10</sub> mode (Mode1) and the horizontally polarized TE<sub>01</sub> mode (Mode2).

More interestingly, the field distribution over the OMT guide obtained from the HFSS package in Figure 3.3 (c) clearly confirms exactly what we expected through the theoretical explanations in the previous sections. The wave flows in the following manner; the arbitrarily polarized input signal is received in the dual-mode waveguide that supports the vertically and horizontally polarized modes (V+H) which are TE<sub>10</sub> and TE<sub>01</sub> in this example. Then, when this combination propagates through the Hybrid Image-NRD-SIW waveguide, the TE<sub>10</sub> mode remains as is, while the TE<sub>01</sub> is converted to be LSM<sub>01</sub><sup>SIW</sup> mode. The TE<sub>10</sub> mode remains in the Hybrid Image-NRD-SIW guide till it reaches port 2, while the LSM<sub>01</sub><sup>SIW</sup> mode couples to the adjacent Image-NRD waveguide. The coupled mode is converted to be LSM<sub>01</sub> and then, extracted through port 3 as a TE<sub>01</sub> mode.

From the scattering parameters shown in Figure 3.5, it can be noticed that the PSC-based OMT achieved about 15% fractional bandwidth around 32 GHz where the return loss is approximately below 10dB. This is for both of the vertically polarized TE<sub>10</sub> mode in Figure 3.5 (a) with isolation below 35dB and for the horizontally polarized TE<sub>01</sub> mode in Figure 3.5 (b) with isolation around

15dB. The simulated insertion loss is about 1.1dB. This loss is mainly due to dielectric loss of the substrate.

There is an important elucidation with regard to the performance and compactness of the proposed OMT when compared to other OMT designs. As an illustration, the OMT designs based on the concept of [75] may produce a better performance or compactness at some frequency ranges.

This advantage comes at the expense of the impossibility of integration with printed circuit board (PCB) applications because those designs are non-planar air-filled structures. For example, the structure in [29] needs six stacked layers to be realized and also the design in [36] is not a planar structure. On the contrary, the proposed planar dielectric-filled PSC-based OMT produces the required simple geometry to be integrated easily with PCB applications.

Before studying the detailed OMT designs based on the PSC concept starting from Sec. 3.1.4, the PSC is used to validate the model introduced in Sec. 2.2.1. This is related to the anisotropic model of the NRD waveguide and the possibility of substrate isotropization as in Sec. 2.2.1.5.

### 3.1.3 Validation of the Isotropization Concept using PSC

In order to validate the proposed analytical model of the NRD waveguide, a dually-polarized structure should be designed for testing the previously-claimed anisotropy effect in Sec. 2.2.1.5 due to the structure periodicity. Implementing this periodic part of the NRD waveguide as the guiding portion could not visualize clearly that effect. Therefore, we chose to implement the periodic part as the main dielectric of the waveguide.

As presented in the PSC structure shown in Figure 3.6 (a), two types of dielectric substrates are used in this design. The green substrate at the input and output waveguide ports are made of Rogers RT/duroid 6002 which has an isotropic dielectric constant of  $\epsilon_{XY} = \epsilon_Z = 2.94$ . The blue substrate that customs the main common waveguide is made of Rogers RT/duroid 6006 which has an anisotropic dielectric constants of  $\epsilon_{XY} = 8.3$  and  $\epsilon_Z = 6.15$ . Both of the substrates have a thickness of  $b = 2.54$  mm. The blue substrate is perforated in a deliberate way based on the discussion in Sec. 2.2.1.5 where the isotropization technique is introduced.

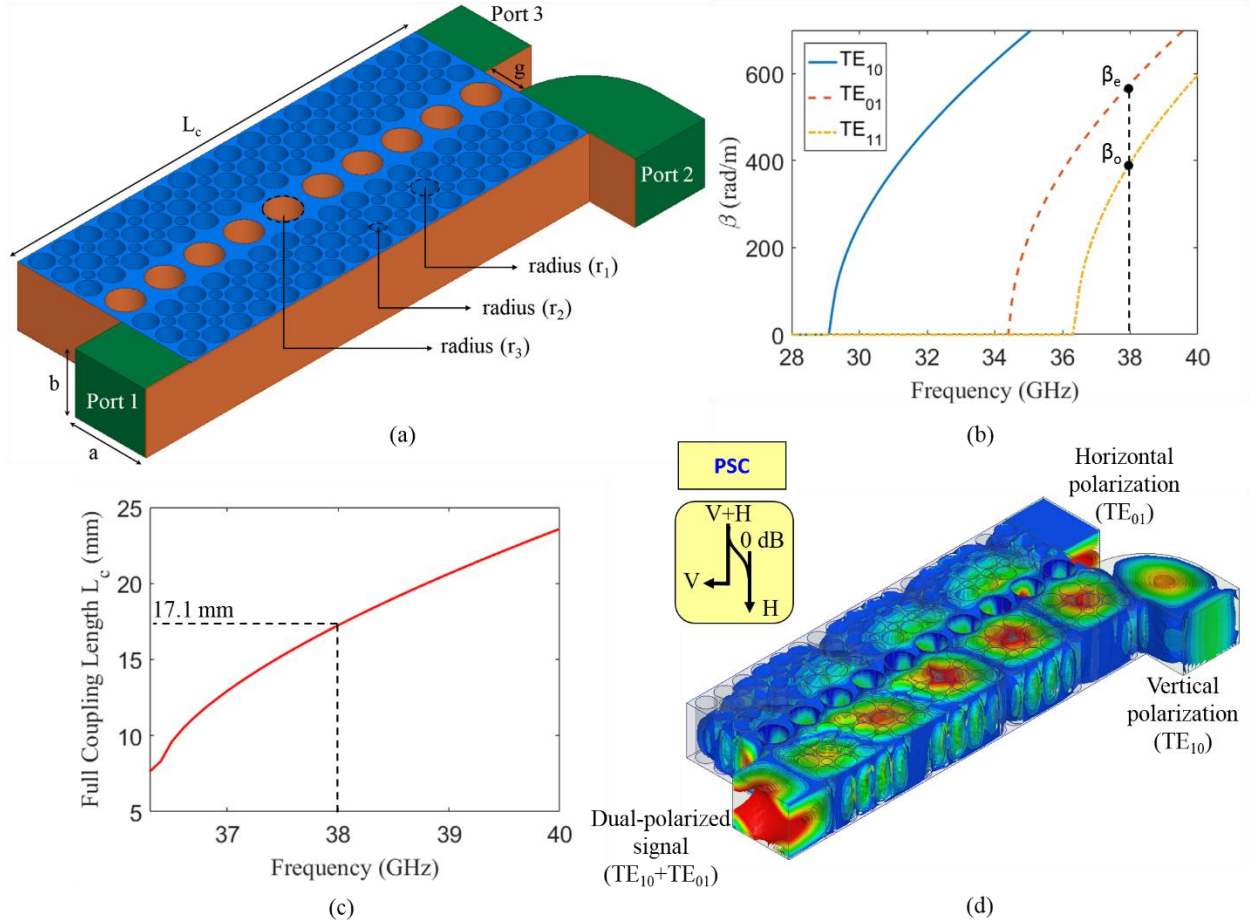


Figure 3.6. (a) Polarization selective coupler (PSC), (b) dispersion curves for the common waveguide, (c) full coupling length versus frequency and (d) field distribution in the PSC at 38 GHz.

The unit cell of Figure 2.5 is used for this isotropization process with  $r_1 = 0.42$  mm,  $r_2 = 0.21$  mm and  $p = 1$  mm. The value of the width  $a$  is chosen to be 3 mm. This selection is to make it sufficient for three periods of perforations in order to guarantee the periodic effect on the operation. The resultant effective permittivity of the blue substrate has the same isotropic value of the green substrate along the frequency range of operation around 38 GHz where,

$$\epsilon_r = \begin{bmatrix} 8.3 & 0 & 0 \\ 0 & 8.3 & 0 \\ 0 & 0 & 6.15 \end{bmatrix} \xrightarrow{\text{perforation}} \epsilon_{eff} = \begin{bmatrix} 2.94 & 0 & 0 \\ 0 & 2.94 & 0 \\ 0 & 0 & 2.94 \end{bmatrix} \quad (3.12)$$

This perforation guarantees that minimum reflections would occur due to the medium change at the input and output waveguides for both of the vertical and horizontal polarizations. The reader is not to be confused with the orange perforations in the structure which corresponds to metallic vias for the purpose of the PSC operation not for the isotropization as explained below. The radius of this metallized vias is chosen based on the fabrication limitation in our Poly-Grames Research Center, where the via diameter should be at least half of the substrate thickness, thus we have  $r_3 = 1.27$  mm, and the width  $g$  is selected to 1.47 mm.

Concerning the operation of the PSC structure, when exciting port 1 with a dual-polarized signal, the vertically polarized mode which is the  $\text{TE}_{10}$  is guided by the metallic vias and transmitted totally to port 2 while port 3 is isolated for that mode. On the contrary, the horizontally polarized mode which is the  $\text{TE}_{01}$  is not guided by those metallic vias. This is because that mode is normal to such a periodic conducting wall. Thus the metallic vias are totally transparent for any horizontally polarized mode. This interesting feature enables the  $\text{TE}_{01}$  mode to couple to the other waveguide and totally received at port 3 while port 2 is isolated for that mode.

The mentioned forward coupling occurs only if the common waveguide has a specific length  $L_c$  that guarantees full forward coupling. In order to achieve full coupling, only the even and odd order modes should appear in the required frequency range of operation. In this case, the even order mode is the  $\text{TE}_{01}$  while the odd order mode is the  $\text{TE}_{11}$ . The required full forward coupling length is calculated based on a relationship as in [72],

$$L_c = \frac{\pi}{\beta_e(\text{TE}_{01}) - \beta_o(\text{TE}_{11})} \quad (3.13)$$

The structure is mainly designed at 38 GHz where the dispersion relation of the common waveguide that has a length of  $L_c$  and width of  $2a + g$  is shown in Figure 3.6 (b). Based on the obtained propagation constants, the resultant coupling length at 38 GHz is 17.1mm as presented in Figure 3.6 (c).

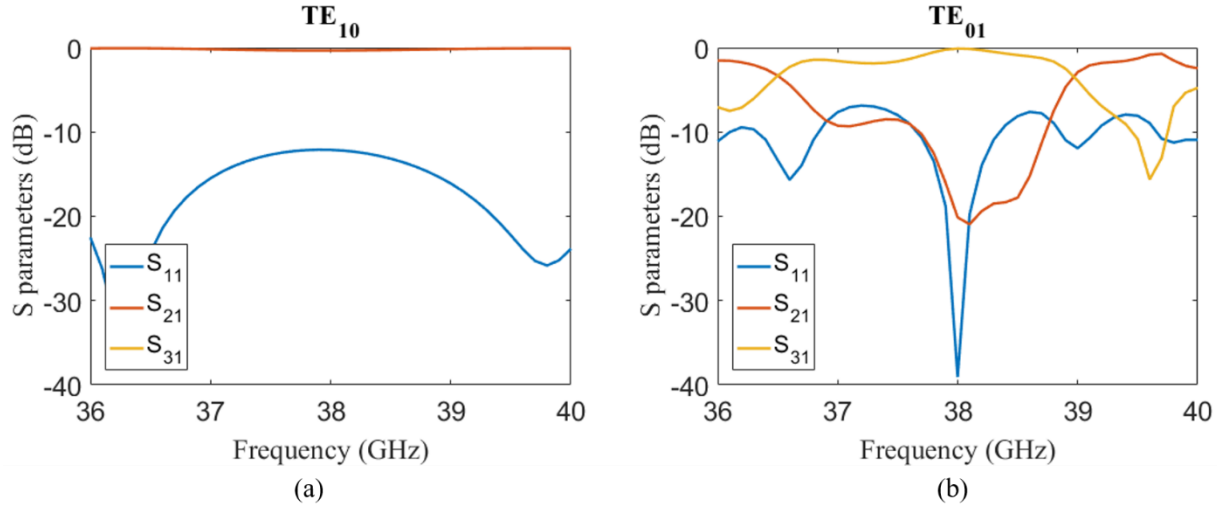


Figure 3.7. Magnitude of scattering parameters for (a) TE<sub>10</sub> mode and (b) TE<sub>01</sub> mode.

The overall PSC structure with the calculated dimensions is simulated on HFSS where the field distribution through the PSC structure is shown in Figure 3.6 (d). It can be clearly observed that the vertically polarized TE<sub>10</sub> mode is totally received at port 2 while port 3 is isolated. On the other hand, the horizontally polarized TE<sub>01</sub> mode is received at port 3 while port 2 is isolated. The simulated scattering parameters of the structure in Figure 3.6 (a) are shown in Figure 3.7. In Figure 3.7 (a), the scattering parameters of the TE<sub>10</sub> mode show a full transmission for such mode with a return loss below 12dB and isolation (S<sub>31</sub>) below 50dB. The same performance appears in Figure 3.7 (b) for the TE<sub>01</sub> mode where a full coupling occurs at 38 GHz with return loss about 40dB and isolation about 20dB. These results confirm that the perforated blue substrate operates exactly as the bare green substrate after the isotropization technique that is applied based on the analytical model presented in details in Sec. 2.2.1.

### 3.1.4 Orthomode Transducer design based on Polarization Selective Coupler

In this work, the concept of the proposed PSC facilitates the OMT design to be in a systematic procedure. In this section, the design procedure of the planar OMT device is explained. The OMT structure dimensions are deduced according to the required operating frequency and medium parameters. The general case of a PSC-based OMT is studied in the first subsection where some

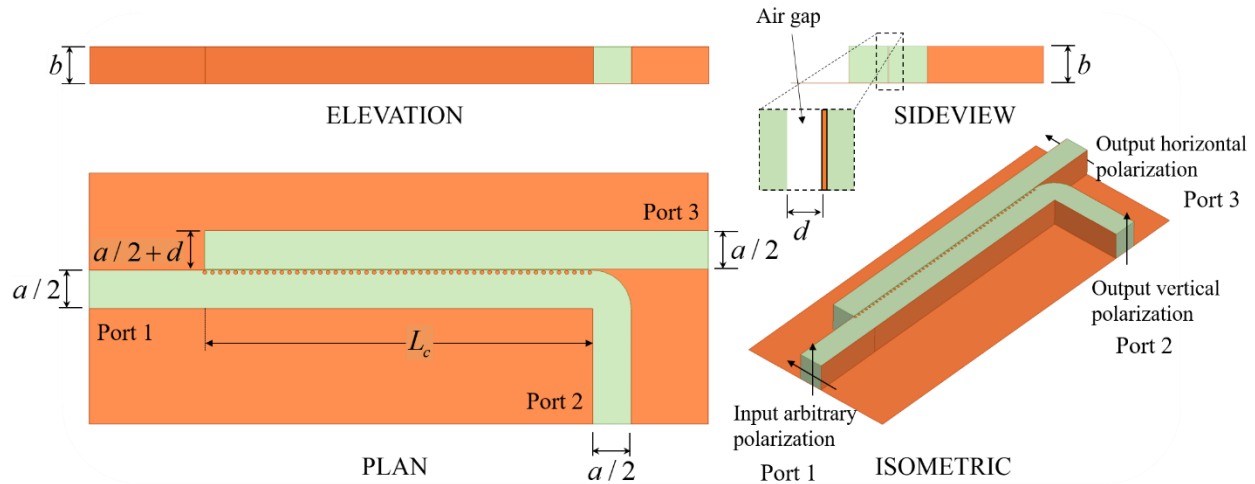


Figure 3.8. Different views for the general form of a dielectric-filled PSC-based OMT shown in elevation, side view, plan, and isometric cuts.

limitations prevent an accurate physical realization of this structure. In the second and third subsections, these limitations are overcome by using dielectric-filled and air-filled fused couplers, respectively. The air-filled structure is integrated with a horn antenna as a validation for the simultaneous separation or combination of the two orthogonal polarizations.

#### 3.1.4.1 OMT design based on isotropic dielectric material filling with air-gap

In this subsection, an isotropic dielectric PSC-based OMT with an air gap is presented. Different views of the complete physical structure are presented in Figure 3.8. In this case, matching sections to standard waveguides should be added for the purpose of measurements over the frequency range of interest. The effective medium as described is considered to be air. Therefore, an air gap should appear between both waveguides as shown in the side view of Figure 3.8. The OMT structure is supposed to be excited by a dually-polarized horn antenna. In practice, the antenna may receive an arbitrarily polarized wave.

It will be the fundamental function of the OMT to decompose the received wave into vertical and horizontal polarizations. Therefore, it is a must to design one input and two independent output sections specifically suitable for each corresponding polarization. Regarding the input section, it is required to support the  $TE_{10}$  and  $LSM_{01}$  modes in the same frequency range. This restricts the cross

section of the input guide to be almost a square. For the output sections, it is required to support single mode operation for each polarization over its corresponding output port.

Since the band allocated for the 5G cellular network includes the starting edge of the mmW band in 28-38 GHz, we choose this band as a proof of concept to design this OMT at the center frequency of 32 GHz. For the vertically and horizontally oriented output waveguides, two matching sections to WR28 waveguides have been optimized for integration with the Ka-band components. The dimensions are calculated using the procedure explained in details below.

The same design procedure presented in the previous section can be followed for getting the required coupling length based on (3.11) where the same previous substrate parameters and dimensions are used here. The gap width between both waveguides, denoted by  $d$ , is selected to have the lowest possible value feasible in the fabrication process in order to guarantee the best coupling between the guides before the occurrence of complete exponential decay of the LSM<sub>01</sub> mode in the air gap. This value should be the same as that of the laser beam width used for the substrate micromachining which is 0.05 mm.

The final structure is implemented on the HFSS simulation from which scattering parameters and field distributions are obtained in Figure 3.5 for the vertically and horizontally polarized modes. It can be clearly observed that the vertically polarized TE<sub>10</sub> mode is received at port 2 with complete isolation from the horizontally polarized LSM<sub>01</sub> mode. On the other hand, the horizontally polarized LSM<sub>01</sub> mode is received at port 3 with acceptable isolation from the vertically polarized TE<sub>10</sub> mode. This attractive feature reflects what is expected through the previous discussions. Nevertheless, some problems will appear if this structure is implemented experimentally and would affect the results, so this should be taken into consideration.

The first problem appears because of the laser beam used in our Poly-Grames Research Center for cutting the substrate in order to realize the air gap. Since the thickness of the used substrate is relatively large, 1.9 mm, it is really difficult to have a homogeneous air gap over this thickness which results in a rough tapered air gap. Therefore, the two guides perhaps touch each other at some points which causes some reflections, and even standing waves may appear as well.

The other and main problem is related to realizing the metallic vias. According to the fabrication limitations in many labs, filling the vias with conductor restricts the diameter of the via to be at least a half of substrate thickness. This restriction contradicts with our last mentioned restriction

for the waveguide cross section to be almost square. In other words, half of the main waveguide cross section should be used just for realizing the metallic vias. This affects dramatically the  $TE_{10}$  mode where high reflections take place due to a huge periodic conducting wall.

For these reasons, the spacing  $d$  in Figure 3.8 is chosen to be simply 0. Therefore, the image-NRD and image-NRD-SIW guides touch each other, then the resulting coupler is converted from a dielectric slab coupler to a fused coupler instead. The detailed operation, design steps and physical implementation of this structure are presented in the next section.

The last issue, which should not be considered as a problem, if carefully taken into consideration is the substrate anisotropy. For the substrates with relatively large dielectric constants, such as the one we use, there is no escape from the anisotropy effect [64], especially for dually-polarized structures. This is because there are two orthogonal modes propagating through the substrate which means each mode experiences a different dielectric constant which should be taken into account. Considering this anisotropy extremely complicates the analysis if the air gap exists which is the reason why we did not consider it in this subsection.

Moreover, the dielectric substrates are commonly used for the vertically polarized dominant  $TE_{10}$  mode, so the substrate dielectric constant is usually known in that direction, while in the perpendicular direction, the exact values of the substrate parameters are not specified precisely. For example, regarding the Roger RT/Duroid 6010 substrate used in this work, Rogers reported that the dielectric constant in the horizontal direction for this substrate ranges between 13 and 14 which cannot lead to accurate design calculations. In addition, frequency dispersion in connection with the dielectric substrate may come into play at mmW frequencies, which may yield a different value of dielectric permittivity compared to the commercial datasheet. This requires adding some modification or tuning to the design in order to facilitate the consideration of such an anisotropy effect.

#### **3.1.4.2 OMT design based on gapless anisotropic dielectric material filling**

For the discussion mentioned in the previous subsection, if the air gap disappears resulting in a homogeneous dielectric substrate, the coupler converges to be a fused coupler. The proposed fused coupler acts as a Riblet junction [76] for the polarization tangential to the slot, while the same coupler acts as a Rosenberg junction [77] for the polarization perpendicular to the common wall.

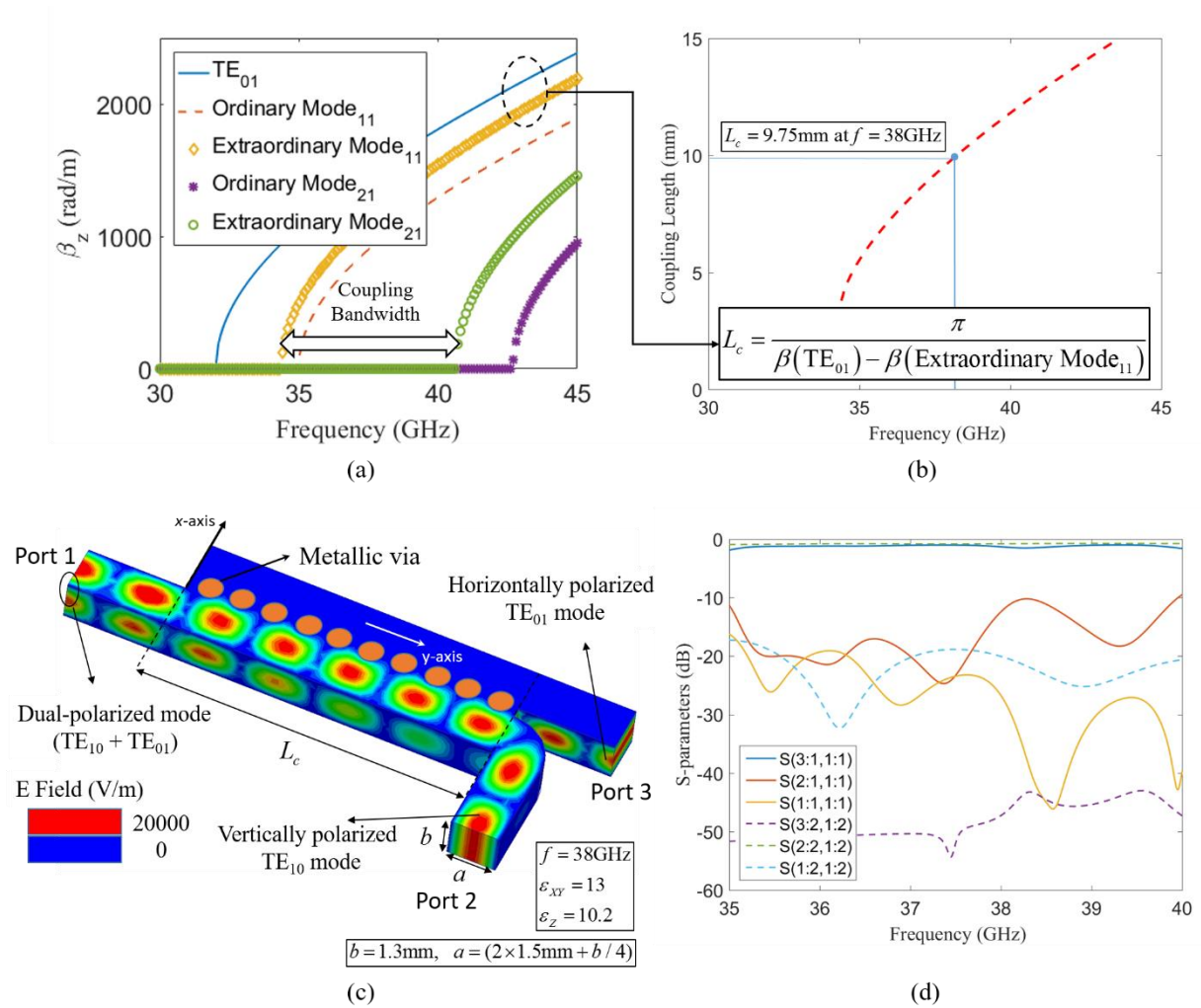


Figure 3.9. PSC-based OMT filled with an anisotropic dielectric material (Roger RT/Duroid 6010): (a) dispersion curves, (b) full coupling length versus frequency, (c) field distribution and (d) simulated S parameters.

Adding the periodic PEC wall at the center of the coupler, preserves the same explained coupling mechanism for the  $TE_{01}$  mode while prevents coupling of the  $TE_{10}$  mode. Based on that, the OMT functionality is achieved. Thus, this modified version of the proposed coupler, with the periodic PEC wall and the square cross-section of input/output waveguides, can be called as *Polarization Selective Top Slot Coupler*, since the slot is on top of the tip of electric field vector of the coupled  $TE_{01}$  mode.

In this case, the above-mentioned problems in the design with the air gap can be handled because the PSC unit is simplified to be a single dielectric substrate enclosed in a rectangular waveguide plated with metallic vias longitudinally in its middle as in Figure 3.9 (c).

Since the PSC-based OMT handles two orthogonal signals, the substrate anisotropy [64] should be taken into consideration. In this case, the input waveguide cross-section is not restricted to be square due to different values of the relative permittivity in the cross-section and the longitudinal directions  $\varepsilon_{XY}$  and  $\varepsilon_Z$ , respectively. The selected operating frequency  $f_{op}$  in this design is 38 GHz and the cross-sectional dimensions can be obtained from the following equations,

$$a/2 = 1.2 \frac{c}{2\sqrt{\varepsilon_Z} f_{op}} \quad , \quad b = 1.2 \frac{c}{2\sqrt{\varepsilon_{XY}} f_{op}} \quad (3.14)$$

The metallic vias can take now an appropriate diameter suitable for the conductor filling process which was not possible in the general case due to the existence of the air gap. Now, the whole PSC width can be considered as  $a + g$  where  $g$  is effectively a half of vias diameter. This is because when adding the metallic vias with their relatively large diameters according to the plating restriction mentioned earlier, reflections could affect the transmission of the guided TE<sub>10</sub> mode. In order to overcome this problem, the width of the common waveguide with length  $L_c$  should be enlarged with at least a half of the via diameter which reasonably results in neglecting the caused reflections. The rectangular waveguide filled with an anisotropic material is solved in [78] where the dispersion characteristics can be obtained by applying the following relations,

$$\det \left\{ |\mathbf{k}|^2 \mathbf{I} - \mathbf{k}\mathbf{k} - k_o^2 \bar{\varepsilon}_r \right\} = 0, \quad (3.15)$$

$$\mathbf{k} = \left( \frac{m\pi}{a+g} \right) \hat{a}_x + \beta_y \hat{a}_y + \left( \frac{n\pi}{b} \right) \hat{a}_z \quad (3.16)$$

In our solution using the commercial substrate Rogers RT/Duroid 6010, the permittivity in the  $z$ -direction  $\varepsilon_Z$  is different from that of the  $xy$ -plane  $\varepsilon_{XY}$  [79]. Therefore, the optic axis in our design is the  $y$ -axis which means that the solution inside the waveguide cannot be written as TE <sup>$y$</sup>  or TM <sup>$y$</sup>  as in [80]. Thus, the coinciding TE<sub>11</sub> and TM<sub>11</sub> (which has a cutoff of 36 GHz in this example) dispersion curves of a conventional isotropically filled rectangular waveguide will split into two separate modes as shown in Figure 3.9 (a). We call them ordinary mode and extraordinary mode with the order “11”. The necessary modes for coupling are the TE<sub>01</sub> mode and the extraordinary

component of the “11” mode because its main component is horizontally polarized. The next mode which has a major horizontal polarization is the extraordinary mode with order “21”. Thus, the bandwidth of this structure is between 35 GHz and 41 GHz.

Based on this discussion, the coupling length relation in (3.11) can be rewritten in the following form according to the modes necessary for coupling.

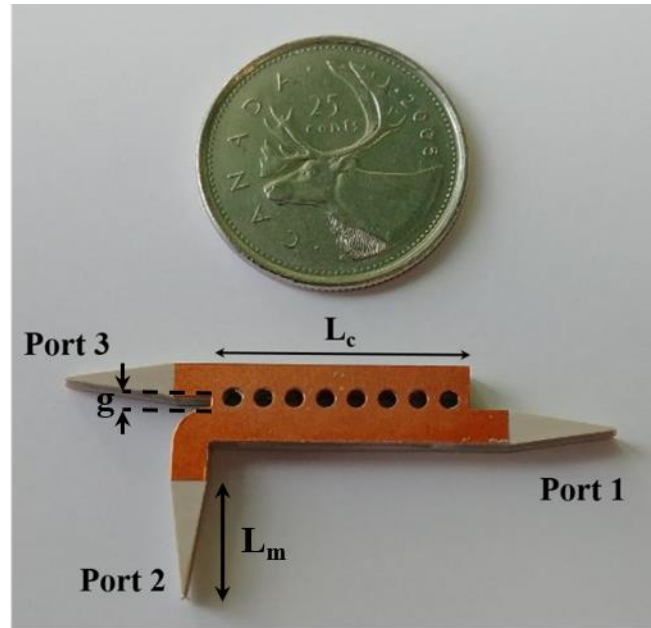
$$L_c = \frac{\pi}{\beta_y(\text{TE}_{01}) - \beta_y(\text{Extraordinary Mode}_{11})} \quad (3.17)$$

The variation of the coupling length over the operating bandwidth is shown in Figure 3.9 (b) where the optimal coupling length at 38 GHz is 9.75 mm. Then, the field distribution and the scattering parameters of the designed structure are shown in Figure 3.9 (c) and (d), respectively. A complete separation between the vertically polarized  $\text{TE}_{10}$  mode and the horizontally polarized  $\text{TE}_{01}$  mode is achieved with isolation between the two output ports.

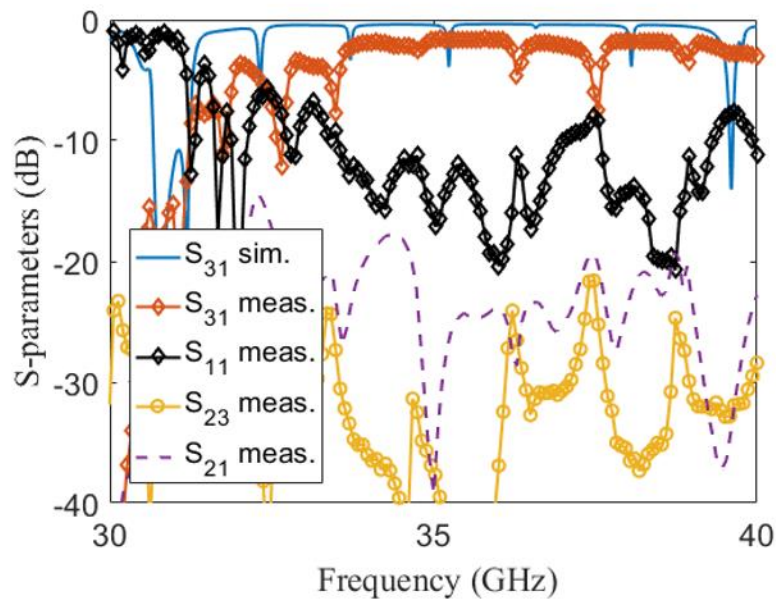
Figure 3.9 (d) shows the simulated S parameters of the OMT where the labels in the graph indicate S (input port number: mode number, output port number: mode number). The port numbering is presented in Figure 3.9 (c), and mode 1 represents the  $\text{TE}_{01}$  mode while mode 2 represents the  $\text{TE}_{10}$  mode. It can be observed from the results that the input dually-polarized signal is decomposed into two separated orthogonal signals where the vertically polarized  $\text{TE}_{10}$  mode is received at port 2 while the horizontally polarized  $\text{TE}_{01}$  is received at port 3.

In order to measure, not to realize, this structure, matching sections to the standard air-filled WR28 waveguide should be designed. Since we make use of a substrate with a high dielectric constant to show the anisotropy effect, the required matching sections are hard to realize. Therefore, we chose to use a dielectric substrate with a lower dielectric constant such as Rogers RT/Duroid 6002 where  $\epsilon_{xy}$  and  $\epsilon_z$  are approximately equal 2.94. This is to validate the concept of the gapless dielectric-filled PSC-based OMT. Although the dielectric used in this implementation is nearly isotropic, it serves to validate the essence of the idea.

The overall structure is prototyped as shown in Figure 3.10 (a) with the parameters specified in the caption where they can be obtained according to the previously explained procedure. The circular vias presented in that figure are plated with a good conducting material through a chemical deposition process. The implemented structure is measured by the vector network analyzer (VNA)



(a)



(b)

Figure 3.10. PSC-based OMT filled with isotropic dielectric material (Roger 6002) (a) prototype and (b) measured versus simulated S parameters of the coupled mode  $TE_{01}$ . Coupling length  $L_c = 21$  mm, optimized matching length  $L_m=9.2$  mm and the waveguide cross-section.

where the S parameters are obtained. For the measuring mechanism of this structure, port 1 is excited firstly with a vertically polarized signal, and then, the output is measured at port 2 while the isolation is measured at port 3. Similarly, port 1 is excited with a horizontally polarized signal and the output is measured at port 3 while the isolation is measured at port 2. The results of the latter case are shown in Figure 3.10 (b) and compared with the simulation results. It is clear from this comparison that there is an acceptable agreement between the simulated and measured results.

This prototype has achieved bandwidth of about 6 GHz where the design frequency is 38 GHz. This bandwidth is measured in the Ka-band where 40 GHz is the maximum frequency. Therefore, the real bandwidth may be wider than the mentioned bandwidth limited by the appearance of higher-order mode (as in Figure 3.9 (a)). However, a slightly high insertion loss,  $S_{31}$ , around 2 dB is observed due to the dielectric loss of the substrate. There is a discrepancy about 1 dB between the simulation and measurement results. This is because the loss in the simulation is based on a very small loss tangent of 0.0012 for the Rogers 6002 substrate. This value is reported in the Rogers datasheet with working conditions up to 10 GHz. The material, however, is used in our design around 38 GHz. We believe this is the cause of that observed discrepancy.

Furthermore, the isolation is represented by the value of  $S_{23}$ . The proposed OMT shows isolation which is better than 20 dB over the whole band. In addition,  $S_{21}$  for the horizontally polarized mode is approximately below -20 dB over the operating band as well. The low values of  $S_{23}$  and  $S_{21}$  guarantee avoiding the reception of unwanted polarization. The structure feeding junctions are the standard WR28 waveguide to coaxial transitions. The WR28 cannot support two modes at a time and the energy contributing to  $S_{21}$  cannot reach the network analyzer. In order to analyze the vertical polarization, different matching sections suitable for this polarization should be designed. The horizontally polarized mode is the mode that is selected to be tested in this subsection because it depends on coupling which mainly governs the OMT design while the vertically polarized mode is received through a normal waveguide without coupling and it has excellent S parameters in the simulation.

According to the previous discussion, for testing both polarizations in a simultaneous manner, a square horn antenna is designed for visualizing the simultaneous performances for both polarizations as explained in the following subsection.

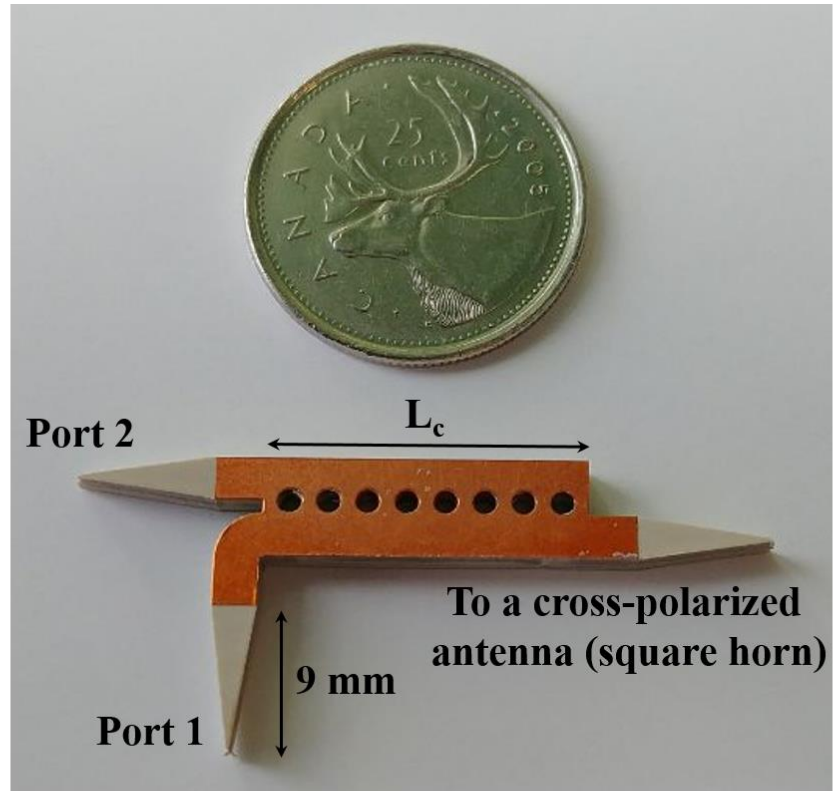
### 3.1.4.3 OMT filled with isotropic material and integrated with horn antenna

A horn antenna is integrated with the PSC-based OMT at the input port where the structure response is measured at the output ports at 37 GHz. The spacing  $d$  between the waveguides in this example also tends to 0. The used dielectric substrate for the prototype is Rogers RT/Duroid 6002 which has an isotropic dielectric constant of 2.94. The thickness of the substrate is  $b = 3$  mm and the width  $a = 3$  mm. Following the previously explained procedure, the necessary length for full coupling of the  $TE_{01}$  mode is  $L_c = 21$  mm.

The final substrate structure according to the mentioned dimensions is shown in Figure 3.11 (a). Two symmetric conducting parts of a metallic enclosure are designed to hold the dielectric substrate as in Figure 3.11 (b). After inserting the substrate inside the metallic enclosure, the final structure becomes ready for measurements in the antenna anechoic room. The final antenna structure in Figure 3.11 (c) has overall dimensions of  $29 \times 29 \times 56$  mm<sup>3</sup>. It should be kept in mind that the metallic box that appears in Figure 3.11 (b) and (c) is used only for measurement in order to match the proposed OMT to the standard WR28 waveguide. While the proposed PSC-based OMT is only the planar dielectric substrate in Figure 3.11 (a).

In order to show the structure bandwidth, the S parameters are measured using the vector network analyzer at port 1 and port 2.  $S_{11}$  is the reflection from port 1,  $S_{22}$  is the reflection from port 2 and  $S_{21}$  is the isolation between port 1 and port 2. Figure 3.12 (a) shows the simulated S parameters while Figure 3.12 (b) shows the measured S parameters. Over the band between 33 GHz and 40 GHz, it can be observed that the reflection at port 1 and port 2 is below 10dB and the isolation between them is below 25dB.

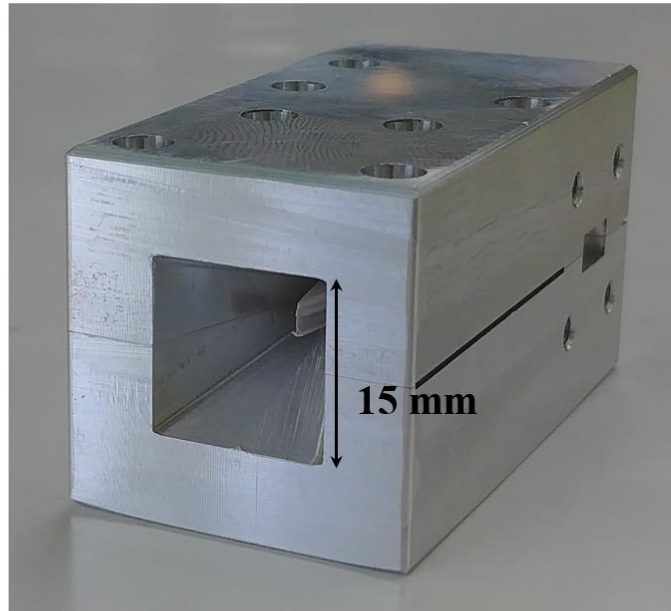
As a validation, the gain is measured at 37 GHz which is approximately the center frequency over a band between 33 and 40 GHz. Then, the measured gain is compared with simulation. The antenna under test is measured in the reception case. The received signal is measured at port 1 while port 2 is terminated with a matched load. Firstly, the transmitting antenna sends a vertically polarized signal. The gains in the azimuth and elevation cuts are shown by the solid curves in Figure 3.13 (a) and Figure 3.13 (c), respectively. Then, the standard horn sends a horizontally polarized signal. The gain, in this case, is shown by the dashed curves in Figure 3.13 (a) and Figure 3.13 (c).



(a)



(b)



(c)

Figure 3.11. PSC-based OMT prototype: (a) the dielectric substrate, (b) the metallic enclosure and (c) the overall structure.

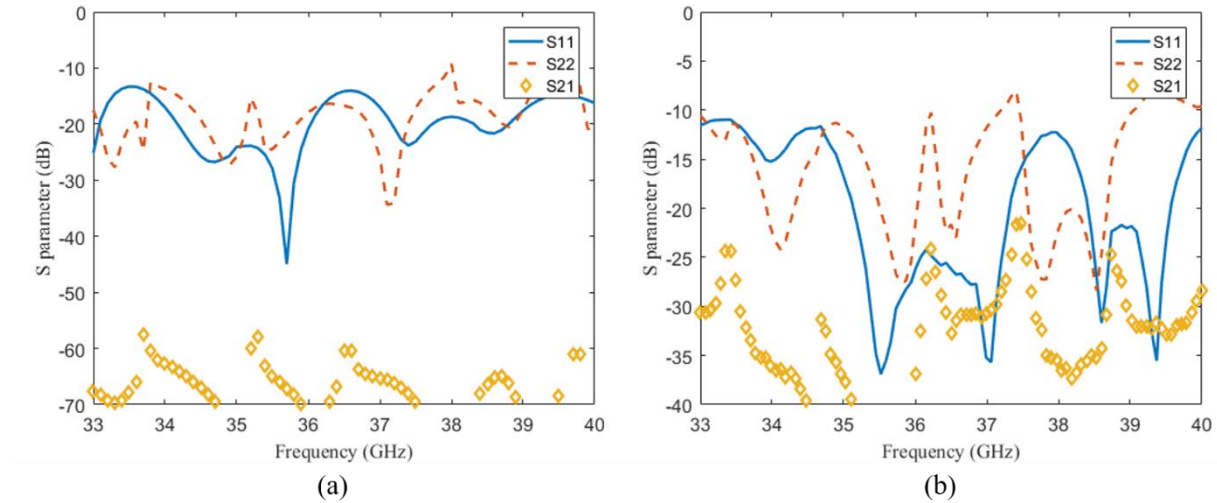


Figure 3.12. Scattering parameters for the PSC-based OMT integrated with a square horn antenna (a) simulation and (b) measurements.

In those cases, the measured values for the co-polarized and cross-polarized gains at  $\varphi = 90^\circ$  are 16.2dB and -2dB, respectively, whereas they are, respectively, 13.3dB and -4.7dB at  $\theta = 90^\circ$ . The whole procedure is then repeated for the case where port 1 is terminated, and the signal is measured at port 2. The measurement results for the repeated procedure are shown in Figure 3.13 (b) and Figure 3.13 (d) for the azimuth and elevation cuts, respectively. The measured values for the co-polarized and cross-polarized gains at  $\varphi = 90^\circ$  are 17.6dB and -2.3dB, respectively, whereas they are, respectively, 13.3dB and -4.3dB at  $\theta = 90^\circ$ . The measurement technique explained above is just based on the standard test setup in the antenna anechoic chamber, but in reality, the proposed structure can receive any orientation of the signal and decompose it into its orthogonal components. This can be simply confirmed if the structure is simulated on the HFSS. The way of setting the input signal polarization is a post-processing step which means it has not any effect on the structure operation. In the mentioned graphs, an excellent agreement appears when comparing the simulation with the measurement results of the specified cases.

Integrating the dielectric-filled PSC-based OMT with a horn antenna, all enclosed in a metallic enclosure leads to the possibility of an air-filled PSC. Consequently, an air-filled PSC-based OMT can be implemented as introduced in the following subsection.

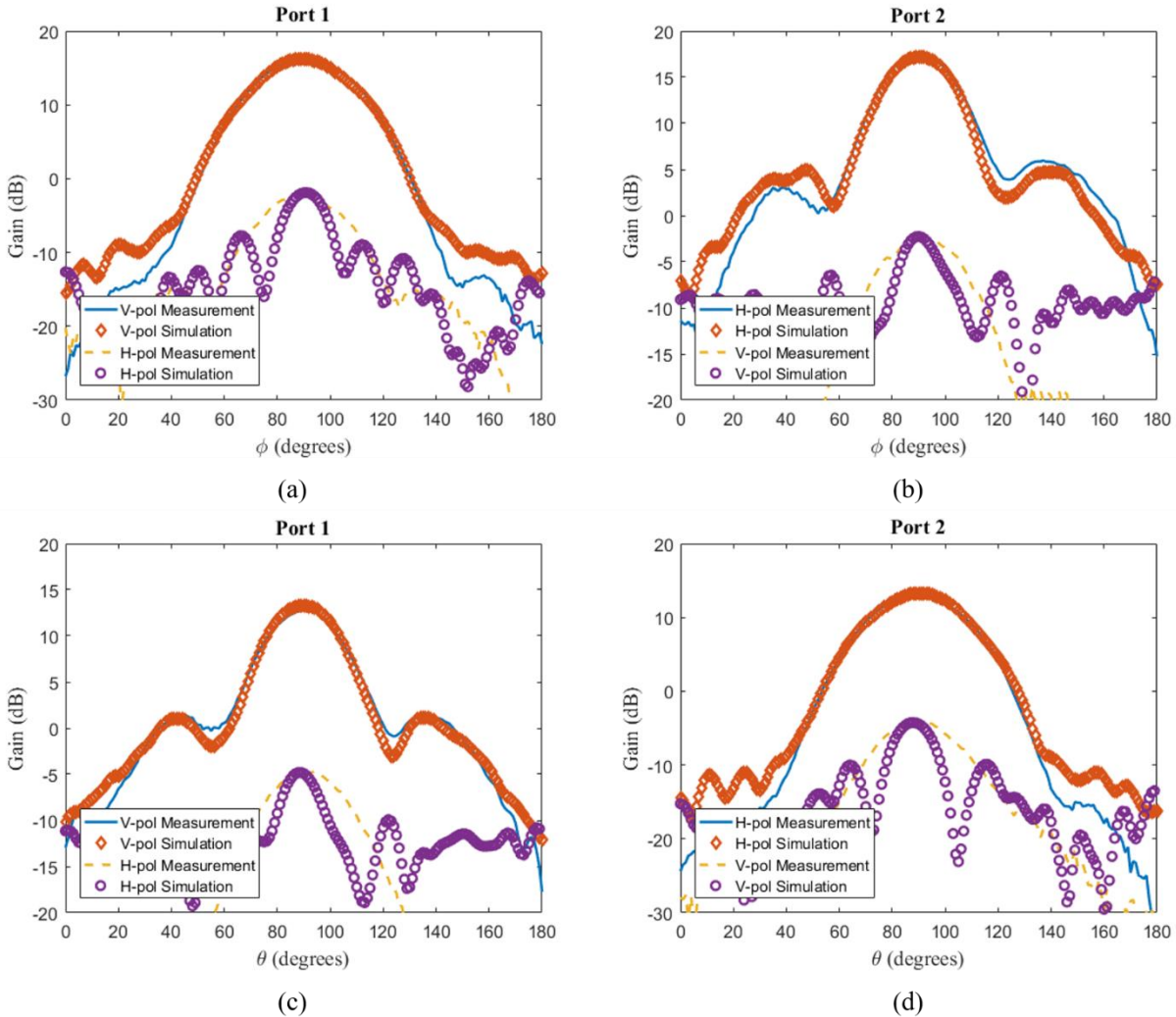
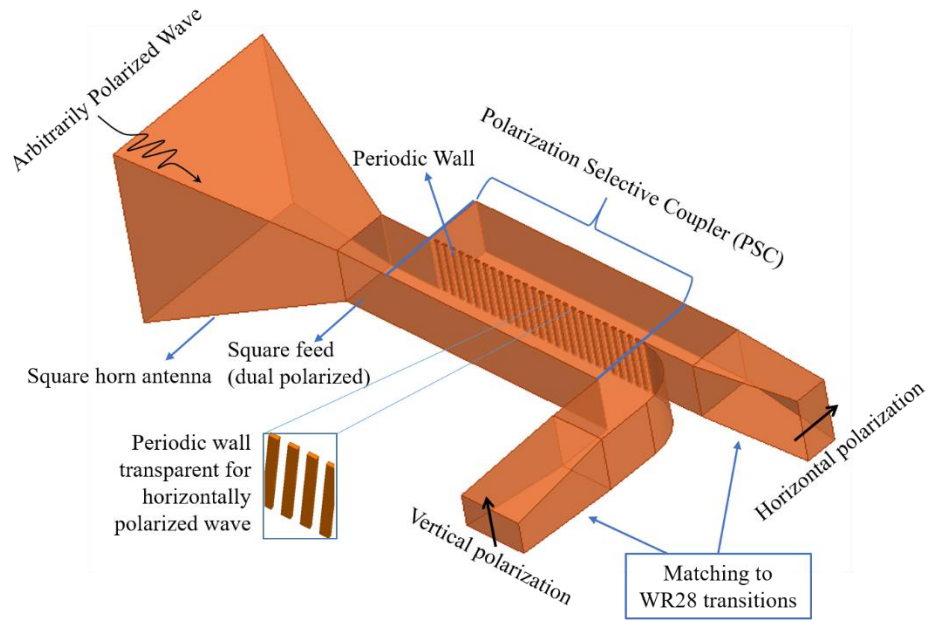


Figure 3.13. Simulated and measured antenna gain at 37 GHz for different excitations: (a) port1: azimuth cut, (b) port 2: azimuth cut, (c) port 1: elevation cut and (d) port 2: elevation cut.

### 3.1.4.4 Air-filled OMT Design

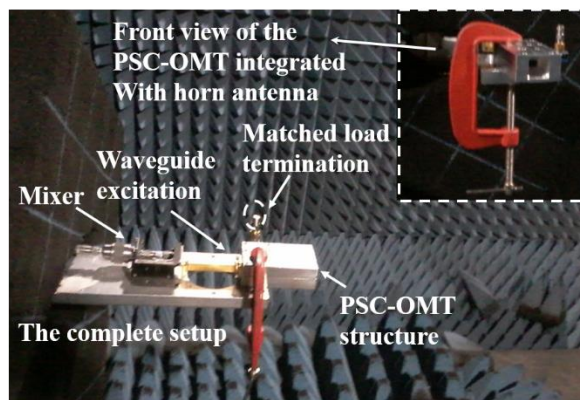
In this example, there is no filling material inside the conducting enclosure. Thus, the dielectric coupler converges to an air-filled top slot coupler. This fact significantly simplifies the structure analysis and the design steps as well. The overall structure is integrated with a square horn antenna as shown in Figure 3.14 (a). Mathematically, the input admittance obtained in (3.3) reduces to the following expression when the air gap disappears,



(a)



(b)



(c)

Figure 3.14. Air-filled PSC-based OMT integrated with horn antenna: (a) isotropic view of the design (b) implemented prototype and (c) measurement setup in antenna anechoic chamber.

$$Y_{in} = \lim_{d \rightarrow 0} \left\{ Y_{eff} \frac{Y_{eff} + Y_d \cot(ua/2) \coth(vd/2)}{Y_{eff} \coth(vd/2) + Y_d \cot(ua/2)} \right\} = Y_d \cot(ua/2) \quad (3.18)$$

More interestingly, closed-form relations can be obtained for the even and odd components of the propagation constant  $\beta_e$  and  $\beta_o$ , respectively as in the following equations,

$$\beta_e(\text{TE}_{01}) = \sqrt{k_o^2 - \left(\frac{\pi}{b}\right)^2} \quad (3.19)$$

$$\beta_o(\text{TE}_{11}) = \sqrt{k_o^2 - \left(\frac{\pi}{b}\right)^2 - \left(\frac{\pi}{a+g}\right)^2} \quad (3.20)$$

So the full coupling length can be easily written in a closed- form as follows,

$$L_c = \frac{\pi}{\sqrt{k_o^2 - \left(\frac{\pi}{b}\right)^2} - \sqrt{k_o^2 - \left(\frac{\pi}{b}\right)^2 - \left(\frac{\pi}{a+g}\right)^2}} \quad (3.21)$$

The last expression in (3.21), obtained from the equivalent circuit model, provides an important design engine for any air-filled (or isotropic dielectric-filled such as the prototype in the previous subsection) PSC-based OMT by knowing the proper dimensions needed for the required operating frequency range. The coupling length closed-form in (3.21) is valid only whenever the modes propagating through the waveguide are only the necessary modes for achieving coupling which are TE<sub>01</sub> mode and TE<sub>11</sub> mode in our case. The appearance of the TE<sub>21</sub> mode will prevent the occurrence of the expected full coupling. This limits the bandwidth of the structure to be between the TE<sub>11</sub> mode and the TE<sub>21</sub> mode as in the following relation,

$$\text{BW} = \frac{c}{2} \left( \sqrt{\left(\frac{2}{a+g}\right)^2 + \left(\frac{1}{b}\right)^2} - \sqrt{\left(\frac{1}{a+g}\right)^2 + \left(\frac{1}{b}\right)^2} \right) \quad (3.22)$$

The design parameters based on the specified criteria are  $a/2 = b = 6$  mm and  $L_c = 27$  mm at  $f_{op} = 30$  GHz. The resulting BW based on (3.22) is 6 GHz. For the sake of completeness, a 20 mm square horn antenna is integrated to the OMT with the length of 20 mm. The final structure is implemented through the HFSS simulation and physically fabricated using CNC machining. The physical structure is easy to fabricate because it is only about the implementation of the conducting enclosure. An important question raised is, how the metallic vias can be implemented although there is no dielectric substrate. This is simply treated by embedding metallic cylinders as

protrusions from the metallic enclosure itself as in [81] where each cylinder is divided into two equal parts, each is  $b/2$  in length, where one part is connected to the upper half of the enclosure, while the other part is connected to its lower half as shown in Figure 3.14 (b). The structure is measured in the antenna anechoic chamber as a receiving antenna as in the setup shown in Figure 3.14 (c).

In the reception case simulation shown in Figure 3.15 (a), an incoming circularly polarized wave at 30 GHz is incident from angles  $\varphi_i = \theta_i = 90^\circ$  is assumed to excite the structure. From the field distribution in Figure 3.15 (a), a pure vertically polarized wave is received at port 1, while a pure horizontally polarized wave is received at port 2. This means that the incoming circularly polarized wave is decomposed into its linear orthogonal components where the vertical component is received at port 1 while the horizontal component is completely coupled and received at port 2. The same concept occurs with any incoming polarization (linear, circular or elliptical).

For a transmission mode operation of the PSC-based OMT, the measured and simulated S parameters over a band between 28 GHz and 33 GHz are shown in Figure 3.15 (b). In this figure, the absolute of  $S_{11}$  represents the return loss of the vertical component at port 1, the absolute of  $S_{22}$  represents the return loss of the horizontal component at port 2 and the absolute of  $S_{21}$  represents the isolation between the orthogonal components at port 1 and port 2. It can be observed that the return loss for both polarizations is below 12 dB over a bandwidth of 4 GHz with isolation below 20 dB. The spikes which appear on the  $S_{11}$  and  $S_{22}$  curves are caused by the matching sections to the WR28 waveguide for measurements, which is not related to the OMT functionality. This can be verified from the S parameters in Figure 3.9 (d) before adding the matching sections.

To validate the full functionality of the prototype, the antenna radiation pattern is measured in an anechoic chamber for the two polarizations at 30 GHz. The measured gain patterns are shown in Figure 3.16 . The prototype is setup as the receiving antenna where a standard gain horn antenna is used as the transmitting antenna. First, the transmitting antenna sends a vertically polarized wave, and the received signal is measured at port 1 while port 2 is terminated with a matched load. The measured gain, in this case, is plotted as the V-pol curve marked with ‘ $\diamond$ ’ versus azimuth and elevation angles in Figure 3.16 (a) and (c), respectively. Then, the transmitting antenna is used to send a horizontally polarized wave, and the measured signal at port1 is plotted as the H-Pol curve marked with ‘O’ in Figure 3.16 (a) and (c) for the azimuth and elevation cuts, respectively.

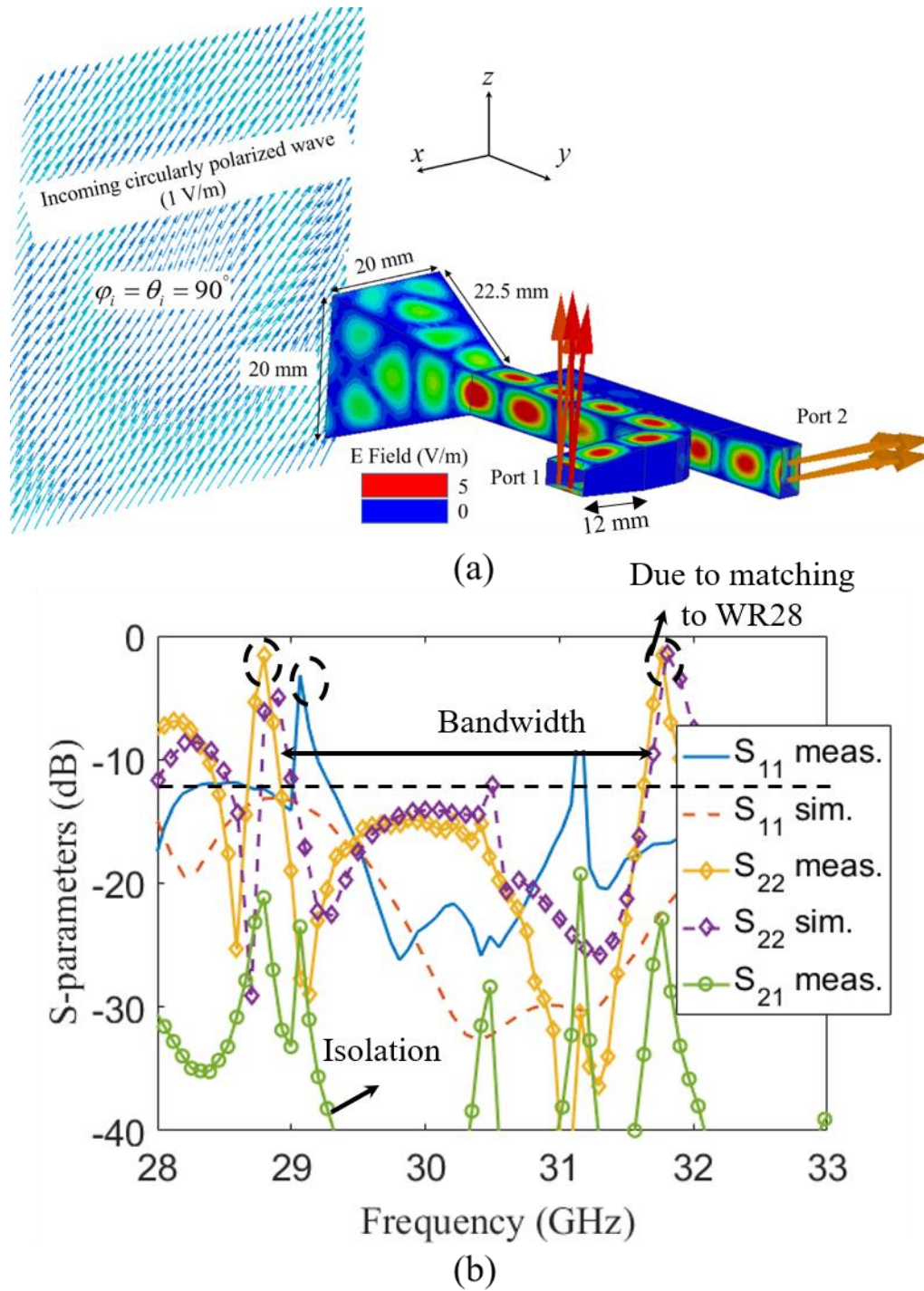


Figure 3.15. Performance analysis of the structure shown in Figure 3.14: (a) simulated field distribution in the receiving case. The polarization state of the incoming wave is arbitrarily chosen to be circular and (b) measured and simulated S parameters in the transmission case.

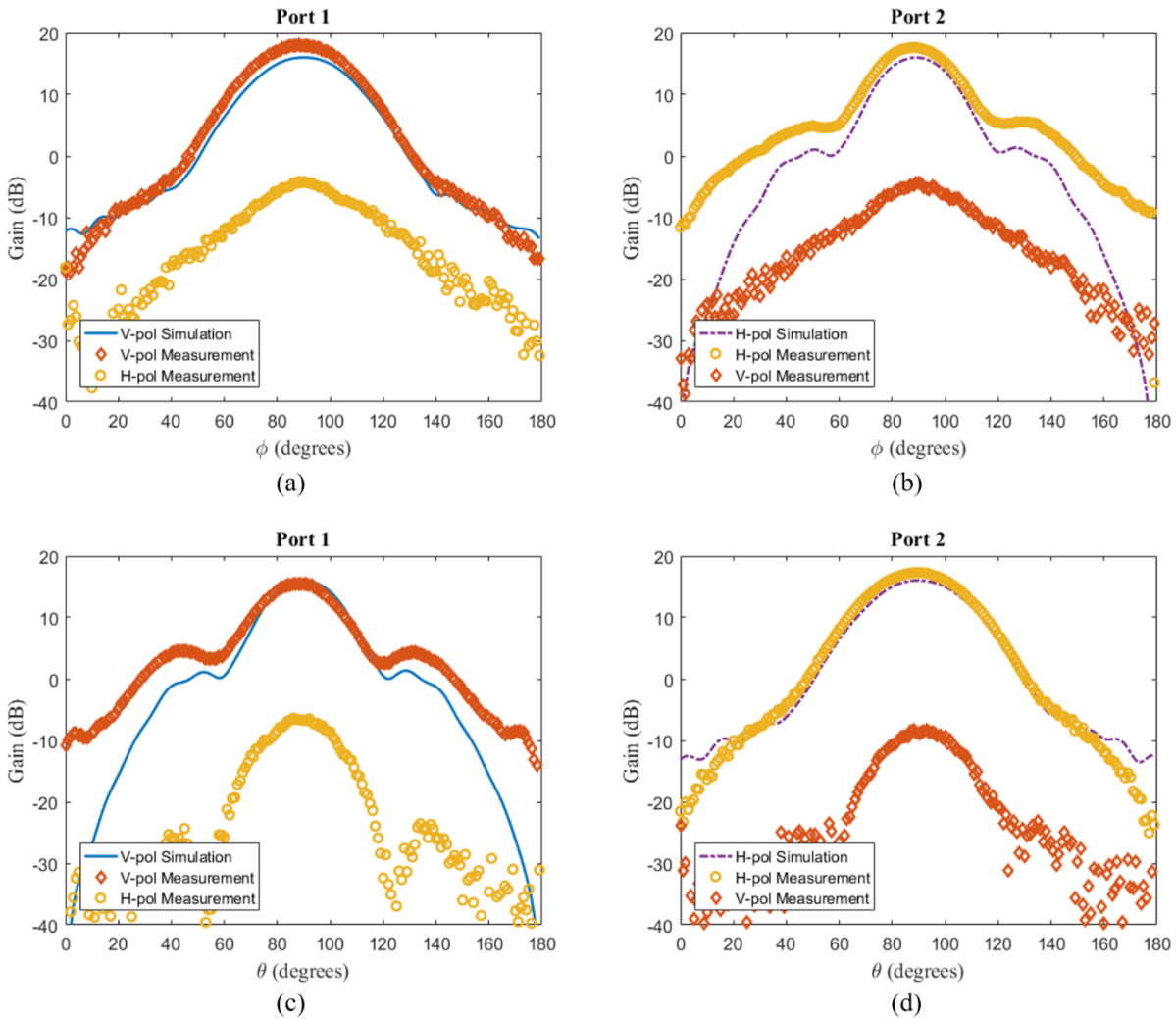


Figure 3.16. Simulated and measured results at (a) port 1: azimuth cut, (b) port 2: azimuth cut, (c) port 1: elevation cut and (d) port 2: elevation cut.

The whole procedure is then repeated while port 1 is terminated with a matched load and the signal is measured at port 2. The measured results, in this case, are shown in Figure 3.16 (b) and (d) for azimuth and elevation cuts, respectively. From that figure, it is deduced that the OMT prototype is functional for all the azimuth and elevation angles with an isolation better than 25 dB at 30 GHz.

## 3.2 Effective polarization independent coupling (EPIC)

A novel planar orthomode transducer (OMT) is introduced based on effective polarization independent coupling (EPIC). The concept of the EPIC is based on a theoretical observation of the relation between the fused coupling length of the  $TE_{10}$  mode and that of the  $TE_{01}$  mode. The EPIC is a traditional Riblet or fused coupler [82] that is excited by a rectangular waveguide. This rectangular waveguide supports the orthogonally-polarized  $TE_{10}$  and  $TE_{01}$  modes at the same frequency range. Along specific band of operation, it is found that the horizontally-polarized  $TE_{01}$  mode needs twice the longitudinal length required by the vertically-polarized  $TE_{10}$  mode in order to achieve full coupling. Therefore, within a specific coupling length, the  $TE_{10}$  mode couples two times while the  $TE_{01}$  mode couples only once. By this concept, a full separation can be achieved between the two orthogonal modes which are the function of an OMT.

This operation occurs for a specific value of the substrate dielectric constant. In order to make this possible over the mentioned specific band of operation, the substrate dielectric constant should be controlled. Full control of the substrate permittivity is achieved deliberately by drilling air holes in the substrate. Hence, the resultant effective uniaxial medium introduces the required parameters. The detailed design procedure, theoretical and simulation results are presented in Sec. 3.2.1.

### 3.2.1 EPIC Operation

The general structure of the EPIC is shown in Figure 3.17 (a). It consists of a common waveguide with width  $2a+g$  and length  $L_c$ . This waveguide is connected to three waveguides with cross section  $a \times b$ . The whole waveguide structure is assumed to be filled with a material that has an anisotropic dielectric constant tensor [70] shown in the inset of Figure 3.17 (b). The relative permittivity is  $\epsilon_{xy}$  and  $\epsilon_z$  in the transverse and longitudinal directions, respectively.

Assuming the design parameters are  $a = 3$  mm,  $b = 3.05$  mm,  $g = 0.5$  mm,  $\epsilon_{xy} = 2.5$  and  $\epsilon_z = 2.4$ . Regarding the common waveguide, the dispersion curves of this waveguide are shown in Figure 3.17 (c) where the solid lines represent the vertically-polarized modes, and the dashed lines represent the horizontally-polarized modes. For the vertically-polarized modes, the necessary even and odd order modes required for achieving full coupling are the  $TE_{10}$  and the  $TE_{20}$  modes, respectively. The appearance of the  $TE_{30}$  mode prevents the full coupling occurrence.

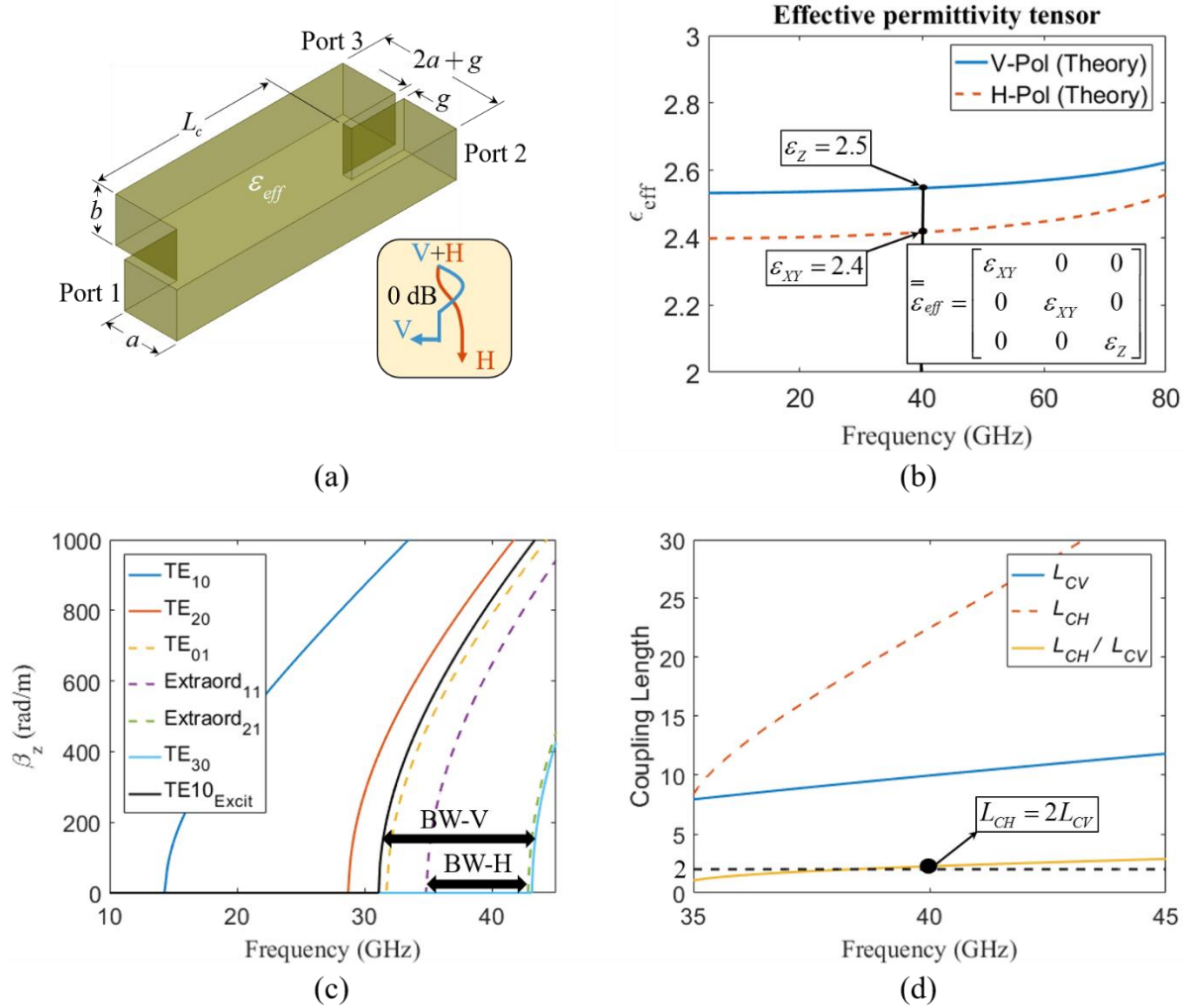


Figure 3.17. Effective polarization-independent coupler (EPIC): (a) general isometric view with its symbol, (b) effective permittivity tensor of a Rogers/duroid 6002 substrate perforated with air holes having the unit cell distribution in Figure 2.2 where  $r = 0.2$  mm and  $p = 0.8$  mm, (c) dispersion curves of the common waveguide when an effective material with the permittivity tensor in Figure 3.17 (b) fills the waveguide structure in Figure 3.17 (a), and (d) coupling lengths for the vertical and horizontal polarizations with the ratio between them.

In this case, the full coupling length  $L_{cv}$  is calculated based on the following relation,

$$L_{cv} = \frac{\pi}{\beta_e(\text{TE}_{10}) - \beta_o(\text{TE}_{20})} \quad (3.23)$$

and the bandwidth is calculated by,

$$\text{BW-V} = \frac{c}{2\sqrt{\varepsilon_z}} \left( \frac{1}{2a+g} \right) \quad (3.24)$$

On the other hand, for the horizontally-polarized modes, the necessary even and odd order modes required for achieving full coupling are the  $\text{TE}_{01}$  and the extraordinary component of the  $\text{TE}_{11}$  modes, respectively [83]. The appearance of the extraordinary component of the  $\text{TE}_{21}$  mode limits the full coupling occurrence. Similarly, the full coupling length  $L_{ch}$  is calculated based on the following relation,

$$L_{ch} = \frac{\pi}{\beta_e(\text{TE}_{01}) - \beta_o(\text{Extraordinary}_{11})} \quad (3.25)$$

and the bandwidth is calculated by,

$$\text{BW-H} \approx \frac{c}{2\sqrt{\varepsilon_{xy}}} \left( \sqrt{\left( \frac{2}{2a+g} \right)^2 + \left( \frac{1}{b} \right)^2} - \sqrt{\left( \frac{1}{2a+g} \right)^2 + \left( \frac{1}{b} \right)^2} \right) \quad (3.26)$$

The overall bandwidth of the EPIC is the intersection between the bandwidth of the vertically-polarized mode and that of the horizontally-polarized mode as shown in Figure 3.17 (c). Fortunately, the full coupling length of the horizontally-polarized mode is twice the full coupling length of the vertically-polarized mode within the common bandwidth of the overall structure as shown in Figure 3.17 (d). This is simply the clue for achieving the OMT functionality. When exciting port 1 with the orthogonally-polarized signal,  $\text{TE}_{10}$  and  $\text{TE}_{01}$  modes, the vertically-polarized  $\text{TE}_{10}$  mode fully couples and returns back to be totally received at port 2. On the other hand, the horizontally-polarized  $\text{TE}_{01}$  mode couples once to be totally received at port 3. Thus, a full separation between the  $\text{TE}_{10}$  and  $\text{TE}_{01}$  modes is achieved which creates the function of an OMT.

### 3.2.2 Controllability of the Dielectric Constant

The achievement of the previously-mentioned concept is restricted by specific values of the material dielectric constant in the different directions. The existing anisotropic commercial substrates limit the operation of the EPIC to be over defined bands of operations. In order to overcome this problem, full control of the material permittivity should be mastered.

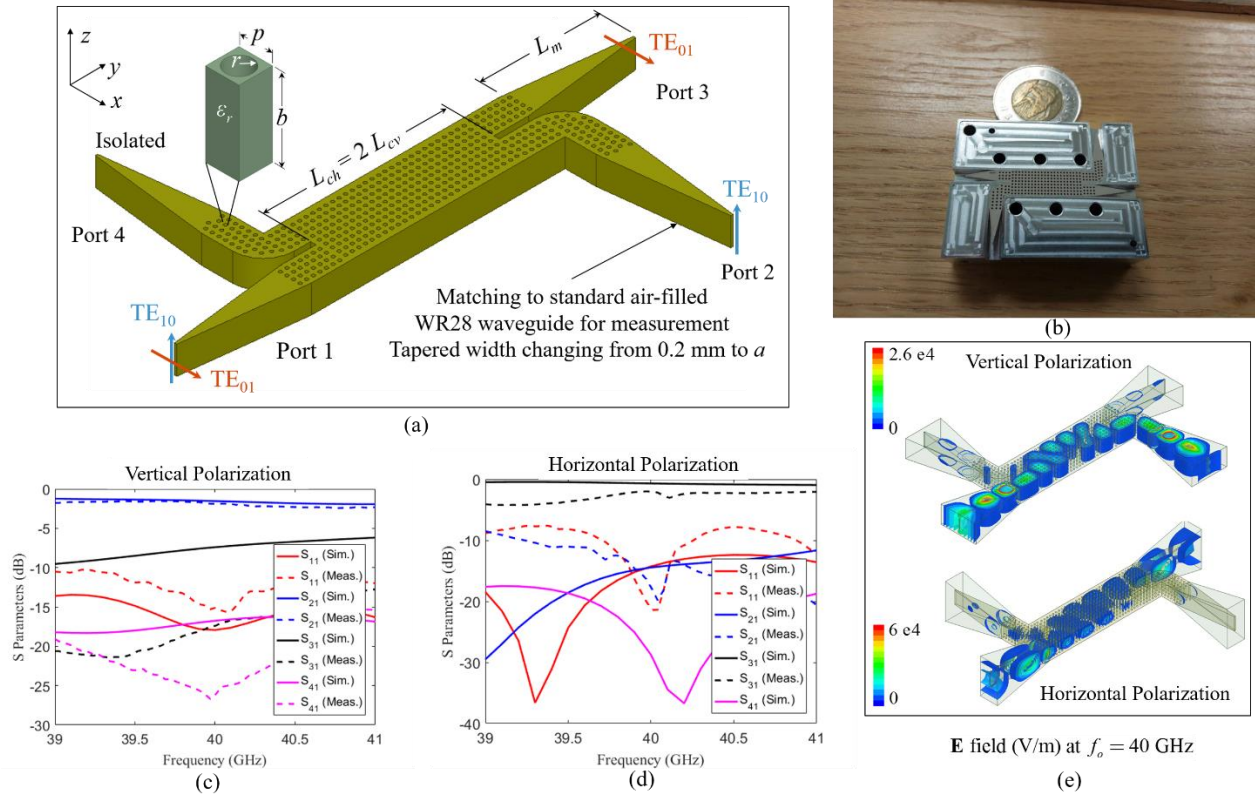


Figure 3.18. Effective polarization independent coupler (EPIC): (a) Physical prototype, (b) effective homogeneous permittivity tensor, (c) scattering parameters of the  $TE_{10}$  mode, (d) scattering parameters of the  $TE_{01}$  mode and (e) field distribution of the two modes.

This control is achieved by drilling air holes in the substrate. The air hole diameters and separations can be controlled to obtain the required permittivity.

For example, the substrate used in this work is the Roger RT/duroid 6002 that has anisotropic permittivity of  $\epsilon_{XY} = 2.95$  and  $\epsilon_Z = 2.94$ . On the other hand, in the example explained in Figure 3.17 (d), the required anisotropic permittivity in the previous section is  $\epsilon_{XY} = 2.5$  and  $\epsilon_Z = 2.4$ . The required downshift in the permittivity value is achieved by drilling air holes periodically in the Roger RT/duroid 6002 substrate. The unit cell of this periodic medium is shown in Figure 3.18 (a). The air hole radius is  $r$  and the period is  $p$ .

In order to get the resultant effective permittivity tensor, an eigenvalue problem for the unit cell has to be formulated as explained in details in the previous chapter. The first two solutions

(eigenvectors) represent the electric field in the unit cell. One being vertically polarized, and the other one is horizontally polarized. The two corresponding eigenvalues represent the relative effective permittivity in the two corresponding directions. It can be obtained using  $r = 0.2\text{mm}$  and  $p = 0.8\text{mm}$  that the effective values of the relative permittivity in the transverse and the longitudinal directions for this pattern of air perforations in the 6002 substrate are 2.5 and 2.4, respectively. Those values are exactly as needed in the EPIC design over the operating bandwidth. Based on the previous discussions, the overall structure is designed and built as shown in Figure 3.18 (a) where  $L_c = L_{CH} = 18\text{ mm}$  and  $b = 3.05\text{ mm}$ . A fourth port, which should be isolated, is added in order to fully characterize the symmetric four-port coupler. The designed unit cell is introduced along the substrate in order to achieve the desired effective permittivity. Tapered matching sections with length a  $L_m = 8\text{mm}$  and width varying from  $0.2\text{ mm}$  to  $a = 3\text{ mm}$  are designed to match the standard air-filled WR28 waveguide to the dielectric substrate for measurement. The overall structure is simulated, prototyped and measured as discussed in the following sections.

### 3.2.3 Results and Discussions

The previously designed EPIC-based OMT is implemented where the prototype is shown in Figure 3.18 (b). In order to measure the structure, a metallic enclosure is implemented to hold the dielectric substrate. This metallic box is integrated with the required matching sections as the interface between the proposed prototype and the network analyzer through WR28 waveguides. The overall OMT structure is measured by a vector network analyzer (VNA).

An important consideration should be taken into account when realizing such a thick perforated substrate. Drilling air holes in a thick substrate may result in getting air holes that are not uniform along the thickness of the substrate. In order to overcome this problem, two substrates with thickness  $1.52\text{ mm}$  for each are perforated and stacked together to create the overall  $3.05\text{ mm}$  required thickness with more accurate air holes. So the prototype shown in Figure 3.18 (b) is only half the overall structure where there is another half that is identical to the shown part.

For the vertically-polarized  $TE_{10}$  mode, the resultant scattering parameters are shown in Figure 3.18 (c). From that figure, it can be clearly observed that the signal is received at port 2 while the reflection at port 1, the transmission at port 3 and the isolation at port 4 are all below  $10\text{ dB}$  over

the bandwidth. For the horizontally-polarized  $TE_{01}$  mode, the resultant scattering parameters are presented in Figure 3.18 (d). In this figure, it is shown that the signal is received at port 3 while the reflection at port 1, the transmission at port 2 and the isolation at port 4 are all below 10 dB over the same bandwidth. In both of Figure 3.18 (c) and (d), there is an insertion loss of about 1dB that is introduced by the substrate loss tangent which is approximately 0.003 within the operating bandwidth.

As a further illustration, it can be clearly observed from the field distribution in Figure 3.18 (e) that the  $TE_{10}$  mode couples twice in order to be received at port 2. Whereas the  $TE_{01}$  mode couples only once in order to be received at port 3. This confirms the functionality of the proposed planar OMT based on the concept of the EPIC.

Based on the discussed results, the precise design of the substrate anisotropy by drilling specific corresponding air holes is verified through the EPIC experiment where a very good agreement is achieved between simulation and measurement results. This confirms the merit of the methodology presented in this work.

For this newly proposed device, a symbol is designed to visualize the functionality of the EPIC-based OMT, as shown in Figure 3.17 (a). The symbol shows a three port device excited with V+H input representing the two orthogonal polarizations. One output side has only the V-pol., shown in blue, after coupling back and forth twice in the common section. Whereas the other output side has only the H-pol., shown in red, after one full coupling in the common section. This proposed device shows a great potential to realize the useful benefits of polarization diversity in the limited space of handheld devices.

### 3.3 Conclusion

In this chapter, the possibility of separating and/or combining orthogonal polarizations within single planar substrate profile is introduced based on PSC and EPIC. A complete design procedure is presented for designing a planar PSC-based OMT structure. This OMT in its general form is validated through simulations where 15% fractional bandwidth is achieved around 32 GHz for insertion loss below 10dB. As a validation, a special case of a PSC-based OMT is designed and prototyped. An excellent agreement is achieved when compared with simulations. The final structure works with a band of frequencies starting from 33 to 40 GHz. The structure is integrated

with a square horn antenna. Upon measuring the horn antenna gain in different orientations with different excitations, it confirmed the full operation of an OMT with antenna gain around 15dB and isolation below 25dB. This experiment validates the proposed theory for the design of a PSC and its application to an OMT. If integrated successfully with mmW antennas, the feature of polarization diversity can be enabled in the future wireless systems making use of the proposed planar device. For full integration, new transitions should be designed to extract the horizontally polarized LSM modes and deliver it to integrated chips on the same PCB. For further elucidation, an EPIC is presented for the same purpose. This EPIC shows the possibility of achieving the same PSC functionality without even having the periodic PEC wall. This comes at the expense of controlling the substrate anisotropy by drilling specific air holes into it. Those presented concepts are used together in order to design planar dually-polarized microwave components as explained in details in the following chapter.

## **CHAPTER 4      APPLICATIONS – PLANAR DUAL-POLARIZED PSC-BASED MICROWAVE COMPONENTS**

Enabling the dual-polarization feature in the development of microwave components is proposed and realized based on polarization selective coupling (PSC). Dual-polarization transmission and reception of electromagnetic waves handling is one of the most promising features for modern wireless systems [2]. The importance of this feature arises due to the resulting efficiency and capacity enhancement of the transmitting and receiving circuitries and systems based on dual-polarization [84-86]. More interestingly, many of the active RFID tag designs are based on the dual-polarization feature [58, 87, 88].

Nevertheless, the majority of microwave components and circuits operate only on a single polarization. This polarization is usually vertically oriented with respect to the plane of the printed circuit board on which those components are integrated. The polarization described here is the polarization state of electromagnetic waves propagating inside microwave components and within interconnects. Dually-polarized passive microwave components are those components which can handle two orthogonal polarizations within their internal structure independently, and can apply the required functionality on the two orthogonal polarizations at the same time without interfering on each other. The analysis and design of such components are far from being trivial. This is in addition to the fact that a different methodology is needed for each individual microwave component to be dually-polarized.

Based on the mentioned motivations, we propose a concept in this work for enabling the dual-polarization features in some fundamental microwave components through one distinct mechanism. Consequently, most of the microwave components can be re-invented as dually-polarized if this mechanism is applied. First, let us compare a typical microwave component to its dually-polarized microwave counterpart as shown in Figure 4.1. As one can observe through this illustration, when a typical microwave component receives an arbitrarily polarized signal, it processes only one component of the received signal, which is usually vertically oriented as explained earlier, while the other component is reflected back resulting in an inefficient treatment for the arbitrarily polarized signal. By contrast, when a dually-polarized microwave component receives an arbitrarily polarized signal, it processes both of its orthogonal components resulting in

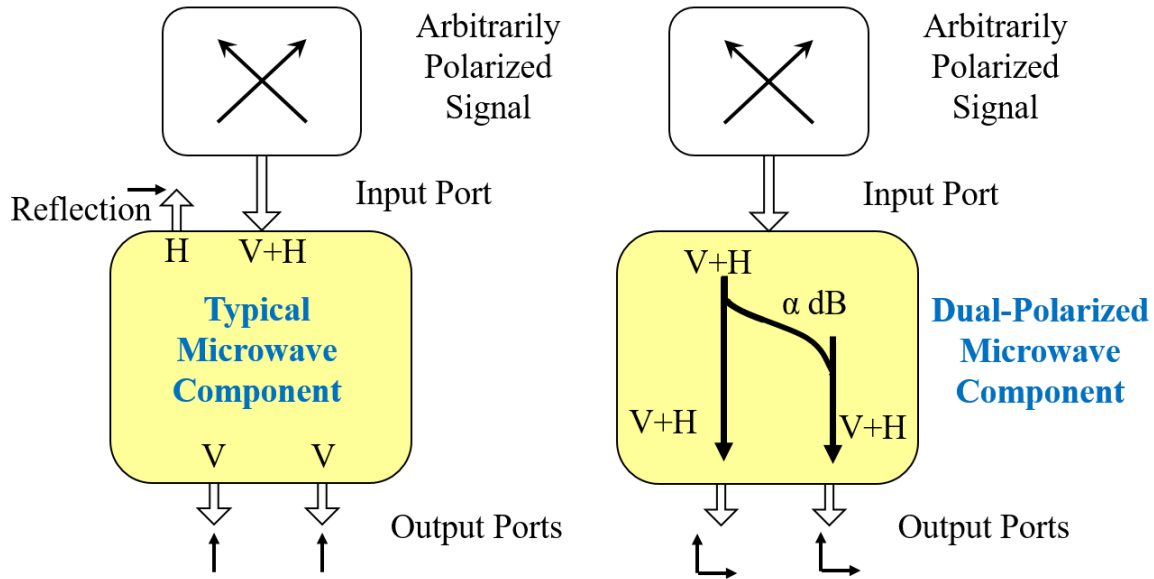


Figure 4.1. Conceptual block diagram for dually-polarized microwave components based on PSC versus typical microwave components.

more efficient reception. Our core idea for implementing this feature is based on our proposed and discussed polarization selective coupling (PSC) [89, 90], which is explained in Sec. 3.1.

As a quick reminder, the PSC is a fused coupler as the couplers presented in [91], [92] with an integrated polarizer wall that is added longitudinally along a specific section of its center line. The integrated polarizer wall is realized as periodic metallic vias or pins such as those in the SIW technology [74]. This polarizer wall can guide only the vertically polarized modes while it looks transparent for the horizontally polarized modes. Therefore, the dually-polarized microwave component works equally for both polarizations.

For example, when developing a dually-polarized 3dB coupler based on the PSC, we begin with the design of a traditional 3dB fused coupler adjusted to work only for horizontally polarized modes. Subsequently, the polarizer wall is added along with a specific part of the longitudinal center-line of the coupler. This part should keep the required coupling length necessary for a 3dB coupling of the vertically polarized mode while it does not affect the horizontally polarized mode. This mechanism is explained extensively in this chapter.

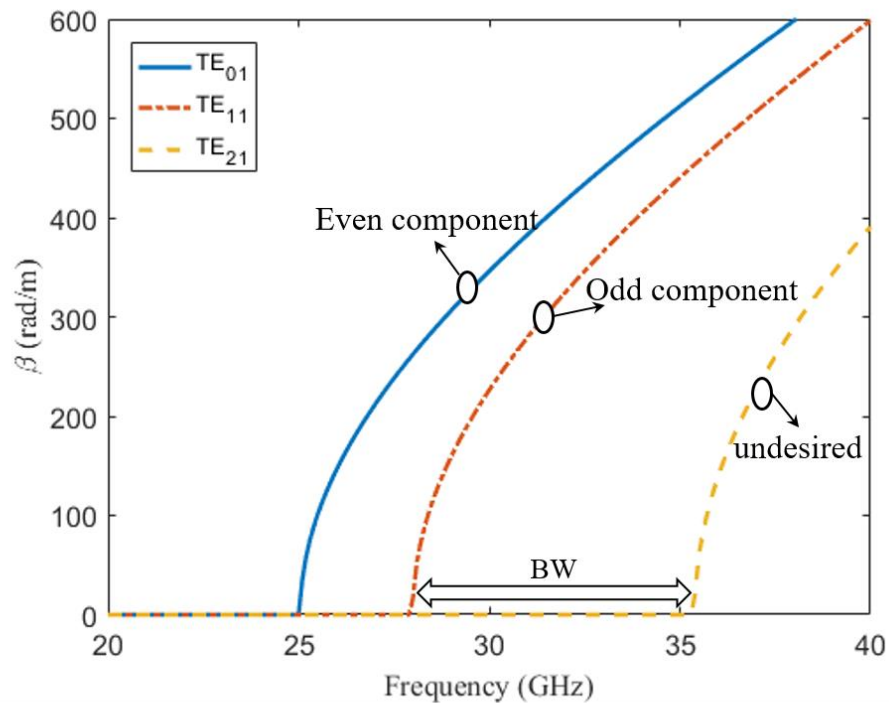
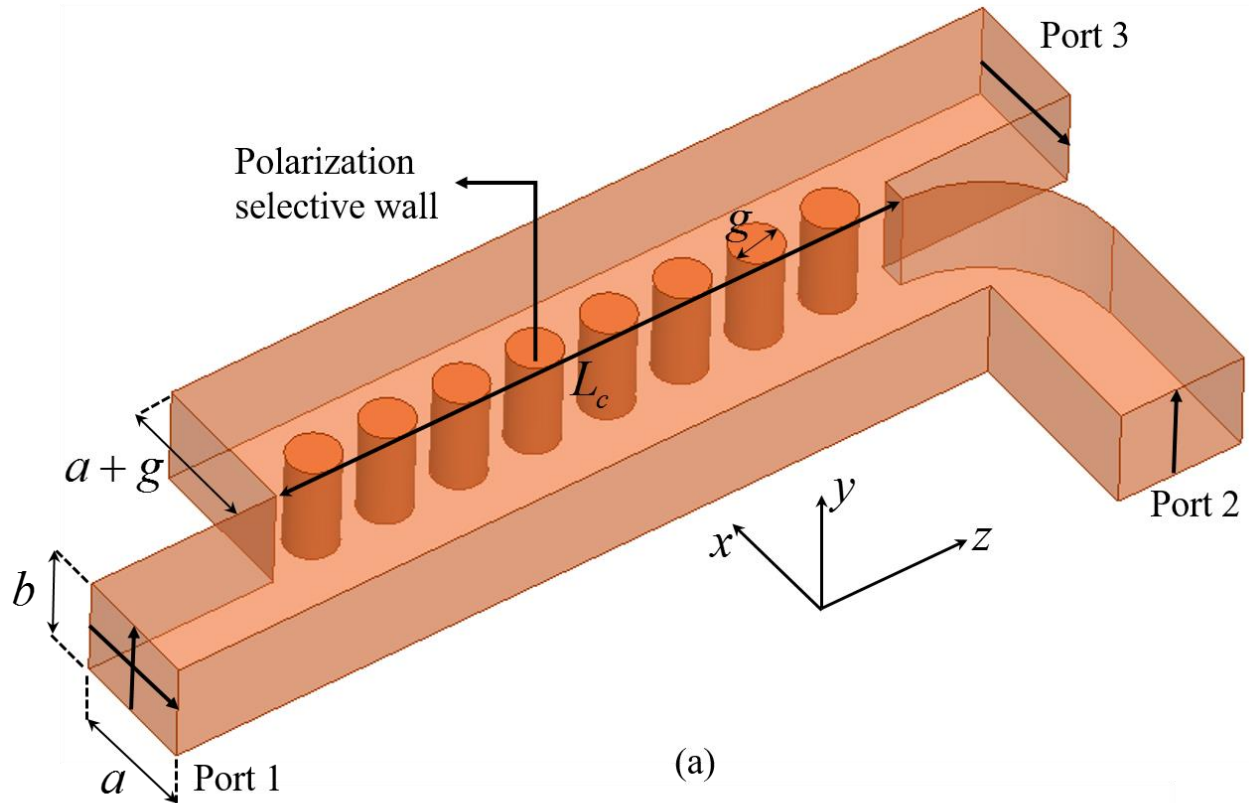


Figure 4.2. Polarization selective coupler (PSC): (a) isometric structural view and (b) dispersion curves for horizontally polarized modes.

## 4.1 Polarization Selective Coupling

In this section, the basic unit of constructing a dually-polarized microwave component is revised. This unit is the PSC. The PSC is a three port planar waveguide structure with a periodic longitudinal conducting wall in its middle as shown in Figure 4.2 (a). When exciting port 1 with two orthogonal polarizations, the vertically polarized component is completely guided by the periodic conducting wall by means of SIW [74]. Thus, it can be received at port 2 as any normal rectangular waveguide based on the fundamental TE<sub>10</sub> mode.

By contrast, the periodic conducting wall which should be made electrically small is transparent for the horizontally polarized component because it is normal to the electric field vector. Therefore, the horizontal component has the possibility of getting fully coupled to the other waveguide by means of the Hadge [91] or Rosenberg [77] concept and then, it can be received at port 3 if the structure has the appropriate coupling length.

In order to design a PSC, the waveguide dimensions  $a$  and  $b$  in addition to the required full coupling length  $L_c$  should be designed according to the required operating frequency  $f_{op}$ . For the air-filled PSC used in this work, the waveguide cross-sections at the different ports should be almost square. This guarantees the excitation of the orthogonally oriented modes, TE<sub>10</sub>, and TE<sub>01</sub> modes, at the same frequency. This allows identical handling or processing for both polarizations. Accordingly, the dimensions of the PSC waveguide are approximately calculated by the following equation,

$$a = b = \frac{0.6c}{f_{op}} \quad (4.1)$$

This equation guarantees the excitation of both of the vertically polarized TE<sub>10</sub> and the horizontally polarized TE<sub>01</sub> in the required band of operation.

For the coupling length calculation, it is directly related to the even and odd components of the propagation constant  $\beta_e$  and  $\beta_o$ , respectively, necessary for achieving full forward coupling. The equation that governs this relation can be written as in [72],

$$L_c = \frac{\pi}{\beta_e - \beta_o} \quad (4.2)$$

One should pay attention to identifying the necessary modes of coupling in the PSC design. The typical couplers are based on the TE<sub>10</sub> and TE<sub>20</sub> modes because they operate specifically for vertical polarization as the Riblet coupler [93] which is not the case in the proposed PSC. Different from the typical couplers, the PSC works specifically for only the horizontally polarized modes. Therefore, the even and odd modes necessary for coupling, in this case, are the TE<sub>01</sub> and TE<sub>11</sub> modes, respectively [77]. The propagation constants for both of them can be written in the following expressions,

$$\beta_e(\text{TE}_{01}) = \sqrt{k_o^2 - \left(\frac{\pi}{b}\right)^2} \quad (4.3)$$

$$\beta_o(\text{TE}_{11}) = \sqrt{k_o^2 - \left(\frac{\pi}{b}\right)^2 - \left(\frac{\pi}{2a+g}\right)^2} \quad (4.4)$$

where  $g$  is the diameter of the metallic cylinder unit cell in the periodic conducting wall, and it is selected to be  $b/4$  according to some fabrication limitations in our Poly-Grames research facilities. Keeping in mind that these modes are related to the wide common waveguide which contains the periodic conducting wall with width  $2a + g$  where the coupling occurs, not the waveguide at the different ports with the width  $a$ .

By substituting from (4.3) and (4.4) in (4.2), the dimension of  $L_c$  can be evaluated. The full forward coupling occurs at the length  $L_c$  whenever there are not any other horizontally polarized mode propagating through the structure rather than the TE<sub>01</sub> and the TE<sub>11</sub> modes. The excitation of the next horizontal higher order TE<sub>21</sub> mode impedes the possibility of full coupling. This limits the bandwidth of the PSC, in this case, to start from the cut off frequency of the TE<sub>11</sub> mode up to the cut off frequency of the TE<sub>21</sub> mode according to the following relation,

$$\text{BW} = \frac{c}{2} \left( \sqrt{\left(\frac{2}{2a+g}\right)^2 + \left(\frac{1}{b}\right)^2} - \sqrt{\left(\frac{1}{2a+g}\right)^2 + \left(\frac{1}{b}\right)^2} \right) \quad (4.5)$$

In this work, the operating frequency is selected to be at 30 GHz. Accordingly from (4.1),  $a = b = 6$  mm and then, the dispersion curves of the horizontally polarized modes which control the coupling functionality can be obtained from (4.3) and (4.4) as shown in Figure 4.2 (b). Consequently, when substituting in (4.2) at 30 GHz, the required coupling length for full forward

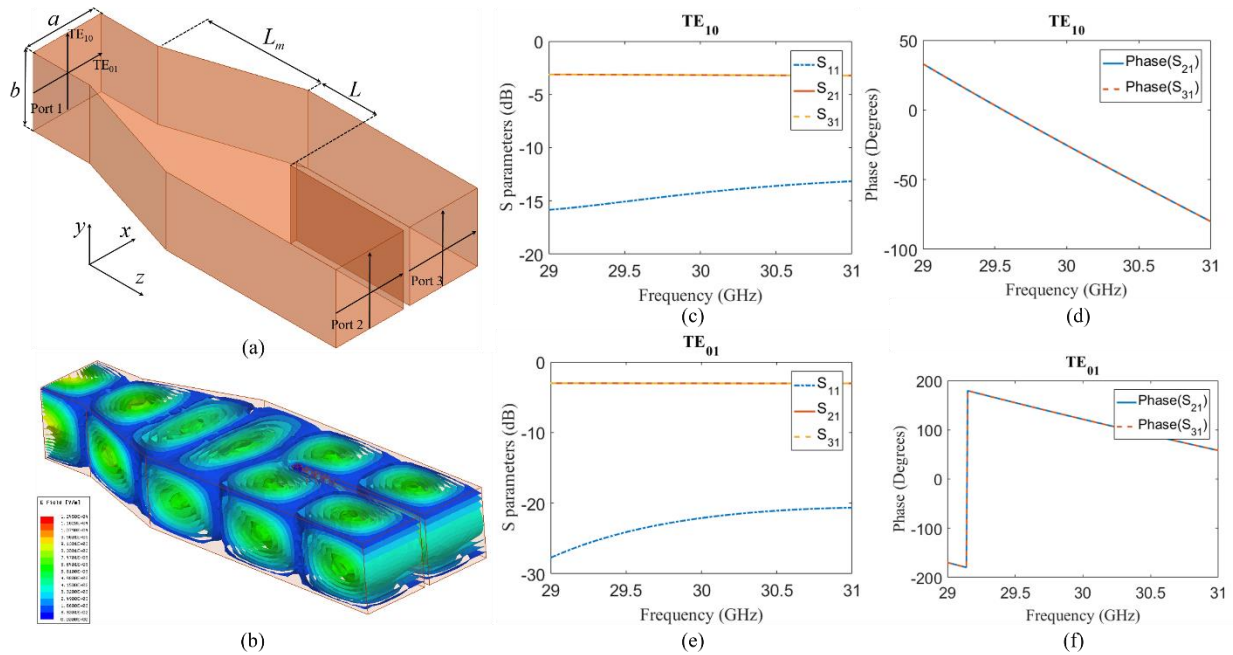


Figure 4.3. Dually-polarized power divider based on PSC: (a) equivalent structure, (b) field distribution, (c) magnitude of scattering parameters for  $TE_{10}$  mode, (d) phase of scattering parameters for  $TE_{10}$  mode, (e) magnitude of scattering parameters for  $TE_{01}$  mode and (f) phase of scattering parameters for  $TE_{01}$  mode.

coupling is  $L_c = 27$  mm. The appearance of the  $TE_{21}$  prevents the full coupling based on (4.5) as presented in Figure 4.2 (b). The BW, in this case, is around 7 GHz.

The air filled PSC presented in this section characterizes the basic concept for a proposed dually-polarized planar component. In the next sections, the PSC concept is applied for designing the different constituent components of the proposed dually-polarized six-port junction and dually-polarized butler matrix as well.

## 4.2 Dual-polarized power divider

The first and simplest dually-polarized component studied is a power divider. In this section, the design of a dually-polarized power divider, which does not need the PSC concept, is introduced. The proposed dually-polarized power divider is a three port waveguide device as shown in Figure 4.3 (a).

This power divider is based on the concept of a straight Y-junction with bifurcation such as the integrated structures introduced in [94-96]. The input and output waveguides have the same cross-section area which is  $a \times b$ . As stated earlier, the dimensions of those waveguides are chosen to support the  $TE_{10}$  and the  $TE_{01}$  modes at the same frequency range, so they have the same dimensions reported in the previous section at 30 GHz which is the operating frequency selected in this design.

The previously-reported power dividers are based on just the fundamental vertically oriented  $TE_{10}$  mode. Theoretically, the same concept must apply to the horizontally oriented  $TE_{01}$  mode. The only difference that should appear due to the change of the waveguide width from  $a$  to  $2a + g$  is higher return loss in case of the  $TE_{01}$  mode than that of the  $TE_{10}$  mode which is negligible. This is because of the electric field vector of the  $TE_{01}$  mode which is horizontally polarized experiences a sudden change in the wall from which it is wavering which is not the case for the  $TE_{10}$  mode. In order to overcome this problem, a matching section should be optimized for a minimum return loss of the  $TE_{01}$  mode. On the other hand, this matching section would not affect negatively the  $TE_{10}$  mode. The length of this optimized matching section  $L_m$  is found to be 10 mm using a full wave analysis.

The distance  $L$  between the end of the matching section and the discontinuity at the output waveguides is optimized to achieve power division and minimum return loss at the input port. This optimization is based on the equivalent circuit model reported in [95]. The same length  $L$  can achieve the required power division for both of the  $TE_{10}$  and the  $TE_{01}$  modes simultaneously. This length is found to be about 5 mm.

Based on the mentioned parameters, the structure is solved using the HFSS simulator. The field distribution of the overall structure is shown in Figure 4.3 (b). It can be observed from this figure that both of the  $TE_{10}$  and  $TE_{01}$  modes are divided between port 2 and port 3 with equal magnitudes, but with different phases. For further illustration, magnitude and phase of scattering parameters for each of the  $TE_{10}$  and  $TE_{01}$  are presented in Figure 4.3 (c), Figure 4.3 (d), Figure 4.3 (e) and Figure 4.3 (f), respectively. From these plots, one can deduce that a power division is achieved for each mode around 30 GHz. On the other hand, the phase shift between the output and the input ports for the  $TE_{10}$  mode is around  $-30^\circ$  which is different from that of the  $TE_{01}$  mode which is around  $120^\circ$  at 30 GHz. This  $150^\circ$  phase difference between the  $TE_{10}$  and  $TE_{01}$  phase shifts does

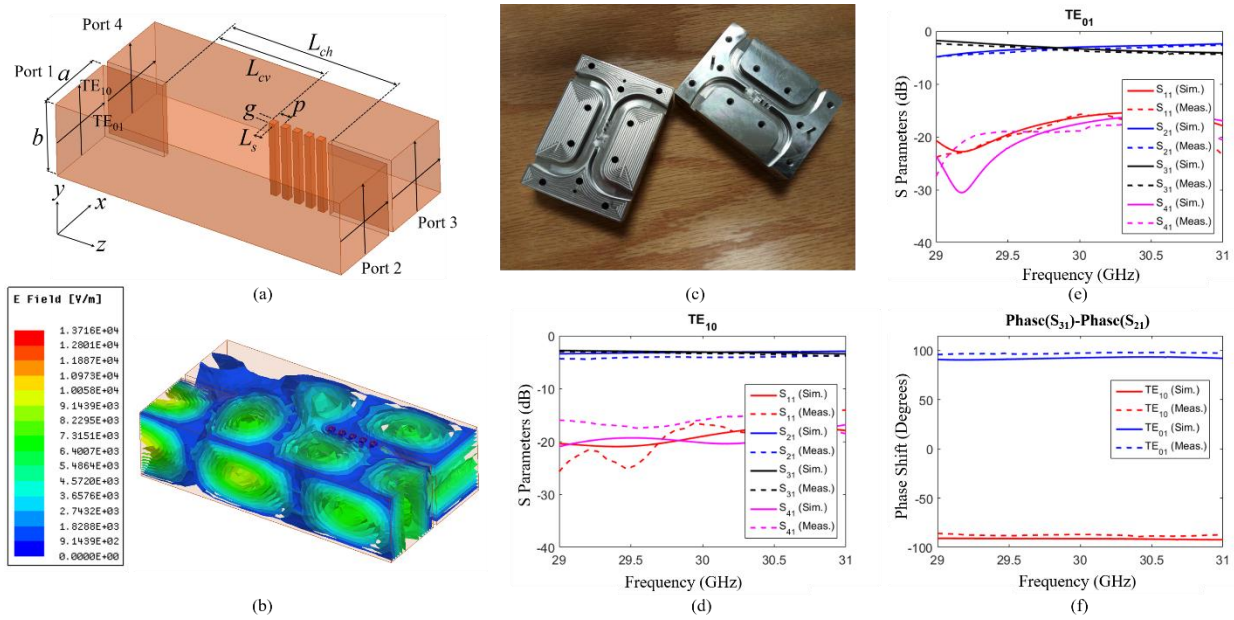


Figure 4.4. Dually-polarized hybrid coupler based on PSC: (a) equivalent structure, (b) field distribution, (c) prototype, (d) magnitude of scattering parameters for  $TE_{10}$  mode, (e) magnitude of scattering parameters for  $TE_{01}$  mode and (f) phase of scattering parameters for both of the  $TE_{10}$  and  $TE_{01}$  modes.

not affect the overall performance of the dually-polarized six-port junction due to the orthogonality of the  $TE_{10}$  and  $TE_{01}$  modes. This is presented later in Sec. 4.5.

### 4.3 Dual-polarized hybrid coupler

The second basic introduced dually-polarized component explained in this section is a dually-polarized hybrid coupler. This coupler is a four port device of which the input is at port 1, the through signal is at port 2, the coupled signal is at port 3, and the isolation is at port 4, as shown in Figure 4.4 (a). When exciting this coupler at port 1 with two orthogonal polarizations, the  $TE_{10}$  and  $TE_{01}$  modes, a 3dB of each of them is delivered to both of port 2 and port 3 while port 4 is isolated. In order to achieve a 3dB coupling level for a particular mode, a specific coupling length should be designed based on the even and odd components of the propagation constant as discussed earlier. This coupling length has different values for each separate mode. Therefore, two different coupling lengths are needed for the  $TE_{10}$  and  $TE_{01}$  along the same structure. This can be simply done by

using the polarization selective conducting wall. Keep in mind that the PSC is a 0 dB coupler for the TE<sub>01</sub> mode while no coupling for the TE<sub>10</sub> mode, thus the polarization selective wall is distributed over the whole common waveguide. On the other hand, the dually-polarized hybrid coupler is a 3 dB coupler for both of the TE<sub>10</sub> and the TE<sub>01</sub> modes. Thus, the polarization selective wall is not distributed over the whole common waveguide as the PSC does.

Firstly, the required length for achieving a 3dB coupling level for the horizontally polarized TE<sub>01</sub> mode is calculated by the following relation,

$$L_{ch} = \frac{\pi}{2(\beta_e(\text{TE}_{01}) - \beta_o(\text{TE}_{11}))} \quad (4.6)$$

Then, the same concept is used for the vertically polarized TE<sub>10</sub> mode from the following relation,

$$L_{cv} = \frac{\pi}{2(\beta_e(\text{TE}_{10}) - \beta_o(\text{TE}_{20}))} \quad (4.7)$$

For physical implementations for both  $L_{ch}$  and  $L_{cv}$  over the same structure, a polarization selective conducting wall is inserted over a length of  $L_{ch} - L_{cv}$  as shown in Figure 4.4 (a). Since this wall guides the TE<sub>10</sub> mode, the coupling level of this mode occurs based only on the length  $L_{cv}$ . On the contrary, this wall is transparent for the TE<sub>01</sub> mode as mentioned earlier. Hence this mode experiences the length  $L_{ch}$  which guarantees the required coupling level for such mode.

The structure is designed at 30 GHz. Similarly based on (4.1),  $a = b = 6$  mm as the input and output waveguide cross-sections. According to the fabrication limitations in our Poly-Grames lab, the period  $p$  of the periodic conducting wall is selected to be 2.5 mm where the conducting strip length  $L_s$  is 1 mm; the strip width  $g$  is 0.5 mm while the opening between the strips is 1.5 mm.

Based on the previously-mentioned parameters, the calculated values for  $L_{ch}$  and  $L_{cv}$  based on (4.6) and (4.7) are around 14 mm and 9 mm, respectively. When exciting port 1 with a dual-polarized signal, the field is equally distributed between port 2 and port 3 as shown in Figure 4.4 (b). This can be clearly demonstrated from the scattering parameters for both of the TE<sub>10</sub> and TE<sub>01</sub> modes between the different ports. A prototype for the dually-polarized 3dB coupler is implemented as shown in Figure 4.4 (c). An excellent agreement is achieved between both of the simulation and measurement results.

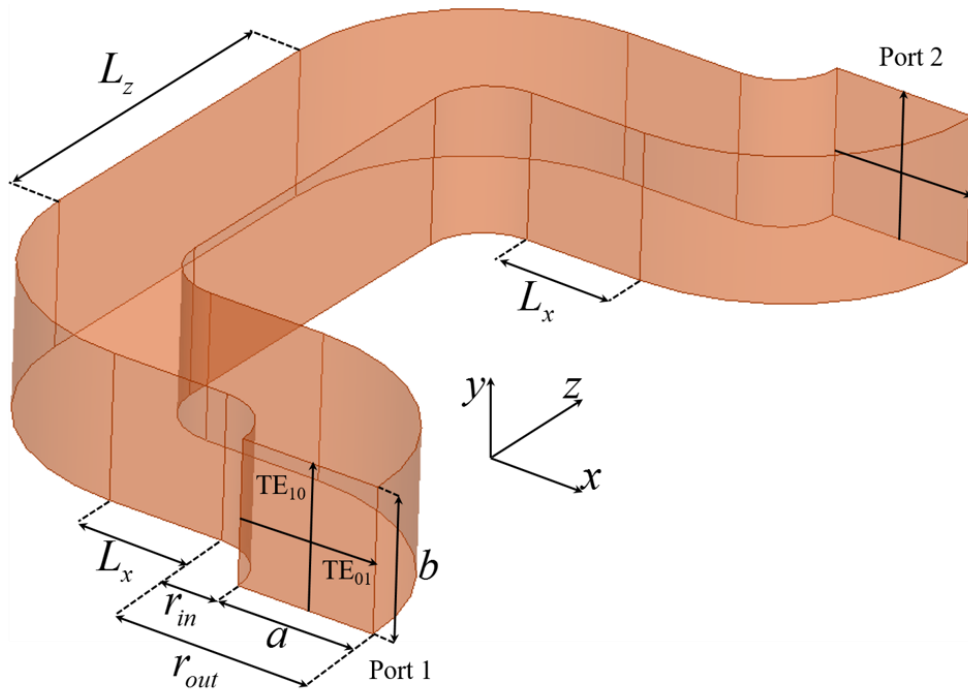
For the magnitude of the scattering parameters for the  $TE_{10}$  mode shown in Figure 4.4 (d), it can be observed that when exciting port 1 with a vertically polarized signal, this signal is divided equally between port 2 and port 3 with a 3dB coupling level where the reflection loss at port 1 and the isolation with port 4 is around 15dB. Concerning the phase difference between port 2 and port 3, it is shown in Figure 4.4 (f) that the phase difference between them is around  $90^\circ$ . Similarly, for the horizontally polarized  $TE_{01}$  mode, it shows a coupling level of 3dB at port 2 and port 3 as in Figure 4.4 (e) and a phase difference about  $90^\circ$  between port 3 and port 4 as shown in Figure 4.4 (f) which is the full function of a dually-polarized hybrid coupler.

In this section, it can be deduced that an excellent response for a dually-polarized hybrid coupler can be obtained based on PSC. This means an equal magnitude and phase responses can be obtained for both of the orthogonal modes. On the other hand, this is not the case for the dually-polarized power divider which shows an identical magnitude response for the  $TE_{10}$  and the  $TE_{01}$  modes while the phase shift is different between both modes which is about  $150^\circ$  as clarified in the previous section. This deviation in the phase between the orthogonal modes requires an equalization in order to achieve a full dual-polarization feature for the proposed six-port junction presented in Sec. 4.5. The part used for this equalization is the cylindrical waveguide bend as introduced in the following section.

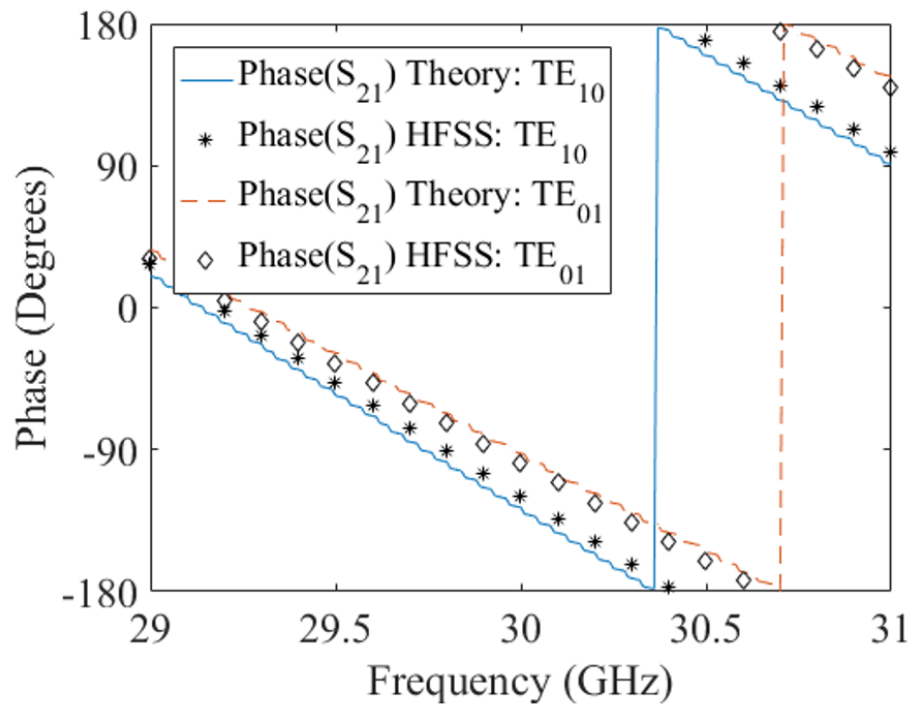
#### 4.4 Waveguide bend for dual-polarization phase equalization

In this section, the waveguide bend is studied from a different perspective. It is mainly used in the six-port junction to connect the power divider with the hybrid coupler in the overall structure as explained later. In order to achieve the highest possible benefit of this bend, it is mathematically designed specifically for introducing the required phase shifts in the overall dually-polarized six-port junction.

In order to show this concept in details, the structure in Figure 4.5 (a) is studied theoretically and through HFSS simulation. This structure consists of four identical circulating waveguide cylindrical bends in addition to three square waveguides. The waveguide cross-section is selected to have  $a = b = 6$  mm as in the previous sections. The inner radius of the bend is  $r_{in} = 2.5$  mm, and the outer radius is  $r_{out} = 8.5$  mm.



(a)



(b)

Figure 4.5. Phase shift bend equalizer: (a) equivalent structure and (b) phase difference between port 1 and port 2 for both of the TE<sub>10</sub> and TE<sub>01</sub> resulted from theory and HFSS simulation.

Two of the rectangular waveguides have a longitudinal length of  $L_x = 5$  mm while the third one has a length of  $L_z = 15$  mm .

Due to the square cross-section of the waveguide, the phase shifts due to the three square waveguides for the TE<sub>10</sub> and TE<sub>01</sub> modes are identical, and it can be calculated from the following relation,

$$(\beta L) = \frac{2\pi f}{c} \sqrt{1 - \left(\frac{c}{2fa}\right)^2} (2L_x + L_z) \quad (4.8)$$

The situation is different in case of a waveguide bend. In this case, the bend introduces different phase shifts for the TE<sub>10</sub> and the TE<sub>01</sub> modes. This can be derived with the help of chapter 5 in Harrington textbook [44].

For the TE<sub>10</sub> mode, the wave function can be represented by the following equation,

$$\psi = [AJ_n(k\rho) + BN_n(k\rho)]e^{-jn\varphi} \quad (4.9)$$

where  $J_n$  is the Bessel function of the first kind,  $N_n$  is the Bessel function of the second kind,  $k$  is the wavenumber,  $\rho$  and  $\varphi$  represent the cylindrical coordinates. It can be deduced from (4.9) and based on the field equations in cylindrical coordinates in the source-free region that  $n$  is a root of the following relation,

$$-\frac{B}{A} = \frac{J_n(k r_{in})}{N_n(k r_{in})} = \frac{J_n(k r_{out})}{N_n(k r_{out})} \quad (4.10)$$

where  $A$  is an arbitrary constant. The phase shift due to the waveguide bend, in this case, is  $n\varphi$ , where  $n = n_{10}$  for the TE<sub>10</sub> mode and  $\varphi$  is the angle of the waveguide bend circulation which is 90° in this example. Similarly for the TE<sub>01</sub> mode, the wave equation in (4.9) is satisfied if  $n$  is a root of the following relation,

$$-\frac{B}{A} = \frac{J'_n(k r_{in})}{N'_n(k r_{in})} = \frac{J'_n(k r_{out})}{N'_n(k r_{out})} \quad (4.11)$$

The phase shift due to the waveguide bend, in this case, is  $n\varphi$ , where  $n = n_{01}$  for the TE<sub>01</sub> mode.

Based on the previous explanation, the total phase shift due to the four waveguide bends for the TE<sub>10</sub>, and TE<sub>01</sub> modes are respectively,

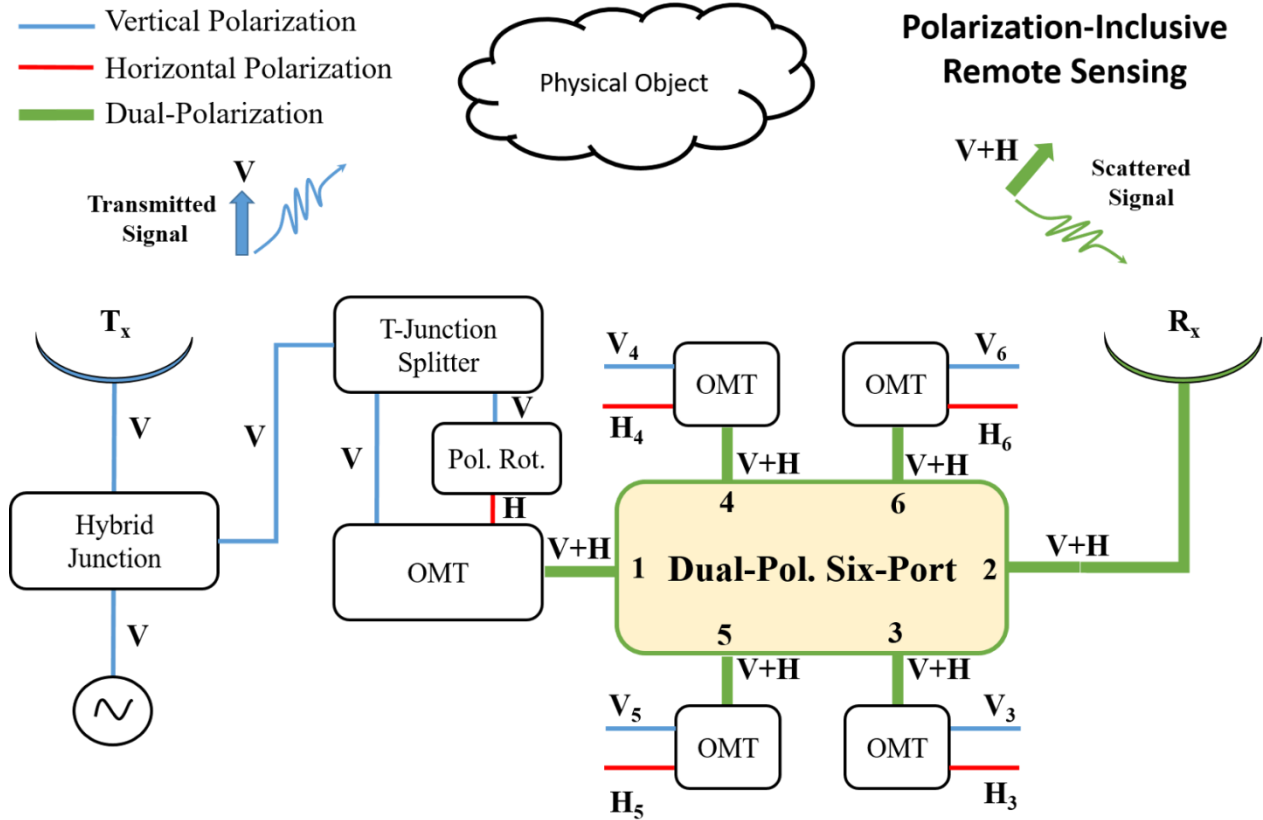


Figure 4.6. Polarization-inclusive remote sensing (PIRS) as a possible application for the dually-polarized six-port junction.

$$\Delta\phi(\text{TE}_{10}) = 4n_{10}(\pi / 2) \quad (4.12)$$

and,

$$\Delta\phi(\text{TE}_{01}) = 4n_{01}(\pi / 2) \quad (4.13)$$

The total phase shift through the overall structure shown in Figure 4.5 (a) is the summation of (4.8) and (4.12) for the  $\text{TE}_{10}$  mode while it is the summation of (4.8) and (4.13) for the  $\text{TE}_{01}$  mode. The resultant theoretical total phase shift of the structure is plotted in Figure 4.5 (b) and compared with the HFSS simulation results where an excellent agreement is achieved. It can be clearly deduced from this figure that the existence of cylindrical waveguide bends produces different phase shifts for the orthogonal  $\text{TE}_{10}$  and  $\text{TE}_{01}$  modes. This should be taken into consideration when designing the overall dually-polarized six-port junction. For example, at 30 GHz the phase shift between port 1 and port 2 is about  $-120^\circ$  for the  $\text{TE}_{10}$  mode while it is about  $-95^\circ$  for the  $\text{TE}_{01}$  mode.

This difference in the phase shift between the  $TE_{10}$  and  $TE_{01}$  modes means that the same bend could not produce the same required phase shift for both of the orthogonal modes which should be identical. This validated fact is discussed in details in the following section in order to design and implement the overall dually-polarized six-port junction that works identically for the  $TE_{10}$  and  $TE_{01}$  modes.

## 4.5 Dually-polarized six-port junction

The proposed application based on the dually-polarized six-port junction in this dissertation is polarization-inclusive remote sensing (PIRS) system as we entitle here. A block diagram of the proposed PIRS system is shown in Figure 4.6. In the traditional remote sensing systems, the transmitting antenna sends an electromagnetic signal with a specific polarization, and the receiving antenna collects the scattered radiation from the sensed physical object with a polarization that is aligned with the transmitted one [97]. Therefore, the information in the polarization perpendicular to the transmitted one is lost. In order to make use of the lost information, the receiving circuitry should be able to handle dual-polarizations simultaneously. This can be implemented using the proposed PIRS system that is mainly based on a dually-polarized six-port junction which signifies the main scope of this chapter.

The PIRS system in Figure 4.6 consists of a hybrid junction connected to an input source. The “through” port of this hybrid junction is connected to the transmitting antenna which transmits a vertically-polarized signal. The “coupled” port of the hybrid junction is connected to a T-junction splitter which generates two vertically-polarized signals with equal amplitudes. One of the outputs of the T-junction is connected to a polarization rotator to convert the vertical polarization into a horizontal polarization. This horizontally-polarized output along with the other vertically-polarized T-junction output are applied to an OMT which combines the orthogonal polarizations and delivers them to the dually-polarized six-port junction at port 1. On the other hand, the receiving antenna receives a dually-polarized signal that is scattered from the sensed physical object. This later signal is fed to the dually-polarized six-port junction at port 2. The output ports of the six-port junction are ports 3, 4, 5 and 6 where each of these ports holds a dually-polarized signal. Each output port is connected to an OMT in order to separate the orthogonal

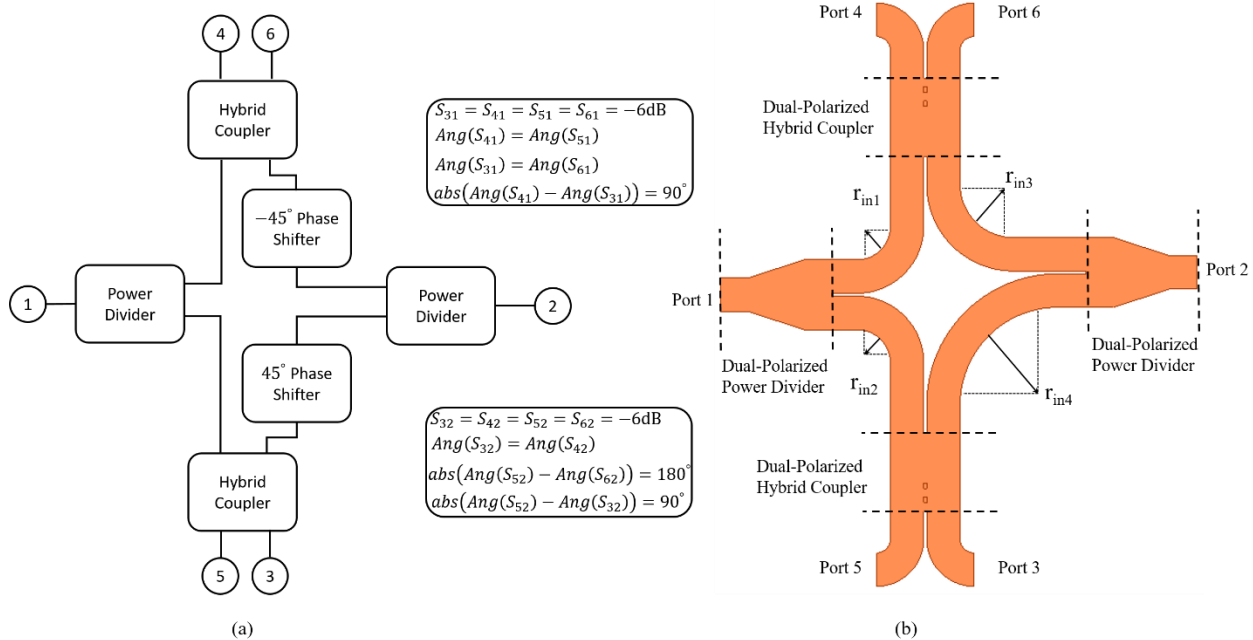


Figure 4.7. Dually-polarized six-port junction based on PSC: (a) block diagram with the ideal theoretical scattering parameters and (b) the overall equivalent structure.

polarizations. By magnitude only measurement of the output of those OMTs [98], the relation between the signals at port 1 and port 2 can be obtained for each polarization, independently. This gives the whole information needed from the scattered signal of the physical object. The full design of a dually-polarized six-port junction is introduced in details through this section.

The development of a dually-polarized six-port junction demonstrates the applicability of polarization diversity in practice because it contains different microwave components as building blocks [99]. This allows testing the dual-polarization feature in many microwave components based on the proposed PSC concept. The overall dual-polarized six-port junction structure is designed and implemented based on PSC. This is because of the importance of the six-port device in many microwave measurement applications [100]. This clearly appears in using the six-port junction for calibrating wireless receiver [101] and estimating the angle of arrival (AOA) of an electromagnetic beam [102]. Furthermore, many microwave components can be designed based on a six-port junction [103]. The contribution of this work is to design a dual-polarized six-port junction based on the mechanism of PSC.

The block diagram of an ideal six-port junction is shown in Figure 4.7 (a). It consists of two power dividers, two 3dB couplers, and two phase shifters. For enabling the dual-polarization feature, the dually-polarized power divider and the dually-polarized hybrid coupler presented in the previous sections are used as they are in implementing the dually-polarized six-port junction. The connections between the power dividers, hybrid couplers, and phase shifters are implemented by waveguides bends. The overall geometry of the implemented structure is presented in Figure 4.7 (b). The proposed dually-polarized six-port junction is similar to that is implemented in [99] for a single polarization. The main advantage is that adding the polarization selective walls to the structure in a deliberate way with the corresponding bend phase calculations allows the propagation of both polarizations together simultaneously.

The main idea for designing a dually-polarized six-port junction is highly related to the carious design for the connecting circulating cylindrical waveguide bends. It can be observed from Figure 4.7 (a) that the power divider which is connected to port 1 is connected directly by the same way to the identical hybrid couplers. Thus, in the design shown in Figure 4.7 (b), we should have  $r_{in1} = r_{in2}$ . Therefore, both of the bends produce the same phase shift. On the contrary, the power divider which is connected to port 2 is connected to the upper hybrid coupler through a  $-45^\circ$  phase shifter while it is connected to the lower hybrid coupler through a  $45^\circ$  phase shifter as appears in Figure 4.7 (a) as well. This  $90^\circ$  phase difference between both of the output of both phase shifters is implemented by designing two non-identical waveguide bends where  $r_{in3} \neq r_{in4}$  as it is clear from Figure 4.7 (b). The design of  $r_{in3}$  and  $r_{in4}$  is the most important part of designing a dually-polarized six-port junction in order to achieve the same required  $90^\circ$  phase shift for both of the  $TE_{10}$  and the  $TE_{01}$  modes.

It is already concluded from the previous section that the circulating bend generally introduces different phase shifts for both of the  $TE_{10}$  and  $TE_{01}$  modes. This occurs for relatively small radii of the circular bend. In another word, there is a critical minimum radius of the bend where it produces almost the same phase shifts for both of the  $TE_{10}$  and  $TE_{01}$  modes. The bend can be considered as dually-polarized if it has a radius larger than or equal to the critical minimum radius.

A trade-off between the bend size and the phase deviation between the  $TE_{10}$  and  $TE_{01}$  modes should be compromised. This can be figured out by plotting the difference between the phase shifts of the

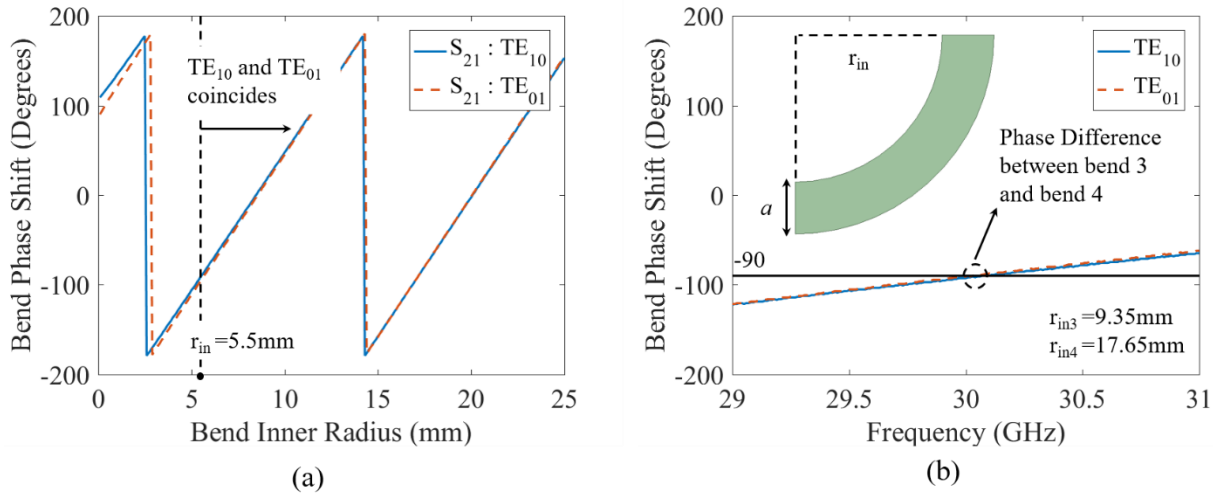


Figure 4.8. (a) Phase shift variation for the TE<sub>10</sub> and TE<sub>01</sub> modes due to a circular bend versus its inner radius and (b) phase difference variation between two circular bends versus frequency.

TE<sub>10</sub> and TE<sub>01</sub> modes as shown in Figure 4.8 (a). The phase shifts due to the TE<sub>10</sub> and the TE<sub>01</sub> modes are obtained using (4.12) and (4.13), respectively by replacing the factor of four with unity because it is a single bend. The bend inner radius is scanned by solving (4.10) and (4.11) for the TE<sub>10</sub> and TE<sub>01</sub> modes, respectively. A minimum of five degrees may be accepted as a deviation between both phase shifts. This starts to occur at  $r_{in} = 5.5$  mm. Therefore, this value is selected to be the design value of  $r_{in1}$  and  $r_{in2}$ .

Regarding the design of  $r_{in3}$  and  $r_{in4}$ , the phase shift due to the TE<sub>10</sub> (or the TE<sub>01</sub>) mode is demonstrated in Figure 4.8 (b) when the inner radius of the bend changes starting from the critical minimum radius. Two considerations should be taken into account when selecting the values of  $r_{in3}$  and  $r_{in4}$ . The first consideration is to maintain the required 90 degrees phase shift between both bends. The other consideration is to make sure that the overall connection of the six-port subcomponents is physically possible with the selected dimensions without affecting the phase shift resulting from other parts of the structure. The selected values of  $r_{in3}$  and  $r_{in4}$  which achieve these considerations are 9.35 mm and 17.65 mm, respectively. The overall structure of the dually-polarized six-port junction with the specified dimensions is implemented through HFSS simulation and prototyped.

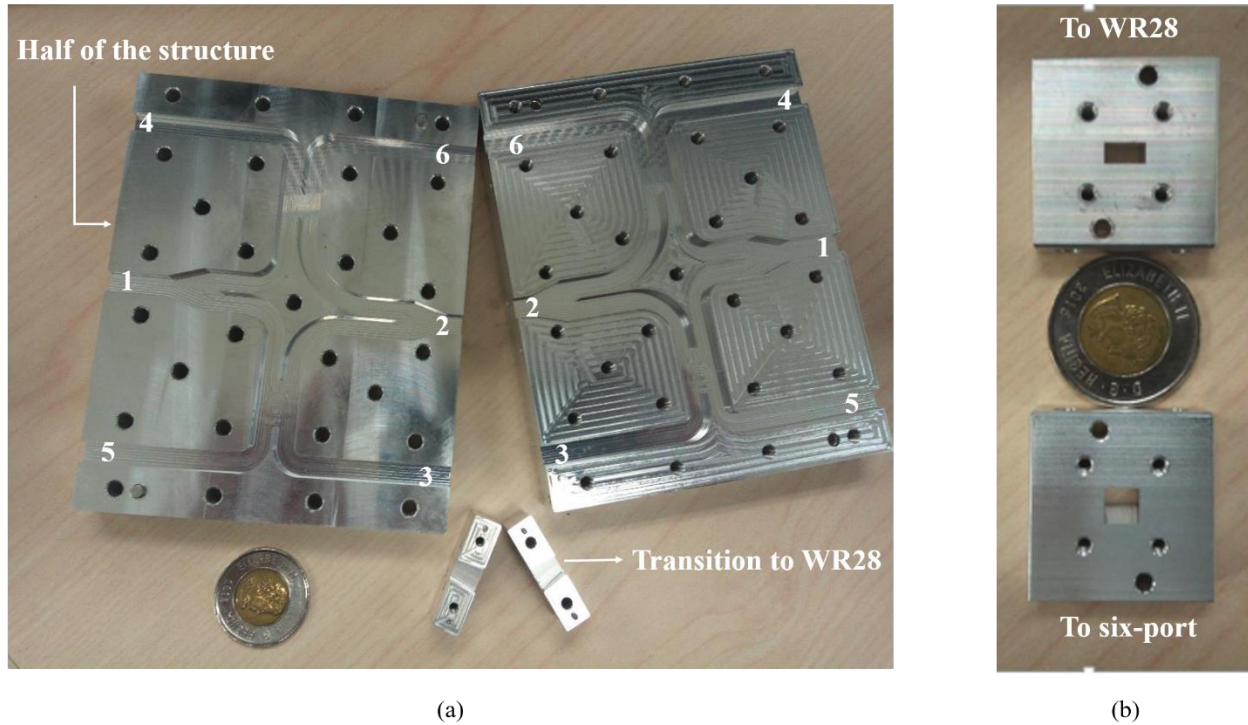


Figure 4.9. Prototype of a dual-polarized six-port junction based on PSC: (a) overall structure and (b) transition to WR28 waveguide.

The overall physical structure is presented in Figure 4.9 (a). A tapered matching transition with the length of 8 mm that is shown in Figure 4.9 (b) is implemented in order to match the proposed six-port junction to the WR28 standard waveguide. The simulated reflections due to the matching section are found to be below -30dB over the whole bandwidth. This transition can be rotated by  $90^\circ$  to suit the orientation of each polarization.

The resultant scattering parameters are shown in Figure 4.10. When exciting the structure from port 1 with the  $TE_{10}$  mode, it can be observed from Figure 4.10 (a) that the magnitude of the signal is divided approximately equal between port 3, port 4, port 5 and port 6 each with a 6dB transmission level while port 2 is isolated with isolation around 20dB and the reflections to port 1 is about 20dB. For the phase difference, it is clear from Figure 4.10 (e) that port 4 and port 5 have the same phase shifts with port 1. The same thing is for port 3 and port 6. This is in addition to a  $90^\circ$  phase difference between port 3 and port 5 or between port 4 and port 6.

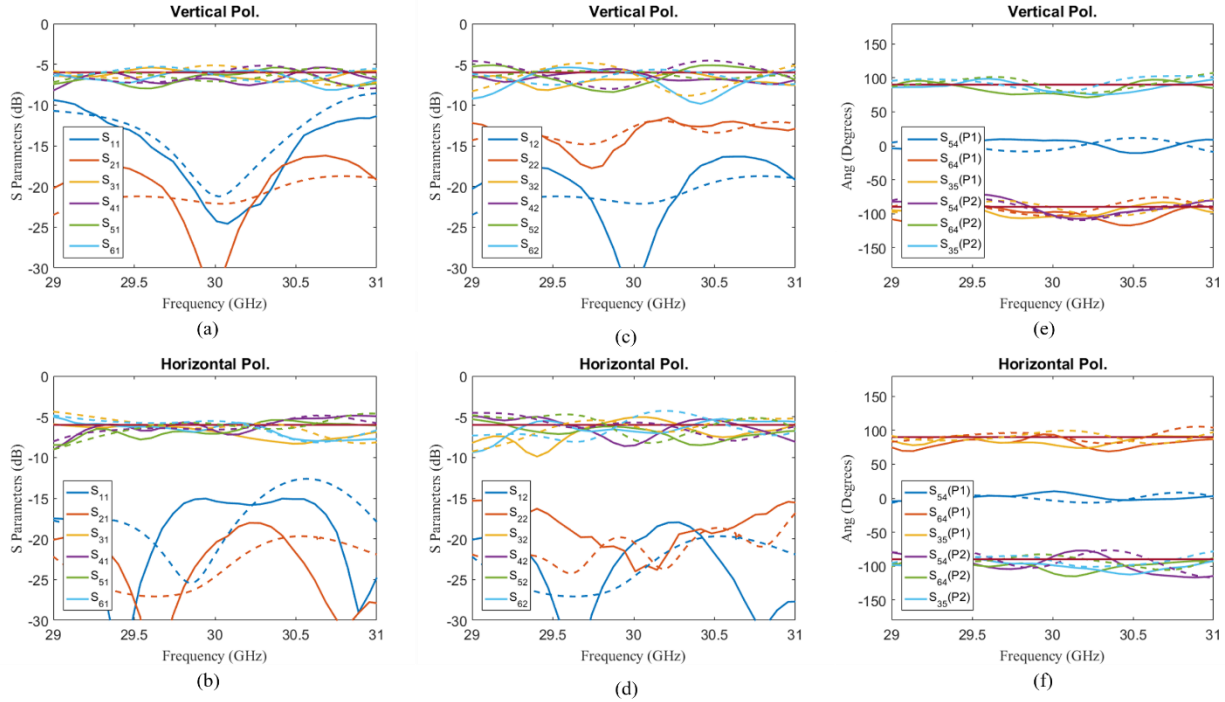


Figure 4.10. Scattering parameters of dually-polarized six-port junction, simulation is solid line while measurement is dotted line: (a) magnitude when exciting  $TE_{10}$  from port 1, (b) magnitude when exciting  $TE_{01}$  from port 1 (c) magnitude when exciting  $TE_{10}$  from port 2 (d) magnitude when exciting  $TE_{01}$  from port 2 (e) phase when exciting  $TE_{10}$  from port 1 and port 2, (f) phase when exciting  $TE_{01}$  from port 1 and port 2.

The same procedure can be traced to validate the whole function of the proposed dually-polarized six-port junction. Figure 4.10 (b) and Figure 4.10 (f) show the structure magnitude and phase response, respectively when it is excited from port 1 with the  $TE_{01}$  mode. On the other hand, Fig. 8(c) and Fig. 8(e) show the structure magnitude and phase response, respectively when it is excited from port 2 with the  $TE_{10}$  mode. Similarly, Figure 4.10 (d) and Figure 4.10 (f) show the structure magnitude and phase response, respectively when it is excited from port 2 with the  $TE_{01}$  mode. For all the presented results, a very good agreement is achieved between simulation and measurement.

In this section, a dually-polarized six-port junction is designed based on PSC. The PSC shows the possibility of holding two orthogonal modes through a planar waveguide structure. This PSC idea is used to design microwave components like a dually-polarized power divider and a dually-polarized hybrid coupler. Those components are used together along with cylindrical waveguide

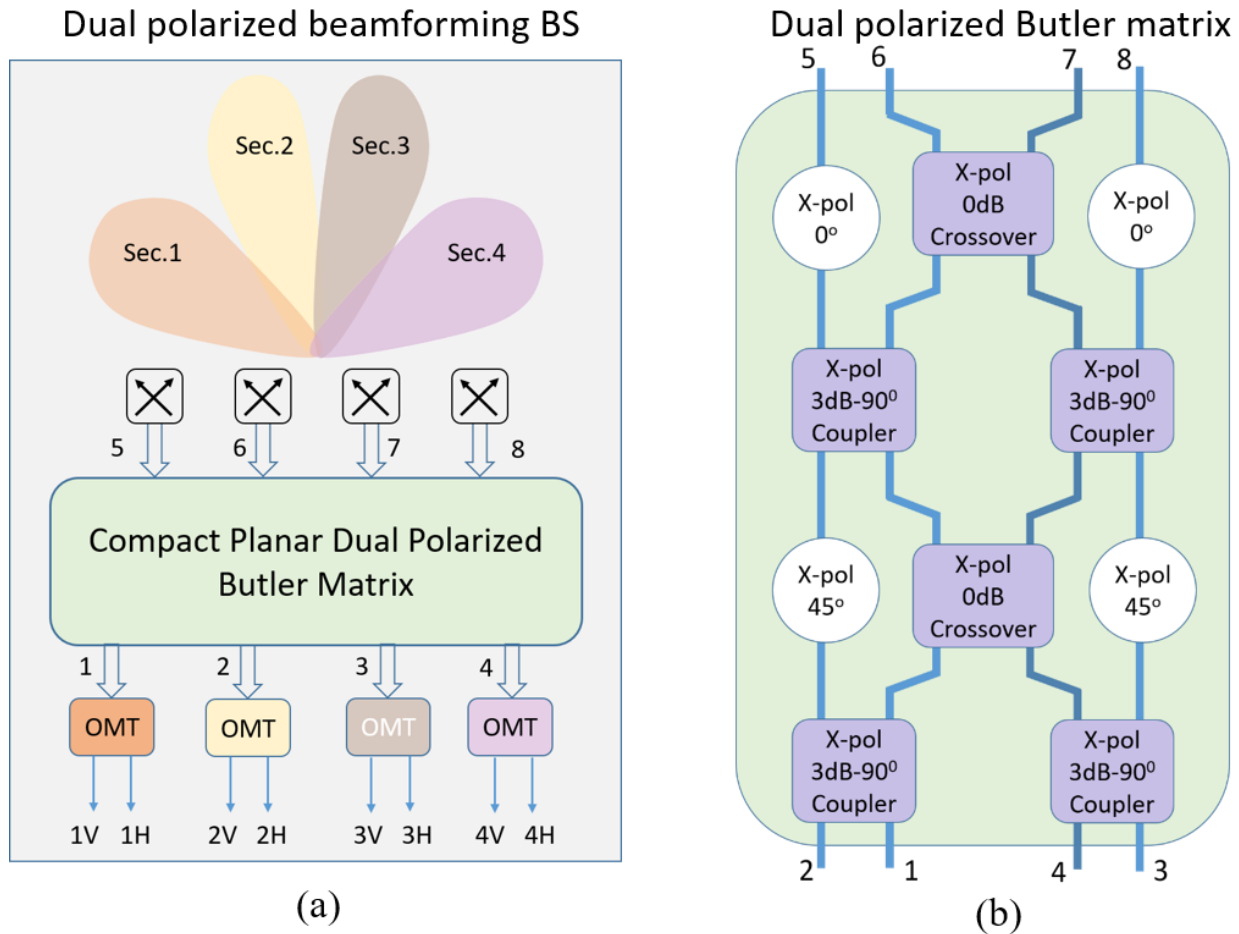


Figure 4.11. Dually-polarized Butler matrix, (a) Architecture of a base-station (BS) incorporating a dually-polarized 4-by-4 Butler matrix and (b) the structure of its internal components.

bends to implement the overall dually-polarized six-port junctions. The waveguide bends are used to support the required phase equalization for both of the orthogonal modes resulted due to the constituent components. The resulted overall dually-polarized six-port junction shows the complete function for both of the orthogonal  $TE_{10}$  and  $TE_{01}$  modes. The functionality is tested by a physical prototype where a very good agreement is achieved between simulation and measurement results.

#### 4.6 Operation principle of dually-polarized Butler matrix

The Butler matrix is named after J. Butler [104]. The standard definition of a Butler matrix is: "A network of 3dB hybrids that provides a passive combining/splitting function for coupling multiple

*radio-frequency (RF) inputs to multiple RF outputs*” [105]. This structure is an indispensable multiple-input-multiple-output device for wireless communication systems.

The function of this device is mainly to generate diverse beam pattern configurations. The operator is to switch between the input ports to get the required beam pattern. This feature is crucial for antenna feeding networks. In order to achieve this feature, a progressive phase shift should be created by the structure geometry at the output ports.

The idea of a switched beamforming was invented decades ago with many different variations. A comprehensive literature survey on the amount of research work reported which is related to switched beamforming, and especially to the Butler matrix, is far beyond the scope of this chapter. However, a brief survey results in the following conclusion. The Butler matrix implementation is still an active topic of research. The most recent work found is on the enhancement of the beam controllability using one bit digitally controlled phase shifter [106]. The oldest work dates back to the late fifties of the twentieth century, such as the Blass matrix reported in [107]. The idea was well established, and even systematic design approaches were developed such as the design methodology by Moody, reported in [108]. The main variations of such beamforming networks result from different building block implementations of 3dB hybrids, 0dB cross-overs and the phase shifters which constitute those networks. For example, most of the reported Butler matrices are implemented in microstrip technology due to the ease of fabrication and integration [109], [110]. Another implementation which is based on multilayer CPW components is reported in [111]. Implementations based on the SIW technology are reported in [112], [113].

Previously, this function is designed specifically for single polarization signals. The novelty of this work is to implement our greening idea on the Butler matrix device. In other words, both of the vertically and horizontally oriented polarizations are handled simultaneously and independently by the same structure to produce the required beamforming. This possibility enables the designers to deploy cross-polarized antennas instead of single-polarized ones in the feeding networks. This enhances the system efficiency and capability as stated in chapter 1.

Our dually-polarized 4x4 Butler matrix feeding network block diagram is shown in Figure 4.11 (a). In this structure, four cross-polarized antennas are feeding the structure. On the other hand, the output is received through four orthomode transducers (OMTs). The function of these OMTs is to separate between the vertically and horizontally-oriented field components.

The dual-polarization mechanism is not maintained only by using cross-polarized antennas instead of single-polarized ones, but the Butler matrix itself must have the capability of treating both polarization equally and independently. This allows the ability to transmit and receive waves of any arbitrary type of polarization. The dually-polarized Butler matrix block diagram is shown in Figure 4.11 (b). It consists of 3 dB couplers, 0 dB crossover couplers, and phase shifters. Each component of them can handle dual-polarizations simultaneously. This function is explained extensively in the following sections.

#### 4.6.1 Dually-polarized couplers with dual-phase-shifts

In this section, the principle of operation of dually-polarized couplers whose coupling ratio is controlled independently for each polarization is revisited from another perspective. The proposed dually-polarized coupler consists of two identical waveguides placed side by side. One common wall between the two waveguides is removed for a certain length. The length of this open section determines the coupling level between the two waveguides.

This type of couplers can be found in the literature in various forms. However, the forms which are mostly related to the proposed coupler are the Riblet coupler [93], [114] and the Rosenberg coupler [77]. The Riblet coupler is also called short-slot coupler and is defined as two rectangular waveguides placed side-by-side. Side-by-side means that the common wall is the wall with the shortest dimension of the rectangular cross-section. Hence, the name short-slot coupler. The coupling modes are the  $TE_{10}$  and  $TE_{20}$  modes which appear in the area where the two waveguides are fused together and compose a wider waveguide. The Rosenberg coupler is also called top-wall coupler or modified Hodge coupler [91]. It consists of two rectangular waveguides placed on top of each other. Removing the common top-wall gives it the name top-wall coupler. The coupling modes are the  $TE_{01}$  and  $TE_{11}/TM_{11}$  modes.

Based on those definitions, we can also define the proposed dually-polarized coupler as in the following: Two square waveguides placed side-by-side, or on top of each other; this does not make any difference since they are both square. The input/output square waveguides support two orthogonal polarizations, namely the  $TE_{10}$  and  $TE_{01}$  modes. Depending on the excited mode in the input port, it acts as either a Riblet or Rosenberg junction. The proposed coupler acts as a Riblet junction for the polarization tangential to the common wall, while the same structure acts as a Rosenberg junction for the polarization perpendicular to the common wall.



becomes functional over the length which is not covered by the periodic PEC wall. Whereas the Rosenberg mechanism is functional over the whole common length unaffected by the presence of the periodic PEC wall. The detailed analysis is shown in the following subsection.

#### 4.6.1.1 Analysis and Design of Dually-Polarized 3dB Coupler

The proposed coupling junction is shown in Figure 4.12. It consists of two square waveguides with dimensions,  $a \times b$  where  $a \approx b$ . The two waveguides are placed side-by-side separated by a distance  $g$ , where  $g$  is the diameter of the metallic pins used to realize the periodic PEC wall. This diameter could be infinitesimally small, limited only by the processing technology used to fabricate it. An even-odd mode analysis can be applied to derive the S-parameters as [72]:

$$S_{21} = S_{43} = \exp\left(-j \frac{(\beta_e + \beta_o)l}{2}\right) \cos\left(\frac{(\beta_e - \beta_o)l}{2}\right) \quad (4.14)$$

$$S_{31} = S_{42} = -j \exp\left(-j \frac{(\beta_e + \beta_o)l}{2}\right) \sin\left(\frac{(\beta_e - \beta_o)l}{2}\right) \quad (4.15)$$

$$S_{41} = S_{32} = 0 \quad (4.16)$$

where  $j = \sqrt{-1}$ ,  $\beta_e$  and  $\beta_o$  are defined differently for each excited mode. The central area of the device is the area where the two waveguides are fused together to form one waveguide as shown in Figure 4.12. This central area can be seen as a rectangular waveguide of dimensions  $(2a + s) \times b$ , where  $s = g/2$  is the separation distance between the two waveguides as shown in Figure 4.12. The dispersion curves of different modes that can be generated in this central area can be calculated according to:

$$\beta_{mn} = \frac{\omega}{c} \sqrt{1 - \left(\frac{f_{c_{mn}}}{f}\right)^2} \quad (4.17)$$

where  $\omega = 2\pi f$ ,  $f$  is the operating frequency,  $c$  is the speed of light in free space and

$$f_{c_{mn}} = \frac{c}{2} \sqrt{\left(\frac{m}{2a + s}\right)^2 + \left(\frac{n}{b}\right)^2} \quad (4.18)$$

When the input port is excited with the vertically oriented  $TE_{10}$  mode, the even and odd modes in the central area become the  $TE_{10}^{2a+s}$  and  $TE_{20}^{2a+s}$ , respectively (the super-script  $2a + s$  is to differentiate those modes from those of the exciting waveguides). The excited modes in the

common area can easily be verified by applying the boundary conditions at the input port. In the other case, where the input port is excited with the horizontally oriented TE<sub>01</sub> mode, the even and odd modes in the central area become the TE<sub>01</sub><sup>2a+s</sup> and the TE<sub>11</sub><sup>2a+s</sup> / TM<sub>11</sub><sup>2a+s</sup> modes respectively.

Given this concept, it is only the length of this central area where the common wall between the two identical waveguides is removed which determines the coupling level from the excited waveguide to the other one. Therefore, the design of a 3dB quadrature coupler follows directly from (4.15), where

$$\text{at } l = L_c^{3dB} : S_{21} = S_{31} = \sqrt{0.5} \Rightarrow L_c^{3dB} = \frac{\pi}{2(\beta_e - \beta_0)} \quad (4.19)$$

$$\text{and at } l = L_c^{3dB} : \frac{S_{31}}{S_{21}} = -j \quad (4.20)$$

However, since the vertically oriented even and odd modes are different from those for the horizontal polarization, the coupling lengths for both cases are different, where

$$L_{cV}^{3dB} = \frac{\pi}{2(\beta_{10} - \beta_{20})} \neq L_{cH}^{3dB} = \frac{\pi}{2(\beta_{01} - \beta_{11})} \quad (4.21)$$

From the physics viewpoint of the problem, one can note that the following condition is always satisfied.

$$L_{cV}^{3dB} < L_{cH}^{3dB} \quad (4.22)$$

The idea proposed here is to realize the dually polarized coupler by dividing the length  $L_{cH}^{3dB}$  into two parts. The first part is equal to  $L_{cV}^{3dB}$  and the other part of the length  $L_{cH}^{3dB} - L_{cV}^{3dB}$ . In the later part, the separation between the two waveguides is realized by periodic metallic vertical pins as shown in Figure 4.12. As a polarizer, this periodic PEC wall is transparent for the horizontally polarized modes, while it acts as solid PEC wall for the vertically oriented modes whose electric field is tangential to the pins. This is true given that the separation between the pins is small enough compared to the operating wavelength.

As a design example, consider  $a = b = 3.2$  mm and  $g = 0.85$ mm at an operating center frequency of  $f_o = 60$  GHz. The dispersion curves of the central coupler part are shown in Figure 4.13 (a).

The structure is built on a CAD model and simulated using full wave simulator (HFSS).

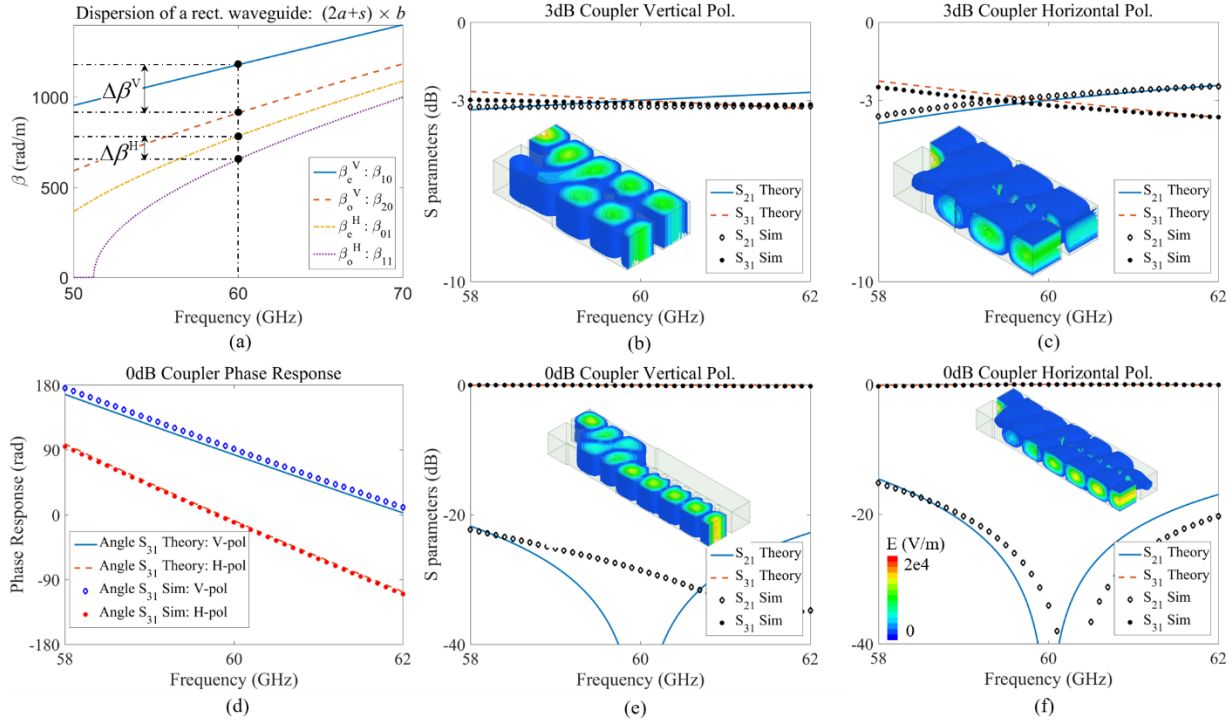


Figure 4.13. Design of dually-polarized couplers, (a) dispersion curves of the common waveguide section, (b) S-parameters and field distribution of the vertically-polarized mode in a 3dB-coupler, (c) S-parameters and field distribution of the horizontally-polarized mode in a 3dB-coupler, (d) phase response of the 0dB coupler for the two polarizations, (e) S-parameters and field distribution of the vertically-polarized mode in a 0dB-coupler and (f) S-parameters and field distribution of the horizontally-polarized mode in a 0dB-coupler.

The coupling lengths, in this case, are calculated based on the numerical values shown in Figure 4.13 (a) and are found to be  $L_{cV}^{3dB} = 5.05\text{mm}$  and  $L_{cH}^{3dB} = 10.6\text{mm}$ . The physical structure is shown in Figure 4.12, where the periodic wall is realized with three circular pins of diameter  $g = 0.85\text{mm}$  and period  $p = 1\text{mm}$  covering a length of  $L_{cH}^{3dB} - L_{cV}^{3dB} = 3 \times 1.85\text{mm}$ . In Figure 4.13 a comparison is shown in the theoretical analysis and the full wave simulation for both polarizations. The comparison shows a nearly perfect agreement with an error less than 1dB. The field distribution is also inset in Figure 4.13 (b) and (c) for the vertical and horizontal polarizations, respectively. The phase difference between the two output ports in the case of the 3dB couplers is always 90 degrees regardless of the frequency as can be deduced from (4.14) and (4.15).

#### 4.6.1.2 Analysis and design of dually-polarized 0dB coupler

The design of a zero-dB coupler (cross over junction) is identical to the 3dB coupler except for the coupling lengths which can be calculated as:

$$\text{at } l = L_c^{0dB} : S_{21} = 0 \text{ and } S_{31} = 1 \Rightarrow L_c^{0dB} = \frac{\pi}{\beta_e - \beta_o} \quad (4.23)$$

Since the output here is delivered totally at only one port, therefore the phase response must be measured relative to the input port. This phase response is given by:

$$\text{at } l = L_c^{0dB} : \angle S_{31} = -\pi \frac{\beta_e}{\beta_e - \beta_o} \quad (4.24)$$

Equation (4.24) becomes very crucial in the design of a Butler matrix as will be shown later. Since the vertically oriented even and odd modes are different from those for the horizontal polarization, the coupling lengths for both cases are different, where

$$L_{cV}^{0dB} = \frac{\pi}{\beta_{10} - \beta_{20}} \neq L_{cH}^{0dB} = \frac{\pi}{\beta_{01} - \beta_{11}} \quad (4.25)$$

Similarly, one can note that the following condition is always satisfied.

$$L_{cV}^{0dB} < L_{cH}^{0dB} \quad (4.26)$$

Thus, the dually polarized 0dB cross over coupler can be physically realized by the integration of a periodic wall of metallic pins of length  $L_{cH}^{0dB} - L_{cV}^{0dB}$ .

As a numerical example, let's consider the same dimensions mentioned in Sec. 4.6.1.1. The numerical values are shown in Figure 4.13 (a) at 60 GHz are substituted in (4.25) to obtain  $L_{cV}^{0dB} = 10.1\text{mm}$  and  $L_{cH}^{0dB} = 21.2\text{mm}$ . By definition, those values are twice the values obtained for the 3dB couplers. The physical structure of the 0dB coupler is identical to the one shown in Figure 4.12, except for the periodic wall which is realized with seven circular pins instead of the three used in the case of the 3dB coupler. It should be noted that six pins with a diameter  $g = 0.85\text{mm}$  and period  $p = 1\text{mm}$  are sufficient to cover a length of  $L_{cH}^{0dB} - L_{cV}^{0dB} = 6 \times 1.85\text{mm}$ . However, since the diameter of the pins is not infinitesimally small, in fact, it is about one-sixth of a wavelength at 60 GHz, therefore, the presence of the pins along the length  $L_{cH}^{0dB} - L_{cV}^{0dB}$  makes it slightly less than the

length sufficient for a full coupling of the horizontal polarization. To compensate for this effect, seven pins are used instead of six.

In Figure 4.13, a comparison is shown between the theoretical analysis and the full-wave simulation for both polarizations. The comparison also shows an excellent agreement with an error less than 1dB. The field distribution is also inset in Figure 4.13 (e) and Figure 4.13 (f) for both vertical and horizontal polarizations, respectively. The phase response between the input and output ports in the case of the 0dB coupler is plotted versus frequency and compared to the theoretical value given by (4.24). An excellent agreement within few degrees is achieved.

It is worth noting from Figure 4.12 that the common section where the coupling of the vertical polarization occurs is slightly narrower than the width of the section where the coupling of the horizontal polarization only occurs. This is to compensate for the existence of the metallic pins in the later section. The effect of parameters  $L_m^V$  and  $s$  is observed only in the isolation and matching ( $S_{11}$  and  $S_{41}$ ) of the coupler. In the original Riblet coupler [93], there is a hemispherical dome-shaped piece of conductor placed on the common bottom wall of the coupler. This capacitive dome is not implemented here to avoid a cross-coupling between the vertical and horizontal polarizations. Instead, the matching and isolation are then optimized by a proper choice of the two parameters  $L_m^V$  and  $s$  as illustrated in Figure 4.12. A similar idea was implemented in [114]. This applies to the two cases of the 3dB and 0dB couplers.

## 4.6.2 Dually-Polarized Phase Shifter

The phase shifter is a crucial component in many applications and especially in beamforming applications. The Butler matrix geometry prevents utilizing the phase shifter bend presented in Sec. 4.4. A simple but very reliable phase shifter is the one which depends on altering the dimensions of the waveguide. This is a waveguide with practically zero insertion loss but with a designed phase response that is achieved by changing the cross-sectional dimensions of the waveguide which affect the phase constant in the longitudinal direction.

Assume a rectangular waveguide with only the dominant  $TE_{10}$  mode propagating. The phase constant  $\beta_{10}$  depends only on the width of the guide. Altering this width by slightly tightening the cross-section of the guide (or enlarging it) for a certain length changes the phase shift produced by

this altered section as compared to a waveguide with the same length but with a uniform cross-section.

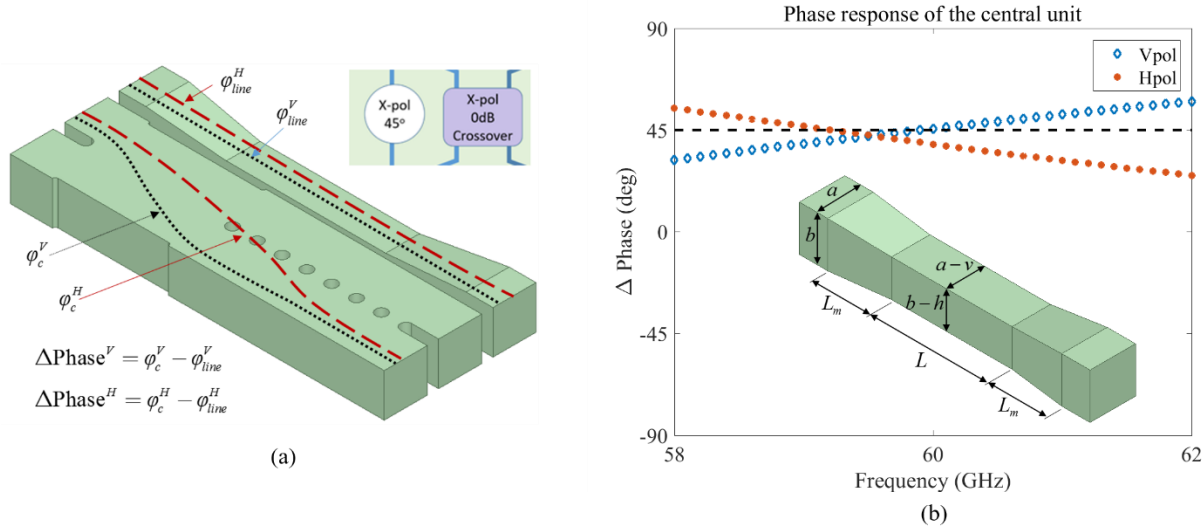


Figure 4.14. Dually-polarized phase shifter, (a) block diagram and principle of operation, (b) detailed geometry of phase shifter and full-wave simulation results for the whole unit.

It can be noted that the phase constant of the  $\text{TE}_{10}$  mode of a rectangular waveguide depends only on the width,  $a$ , whereas the phase constant of the  $\text{TE}_{01}$  mode depends only on the height of the guide,  $b$ . Therefore, in the central area of the structure shown in the inset of Figure 4.14 (b), the phase constant of the two orthogonal modes can be written explicitly as

$$\beta_{10} = \frac{\omega}{c} \sqrt{1 - \left( \frac{c/2(a-v)}{f} \right)^2} \quad (4.27)$$

and

$$\beta_{01} = \frac{\omega}{c} \sqrt{1 - \left( \frac{c/2(b-h)}{f} \right)^2} \quad (4.28)$$

where  $v$  and  $h$  are the design parameters used to control the phase shifts of the orthogonal polarizations, independently.

To keep the insertion loss as minimum as possible, the alteration of the cross-sectional dimensions should be made gradually by tapering the cross section from  $a$  to  $a-v$  and from  $b$  to  $b-h$ . Although it is hard to find an analytical solution for the phase shift in the tapered waveguide, it is

very easy to create a calibration curve for the whole structure to obtain the achieved phase shift versus the amount of alteration.

The dually-polarized phase shifter in a Butler matrix is required to produce a certain phase shift, say 45 degrees, as compared to the phase shift experienced by the wave in the central cross-over unit.

This is illustrated in Figure 4.14 (a), where the dotted lines represent the path of the vertically-polarized mode, and the dashed lines represent the path of the horizontally-polarized modes. The dotted curved path produces a phase shift given from (4.25) by:

$$\varphi_c^V = -\pi \frac{\beta_{10}}{\beta_{10} - \beta_{20}} - \beta_{10} (L_{cH}^{0dB} - L_{cV}^{0dB}) \quad (4.29)$$

Whereas the dashed curved path produces a phase shift which can also be found from (4.25) as:

$$\varphi_c^H = -\pi \frac{\beta_{01}}{\beta_{01} - \beta_{11}} \quad (4.30)$$

where  $\beta_{mn}$  in (4.29) and (4.30) represent the phase constant of the mode of order  $m, n$  in the common waveguide section.

If the required phase difference is  $45^\circ$ , then the two parameters  $v$  and  $h$  can be tweaked until this required value is obtained independently for the two orthogonal polarizations. Assume  $a = b = 3.2$  mm at operating frequency  $f = 60$  GHz. The tapered waveguide has a length  $L_m = 6$ mm and the central phase shifter part has a length  $L = 11.9$ mm. The results of full wave analysis for this example is shown in Figure 4.14 (b). To get these results, one has to perform a full wave simulation for the structure shown in the inset of Figure 4.14 (b). Then, one should do a parametric sweep on the parameters  $v$  and  $h$ , and then create a phase calibration curve for the structure. Use this calibration curve along with the phase response shown in Figure 4.13 (d) to obtain the required value of  $\Delta\text{Phase}$ . Following this procedure, it is found that to achieve  $\Delta\text{Phase}^V = \Delta\text{Phase}^H = 45^\circ$ , the parameters  $v$  and  $h$  should take the values of 0.11 and -0.15 mm, respectively. The negative sign means that the phase shifter central part is wider than the main waveguide section by the designated value.

Since the rate of change of the phase constant with respect to frequency in (4.27) and (4.28) is different from the rate of change deduced from (4.25), the required value of  $\Delta\text{Phase}$  cannot be

achieved except at one single frequency as shown in Figure 4.14 (b). It is still possible to get the required value of  $\Delta\text{Phase}$  for both polarizations at the same operating frequency.

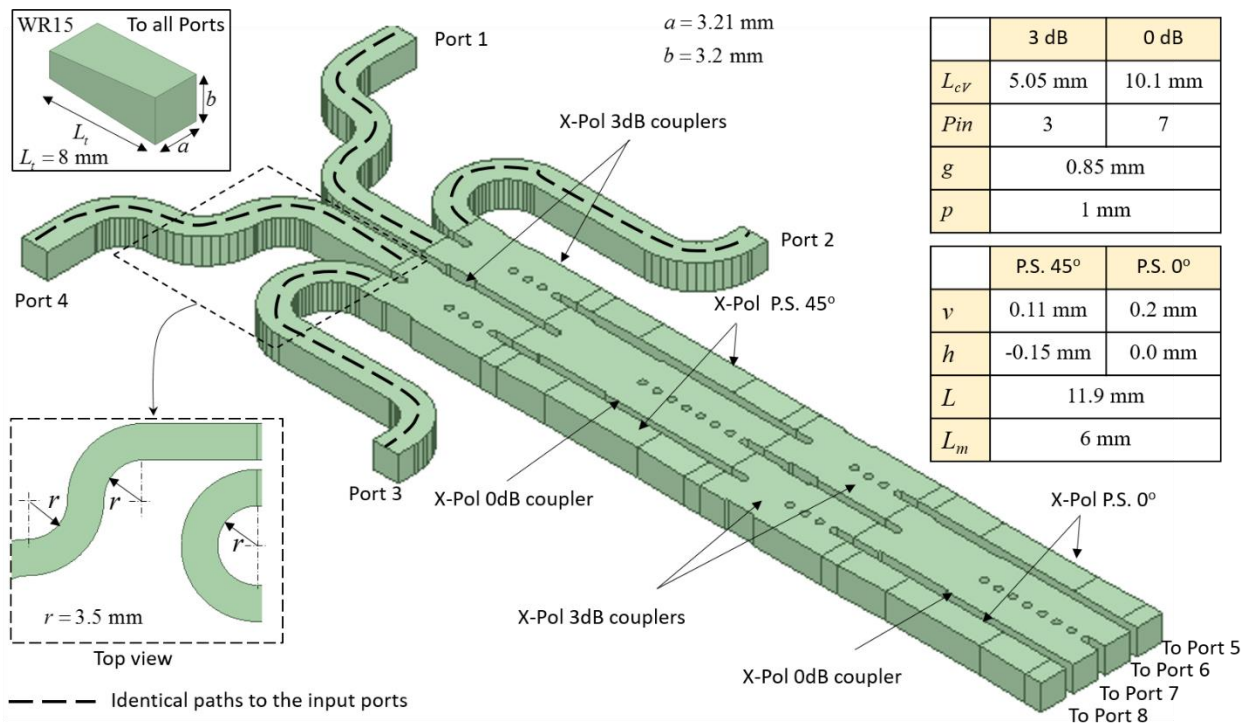


Figure 4.15. The complete assembly of the dually-polarized Butler matrix with detailed tabulated dimensions of each component. Ports 5 to 8 can be connected directly to the radiating cross-polarized antennas. In the prototype shown in the next section, those ports are connected to a mirrored image of the four curved paths connected at the input ports 1 to 4. All ports are connected to WR-15 transitions via the matching section shown in the top left corner. The width,  $a=3.21\text{mm}$ , is made slightly larger than  $b=3.2\text{mm}$  to be able to differentiate between the modes numerically.

However, as frequency shifts from the design value, the achieved phase shift changes with different rates for each polarization. This is the main limitation on the bandwidth of the Butler matrix shown in the following section.

### 4.6.3 The Complete Dually Polarized Butler Matrix

In this section, the design procedure for a complete dual polarized Butler matrix is presented and evaluated. A 2x2 dual polarized Butler matrix is simply a dual polarized hybrid 3B coupler

presented in Sec. 4.3 and Sec. 4.6.1. As the number of input and output ports increases, the design gets more and more complicated, because more elements are required. A 4-by-4 Butler matrix, as the one shown in Figure 4.11, consists of four hybrid 3dB couplers, two 0dB couplers (crossover) and four phase shifters. The main objective of this design is the adjustment of the phase response to get the required progressive phase shifts at the output ports which should be feeding the antennas.

Consider the Butler matrix in the transmitting case. Let's assume that the four input ports are ports 1-4 and the output ports are 5-8. The ideal response of the Butler matrix is to divide the magnitude of the power fed at one of the input ports equally among the output ports. This should correspond to -6dB insertion loss between any two input and output ports. The required phase response is achieved by the hierarchy shown in Figure 4.11 (b).

First, each individual component must be designed individually. The four required 3dB couplers are identical. Let's assume the operating frequency is 60 GHz. The analytical design procedure shown in Sec. 4.6.1.1 is repeated to obtain the required dimensions. Then, the four couplers are placed as shown in Figure 4.15. Similarly, the two required 0dB couplers are identical, and the same design procedure explained in Sec. 4.6.1.2 is repeated to obtain the required dimensions. Then, the two 0dB couplers are placed as shown in Figure 4.15. For the phase shifters, two of them must be identical satisfying a  $\Delta\text{Phase}$  value of  $45^\circ$  and the other two must be identical and satisfying a  $\Delta\text{Phase}$  value of  $360^\circ$ . Thus, the design procedure explained in Sec. 4.6.2 must be repeated twice to obtain the dimensions for the two required designs. Then, the four phase shifters are placed as shown in Figure 4.15. The inset table in Figure 4.15 shows all the design dimensions.

The final design step is to design the waveguides which will carry the input power to the four input ports. The standard waveguide to coaxial transition WR15 of dimensions  $3.76 \times 1.88$  mm is suitable for the chosen operating frequency of 60 GHz. A tapered matching section with a length  $L_t = 8\text{mm}$  is designed to convert the square cross-section of the design to the WR15 dimensions. By rotating those transitions, the required polarization can be excited and/or measured.

Due to the physical size of the standard WR15, the four input ports must be physically separated by enough distance to enable the physical connection of the input source to each individual port. As shown in Figure 4.15, this separation is achieved by bending the waveguides to the input ports in different directions. The radius of the bends is designed to minimize the reflections and is chosen to be 3.5mm. Each path from the input source to the input port encounters four circular bends each

with a sectorial angle of  $90^\circ$ . It is important to keep the length of all curved paths labeled by the thick dashed lines in Figure 4.15 identical.

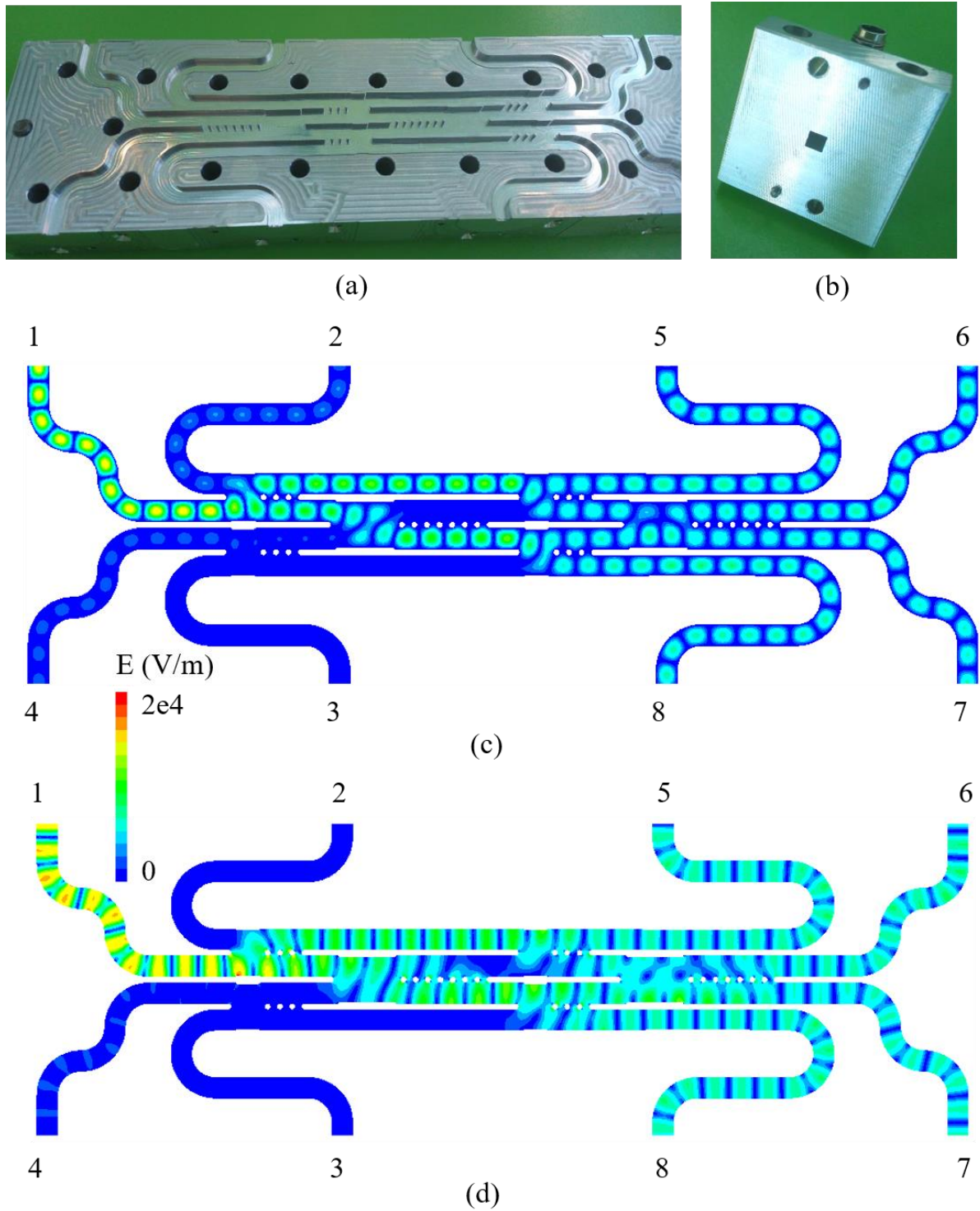


Figure 4.16. The complete prototype of the proposed dually-polarized Butler matrix, (a) Aluminum block with the waveguide cavities engraved into it, (b) A transition from square waveguide to the standard WR15 transition, (c) Field distribution for the vertical polarization calculated on HFSS at 60 GHz and (d) horizontal polarization.

The output ports should be connected to the antennas as shown in Figure 4.11 (a). At this band of frequency, the radiating elements could be simply open apertures of the square waveguide at ports 5-8. However, in order to examine the functionality of the designed Butler matrix separately, the four output ports are connected to a mirrored image of the four curved paths connected at ports 1-4. In this case, it is possible to measure the scattering parameters of the Butler matrix on a VNA without including the effect of the radiating elements.

The complete assembly of the Butler matrix is realized by CNC machining of an Aluminum block of overall dimensions  $150 \times 50$  mm in our Poly-Grames Research Center. The prototype is shown in the picture of Figure 4.16 (a). The transition from the square waveguide to WR15 to coaxial is shown in Figure 4.16 (b). This separate transition can be oriented freely to excite any of the two required polarizations.

From our full-wave analysis, the electric field distribution on the structure when port 1 is excited with vertical and horizontal polarizations is shown in Figure 4.16 (c) and (d), respectively. The color-map scale is chosen to cover a 20 dB range from maximum to minimum. Accordingly, one can notice that the isolation between port 1 and the other input ports is around 20dB. The isolation between the input ports for the vertical mode is slightly worse than that of the horizontal mode. The reason for that being that for the  $TE_{10}$  mode, it is the guiding walls that are being opened to form the coupling section, while for the  $TE_{01}$  mode, the guiding walls are the top and bottom walls and they are at fixed height all over the structure. This is actually one of the most important advantages of the proposed design which is being completely planar, and the machining is only in one plane. This is true except for the phase shifter for the horizontal polarization which needs machining in the vertical plane. However, there is a solution for this problem which can be done by separating the two polarizations and feeding them into two different waveguide bends and then combine them one more time. This solution, however, increases the overall dimension of the network. This enables the full integration of such a design with other circuitry on printed boards if required.

The performance is measured for all other ports and shown as magnitude and phase of S-parameters plotted in Figure 4.17 and Figure 4.18, respectively. The magnitude response shown in Figure 4.17 is measured in a sequential manner using two-port VNA measurements.

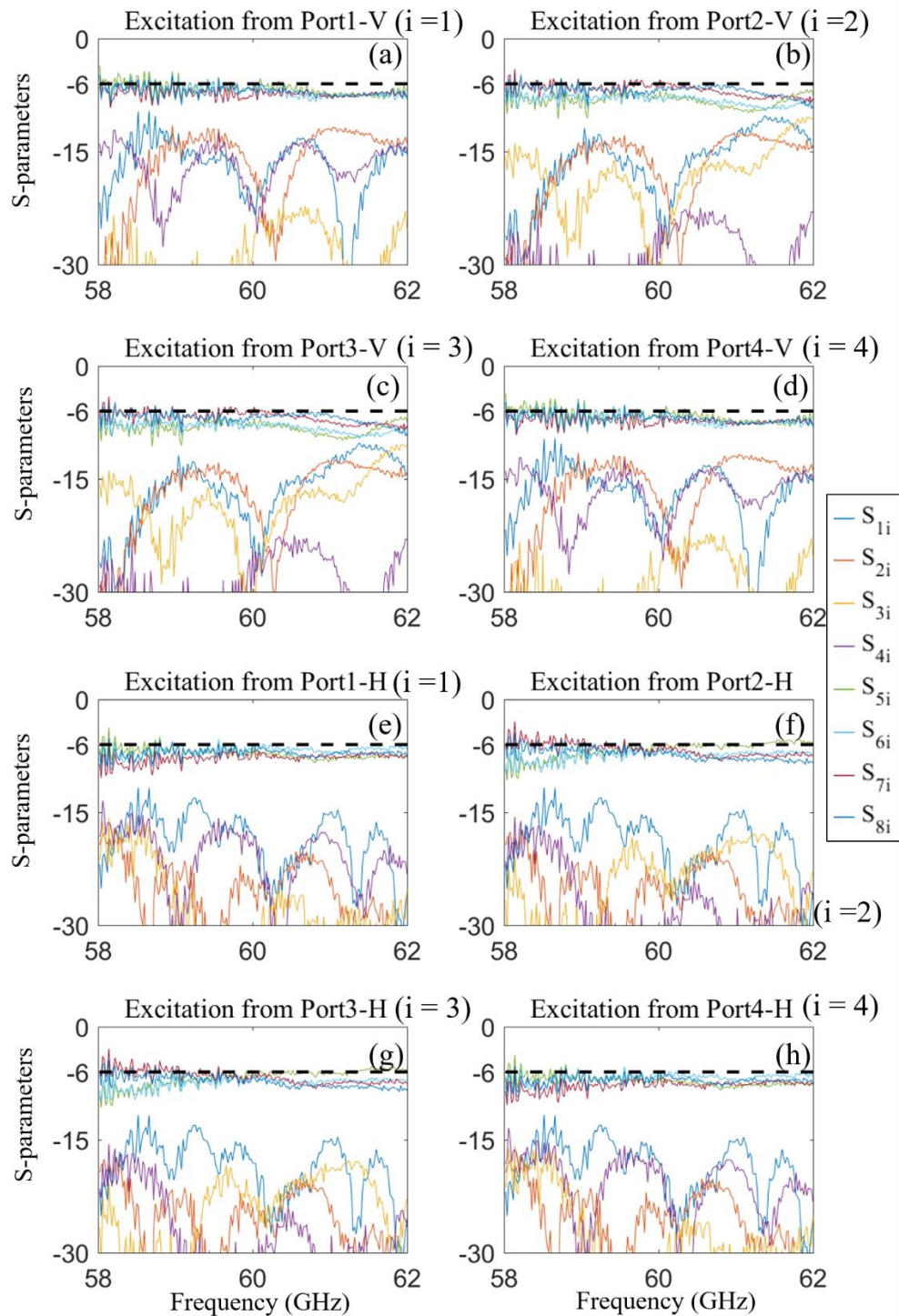


Figure 4.17. Measurement results of the prototype using Agilent vector network analyzer PNA-X from 58 to 62 GHz. The network is excited sequentially by vertical polarization at (a) port 1, (b) port 2, (c) port 3, and (d) port 4 and by horizontal polarization at (e) port 1, (f) port 2, (g) port 3 and (h) port 4. The dashed lines represent the theoretical result to be achieved.

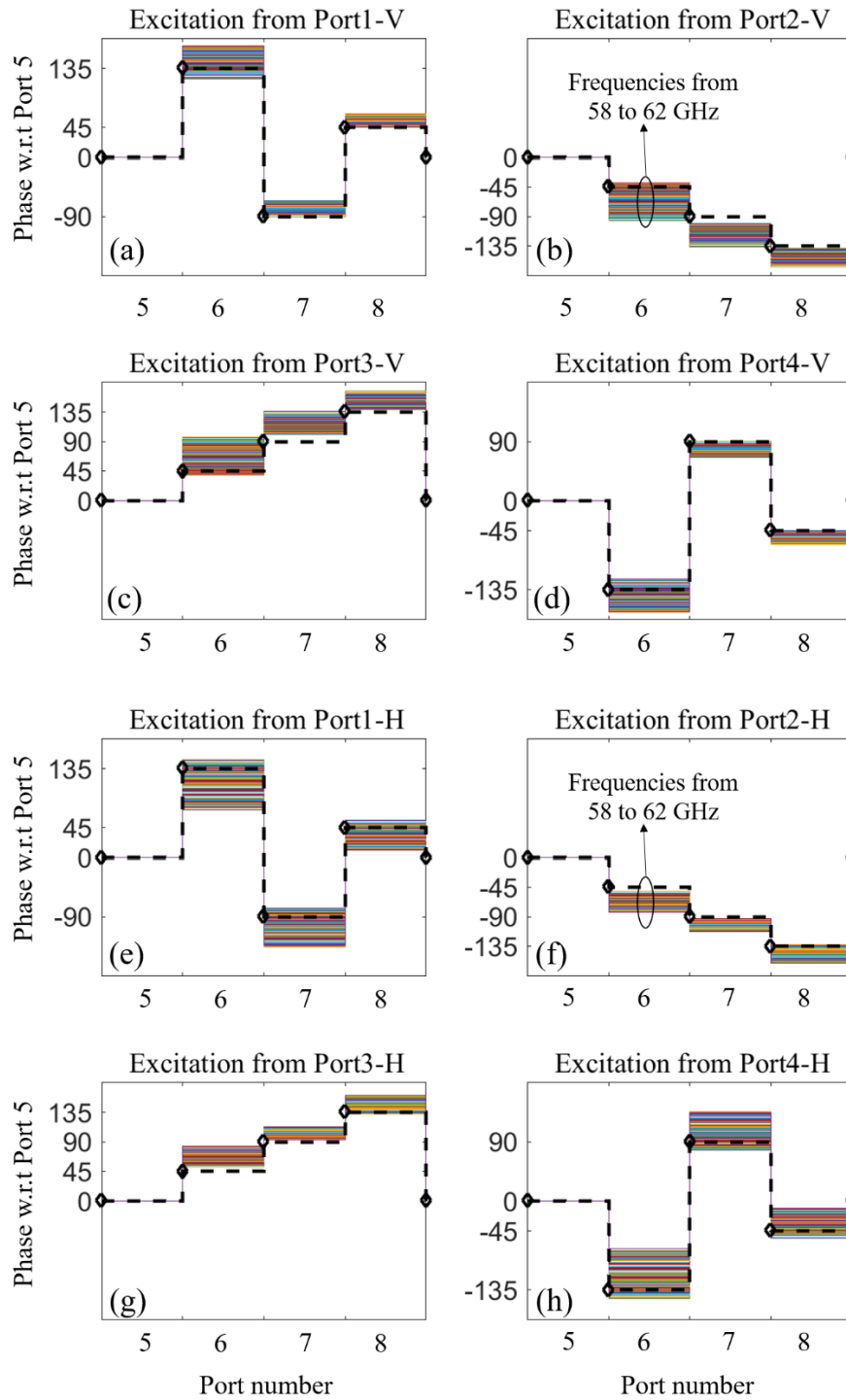


Figure 4.18. Progressive phase shift between the output ports of the dually polarized Butler matrix when excited sequentially by vertical polarization at (a) port 1, (b) port 2, (c) port 3, (d) port 4, and by horizontal polarization at (e) port 1, (f) port 2, (g) port 3 and (h) port 4. The dashed lines represent the theoretical result to be achieved.

First, Port 1 is excited with vertical polarization, and the output at each port is measured sequentially with the transition oriented in the vertical position. The results,  $S_{11}$  to  $S_{81}$ , are shown in dB in Figure 4.17 (a). Second, port 2 is excited, and the same procedure is repeated. The results when port 2 is excited are shown in Figure 4.17 (b). Then ports 3 and 4 are excited, and the results are shown in Figure 4.17 (c) and Figure 4.17 (d), respectively.

Next, port 1 is excited with horizontal polarization, and the output is measured at all other ports with the transition oriented in the horizontal direction. The results for this case are shown in Figure 4.17 (e). Then, the procedure is repeated for the horizontal polarization when ports 2, 3 and 4 are excited. The results are plotted in Figure 4.17 (f), (g) and (h), respectively.

The corresponding phase response of the eight setups of Figure 4.17 is shown in Figure 4.18. The phase response is plotted as a progressive phase shift taking port 5 as a reference. For example, when port 1 is excited by vertical polarization, the phase angle of  $S_{51}$  is subtracted from the phase angle of  $S_{61}$ ,  $S_{71}$  and  $S_{81}$ , and plotted versus the port number, as shown in Figure 4.18 (a). The results at all frequency points within the band 58-62 GHz are overlapped on top of each other along with the theoretical progressive phase shift required to achieve the orthogonal beams of the Butler matrix. The same procedure is repeated when ports 2, 3 and 4 are excited with vertical polarization and the results are plotted in Figure 4.17 (b), (c) and (d), respectively. The phase measurement results for the horizontal polarization are shown in Figure 4.17 (e) to (h).

At the center frequency of 60 GHz, the design is perfectly matching the requirements in terms of magnitude and phase. Over a bandwidth of 4GHz (i.e., a bandwidth of about 6%) the magnitude response is fairly close to -6dB at the four output ports, while the isolation is fairly around -15dB. As discussed in the previous section, the phase response is widely spread around the theoretical required value according to the rate of change dictated by (4.24), (4.27) and (4.28).

Let's consider that the four output ports are feeding an array of isotropic radiators with inter-element separation of a half wavelength at 60 GHz. The array factor,  $AF$ , is plotted in Figure 4.19 for both polarizations as

$$AF_i = \sum_{p=1}^4 S_{(p+4)i} \exp(-j(p-1)\pi \sin \varphi) \quad (4.31)$$

where  $\varphi$  is the scanning angle measured from the array line.

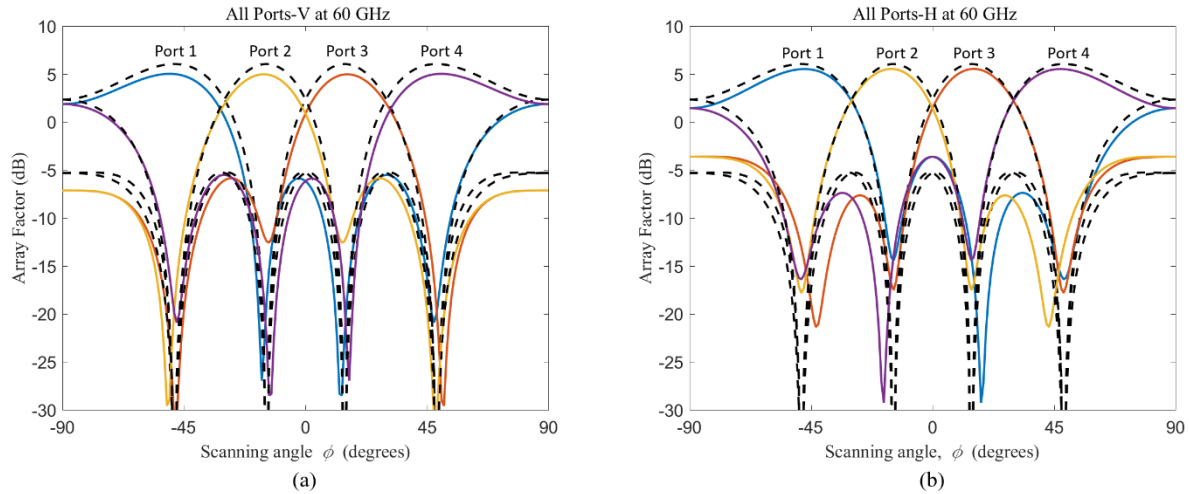


Figure 4.19. The array radiation pattern calculated based on the measured S-parameters (solid lines) as compared to the theoretical pattern (dashed lines): (a) vertical polarization, and (b) horizontal polarization.

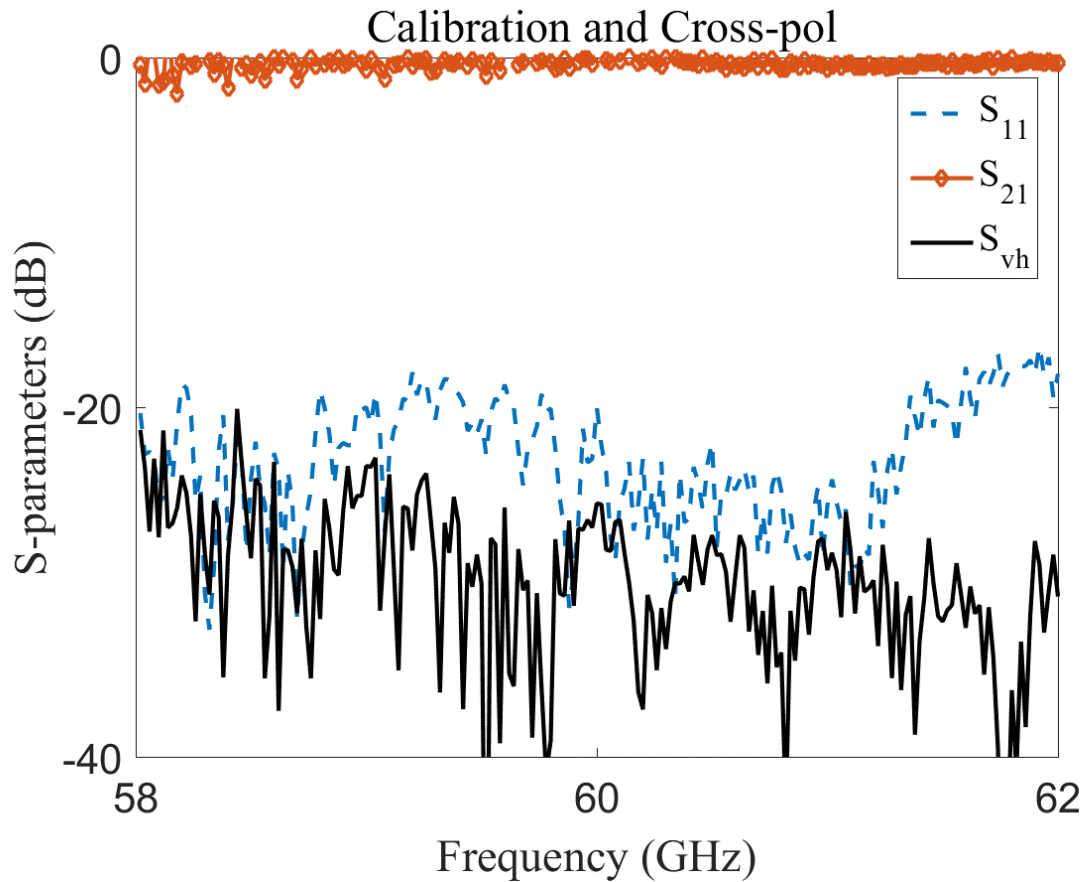


Figure 4.20. Performance of back-to-back square-to-WR15 transitions ( $S_{11}$  and  $S_{21}$ ) and the cross-talk between the two orthogonal polarizations within the fabricated network ( $S_{vh}$ ).

The figure shows that a deviation of less than 1 dB in the main lobe gain for all the orthogonal patterns in both polarizations is achieved.

This shows how successful a dually-polarized beamforming network could be if designed based on the analytical procedures and equations as shown in the work. No empirical formulas or trial and error procedures are required to get the initial dimensions of the design.

Finally, the cross-talk between the two orthogonal polarizations within the designed structure is examined. The calibration of our VNA is carried out with the reference plane defined at the interface of the WR15 transition. The designed square-to-WR15 transitions are considered as a part of the device. The performance of the square transitions is measured by placing them back-to-back. The results are defined as  $S_{21}$  and  $S_{11}$  shown in Figure 4.20. The cross-talk is then measured by exciting port 1 of the Butler matrix with horizontal polarization, and then the output at port 8, for example, is measured with the transition oriented vertically. The resulting cross-talk is labeled  $S_{vh}$  and shown in Figure 4.20. The cross-talk is observed to be lower than -20 dB over the whole bandwidth of the measurement.

## 4.7 Conclusion

In this chapter, the possibility of implementing planar dually-polarized microwave components is presented based on the PSC. Dually-polarized hybrid junctions are designed. A full demonstration for the controllability of the phase shift is introduced using circular bends. Mastering the controllability of handling dual-polarization allows the design of complicated microwave components to be dual-polarized such as the six-port junction and Butler matrix. Both structures have been prototyped and showed great potential. Exciting such structures requires special treatment because previously it is used to design transitions to microstrip lines in order to excite the traditionally fundamental vertically oriented mode. In our case, we need to excite the horizontally oriented mode as well. This requires the rotation of the traditionally excited vertically polarized mode to be horizontally polarized. A full explanation of this scheme is presented in details in the next chapter.

## **CHAPTER 5      INTEGRATED POLARIZATION CONVERTER FOR PLANAR CROSS-POLARIZED MILLIMETER WAVE COMPONENTS**

In the mmW band, it is possible to excite signals in printed circuit boards or PCB where the electric field is parallel to the plane of the substrate and bounded by the upper and lower conducting layers of the PCB. Based on this concept, dually-polarized mmW components have been developed recently to double the capacity of those components. The integration of dually-polarized and conventional single polarized components on one substrate creates a significant bottleneck. The solution for this bottleneck is the design of an integrated polarization converter which fully rotates the horizontally polarized field. This rotation converts the horizontal field to be vertical so to get easily fed to the rest of the circuit with minimum loss. The polarization conversion is achieved by an artificially induced skew anisotropy, which is realized by drilling tilted holes in the conventional isotropic substrate.

### **5.1 Motivation: Feasibility of Planar Integrated Cross-Polarized mmW Components**

It is the vector nature of electromagnetic fields that gives rise to its polarization. Due to this nature, the optimum reception of an electromagnetic signal can never be achieved without probing all three components of its electric field vector in a three-dimensional space. Due to their transversal nature, any electromagnetic wave can be represented in free space as a summation of two orthogonally polarized fields lying in the plane perpendicular to its direction of propagation (plane TEM wave). Therefore, the optimum reception can be achieved by capturing those two orthogonal polarizations. This concept has been applied in cellular communications, microwave links, satellite communications and many other wireless systems by the name of polarization diversity.

Recent efforts have been exerted to enable this feature of diversity in planar printed mmW circuits and systems. This is to meet the exploding need for green environment-friendly wireless technologies in this unexplored or limited explored region of the frequency spectrum of radio waves. This feature of diversity makes it possible for a printed planar transmission line to carry two orthogonally polarized signals without interfering with each other. This is possible by developing hybrid integrated multi-mode waveguides where the two orthogonal polarizations are carried by different modes, and each mode is guided by a different mechanism.

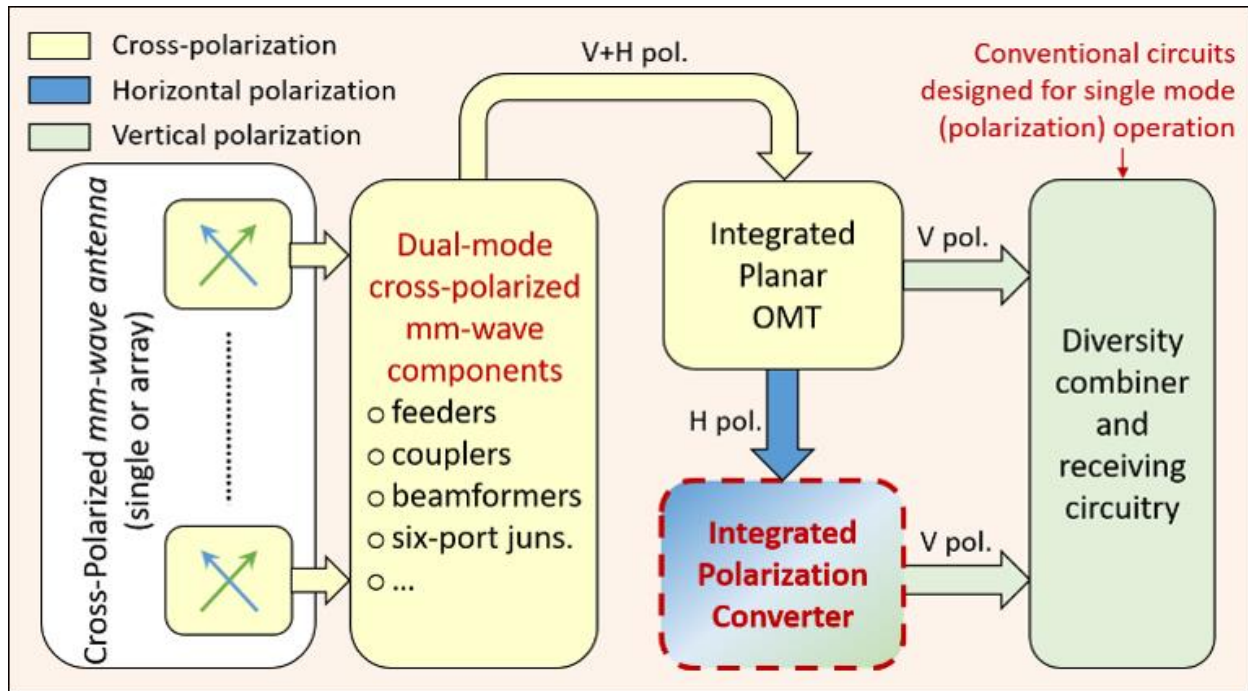


Figure 5.1. Block diagram of cross-polarized mmW printed circuits including the polarization converter which is proposed in this dissertation.

In such waveguides, one polarization is orthogonal to the plane of the substrate of the printed circuit board or PCB. This is called here vertical polarization. Whereas the other polarization is called horizontal; being parallel to the plane of the PCB and bounded inside the substrate by the upper and lower conducting layers. Many different components can be developed based on those integrated cross-polarized waveguides such as cross-polarized couplers, Butler matrix, six-port junctions and orthomode transducers, as illustrated in the previous chapters.

A bottleneck which appears is the integration of the cross-polarized components with conventional single-polarized parts of PCB as shown in Figure 5.1. That is, at some point, the horizontal polarization needs to be combined with the other polarization or at least demodulated and get its information extracted. This means that the horizontal component of the electric field needs to excite a conventional vertically polarized transmission line which will always be at the interface of conventional circuits and chips. A solution for this problem has been proposed in [68, 115] based on multilayer substrates where a conventional transmission line is excited by the horizontal component of the field through slots in the conductors between the different layers.

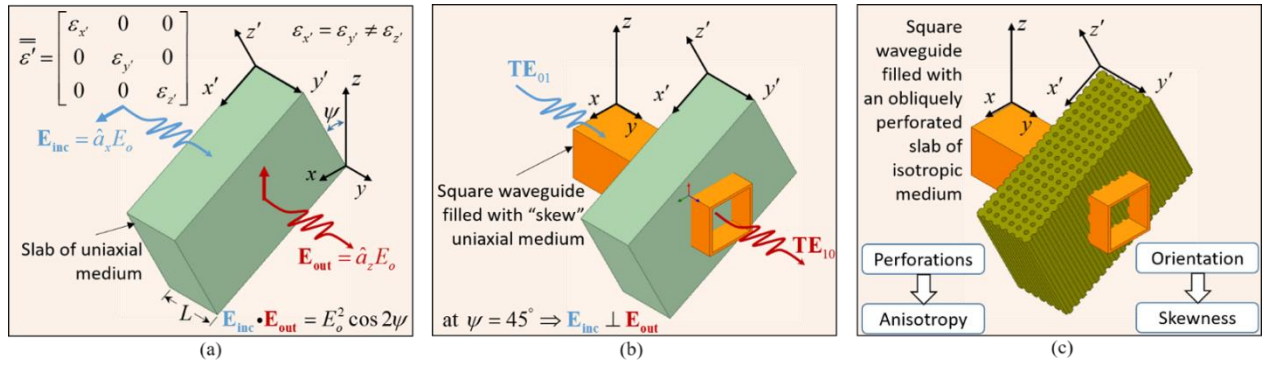


Figure 5.2. Concept of field rotation in uniaxially anisotropic media, (a) Unbounded slab of uniaxial medium, (b) Bounded slab of uniaxial medium enclosed by the metallic walls of a square waveguide. In the coordinate system of the waveguide, the material is called skew uniaxial dielectric [2] and (c) Artificially induced anisotropy and skewness in isotropic materials by tilted air-hole perforations.

However, a significant insertion loss of 4 to 5 dB is always observed in all the previously proposed solutions. This high loss makes the whole idea of polarization diversity loses its true value.

The objective of this chapter is to develop a different concept for the design of a single-layer integrated polarization converter, as shown in Figure 5.1, with perfect performance specifically regarding its insertion loss.

## 5.2 Field Rotation in Uniaxial Media: Wave-Plates

Uniaxial anisotropic media can be found in nature and are characterized by their anisotropic response to incident electric fields. Uniaxial media are modelled by a relative permittivity tensor in the form shown in Figure 5.2 (a). The term *uniaxial* means that the dielectric constant seen by an electric field oriented in one specific direction called the *optic axis*, say  $z'$  in Figure 5.2 (a), is different from that seen by all the other electric fields in the plane  $x' - y'$ . Waves in such media are studied extensively in [80]. Solutions of Maxwell's equations in uniaxial media can take the form of plane waves with two distinct phase velocities depending on the direction of electric field. Numerous applications of uniaxial slabs are developed in the field of optics where they are called *polarizers* or *wave-plates*. Depending on the length of the slab and the direction of the incident electric field with respect to the optic axis, the polarization of wave can be altered from one state

to another. This is achieved by the interaction of the incident wave and those waves with the different velocities in the slab.

Rectangular waveguides filled with uniaxial materials with optic axis aligned with their longitudinal direction are studied in [83], while *skew* uniaxial fillings where the optic axis lies anywhere in the transverse plane of the guide as shown in Figure 5.2 (b) are studied in [116]. Other directions of skewness and full field expressions have been given recently in [117]. Those structures arise in a narrow range of applications such as the design of particular travelling-wave masers [116]. The reason for this could be a high dielectric loss tangent of uniaxial media in the microwave and mmW bands as compared to the optical frequencies. This is in addition to the low available control on the angle of skewness of the natural optic axis of the material with respect to the walls of the waveguide.

The main idea in this chapter is illustrated in Figure 5.2 (c). It is proposed to induce in a slab of isotropic material to a controlled level of artificial uniaxial anisotropy. This is done by perforating the isotropic material, as shown in Figure 5.2 (c). The optic axis of the induced anisotropy is parallel to the axis of the air perforations. Thus, full control on the skewness of the material with respect to the metallic walls of the guide to be filled is achieved. An incident horizontally polarized  $TE_{01}$  mode excites the two distinct modes in the skew uniaxial slab. After a certain length, and due to the different phase velocities of the excited modes, the field will be perfectly orthogonal to the incident mode, i.e., it becomes the vertically polarized  $TE_{10}$  mode. The full design procedure is explained briefly in the following section.

### 5.3 Design Methodology and Performance Analysis of Uniaxial Polarization Converter

Let us consider a slab of isotropic material as shown in Figure 5.2 (c) with constant relative permittivity  $\epsilon'_r$ . In the primed set of coordinates  $x', y', z'$ , the effect of drilling periodic air-holes as shown in Figure 5.3 (a) is to alter that scalar permittivity  $\epsilon'_r$  to take the tensor form shown in Figure 5.2 (a), where  $\epsilon'_x = \epsilon'_y \neq \epsilon'_z$ . The period,  $p$  is chosen such that below the maximum desired frequency of operation, the perforated slab acts as a non-dispersive medium with at most 10% variation of the effective permittivity. This maximum frequency,  $f_{\max}$ , vs.  $p$  is shown in Figure 5.3 (b) for three commercial dielectric substrates, namely the Rogers RT/duroid 6002, 6006 and 6010

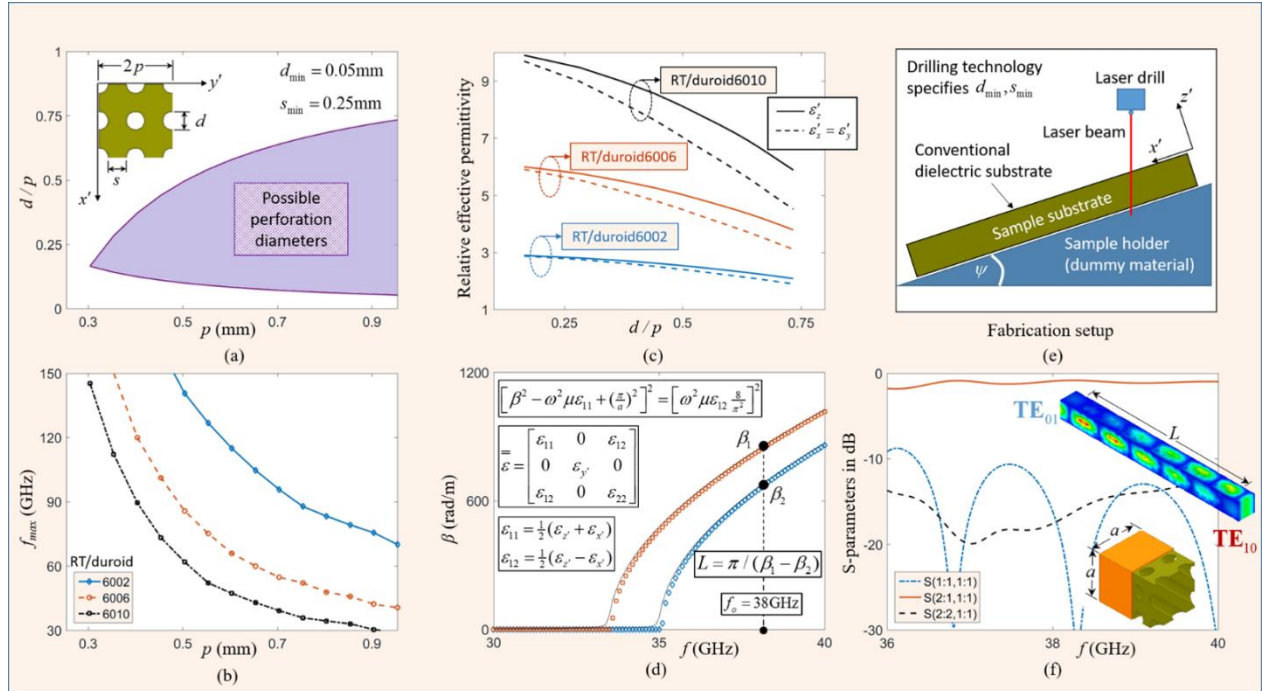


Figure 5.3. Design procedure, simulation and fabrication of the polarization converter, (a) Geometry of the air-hole perforations and the possible range of air-hole diameters limited by the technology used for drilling, (b) Maximum frequency below which the perforated medium can be modelled as an effective homogenous medium with a constant permittivity tensor, (c) Effective uniaxial permittivity versus perforation diameters, (d) Dispersion of a 2mm square waveguide filled with perforated RT/duroid6006 with period,  $p=0.9\text{mm}$ ,  $d/p$  ratio of 0.5 and tilting angle of 45 degrees, (e) Setup for fabrication and (f) Electric field distribution and s-parameters of the prototype.

with typical background  $\epsilon'_r$  of 2.94, 6.15 and 10.2, respectively. Limited by the technology used for drilling, the minimum hole-diameter,  $d$ , and inter-separation between holes,  $s$ , specify the possible range of the  $d/p$  ratios as shown in Figure 5.3 (a). Given a certain  $d/p$  ratio and a given background  $\epsilon'_r$ , one can solve an eigenvalue problem for the unit cell shown in Figure 5.3 (a) to find the effective permittivity tensor representing the perforated slab. In this eigenvalue problem, the first two solutions represent the ordinary and extraordinary waves in the resulting effective uniaxial slab [80], with one eigenvector parallel to the axis of perforations and the other being normal to it.

The two corresponding eigenvalues are used to extract the values of  $\epsilon'$  in the  $z'$ -direction and in the plane  $x'-y'$  as shown in Figure 5.3 (c). The design procedure starts by selecting the substrate to be used and the maximum frequency of operation. Assuming the required center frequency,  $f_o$  is at 38 GHz and  $f_{\max}$  at 40 GHz.

For the RT/duroid-6006,  $\epsilon'_r = 6.15$ , the value of  $p$  can be selected to be 0.9 mm. From Figure 5.3 (c), a  $d/p$  ratio of 0.5 results in a tensor permittivity with diagonal entries of  $\epsilon'_x = \epsilon'_y = 4.518$  and  $\epsilon'_z = 5.037$ . In the unprimed set of coordinates  $x, y, z$  shown in Figure 5.2, where the angle between the  $z'$  – and  $z$  – axis in the  $x$ - $z$  plane is  $\psi = 45^\circ$ , the permittivity tensor is rotated to take the form shown in Figure 5.3 (d). Assuming a square waveguide with cross-section dimension  $a = 2\text{mm}$ , the dispersion of the first two modes in the square waveguide is shown in Figure 5.3 (d) as the first two positive solutions of the equation shown in the figure [117]. Given the numerical value of the two different phase constants, one can easily prove that the length required to get a  $90^\circ$  rotation of the incident field is given by  $L = \pi / (\beta_1 - \beta_2)$  which is found to be 17.6 mm at 38 GHz in this example. The fabrication setup is shown in Figure 5.3 (e), where the conventional 6006 substrate is placed tilted under the vertical laser beam used for drilling, i.e., the drilled cylindrical holes have their axis tilted by the angle  $\psi$  with respect to the direction normal to the substrate. The results of a full wave analysis are shown in Figure 5.3 (f), where the field distribution at 38 GHz shows clearly the conversion of the input  $\text{TE}_{01}$  mode to the output  $\text{TE}_{10}$  mode of the square waveguide. The achieved bandwidth is about 15% limited by the cutoff of the two necessary modes from the lower side and by the period  $p$  and the cutoff of the higher order mode from the other side. The insertion loss is less than 1 dB and caused by the loss tangent of the material. It is worth noting that the periodicity in the  $y$ -direction is not needed in this example, and the tilted holes can be combined to be tilted slots to speed up the fabrication.

#### 5.4 Prototype of an Integrated Planar Mode Converter

In order to undergo the fabrication limitations in our Poly-Grames laboratory, the number of the tilted holes should be minimized as much as possible. This is because, for a tilted substrate, the laser beam should be refocused for each hole in order to maintain the required spacing between the laser source and the substrate. Therefore, the structure has been approximated to have a single

## Explanation of the design with inclined slot

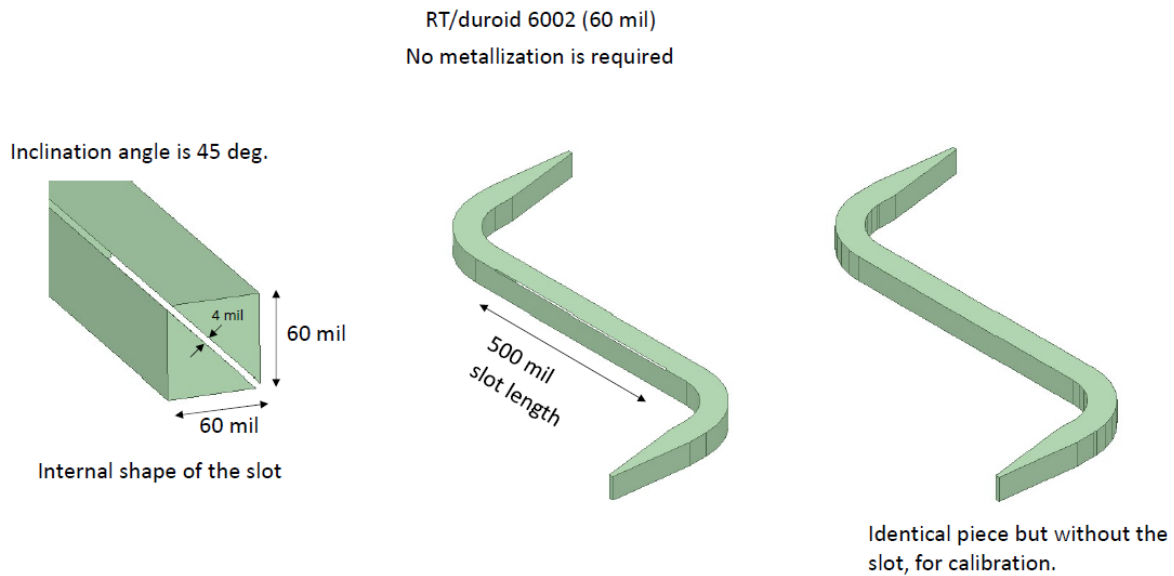


Figure 5.4. Structure of an approximate mode converter made of Rogers RT/duroid 6002.

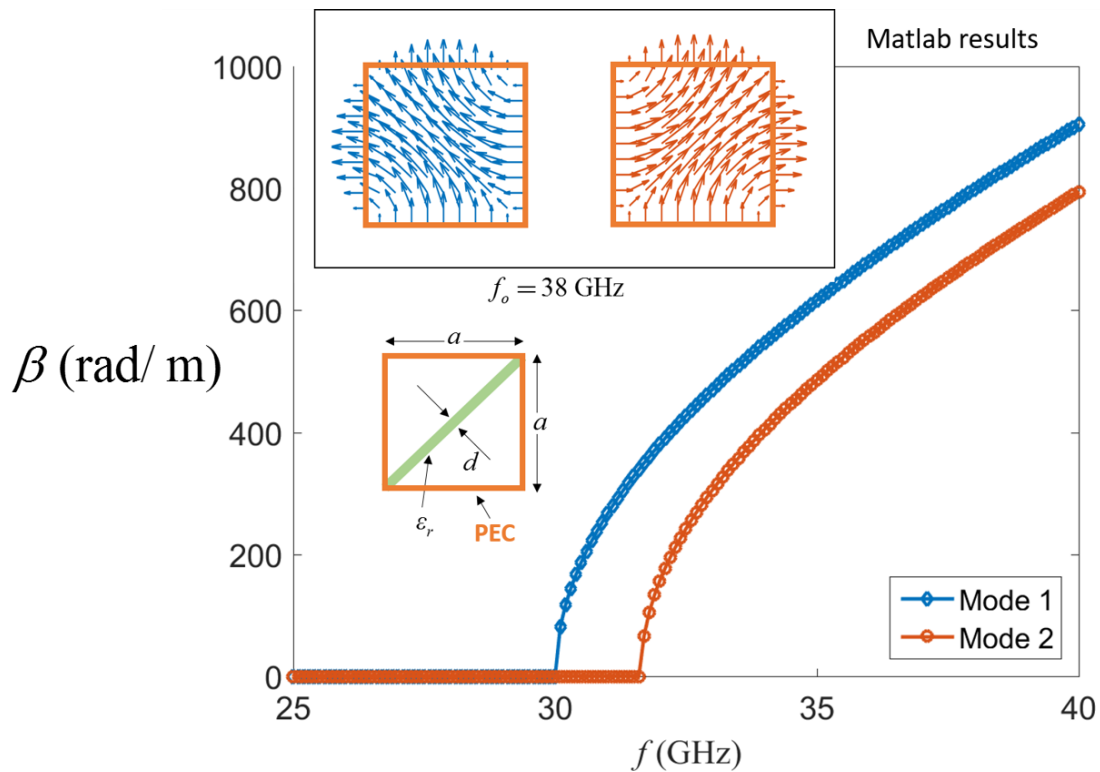


Figure 5.5. Dispersion curves and field distribution for the ordinary and extraordinary modes for the approximate mode converter with one tilted slot over the cross-section diagonal.

period in the  $x'$  – direction. Furthermore, since the excited ordinary and extraordinary modes have not an electric field vector in  $z'$  – direction, the periodicity in that direction does not affect the field rotation. Therefore, the holes in  $z'$  – direction can be connected together. As a result of the mentioned modifications, the structure will converge to a continuous tilted slot as shown in Figure 5.4 with the specified dimensions. Since this structure is designed at high frequency where there is no accurate information about its parameters, a reference substrate has been implemented with the same dimensions but without slot for calibration. Tapered matching sections are optimized for matching the dielectric-filled structure to the standard air-filled waveguide for measurements.

The structure with a single tilted slot in Figure 5.4 has been analyzed to confirm the desired mode conversion. When exciting the structure with the  $TE_{01}$  mode, it excites the ordinary and extraordinary modes which have field distributions parallel and perpendicular to the tilted slot, respectively, as shown in Figure 5.5. The difference between the propagation phase delays of Mode 1 and Mode 2 in Figure 5.5 is responsible for ensuring the mode rotation after the length specified in Figure 5.3 (d).

The structure is prototyped as shown in Figure 5.6 where a metallic enclosure is designed. Two metallic transitions are designed as well. when the transition is rotated by 90 degrees, the orientation of the excited mode is changed from  $TE_{10}$  (V) to  $TE_{01}$  (H) or from  $TE_{01}$  to  $TE_{10}$ . The structure is connected to the VNA as shown in Figure 5.6 and the resultant scattering parameters are shown in Figure 5.7. From that figure, it can be deduced that when exciting the structure with a  $TE_{01}$  mode (H), and measuring the output at the other transition when it is oriented to receive the  $TE_{10}$  mode (V), the mode has been successfully rotated, but with about -5 dB transmission level. For this reason, the substrate without slot has been measured to calculate the dielectric losses at the operating frequency (around 80 GHz). It has been found that, the dielectric without the slot introduces the same transmission level of -5 dB which confirms that these losses are due to the dielectric loss tangent of the substrate not due to the mode conversion.

As a conclusion, the resultant scattering parameters confirms that a full rotation for the electric field is achieved based on a tilted continuous slot which shows the potential of having this feature in the PCB applications that requires planar geometry.

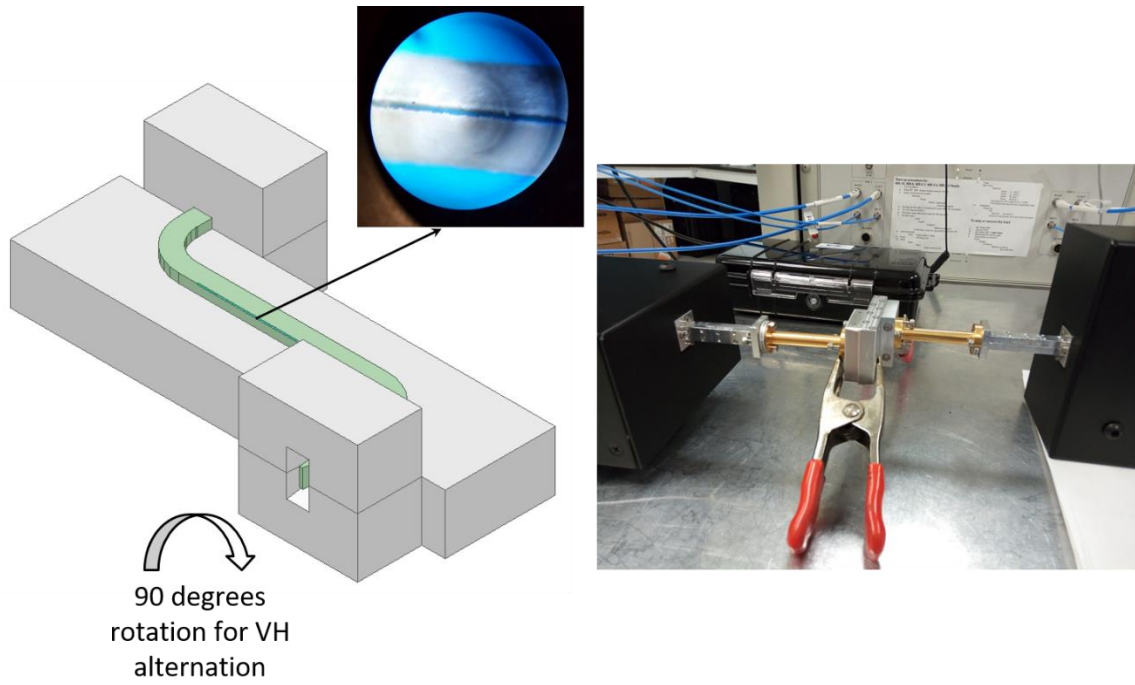


Figure 5.6. The mode converter prototype and the setup for measurement.

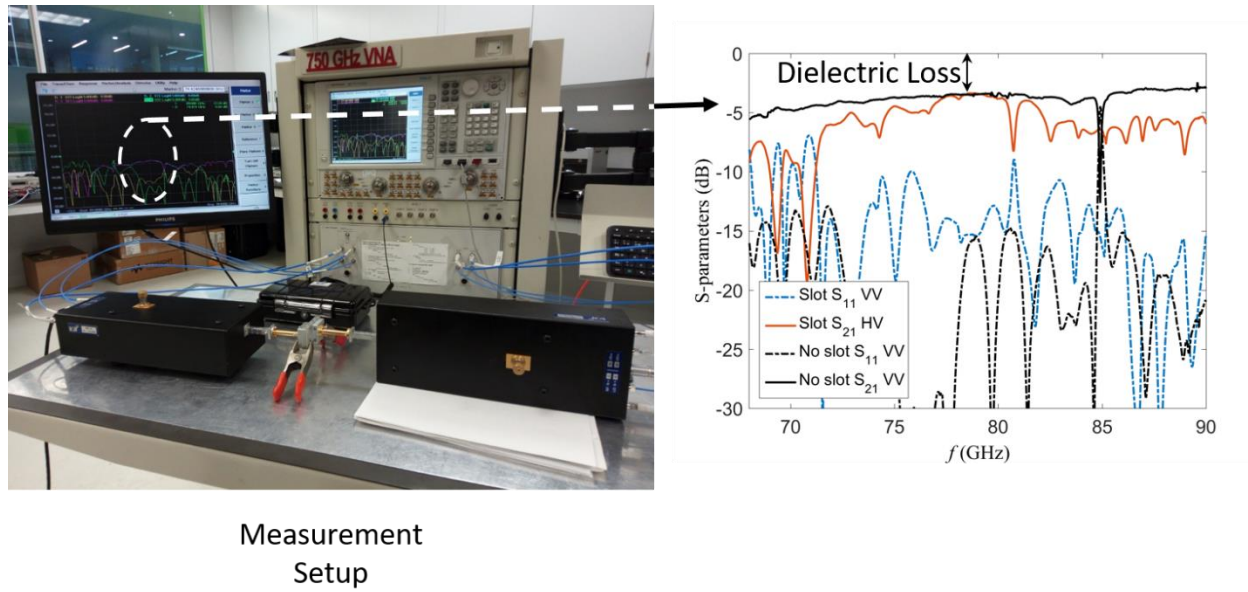


Figure 5.7. The resultant scattering parameters.

## CHAPTER 6 CONCLUSION AND RECOMMENDATIONS

With the great explosion of wireless systems and their applications and also with the limited enabling energy and spectrum resources available, it becomes more and more crucial to focus on the reduction of the energy use in future wireless systems. The most efficient way of electromagnetic wave energy reception is to fully capture the two orthogonal components of its field vector in connection with polarization diversity. This thesis shows how to exploit the concept of polarization diversity over the mmW frequency band which has been assigned for wireless applications. This is done by developing the theory of operation and design procedure of dually-polarized mmW components based on PSC. The novelty presented in this work lies in developing a principle of operation so to come up with a class of dually-polarized mmW components, namely 3dB couplers, 0dB couplers and phase shifters. This allows the development of dually-polarized beamforming networks such as Butler matrix and remote sensing applications based on the six-port junction. A full analytical design procedure is presented with verifications through full-wave simulations and prototype measurements.

The problem of enabling the feature of polarization diversity in integrated microwave components is studied. Different types of waveguides have been investigated extensively, namely NRD, image-NRD, Hybrid NRD-SIW, and image-NRD-SIW waveguides. Two types of those studied waveguides are used together to form our proposed polarization selective coupler (PSC), namely the image NRD-SIW and the image-NRD waveguides. This PSC is used to design an OMT suitable for the 5G applications. A complete design procedure is presented for designing a planar PSC-based OMT structure. This OMT in its general form is validated through simulations where 15% fractional bandwidth is achieved around 32 GHz for insertion loss below 10dB. As a validation, a special case of PSC-based OMT is designed and prototyped. An excellent agreement is achieved when compared with simulations. The final structure works with a band of frequencies starting from 33 GHz to 40 GHz. The structure is integrated with a square horn antenna. Upon measuring the horn antenna gain in different orientations with different excitations, it confirmed the full operation of an OMT with antenna gain around 15dB and isolation below 25dB.

This experiment validates the proposed theory for the design of a PSC and its application to an OMT. If integrated successfully with mmW antennas, the feature of polarization diversity can be enabled in the future wireless systems, thus making use of the proposed planar device. For full

integration, new transitions should be designed to extract the horizontally polarized LSM modes and deliver it to integrated chips on the same printed circuit board. The design of such transitions is considered as future work. The detailed design methodologies which take into consideration the anisotropy of the substrate and the mechanism of the fused coupling in the design of a PSC-based OMT are also presented.

The practical design procedure for the proposed planar OMT is presented and evaluated. The core idea of the proposed OMT depends on the design of a polarization selective coupler (PSC). The PSC is studied through a simple equivalent circuit model by which the dispersion characteristics are obtained. The general form of a PSC-based OMT structure with the matching sections is designed, and the fabrication limitations are discussed, namely, the hard-to-realize gap width and the metallic via conductor plating. As a solution for the fabrication limitations, the image-NRD and image-NRD-SIW waveguides are fused into one waveguide. The anisotropy of typical materials is taken into account with an exact analytical procedure. A complete design recipe is explained for obtaining structure dimensions and operation bandwidth for a specific frequency range. This analytical procedure that takes the anisotropy into account is validated through full-wave simulations. However, it was not physically realized due to the complicated required matching sections to air-filled waveguide transitions. Two prototypes are implemented and measured. The first prototype is to validate the design procedure and concept of the isotropic dielectric-based fused PSC. In this prototype, the air gap is totally eliminated to overcome the hard realization of uniform gap width. Finally, the dielectric material is removed altogether, getting rid of the dielectric loss at the expense of a larger physical size. This might be suitable to the applications where the sensitivity and reliability are more important than the size. As another proof of concept, this air-filled design is realized and integrated with a square horn antenna. An excellent agreement is achieved with the simulation results. The design of transitions to other transmission lines such as CPW and microstrip lines is considered as future work. This will facilitate the full integration of the proposed OMT with low profile handheld equipment.

Subsequently, some dually-polarized microwave components are designed based on the introduced PSC concept. A dually-polarized six-port junction is designed and demonstrated. The PSC shows the possibility of handling two orthogonal modes through a planar waveguide structure. This PSC technique is used to design microwave components such as a dually-polarized hybrid coupler. This is in addition to the dually-polarized power divider. Those components are used together along

with circular waveguide bends phase shifter to implement the overall dually-polarized six-port junctions. The waveguide bends are used to realize the required phase equalization for both of the orthogonal modes. The analytical steps for the whole design procedure are given in details. The realized overall dually-polarized six-port junction shows the complete functionality for both of the orthogonal  $TE_{10}$  and  $TE_{01}$  modes. The functionality is tested by a physical prototype for which an accepted agreement is achieved between the simulation and measurement results. The overall bandwidth of the structure is about 7% around 30 GHz. The structure is fully planar, which means that it can be easily implemented in substrate integrated technology. The thickness of the available commercial dielectric substrates enables the incorporation of the proposed dual-polarization feature on printed circuit boards. However, the high dielectric loss of commercial dielectric substrates is the main limitation. A solution for this problem needs to be found to apply the proposed concept on fully integrated circuits.

In addition, the full design concept and technique of a dually-polarized beamforming network in the mmW band are presented. A 4x4 dually-polarized Butler matrix design is shown as an example and proof of concept. The analytical design procedure is explained in full details. The proposed solution depends on the square air-filled waveguide technology that can be easily extended to a dielectric substrate based manufacturing. The proposed solution depends on two-dimensional machining only, making the design fully planar. The bottleneck of the presented solution is the dually-polarized phase shifter. The phase shifter presented in this thesis work depends on altering the dimensions of the cross-section of the waveguide. While this phase shifter is not fully planar, it requires very small machining in the orthogonal plane which is easily achieved by CNC machine, and it serves the purpose of giving a complete analytical procedure for the whole design of the beamforming network. The achieved four spatially orthogonal main lobes of the radiation pattern are within 1dB from the ideal pattern at the center frequency.

The research effort presented in this work automatically expose two main research tasks which require attention. First, the design of an optimized dually-polarized waveguide phase shifter which is compact in size and with a phase response that matches the frequency dependence of the phase response of a 0dB coupler. This task is to enhance the bandwidth performance of the network. Second, the integration of a radiating antenna element that is exactly of the same physical size of the open aperture of the square waveguide. This will eliminate the need for any more bends at the

output ports. A good candidate is the dielectric resonator antenna of square shape. This is considered as future work.

Finally, we believe that the main future work of this dissertation is the implementation of the polarization diversity on the IC chip level. In this work, we implemented the polarization diversity within planar integrated microwave passive components. The same concepts can be applied using different fabrication technologies such as CMOS to be implemented over a full RF system on the IC chip level.

## BIBLIOGRAPHY

- [1] A. Goldsmith, *Wireless Communications*: Cambridge University Press, 2005.
- [2] K. Fujimoto, *Mobile Antenna Systems Handbook*: Artech House, 2008.
- [3] F. Hillebrand, "The creation of standards for global mobile communication: GSM and UMTS standardization from 1982 to 2000," *IEEE Wireless Communications*, vol. 20, pp. 24-33, 2013.
- [4] M. Elkashlan, T. Q. Duong, and H.-H. Chen, "Millimeter-wave communications for 5G: fundamentals: Part I," *IEEE Communications Magazine*, vol. 52, pp. 52-54, 2014.
- [5] M. Elkashlan, T. Q. Duong, and H.-H. Chen, "Millimeter-wave communications for 5G??? Part 2: applications," *IEEE Communications Magazine*, vol. 53, pp. 166-167, 2015.
- [6] A. I. Sulyman, A. Alwarafy, G. R. MacCartney, T. S. Rappaport, and A. Alsanie, "Directional Radio Propagation Path Loss Models for Millimeter-Wave Wireless Networks in the 28-, 60-, and 73-GHz Bands," *IEEE Transactions on Wireless Communications*, vol. 15, pp. 6939-6947, 2016.
- [7] A. I. Sulyman, A. T. Nassar, M. K. Samimi, G. R. Maccartney, T. S. Rappaport, and A. Alsanie, "Radio propagation path loss models for 5G cellular networks in the 28 GHz and 38 GHz millimeter-wave bands," *IEEE Communications Magazine*, vol. 52, pp. 78-86, 2014.
- [8] H. Zhao, *et al.*, "28 GHz millimeter wave cellular communication measurements for reflection and penetration loss in and around buildings in New York City," in *Proc. IEEE Int. Conf. Commun.*, 2013, pp. 5163-5167.
- [9] J. Helander, K. Zhao, Z. Ying, and D. Sjöberg, "Performance Analysis of Millimeter-Wave Phased Array Antennas in Cellular Handsets," *IEEE Antennas Wireless Propag. Lett.*, vol. 15, pp. 504-507, 2016.
- [10] J. Song, J. Choi, S. G. Larew, D. J. Love, T. A. Thomas, and A. A. Ghosh, "Adaptive Millimeter Wave Beam Alignment for Dual-Polarized MIMO Systems," *IEEE Trans. Wireless Commun.*, vol. 14, pp. 6283-6296, 2015.
- [11] S. Liao, *et al.*, "Passive Millimeter-Wave Dual-Polarization Imagers," *IEEE Trans. Instrum. Meas.*, vol. 61, pp. 2042-2050, 2012.
- [12] M. Alzenad, M. Z. Shakir, H. Yanikomeroğlu, and M. S. Alouini, "FSO-Based Vertical Backhaul/Fronthaul Framework for 5G+ Wireless Networks," *IEEE Communications Magazine*, vol. 56, pp. 218-224, 2018.
- [13] J. A. Ruiz-Cruz, J. R. Montejo-Garai, and J. M. Rebollar, "Optimal configurations for integrated antenna feeders with linear dual-polarisation and multiple frequency bands," *IET Microwaves Antennas & Propagation*, vol. 5, pp. 1016-1022, Jun 6 2011.
- [14] D. Dousset, S. Claude, and K. Wu, "A Compact High-Performance Orthomode Transducer for the Atacama Large Millimeter Array (ALMA) Band 1 (31-45 GHz)," *IEEE Access*, vol. 1, pp. 480-487, 2013.

- [15] J. Lahtinen, J. Pihlflyckt, K. Mononen, S. J. Tauriainen, M. Kempainen, and M. T. Hallikainen, "Fully polarimetric microwave radiometer for remote sensing," *IEEE Transactions on Geoscience and Remote Sensing*, vol. 41, pp. 1869-1878, Aug 2003.
- [16] J. A. Ruiz-Cruz, J. R. Montejo-Garai, J. M. Rebollar, and J. M. Montero, "C-band orthomode transducer for compact and broadband antenna feeders," *Electronics Letters*, vol. 45, pp. 813-814, 2009.
- [17] A. Morshedi and M. Torlak, "Measured Comparison of Dual-Branch Signaling Over Space and Polarization Diversity," *IEEE Transactions on Antennas and Propagation*, vol. 59, pp. 1678-1687, May 2011.
- [18] P. Y. Qin, Y. J. Guo, and C. H. Liang, "Effect of Antenna Polarization Diversity on MIMO System Capacity," *IEEE Antennas and Wireless Propagation Letters*, vol. 9, pp. 1092-1095, 2010.
- [19] M. Esquius-Morote, M. Mattes, and J. R. Mosig, "Orthomode Transducer and Dual-Polarized Horn Antenna in Substrate Integrated Technology," *IEEE Trans. Antennas Propag.*, vol. 62, pp. 4935-4944, 2014.
- [20] A. M. Boifot, E. Lier, and T. Schaugpettersen, "Simple and Broad-Band Orthomode Transducer," *IEE Proceedings-H Microwaves Antennas and Propagation*, vol. 137, pp. 396-400, Dec 1990.
- [21] A. Navarrini and R. L. Plambeck, "A turnstile junction waveguide orthomode transducer," *IEEE Transactions on Microwave Theory and Techniques*, vol. 54, pp. 272-277, 2006.
- [22] G. Pisano, L. Pietranera, K. Isaak, L. Piccirillo, B. Johnson, B. Maffei, *et al.*, "A broadband WR10 turnstile junction orthomode transducer," *IEEE Microwave and Wireless Components Letters*, vol. 17, pp. 286-288, Apr 2007.
- [23] W. Hongjian, Y. Min, L. Guang, and C. Xue, "Potter Horn and Compact Orthomode Transducer at 150 GHz," *IEEE Transactions on Antennas and Propagation*, vol. 62, pp. 5403-5405, 2014.
- [24] C. A. Leal-Sevillano, T. J. Reck, G. Chattopadhyay, J. A. Ruiz-Cruz, J. R. Montejo-Garai, and J. M. Rebollar, "Development of a Wideband Compact Orthomode Transducer for the 180-270 GHz Band," *IEEE Transactions on Terahertz Science and Technology*, vol. 4, pp. 634-636, 2014.
- [25] A. Navarrini and R. Nesti, "Symmetric Reverse-Coupling Waveguide Orthomode Transducer for the 3-mm Band," *IEEE Transactions on Microwave Theory and Techniques*, vol. 57, pp. 80-88, 2009.
- [26] O. A. Peverini, R. Tascone, G. Virone, A. Olivieri, and R. Orta, "Orthomode transducer for millimeter-wave correlation receivers," *IEEE Transactions on Microwave Theory and Techniques*, vol. 54, pp. 2042-2049, 2006.
- [27] J. Esteban, C. Camacho-Penalosa, "Compact Orthomode Transducer Polarizer Based on a Tilted-Waveguide T-Junction," *IEEE Transactions on Microwave Theory and Techniques*, vol. 63, pp. 3208-3217, 2015.
- [28] C. A. Leal-Sevillano, K. B. Cooper, J. A. Ruiz-Cruz, J. R. Montejo-Garai, and J. M. Rebollar, "A 225 GHz Circular Polarization Waveguide Duplexer Based on a Septum

- Orthomode Transducer Polarizer," *IEEE Trans. THz Sci. Technol.*, vol. 3, pp. 574-583, 2013.
- [29] C. A. Leal-Sevillano, Y. Tian, M. J. Lancaster, J. A. Ruiz-Cruz, J. R. Montejo-Garai, and J. M. Rebollar, "A Micromachined Dual-Band Orthomode Transducer," *IEEE Transactions on Microwave Theory and Techniques*, vol. 62, pp. 55-63, 2014.
- [30] G. Virone, O. A. Peverini, M. Lumia, G. Addamo, and R. Tascone, "Platelet Orthomode Transducer for Q-Band Correlation Polarimeter Clusters," *IEEE Trans. Microw. Theory Techn.*, vol. 62, pp. 1487-1494, 2014.
- [31] J. H. Hwang and Y. Oh, "Compact Orthomode Transducer Using Single-Ridged Triangular Waveguides," *IEEE Microw. Compon. Lett.*, vol. 21, pp. 412-414, 2011.
- [32] M. K. Mandal, K. Wu, and D. Deslandes, "A compact planar orthomode transducer," in *2011 IEEE MTT-S International Microwave Symposium*, 2011, pp. 1-4.
- [33] M. Esquiús-Morote, M. Mattes, and J. R. Mosig, "Orthomode Transducer and Dual-Polarized Horn Antenna in Substrate Integrated Technology," *IEEE Transactions on Antennas and Propagation*, vol. 62, pp. 4935-4944, 2014.
- [34] O. A. Peverini, R. Tascone, G. Virone, A. Olivieri, and R. Orta, "Orthomode transducer for millimeter-wave correlation receivers," *IEEE Trans. Microw. Theory Techn.*, vol. 54, pp. 2042-2049, 2006.
- [35] M. K. Mandal, K. Wu, and D. Deslandes, "A compact planar orthomode transducer," in *IEEE MTT-S Int. Microw. Symp. Dig.*, 2011, pp. 1-4.
- [36] U. Rosenberg and R. Beyer, "Compact T-junction orthomode transducer facilitates easy integration and low cost production," in *2011 41st European Microwave Conf.*, 2011, pp. 663-666.
- [37] T. Yoneyama and S. Nishida, "Nonradiative Dielectric Waveguide for Millimeter-Wave Integrated Circuits," *IEEE Trans. Microw. Theory Techn.*, vol. 29, pp. 1188-1192, 1981.
- [38] D. Deslandes and K. Wu, "Accurate modeling, wave mechanisms, and design considerations of a substrate integrated waveguide," *IEEE Trans. Microw. Theory Techn.*, vol. 54, pp. 2516-2526, 2006.
- [39] X. Feng and K. Wu, "Guided-wave and leakage characteristics of substrate integrated waveguide," *IEEE Transactions on Microwave Theory and Techniques*, vol. 53, pp. 66-73, 2005.
- [40] F. Xu and K. Wu, "Guided-wave and leakage characteristics of substrate integrated waveguide," *IEEE Transactions on Microwave Theory and Techniques*, vol. 53, pp. 66-73, Jan 2005.
- [41] Y. Cassivi and K. Wu, "Substrate integrated nonradiative dielectric waveguide," *IEEE Microwave and Wireless Components Letters*, vol. 14, pp. 89-91, Mar 2004.
- [42] F. Xu and K. Wu, "Substrate Integrated Nonradiative Dielectric Waveguide Structures Directly Fabricated on Printed Circuit Boards and Metallized Dielectric Layers," *IEEE Transactions on Microwave Theory and Techniques*, vol. 59, pp. 3076-3086, Dec 2011.

- [43] T. Yoneyama and S. Nishida, "Nonradiative Dielectric Waveguide for Millimeter-Wave Integrated Circuits," *IEEE Transactions on Microwave Theory and Techniques*, vol. 29, pp. 1188-1192, 1981.
- [44] R. F. Harrington, *Time-Harmonic Electromagnetic Fields*: Wiley, 2001.
- [45] T. Yoneyama, "Recent development in NRD-guide technology," *Annals of Telecommunications*, vol. 47, pp. 508-514, 1992.
- [46] D. Li, Y. Cassivi, P. Yang, and K. Wu, "Analysis and design of bridged NRD-guide coupler for millimeter-wave applications," *IEEE transactions on microwave theory and techniques*, vol. 53, pp. 2546-2551, 2005.
- [47] J. Attari, T. Djerafi, and K. Wu, "A Compact 94 GHz Image Substrate Integrated Non-Radiative Dielectric (iSINRD) Waveguide Cruciform Coupler," *IEEE Microwave and Wireless Components Letters*, vol. 23, pp. 533-535, 2013.
- [48] P. Mondal and K. Wu, "A Leaky-Wave Antenna Using Periodic Dielectric Perforation for Millimeter-Wave Applications," *IEEE Transactions on Antennas and Propagation*, vol. 64, pp. 5492-5495, 2016.
- [49] P. Mondal and K. Wu, "A Leaky-Wave Antenna in Substrate Integrated Non-Radiative Dielectric (SINRD) Waveguide With Controllable Scanning Rate," *IEEE Transactions on Antennas and Propagation*, vol. 61, pp. 2294-2297, 2013.
- [50] Y. Cassivi and W. Ke, "Substrate integrated nonradiative dielectric waveguide," *IEEE Microwave and Wireless Components Letters*, vol. 14, pp. 89-91, 2004.
- [51] F. Xu, K. Wu, and W. Hong, "Finite-Difference Time-Domain Modeling of Periodic Guided-Wave Structures and Its Application to the Analysis of Substrate Integrated Nonradiative Dielectric Waveguide," *IEEE Transactions on Microwave Theory and Techniques*, vol. 55, pp. 2502-2511, 2007.
- [52] L. Duochuan, Y. Ping, and K. Wu, "An order-reduced volume-integral equation approach for analysis of NRD-guide and H-guide millimeter-wave circuits," *IEEE Transactions on Microwave Theory and Techniques*, vol. 53, pp. 799-812, 2005.
- [53] L. Duochuan and K. Wu, "A generalized surface-volume integral-equation (SVIE) approach for analysis of hybrid planar/NRD-guide integrated circuits," *IEEE Transactions on Microwave Theory and Techniques*, vol. 53, pp. 2732-2742, 2005.
- [54] J. Attari, H. Boutayeb, and K. Wu, "A Simplified Implementation of Substrate Integrated Non-Radiative Dielectric Waveguide at Millimeter-Wave Frequencies," *Progress In Electromagnetics Research C*, vol. 55, pp. 83-94, 2014.
- [55] M. Z. A. A. Aziz and M. K. A. Rahim, "Wireless MIMO Channel Capacity Using Double Stage Diversity Technique," *Wireless Personal Communications*, vol. 85, pp. 2067-2081, Dec 2015.
- [56] H. C. Lo, D. B. Lin, T. C. Yang, and H. J. Li, "Effect of Polarization on the Correlation and Capacity of Indoor MIMO Channels," *International Journal of Antennas and Propagation*, 2012.

- [57] P. Mondal and K. Wu, "Single Mode Operation of Substrate Integrated Non-Radiative Dielectric Waveguide and an Excitation Scheme of LSE<sub>11</sub> Mode," *IEEE Microwave and Wireless Components Letters*, vol. 23, pp. 418-420, 2013.
- [58] F. Costa, S. Genovesi, and A. Monorchio, "Normalization-Free Chipless RFIDs by Using Dual-Polarized Interrogation," *IEEE Transactions on Microwave Theory and Techniques*, vol. 64, pp. 310-318, 2016.
- [59] O. A. Peverini, G. Virone, G. Addamo, and R. Tascone, "Development of passive microwave antenna-feed systems for wide-band dual-polarisation receivers," *IET Microwaves, Antennas & Propagation*, vol. 5, pp. 1008-1015, 2011.
- [60] J. D. Joannopoulos, S. G. Johnson, J. N. Winn, and R. D. Meade, *Photonic Crystals: Molding the Flow of Light*: Princeton University Press, 2011.
- [61] M. Plihal, A. Shambrook, A. A. Maradudin, and P. Sheng, "Two-dimensional photonic band structures," *Optics communications*, vol. 80, pp. 199-204, 1991.
- [62] "ANSYS® Academic Research, Release 16.2."
- [63] D. Gottlieb and C.-W. Shu, "On the Gibbs phenomenon and its resolution," *SIAM review*, vol. 39, pp. 644-668, 1997.
- [64] J. Coonrod, "General information of dielectric constants for circuit design using Rogers high frequency materials," *Rogers Corp., Tech. Rep*, 2010.
- [65] T. Shimizu and T. Yoneyama, "NRD-guide and waveguide H-plane transition and its application for lens antenna feeding structure," *Electronics and Communications in Japan Part II-Electronics*, vol. 90, pp. 39-48, 2007.
- [66] P. Mondal and K. Wu, "Single Mode Operation of Substrate Integrated Non-Radiative Dielectric Waveguide and an Excitation Scheme of LSE<sub>11</sub> Mode," *IEEE Microwave and Wireless Components Letters*, vol. 23, pp. 418-420, Aug 2013.
- [67] A. Y. Simba, M. Yamamoto, T. Nojima, and K. Itoh, "Broadside linear array of resonant type leaky-wave antenna composed of image NRD guide," *IEE Proceedings - Microwaves, Antennas and Propagation*, vol. 151, pp. 404-408, 2004.
- [68] M. Esquiús-Morote, B. Fuchs, J. F. Zürcher, and J. R. Mosig, "Extended SIW for TE<sub>m0</sub> and TE<sub>0n</sub> Modes and Slotline Excitation of the TE<sub>01</sub> Mode," *IEEE Microwave and Wireless Components Letters*, vol. 23, pp. 412-414, 2013.
- [69] D. M. Pozar, *Microwave Engineering, 4th Edition*: Wiley, 2011.
- [70] J. C. Rautio and S. Arvas, "Measurement of Planar Substrate Uniaxial Anisotropy," *IEEE Transactions on Microwave Theory and Techniques*, vol. 57, pp. 2456-2463, 2009.
- [71] A. A. Sakr, W. Dyab, and K. Wu, "Image theory based miniaturization of nonradiative dielectric coupler for millimeter wave integrated circuits," in *IEEE MTT-S Int. Microw. Symp. Dig.*, 2017, pp. 463-465.
- [72] R. Mongia, I. J. Bahl, P. Bhartia, and S. J. Hong, *RF and Microwave Coupled-line Circuits*: Artech House, 2007.
- [73] C. Yeh, *et al.*, "Accuracy of directional coupler theory in fiber or integrated optics applications," *JOSA*, vol. 68.8, pp. 1079-1083, 1978.

- [74] D. Deslandes and K. Wu, "Accurate modeling, wave mechanisms, and design considerations of a substrate integrated waveguide," *IEEE Transactions on Microwave Theory and Techniques*, vol. 54, pp. 2516-2526, 2006.
- [75] J. Uher, J. Bornemann, and U. Rosenberg, *Waveguide Components for Antenna Feed Systems: Theory and CAD*: Artech House, 1993.
- [76] H. J. Riblet, "The Short-Slot Hybrid Junction," *Proceedings of the IRE*, vol. 40, pp. 180-184, 1952.
- [77] U. Rosenberg and W. Speldrich, "A new waveguide directional coupler/hybrid type-favorably suited for millimeter wave application," in *IEEE MTT-S Int. Microw. Symp. Dig.*, 2000, pp. 1311-1314 vol.3.
- [78] S. Liu, L. W. Li, M. S. Leong, and T. S. Yeo, "Rectangular Conducting Waveguide Filled With Uniaxial Anisotropic Media: a Modal Analysis and Dyadic Green's Function - Abstract," *J. electromagn. waves appl.*, vol. 14, pp. 45-47, 2000/01/01 2000.
- [79] J. C. Rautio and S. Arvas, "Measurement of Planar Substrate Uniaxial Anisotropy," *IEEE Trans. Microw. Theory Techn.*, vol. 57, pp. 2456-2463, 2009.
- [80] J. A. Kong, *Electromagnetic Wave Theory*: Wiley, 1990.
- [81] A. Navarrini and R. Nesti, "Symmetric Reverse-Coupling Waveguide Orthomode Transducer for the 3-mm Band," *IEEE Trans. Microw. Theory Techn.*, vol. 57, pp. 80-88, 2009.
- [82] J. A. Ruiz-Cruz, J. R. Montejo-Garai, and J. M. Rebollar, "Short-slot E- and H-plane waveguide couplers with an arbitrary power division ratio," *International Journal of Electronics*, vol. 98, pp. 11-24, 2011.
- [83] S. Liu, L. Li, M. Leong, and T. Yeo, "Rectangular conducting waveguide filled with uniaxial anisotropic media: A modal analysis and dyadic Green's function," *Progress In Electromagnetics Research*, vol. 25, pp. 111-129, 2000.
- [84] J. Helander, K. Zhao, Z. Ying, and D. Sjöberg, "Performance Analysis of Millimeter-Wave Phased Array Antennas in Cellular Handsets," *IEEE Antennas and Wireless Propagation Letters*, vol. 15, pp. 504-507, 2016.
- [85] J. Song, J. Choi, S. G. Larew, D. J. Love, T. A. Thomas, and A. A. Ghosh, "Adaptive Millimeter Wave Beam Alignment for Dual-Polarized MIMO Systems," *IEEE Transactions on Wireless Communications*, vol. 14, pp. 6283-6296, 2015.
- [86] S. Liao, N. Gopalsami, T. W. Elmer, E. R. Koehl, A. Heifetz, K. Avers, *et al.*, "Passive Millimeter-Wave Dual-Polarization Imagers," *IEEE Transactions on Instrumentation and Measurement*, vol. 61, pp. 2042-2050, 2012.
- [87] A. A. Omar and Z. Shen, "Double-Sided Parallel-Strip Line Resonator for Dual-Polarized 3-D Frequency-Selective Structure and Absorber," *IEEE Transactions on Microwave Theory and Techniques*, vol. PP, pp. 1-9, 2017.
- [88] M. A. Islam and N. C. Karmakar, "Real-World Implementation Challenges of a Novel Dual-Polarized Compact Printable Chipless RFID Tag," *IEEE Transactions on Microwave Theory and Techniques*, vol. 63, pp. 4581-4591, 2015.

- [89] A. A. Sakr, W. M. Dyab, and K. Wu, "Theory of Polarization Selective Coupling and its Application to Design of Planar Orthomode Transducers," *IEEE Transactions on Antennas and Propagation*, vol. PP, pp. 1-1, 2017.
- [90] A. A. Sakr, W. Dyab, and K. Wu, "Design Methodologies of Compact Orthomode Transducers Based on Mechanism of Polarization Selectivity," *IEEE Transactions on Microwave Theory and Techniques*, vol. PP, pp. 1-12, 2018.
- [91] E. Hadge, "Compact Top-Wall Hybrid Junction," *Transactions of the IRE Professional Group on Microwave Theory and Techniques*, vol. 1, pp. 29-30, 1953.
- [92] U. Rosenberg and W. Speldrich, "A new waveguide directional coupler/hybrid type-favorably suited for millimeter wave application," in *2000 IEEE MTT-S International Microwave Symposium Digest (Cat. No.00CH37017)*, 2000, pp. 1311-1314 vol.3.
- [93] H. J. Riblet, "The Short-Slot Hybrid Junction," *Proc. IRE*, vol. 40, pp. 180-184, 1952.
- [94] H. Uchimura, T. Takenoshita, and M. Fujii, "Development of a "laminated waveguide"," *IEEE Transactions on Microwave Theory and Techniques*, vol. 46, pp. 2438-2443, 1998.
- [95] S. Germain, D. Deslandes, and K. Wu, "Development of substrate integrated waveguide power dividers," in *CCECE 2003 - Canadian Conference on Electrical and Computer Engineering. Toward a Caring and Humane Technology (Cat. No.03CH37436)*, 2003, pp. 1921-1924 vol.3.
- [96] T. Djerafi, A. Patrovsky, K. Wu, and S. O. Tatu, "Recombinant Waveguide Power Divider," *IEEE Transactions on Microwave Theory and Techniques*, vol. 61, pp. 3884-3891, 2013.
- [97] F. M. Ghannouchi and A. Mohammadi, *The six-port technique with microwave and wireless applications*: Artech House, 2009.
- [98] C. A. Hoer and K. C. Roe, "Using an Arbitrary Six-Port Junction to Measure Complex Voltage Ratios," *IEEE Transactions on Microwave Theory and Techniques*, vol. 23, pp. 978-984, 1975.
- [99] X. Xu, R. G. Bosisio, and K. Wu, "A new six-port junction based on substrate integrated waveguide technology," *IEEE Transactions on Microwave Theory and Techniques*, vol. 53, pp. 2267-2273, 2005.
- [100] G. F. Engen, "The Six-Port Reflectometer: An Alternative Network Analyzer," in *1977 IEEE MTT-S International Microwave Symposium Digest*, 1977, pp. 44-46.
- [101] N. Chagtmi, N. Boulejfen, and F. M. Ghannouchi, "Augmented Hammerstein model for six-port-based wireless receiver calibration," *IET Communications*, vol. 11, pp. 951-960, 2017.
- [102] J. Moghaddasi, T. Djerafi, and K. Wu, "Multiport Interferometer-Enabled 2-D Angle of Arrival (AOA) Estimation System," *IEEE Transactions on Microwave Theory and Techniques*, vol. 65, pp. 1767-1779, 2017.
- [103] B. Jokanovic and A. Marincic, "Microwave circuits based on six-port junction," in *6th International Conference on Telecommunications in Modern Satellite, Cable and Broadcasting Service, 2003. TELSIKS 2003.*, 2003, pp. 218-222 vol.1.

- [104] J. Butler, "Beam-forming matrix simplifies design of electronically scanned antennas," *Electronic design*, vol. 12, pp. 170-173, 1961.
- [105] "American National Standard Methods of Measurement of the Electromagnetic and Operational Compatibility of Unlicensed Personal Communications Services (UPCS) Devices - Redline," *ANSI C63.17-2013 - Redline*, pp. 1-126, Oct. 9 2013.
- [106] H. N. Chu and T. G. Ma, "An Extended 4 x 4 Butler Matrix With Enhanced Beam Controllability and Widened Spatial Coverage," *IEEE Transactions on Microwave Theory and Techniques*, vol. PP, pp. 1-11, 2017.
- [107] J. Blass, "Multidirectional antenna-a new approach to stacked beams," in *1958 IRE International Convention Record*, 1960, pp. 48-50.
- [108] H. Moody, "The systematic design of the Butler matrix," *IEEE Transactions on Antennas and Propagation*, vol. 12, pp. 786-788, 1964.
- [109] C. H. Tseng, C. J. Chen, and T. H. Chu, "A Low-Cost 60-GHz Switched-Beam Patch Antenna Array With Butler Matrix Network," *IEEE Antennas and Wireless Propagation Letters*, vol. 7, pp. 432-435, 2008.
- [110] C. C. Chang, R. H. Lee, and T. Y. Shih, "Design of a Beam Switching/Steering Butler Matrix for Phased Array System," *IEEE Transactions on Antennas and Propagation*, vol. 58, pp. 367-374, 2010.
- [111] M. Nedil, T. A. Denidni, and L. Talbi, "Novel butler matrix using CPW multilayer technology," *IEEE Transactions on Microwave Theory and Techniques*, vol. 54, pp. 499-507, 2006.
- [112] P. Chen, W. Hong, Z. Kuai, J. Xu, H. Wang, J. Chen, *et al.*, "A Multibeam Antenna Based on Substrate Integrated Waveguide Technology for MIMO Wireless Communications," *IEEE Transactions on Antennas and Propagation*, vol. 57, pp. 1813-1821, 2009.
- [113] T. Djerafi and K. Wu, "A Low-Cost Wideband 77-GHz Planar Butler Matrix in SIW Technology," *IEEE Transactions on Antennas and Propagation*, vol. 60, pp. 4949-4954, 2012.
- [114] L. T. Hildebrand, "Results for a simple compact narrow-wall directional coupler," *IEEE Microwave and Guided Wave Letters*, vol. 10, pp. 231-232, 2000.
- [115] Y. Cassivi and K. Wu, "Substrate integrated circuits concept applied to the nonradiative dielectric guide," *IEE Proceedings - Microwaves, Antennas and Propagation*, vol. 152, pp. 424-433, 2005.
- [116] J. B. Davies, "Propagation in Rectangular Waveguide Filled with Skew Uniaxial Dielectric," *IEEE Transactions on Microwave Theory and Techniques*, vol. 15, pp. 372-376, 1967.
- [117] K. Sun, J. K. Lee, and J. W. Graham, "Fields and Wave Modes Analysis of Rectangular Waveguide Filled With Uniaxial Medium," *IEEE Transactions on Microwave Theory and Techniques*, vol. 64, pp. 3429-3440, 2016.

## APPENDIX A – LIST OF PUBLICATIONS

### Patent

[1] **Sakr, A.**, Dyab, W. & Wu, K. (2017). "Polarization Selective Coupler (PSC)." Submitted to U.S. Patent with application No. 15/853,312. 22 Dec. 2017.

### Peer reviewed Journal Papers

- [1] **A. A. Sakr**, W. Dyab and K. Wu, "A Dually-Polarized Six-Port Junction Based on Polarization Selective Coupling for Polarization-Inclusive Remote Sensing". In *IEEE Transactions on Microwave Theory and Techniques*.
- [2] **A. A. Sakr**, W. Dyab and K. Wu, "Modelling Effective Anisotropy of Substrate Integrated Nonradiative Dielectric Waveguide for Polarization Diversity". In to *IEEE Transactions on Microwave Theory and Techniques*.
- [3] W. Dyab, **A. A. Sakr** and K. Wu, "Empowering Technologies for Green Wireless Systems: Theory of Dually-Polarized Components for Beamforming Applications". Submitted to *IEEE Transactions on Microwave Theory and Techniques*.
- [4] **A. A. Sakr**, W. Dyab and K. Wu, "Theory of Polarization Selective Coupling and its Application to Design of Planar Orthomode Transducers". In *IEEE Transactions on Antennas and Propagation*, vol. 66, no. 2, pp. 749-762, Feb. 2018.
- [5] **A. A. Sakr**, W. Dyab and K. Wu, "Design Methodologies of Compact Orthomode Transducers Based on Mechanism of Polarization Selectivity," In *IEEE Transactions on Microwave Theory and Techniques*, vol. 66, no. 3, pp. 1279-1290, March 2018.

### Refereed Conference Papers and Presentations

- [1] **A. A. Sakr**, W. Dyab and K. Wu, "Dually-Polarized Hybrid Junction Based on Polarization-Selective Periodic Wall," Accepted in International Microwave Symposium (IMS2018).
- [2] W. Dyab, **A. A. Sakr** and K. Wu, "Integrated Polarization Converter for Planar Cross-Polarized Millimeter Wave Components," Accepted in International Microwave Symposium (IMS2018).

- [3] **A. A. Sakr**, W. Dyab and K. Wu, “Planar Orthomode Transducer Based on Effective Polarization-Independent Coupling,” Accepted in International Microwave Symposium (IMS2018).
- [4] **A. A. Sakr**, W. Dyab and K. Wu, “Image Theory based Miniaturization of Nonradiative Dielectric Coupler for Millimeter Wave Integrated Circuits,” International Microwave Symposium (IMS2017), Honolulu, HI, June 2017.
- [5] W. Dyab, **A. A. Sakr** and K. Wu, “Characterization of Substrate Integrated Non Radiative Dielectric Slab Waveguide for Cross-Polarized mm-wave Components,” International Microwave Symposium (IMS2017), Honolulu, HI, June 2017.
- [6] W. Dyab, **A. A. Sakr** and K. Wu, “Millimeter-Wave Polarization-Inclusive Remote Sensing System Based on Dually-Polarized Six-Port Junction,” Accepted in Global Symposium on Millimeter waves (GSMM2018).
- [7] W. Dyab, **A. A. Sakr** and K. Wu, “Arbitrarily Polarized Antennas Based on Periodic Media With Tilted Axis of Periodicity,” Accepted in the 18th International Symposium on Antenna Technology and Applied Electromagnetics ANTEM.